Modeling wave propagation in nonlinear solids with slow dynamics

Harold Berjamin

Aix-Marseille Université
École Doctorale 353 – Sciences pour l'Ingénieur :
Mécanique, Physique, Micro et Nanoélectronique
Laboratoire de Mécanique et d'Acoustique

Thèse présentée pour obtenir le grade universitaire de docteur

Discipline : Sciences pour l'Ingénieur
Spécialité : Acoustique

Modeling wave propagation in nonlinear solids with slow dynamics

Harold BERJAMIN

Soutenue le 29/11/2018 devant le jury composé de

M. Claude-Henri LAMARQUE	Professeur, ENTPE	Président
M. Jean-Jacques MARIGO	Professeur, École Polytechnique	Rapporteur
M. William J. PARNELL	Professeur, University of Manchester	Rapporteur
M^{me} Sonia FLISS	Maître de Conférences, ENSTA ParisTech	Examinateur
M. Koen VAN DEN ABEELE	Professeur, KU Leuven	Examinateur
M. Bruno LOMBARD	Directeur de Recherche, CNRS	Directeur de thèse
M. Guillaume CHIAVASSA	Professeur, École Centrale de Marseille	Co-directeur de thèse
M. Nicolas FAVRIE	Maître de Conférences, Aix-Marseille Université	Co-directeur de thèse

Numéro national de thèse/suffixe local : 2018AIXM0680/043ED353

I also remember a remark of Albert Einstein, which certainly applies to music. He said, in effect, that everything should be as simple as it can be but not simpler!

— Roger Sessions
In *The New York Times*, January 8, 1950

Acknowledgments

À l'automne 2015, on parlait de la COP21, de la présence d'eau liquide sur Mars, de Vigipirate et du Bataclan. Il y a trois ans déjà ? Oui, cela fait déjà trois ans que je me suis installé dans les nouveaux locaux du LMA, suite à l'obtention de mon financement doctoral. À ce titre, je voudrais remercier le personnel de l'école doctorale et du laboratoire qui a contribué à mon intégration dans mon nouvel environnement de travail.

Courant 2014, un stage au LMA encadré par Bruno Lombard et Christophe Vergez avait satisfait mon appétit naissant d'activités de recherche en acoustique. Merci Bruno et Christophe de m'avoir donné le virus ! C'était évident pour moi de poursuivre dans cette voie. Bruno, je n'oublierai pas ton implication exemplaire tout au long de cette thèse, tes bons conseils, et les débats variés qui ont jalonné ce travail. La collaboration avec Guillaume Chiavassa et Nicolas Favrie a été très précieuse. Merci Guillaume pour ton implication dans le développement de schémas numériques qui marchent, et pour tout le reste. Merci Nicolas pour ta contribution — et vive les systèmes hyperboliques d'ordre un ! Ce travail a aussi fait l'objet d'un Défi Infiniti (avec Cédric Payan, Guillaume Renaud, Sylvain Haupert et Stéphane Junca), et a bénéficié de la participation d'Emmanuelle Sarrouy et de Marcel Rémillieux. Pendant ces trois années, j'ai eu la chance de rencontrer de nombreux scientifiques qui m'ont fait avancer. Il serait indigeste de les nommer tous, comme il serait injuste d'en nommer quelques-uns seulement. Merci à vous tous.

En repensant au jour de la soutenance, il m'est impossible de ne pas mentionner le jury ; un grand merci aux rapporteurs (Jean-Jacques Marigo, William Parnell) et aux examinateurs (Claude-Henri Lamarque, Sonia Fliss, Koen Van Den Abeele). Je me souviendrai de votre bienveillance quand la qualité de la liaison par visioconférence avec Manchester s'est dégradée jusqu'au point de devoir utiliser mon téléphone portable. En fin de soutenance, on m'avait soumis la question « Si c'était à refaire, qu'aurais-tu fait différemment ? »(N. Favrie). Si c'était à refaire. . .Eh bien, j'aurais opté pour un système de conférence téléphonique !

Merci à ma famille qui me soutient depuis le début ; merci à mes amis qui ont su être disponibles et me divertir de la plus belle façon, notamment ceux avec qui j'ai partagé le plaisir de faire de la musique. Un chaleureux merci aux doctorants et post-doctorants voisins qui m'ont supporté au quotidien, dans tous les sens du terme.

Marseille, le 10 janvier 2019.

Contents

CHAPTER 1

Introduction

ROCKS AND CONCRETE are solid materials encountered in many branches of engineering, such as civil, mining or petroleum engineering. In construction engineering, they provide durable and long-lasting structures which don't rust, rot, or burn. Both sedimentary rocks and concrete enter the category of consolidated granular solids. They are heterogeneous, made of grains embedded in a matrix.

During its lifetime, the material is submitted to various external solicitations, such as gravity, earthquakes, vibrations, fluid flow, impacts, temperature variations, radiation, etc. Intense external solicitations may modify the material by causing aging, e.g. the initiation and the propagation of cracks, which is one of the core concerns of damage mechanics. The non-destructive evaluation (NDE) of damage in concrete structures is an active research topic, with many applications in civil engineering. In laboratory experiments, ultrasound has shown to be a reliable inspection means to monitor damage. Developments are undergoing to adapt the technology to real engineering structures. In this context, the development of models and corresponding numerical methods is needed to benchmark NDE techniques.

Many laboratory experiments show that the mechanical behavior of rocks and concrete is complex and highly nonlinear. In this chapter, we present several experimental results from the literature (Section 1). Then, we present various models, which were introduced to reproduce the experiments (Section 2). The scope of the present study is the phenomenological modeling of geomaterials regarding wave propagation, in the framework of continuum thermomechanics (Section 3). Particular efforts are dedicated to the development of numerical

methods, suitable for making predictions about the mechanical response to small-amplitude dynamic solicitations.

1. Experimental observations

As done in other literature reviews [43, 44, 101], we present a list of observations from quasistatic and dynamic experiments. Details on the experimental conditions can be found in the corresponding bibliographical references.

1.1. Quasistatic experiments

In the early twentieth century, several quasistatic experiments have been made, in order to measure the elastic constants of various types of rock (marble, granite, sandstone). The following statements are made by H. Nagaoka in 1900 [9, 92]:

> "Preliminary experiments with granite showed that Hooke's law does not hold even for very small flexure and tension, and that the after-effect is very considerable when the prism is sufficiently loaded or twisted; the deviation from the direct proportionality between the strain and stress was incomparably great as compared with that observed in common metals. [. . .] The deviation from Hooke's law was prominent in certain specimens of sandstone, and it was more marked in tension than in flexure experiments. In certain rocks it is indeed doubtful if anything like a proportionality between stress and strain can be found even for extremely small change of shape."

The results highlight such features as the nonlinearity of the material, its relaxation in time, and its memory of the loading history. In particular, loading-unloading experiments reveal the phenomenon of *hysteresis*. That is to say, the stress-strain curve for decreasing loads differs from that for increasing loads, and forms a closed loop with it after a sufficient number of cycles has been applied [9]. At small strains, these key features are also reported in later works using various experimental setups [26, 28, 41, 48, 86], which suggest that the stress may not only be a function of the strain, even a nonlinear one. Rock plasticity — i.e., non-reversible change of shape in response to applied forces [10, 120] — and rock failure occur at larger strains, but such responses are beyond the scope of the present document.

1.2. Dynamic experiments

Back to the early twentieth century, a dynamic experiment of resonance type has been developed to measure elastic moduli [61]. However, the results for rocks are hardly interpretable, partly due to the influence of experimental conditions (temperature and moisture). In the present section, we show later experimental results obtained with rock and concrete samples using dynamic solicitations.

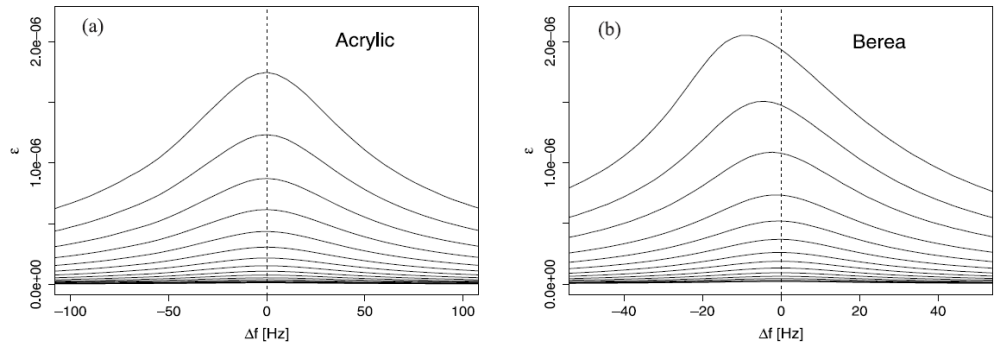

Figure 1.1. Resonance curves for (a) acrylic and for (b) Berea sandstone at different input voltages. Nonlinearity is evidenced in Berea sandstone by the shift of the resonance peak. The reference center frequency is 2150 Hz for acrylic and 2765 Hz for Berea sandstone. Reproduced from [105] (Fig. 1), with permission of AGU Publications.

1.2.a. *Resonance experiments*

A bar of material with length $\sim$ 30 cm is suspended on strings. Forced longitudinal vibration is induced in the sample by a piezoelectric disk glued at one of its ends. At the same time, the acceleration or the velocity of the free end is recorded [55, 115]. The first harmonic amplitude of the recorded signal is then converted into strain. A sweep of the exciting signal's frequency is performed, and the procedure is repeated for several input voltages. Figure 1.1 compares the resonance curves obtained with acrylic and with Berea sandstone. One observes a frequency-shift of the resonance peak with increasing amplitudes of solicitation in the case of Berea sandstone, which is a signature of nonlinearity. This phenomenon occurs at small strains with magnitude $\varepsilon \sim 10^{-6}$. Since the resonance frequency is proportional to the square root of the elastic modulus, this decrease of the resonance frequency is interpreted as a *softening* of the material. Moreover, the generation of higher-order harmonics has been reported [55]. Such resonance experiments have also been conducted on concrete, and in non-longitudinal setups [107].

■ *Slow dynamics.* In these experiments, a high sensitivity to the sweep rates has been found [73, 115]. A relaxation effect with long transients has been noted, and has therefore been called *slow dynamics* [132, 135]. Indeed, when forcing the sample at its fundamental resonance frequency, the softening of the material — i.e., the shift of the resonance peak — is not instantaneous. Then, when the forcing is turned off, the fundamental resonance frequency recovers gradually its initial value (*recovery*). A logarithmic time-evolution of the resonance frequency is in agreement with experimental results [133].

1.2.b. *Dynamic acousto-elastic testing*

Dynamic acousto-elastic testing (DAET) is based on the previous resonance setup [117, 118]. The sample is a bar excited around a resonance frequency by a piezoelectric device (low-frequency pump). Simultaneously, acoustic pulses propagating over a short distance are used to probe the material locally by

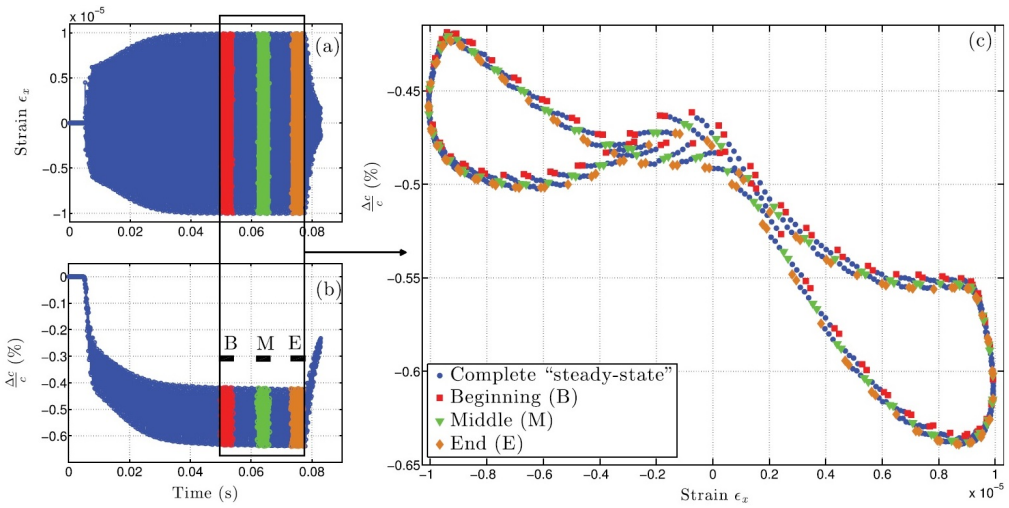

Figure 1.2. Dynamic acousto-elastic testing of Berea sandstone. (a) Evolution of the axial strain ε at the location of the probe over time. (b) Relative variation $\Delta c/c$ of the sound speed with respect to its initial value over time. (c) Hysteresis loop: $\Delta c/c$ versus ε in steady state. Reproduced from [118] (Fig. 12), with permission of AIP Publishing.

recording their arrival times (high-frequency probe). The arrival times are then converted into a measurement of the speed of sound in the material. Figure 1.2 shows experimental results so-obtained. In Fig. 1.2b, one observes the softening of the material after the pump is switched on, which is consistent with the measurements of the softening made in the resonance setup. A fast drop of the speed of sound followed by a long-time relaxation is observed (slow dynamics). In steady state, the evolution of the speed of sound with respect to the strain has the shape of an hysteresis loop (Fig. 1.2c). When the pump is switched off, the speed of sound recovers gradually its original value. The beginning of this recovery phase is shown in Fig. 1.2b. An overview of more recent developments can be found in [116].

1.2.c. *Pulse propagation*

A bar of material with length ~ 2 m is used. Similarly to the resonance experiments, a piezoelectric transducer is glued at one end of the sample. Here, the input signal is a short sinusoidal pulse (tone burst with Gaussian-shaped envelope). The acceleration or the particle velocity is recorded at several abscissas along the sample [87, 116, 131]. In the recorded signals, the amplitude of higher-order harmonics is shown to increase with the propagation distance, which is a typical nonlinear feature. Moreover, the arrival of the pulse at one given abscissa is all the more delayed as the amplitude of the pulse is large, which illustrates the softening of the material with increasing amplitudes. The nonlinear distortion leading to triangular signals and the delay of the pulse are both illustrated in Fig. 1.3.

The section on experimental observations can be summarized as follows. Even at low strain amplitudes, quasistatic experiments reveal nonlinear hysteretic stress-strain relationships. Dynamic experiments highlight a nonlinear behavior

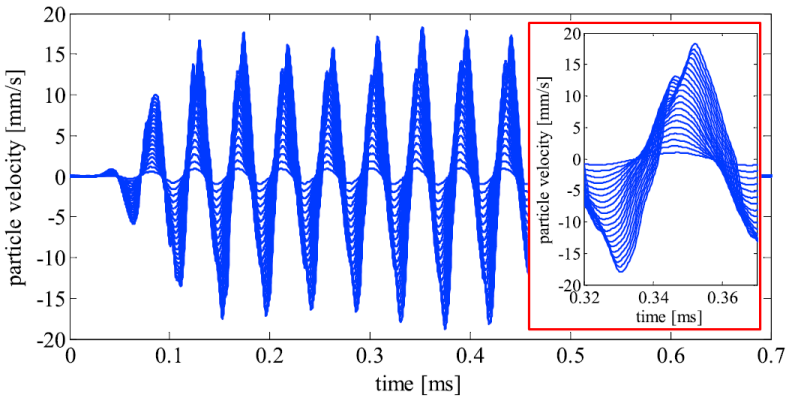

Figure 1.3. Pulse propagation in Berea sandstone. Time histories of the axial component of the particle velocity measured at 500 mm from the source for several amplitudes of a pulse centered at 22.4 kHz. Reproduced from [116] (Fig. 9), with permission of AGU Publications.

with long-time softening/recovery processes (slow dynamics). One should also mention that dissipation occurs in the material.

2. Models

The characterization of geomaterials has been taken up using various modeling approaches. In the present section, we review several types of models, aimed at reproducing the experimental observations. As indicated in [116, 118], a model which reproduces all these features is not known. The mechanical modeling of geomaterials is still an open subject.

2.1. Nonlinear viscoelasticity

■ *Hyperelasticity.* The observation of harmonic generation and wavefront distortion in one-dimensional experiments suggests to develop nonlinear stress-strain relationships. The simplest of such models is based on the assumption that the axial stress σ is a polynomial function of the axial strain ε, e.g.

$$\sigma = M_0\,\varepsilon\left(1-\beta\varepsilon-\delta\varepsilon^2\right), \tag{1.1}$$

where $M_0 > 0$ denotes the elastic modulus, and β, δ are higher-order elastic constants. The stress (1.1) may be written as the derivative of the strain energy density function $W = (\frac{1}{2} - \frac{1}{3}\beta\varepsilon - \frac{1}{4}\delta\varepsilon^2)\,M_0\,\varepsilon^2$ with respect to the strain. The notion of *hyperelastic material* refers to the three-dimensional case, where a similar definition holds. Instead of being a function of the scalar strain ε, the strain energy W is a function of a strain tensor $\boldsymbol{\chi}$. The polynomial constitutive law (1.1) and other models of hyperelasticity are discussed in the next chapter (p. 15).

In hyperelasticity, the speeds of sound are modified when an external load is applied, and their variations depend explicitly on the elastic constants. Called *acousto-elasticity*, this effect enables the measurement of higher-order elastic

constants, by measuring the speeds of sound in a statically loaded sample [51]. Under the assumption that geomaterials have a hyperelastic behavior, such experiments have been conducted on rocks and concrete. Several sets of numerical values can be found in the literature [15, 54, 71], which show that the effective nonlinearity parameters β, δ in (1.1) are much larger in geomaterials than in other solids.

■ *Viscoelastic dissipation.* The relaxation in time observed in quasistatic experiments evidences the viscoelastic behavior of geomaterials, i.e. they do not strain instantaneously when a static load is applied. One consequence of such a dissipative relaxation mechanism is the finite height of the resonance peaks obtained in dynamic experiments. An extensive literature on viscoelastic behavior can be found in relation with polymers and rubber-like materials [32, 47, 50, 66, 143]. In the uniaxial case, the simplest rheological model is the Kelvin–Voigt model

$$\sigma = M_0\,\varepsilon\left(1-\beta\varepsilon-\delta\varepsilon^2\right)+\nu\dot{\varepsilon}\,, \tag{1.2}$$

where $\nu > 0$ is the viscosity and $\dot{\varepsilon} = \partial_t\varepsilon$ is the strain rate. This model has a single characteristic relaxation time ν/M_0.

To examine the ability of (1.2) to reproduce the dynamic experimental features, we follow the steps in [18, 29]. A bar of length L with density ρ_0 is considered. A displacement forcing $u|_{x=0} = U$ is applied at the abscissa $x = 0$. A free end is located at the abscissa $x = L$, i.e. $\sigma|_{x=L} = 0$. The displacement is written $u(x,t) = U(t)+q(t)\,\Phi_0(x)$, where $\Phi_0(x) = \sin(k_0x)$ is the first mode shape of the undamped linear system, corresponding to the wavenumber $k_0 = \pi/(2L)$. This Ansatz is injected in the conservation of momentum $\rho_0\partial_{tt}u = \partial_x\sigma$, where σ satisfies (1.2) and $\varepsilon = \partial_x u$. Multiplication by Φ_0 and integration over $x \in [0, L]$ gives the nonlinear oscillator equation

$$\ddot{q}+\frac{\omega_0}{Q}\dot{q}+{\omega_0}^2\left(q-\gamma_2q^2-\gamma_3q^3\right)=F\,, \tag{1.3}$$

where $\omega_0 = k_0\sqrt{M_0/\rho_0}$, $Q \propto \nu^{-1}$, $\gamma_2 \propto \beta$, $\gamma_3 \propto \delta$, and $F \propto \ddot{U}$. Eq. (1.3) amounts to the Duffing equation if $\gamma_2 = 0$, i.e. $\beta = 0$ [59].

In the harmonic regime where $F = V\cos(\omega t)$ and $q \simeq A\cos(\omega t+\phi)$, the Duffing oscillator reproduces the resonance curves in Fig. 1.1b at low strain regime [105, 134]. The resonance angular frequency corresponding to Fig. 1.1b is $\omega_0\sqrt{1-(2Q^2)^{-1}} = 2\pi\times 2765$ rad/s and the quality factor is $Q = 65$. The characteristic relaxation time $2Q/\omega_0 \approx 7.5$ ms of the oscillator (1.3) has the same order of magnitude as the ring-up time of Fig. 1.2a (the experimental setups of Figs. 1.1 and 1.2 are comparable). At the abscissa $x = 0$, the effective elastic modulus $M = \partial\sigma/\partial\varepsilon$ equals

$$M|_{x=0} = M_0\left(1-3\delta A^2{k_0}^2\cos^2(\omega t+\phi)\right), \tag{1.4}$$

which periodically equals M_0 (here, $\beta = 0$). Thus, the model (1.2) is not able to reproduce the drop of the elastic modulus in Fig. 1.2b.

2.2. Hysteretic nonlinearity

Several constitutive models incorporate explicitly the hysteresis observed in quasistatic experiments (see e.g. [52, 70, 88, 144] for an overview). In the field of solid mechanics, some models of hysteresis are used to describe plastic behavior. The present section focuses on hysteresis models used in nonlinear acoustics.

■ *Preisach–Mayergoyz (PM).* The Preisach model of hysteresis was introduced to represent scalar ferromagnetism [144]. It belongs to a class of discontinuous hysteresis models with internal variables, which is based on a population of hysteretic elements. As such, its number of parameters is linked to the number of hysteretic elements. For a sinusoidal strain excitation, the hysteretic elements yield a constitutive law of the form [42, 140, 141]

$$\sigma = M_0\,\varepsilon\left(1-\beta\varepsilon-\delta\varepsilon^2\right)+\sigma_H \tag{1.5}$$

where

$$-\frac{\sigma_H}{M_0}=\int\alpha\,(\varepsilon_\mathrm{m}+\varepsilon\,\mathrm{sgn}\,\dot\varepsilon)\,\mathrm{d}\varepsilon\,. \tag{1.6}$$

Here, the stress depends on the sign of the strain rate $\mathrm{sgn}\,\dot\varepsilon$, and on the maximum strain excursion ε_m (i.e., the strain amplitude over one period of signal). The constant α is the strength of the hysteresis. A stress-strain relationship deduced from (1.5)-(1.6) is represented in Fig. 1.4a. A hysteresis curve is obtained, which has sharp changes of slope at its extremities. A similar equation to (1.5)-(1.6) is obtained in [88] for the Hogdon hysteresis model.

The phenomenological Preisach framework can represent real microscopic features such as rough surfaces interacting via adhesion forces [13, 109]. An extension of the model with random transitions can account for long-time relaxation (slow dynamics) as well [122]. A quantitative method to reproduce stress-strain curves is proposed in [41]. However, later works point out several issues with the model [26].

■ *Nazarov et al.* Two kinds of models for hysteretic nonlinearity have been proposed [70], which both write as

$$\sigma = M_0\,\varepsilon+\sigma_H+\nu\dot\varepsilon\,, \tag{1.7}$$

when Kelvin–Voigt viscoelasticity with constant ν is taken into account. In the case of a sinusoidal strain excitation, the first hysteretic model reads [95]

$$-\frac{\sigma_H}{M_0}=\alpha\varepsilon_\mathrm{m}\varepsilon+\begin{cases}\dfrac{\beta_1}{2}\varepsilon^2-\dfrac{\beta_1+\beta_2}{4}{\varepsilon_\mathrm{m}}^2, & \dot\varepsilon>0,\\[2ex] -\dfrac{\beta_2}{2}\varepsilon^2+\dfrac{\beta_1+\beta_2}{4}{\varepsilon_\mathrm{m}}^2, & \dot\varepsilon<0,\end{cases} \tag{1.8}$$

where $\alpha,\beta_{1,2}$ are material parameters. The symbol ε_m denotes the strain amplitude over one period of signal. The case $\beta_1=\beta_2$ is discussed in [102]. The second

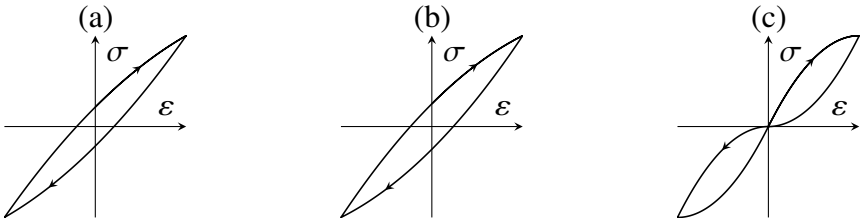

Figure 1.4. (a) Typical stress-strain relationship obtained with the law (1.5)-(1.6) when the strain is a sinusoidal function of time. (b)-(c) Similar curves deduced from the models (1.7)-(1.8) and (1.7)-(1.9) respectively, where $\nu = 0$. The arrows indicate how time increases along the curve.

hysteretic model reads [94]

$$-\frac{\sigma_H}{M_0} = \frac{1}{n}\begin{cases} \gamma_1 \varepsilon^n, & \varepsilon > 0, \dot{\varepsilon} > 0, \\ -\gamma_2 \varepsilon^n + (\gamma_1 + \gamma_2)(\varepsilon_{\rm m})^{n-1}\varepsilon, & \varepsilon > 0, \dot{\varepsilon} < 0, \\ -\gamma_3 \varepsilon^n, & \varepsilon < 0, \dot{\varepsilon} < 0, \\ \gamma_4 \varepsilon^n - (\gamma_3 + \gamma_4)(-\varepsilon_{\rm m})^{n-1}\varepsilon, & \varepsilon < 0, \dot{\varepsilon} > 0, \end{cases} \tag{1.9}$$

where $\gamma_{1,2,3,4}$ and $n \in \{2, 3\}$ are material parameters[1]. Stress-strain relationships deduced from (1.7)-(1.8) and (1.7)-(1.9) are represented in Fig. 1.4b and Fig. 1.4c, respectively.

■ *Pecorari.* Several constitutive laws have been proposed in [111], where the strain is expressed in terms of the stress:

$$\varepsilon = \frac{\sigma}{M_0} + \varepsilon_H \,. \tag{1.10}$$

For so-called "dislocations-glide point defects interaction", the constitutive law (1.10) is given by [110, 111]

$$\varepsilon_H = S_1 \,\mathrm{H}(\sigma_{\rm m} - \sigma_{\rm c}) \begin{cases} (-\sigma_{\rm m} + \sigma_{\rm c})\,\mathrm{H}(-\sigma_{\rm m} + 2\sigma_{\rm c} - \sigma) \\ \quad + (\sigma - \sigma_{\rm c})\,\mathrm{H}(\sigma + \sigma_{\rm m} - 2\sigma_{\rm c}), & \dot{\sigma} > 0, \\ (\sigma_{\rm m} - \sigma_{\rm c})\,\mathrm{H}(\sigma - \sigma_{\rm m} + 2\sigma_{\rm c}) \\ \quad + (\sigma + \sigma_{\rm c})\,\mathrm{H}(\sigma_{\rm m} - 2\sigma_{\rm c} - \sigma), & \dot{\sigma} < 0, \end{cases} \tag{1.11}$$

and H denotes the Heaviside step function. Here, S_1 is a material parameter, $\sigma_{\rm m}$ represents the stress amplitude, and $\sigma_{\rm c}$ is a critical stress which activates the hysteresis. The latter follows a given distribution, and averaging of (1.11) over the values of $\sigma_{\rm c}$ is performed. Then, [111] introduces micro-cracks with finite stiffness, which constitutive law (1.10) is given by

$$\varepsilon_H = S_1 \mathrm{H}(\sigma + \sigma_{\rm c})\,(\sigma + \sigma_{\rm c})\,. \tag{1.12}$$

Again, an averaging procedure is applied. A composite model combining both mechanisms (1.11)-(1.12) is presented in [110, 111], showing qualitative agreement with experimental features (softening, hysteresis loops), except the slow dynamics.

[1] A sign mistake has been found in Eq. (4) of [95], which corresponds to the case $n = 2$. For $n = 2$, the case $\gamma_2 = \gamma_4 = 0$ is discussed in [93]. The case $\gamma_1 = \cdots = \gamma_4 \neq 0$ is discussed in [102].

■ *Lebedev et al.* A model was introduced to describe the hysteresis due to adhesive intergrain contacts, and the long-time recovery (slow dynamics) [64]. Both effects are activated when a critical strain level is exceeded. Under this barrier, the stress is a polynomial function of the strain. According to [64, 100], the stress may be written as

$$\sigma = M_0\,\varepsilon\left(1-\beta\varepsilon-\delta\varepsilon^2\right)+\sigma_H+\Lambda\ln(a+\dot{\varepsilon})\,. \tag{1.13}$$

The hysteretic stress σ_H is obtained by averaging,

$$\sigma_H = \iint w(R,\xi)\,\tilde{\sigma}_H(R,\xi)\,\mathrm{d}R\,\mathrm{d}\xi\,, \tag{1.14}$$

where $\tilde{\sigma}_H$ is the stress deduced from the adhesive force at an elementary contact with curvature radius R and pre-compressed indentation depth ξ. The contact parameters R, ξ are normally distributed with distribution w. The parameters Λ, a in (1.13) control the slow dynamics.

In the case of penny-shaped adhesive cracks, a similar model has been developed by another group to model the hysteresis [13]. In these works, the slow dynamics is justified by the fact that "due to thermally induced creep motion the internal roughness may slowly vary in time", but is not included in the model. By the same authors, similar work justifies the hysteresis using dry friction [12].

All these models have in common the hysteresis in the stress-strain relationship, i.e. brutal changes of slope with the sign of the strain rate. Thus, singularities are introduced in the constitutive law, which must be handled with care when solving the equations of motion. Almost all models involve the amplitude of a sinusoidal signal, which restricts the use to periodic solicitations. In the dedicated literature, well-posedness considerations are often discarded, which leads to questioning the validity of the approach. Nevertheless, many of these models have shown at least qualitative agreement with experiments, which is one reason for their success in the communities of NDE and geophysics.

2.3. Framework of continuum damage theories

The study of cracked solids has lead to the development of damage mechanics models [57, 58, 66, 67]. This type of approach does not incorporate explicitly a hysteresis in the constitutive law. Instead, it is assumed that damage can be accounted for by a set of variables of state (in the simplest case, a scalar variable g). Whether related to micromechanics or of purely phenomenological nature, these variables represent the effect of damage evolution on the material behavior. The choice of a given constitutive damage model is guided by experiments and by the principles of continuum thermomechanics, sometimes also by micromechanical considerations.

In this section, we present several models of this type. They all introduce a scalar variable g which modifies the elastic constants of the material. A particularity of the models presented hereinafter is that they allow the variable g to increase (destruction/softening process, $\dot{g} \geqslant 0$) or to decrease (healing/recovery

process, $\dot{g} \leqslant 0$), whereas classical continuum damage mechanics does only consider destruction processes. This type of approach is the background of the present study.

■ *Lyakhovsky et al.* A continuum damage model is proposed, which has a transition between two regimes [74]. The first regime is ductile (healing is possible), whereas the second regime is brittle (irreversible damage). The model is based on a specific free energy ψ which satisfies

$$\rho_0 \psi = \tilde{W}(\boldsymbol{\varepsilon}, g) + \phi(g) + \hat{\beta}\,\mathrm{tr}(\boldsymbol{\varepsilon})\,(T - T_0)\,, \tag{1.15}$$

where ρ_0 is the reference mass density. The parameter $\hat{\beta}$ is the temperature expansivity by unit of reference volume, while T is the absolute temperature and T_0 its reference value. The infinitesimal strain tensor $\boldsymbol{\varepsilon} = \frac{1}{2}(\mathbf{grad}\,\boldsymbol{u} + \mathbf{grad}^{\top}\boldsymbol{u})$ where $\boldsymbol{u}$ is the displacement field may be decomposed into an elastic part and a viscoelastic part. The strain energy reads $\tilde{W} = \frac{1}{2}\lambda{\varepsilon_{\mathrm{I}}}^2 + \mu\varepsilon_{\mathrm{II}} - \gamma\varepsilon_{\mathrm{I}}\sqrt{\varepsilon_{\mathrm{II}}}$, where $\varepsilon_{\mathrm{I}} = \mathrm{tr}(\boldsymbol{\varepsilon})$, $\varepsilon_{\mathrm{II}} = \mathrm{tr}(\boldsymbol{\varepsilon}^2)$ are the first two invariants of $\boldsymbol{\varepsilon}$, and the elastic moduli are linear in g:

$$\lambda = \lambda_0 + g\lambda_1\,, \qquad \mu = \mu_0 + g\mu_1\,, \qquad \gamma = g\gamma_1\,. \tag{1.16}$$

The potential ϕ reads $\phi = \hat{\kappa}\,(g - g_1)^2\,(g - g_2)^2$, where $\hat{\kappa} > 0$ and $0 < g_1 < g_2 < 1$ are material parameters. Based on thermodynamics, the two following model equations are obtained. The Cauchy stress tensor is given by $\boldsymbol{\sigma} = \rho_0 \partial\psi/\partial\boldsymbol{\varepsilon}$, i.e.

$$\boldsymbol{\sigma} = \left(\lambda\varepsilon_{\mathrm{I}} - \gamma\sqrt{\varepsilon_{\mathrm{II}}}\right)\boldsymbol{I} + \left(2\mu - \gamma\varepsilon_{\mathrm{I}}/\sqrt{\varepsilon_{\mathrm{II}}}\right)\boldsymbol{\varepsilon}\,, \tag{1.17}$$

where $\boldsymbol{I} = \boldsymbol{\varepsilon}^0$ is the metric tensor. The evolution of the damage variable satisfies $\dot{g} = -C\partial\psi/\partial g$ where $C > 0$ is a constant:

$$\begin{aligned}\dot{g} = -C\Bigg(&\frac{\lambda_1}{2}{\varepsilon_{\mathrm{I}}}^2 + \mu_1\varepsilon_{\mathrm{II}} - \gamma_1\varepsilon_{\mathrm{I}}\sqrt{\varepsilon_{\mathrm{II}}} \\ &+ 4\hat{\kappa}\,(g - g_1)\left(g - \frac{g_1 + g_2}{2}\right)(g - g_2)\Bigg)\,.\end{aligned} \tag{1.18}$$

The evolution equation (1.18) has two stable equilibria, which are interpreted as ductile ($g \simeq g_1$) and brittle ($g \simeq g_2$).

In later works [75], a related model is derived, which has superseded its original version [74] since then. The free energy (1.15) is reduced to $\rho_0\psi = \tilde{W}(\varepsilon, g)$, i.e. $\hat{\beta} = 0$ and $\hat{\kappa} = 0$. Moreover, the modulus λ is assumed independent on g, i.e. $\lambda_1 = 0$ in (1.16). Hence, the damage evolution equation (1.18) becomes $\dot{g} = C_{\mathrm{d}}\,(\xi - \xi_0)\,\varepsilon_{\mathrm{II}}$, where $\xi = \varepsilon_{\mathrm{I}}/\sqrt{\varepsilon_{\mathrm{II}}}$, $\xi_0 = \mu_1/\gamma_1$ and $C_{\mathrm{d}} = C\gamma_1$. The strain invariants ratio ξ reduces to $\xi = \varepsilon/|\varepsilon|$ in the case of uniaxial strain. A given critical value $\xi_0 \approx -0.8$ of the invariants ratio marks the transition between destruction ($\xi > \xi_0$) and healing ($\xi < \xi_0$). In that respect, the authors make the following statement:

> "We note that (10) [$\dot{g} = -C\partial\psi/\partial g$] describes not only damage increase, but also a process of material recovery associated with healing of microcracks, which is favored by high confining pressure, low shear stress, and especially high temperature."

To avoid that the healing process is linear in time (which is not consistent with experimental observations), the following damage evolution is introduced [75]:

$$\dot{g} = \begin{cases} C_{\mathrm{d}}\,(\xi - \xi_0)\,\varepsilon_{\mathrm{II}} & \text{if } \xi \geqslant \xi_0\,, \\ C_1 \exp(g/C_2)\,(\xi - \xi_0)\,\varepsilon_{\mathrm{II}} & \text{if } \xi \leqslant \xi_0\,, \end{cases} \tag{1.19}$$

where $C_{1,2} > 0$ are material parameters governing the healing process.

Later, several refinements have been introduced. The previous model [75] has been generalized to poroelasticity [46], Maxwell viscoelasticity [45], non-local damage [77], and solid-granular transitions [78–80]. In a related study, a configuration with uniaxial strain and constant damage levels g is considered. A Kelvin–Voigt rheology combined with damage-dependent bimodular elasticity gives the constitutive law $\sigma = M_0\big(\varepsilon - \frac{1}{2}g(\varepsilon + |\varepsilon|)\big) + \nu\dot{\varepsilon}$ (Fig. 1.5a). Using the spectral element method, qualitative agreement with resonance experiments has been obtained [76].

■ *The soft-ratchet model of Vakhnenko et al.* A continuum model is proposed, by analogy with nonlinear resonant tunneling of electrons through a set of potential barriers [137, 138]. Even if the construction of the model does not refer explicitly to damage mechanics, the soft-ratchet model can be considered within this perspective. The model introduces a concentration of defects g, playing the role of a damage parameter in the constitutive law. This concentration of defects does not exceed a given critical value g_{cr}. A strain energy similar to the Lennard–Jones potential and Kelvin–Voigt viscoelasticity with parameter ν are used, so that one writes

$$\sigma = (1 - g/g_{\mathrm{cr}})\,\frac{M_0\,d}{r - a}\left((1 + \varepsilon/d)^{-(1+a)} - (1 + \varepsilon/d)^{-(1+r)}\right) + \nu\dot{\varepsilon}\,, \tag{1.20}$$

with the material parameters $0 < g_{\mathrm{cr}} \leqslant 1$, $0 < a < r$, and $0 < d \leqslant 1$ (see Fig. 1.5b where $g_{\mathrm{cr}} = 1$). Although the model equations are stated differently in [137, 138], one can show that g satisfies the evolution equation

$$\dot{g} = \big(\mu_1\,\mathrm{H}(g - g_{\mathrm{eq}}(\sigma)) + \mu_2\,\mathrm{H}(g_{\mathrm{eq}}(\sigma) - g)\big)\,(g_{\mathrm{eq}}(\sigma) - g)\,, \tag{1.21}$$

where $0 < \mu_1 \ll \mu_2$. The reason for choosing different rates μ_1, μ_2 in (1.21) is the following [138]:

> "Similarly, there are various ways for an already existing crack in equilibrium to be further expanded when surplus tensile load is applied. However, under compressive load a crack, once formed, has only one spatial way to be annihilated or contracted."

The equilibrium value of g in (1.21) follows Arrhenius' equation $g_{\mathrm{eq}}(\sigma) = g_0 \exp(\sigma/\tilde{\sigma})$, with the material parameters $g_0 > 0$ and $\tilde{\sigma} > 0$.

Several modifications of the previous model are proposed in [38]. The expression of the equilibrium value g_{eq} is fixed as

$$g_{\mathrm{eq}}(\sigma) = \frac{g_{\mathrm{cr}}}{2}\left(1 + \tanh\big(\sigma/\tilde{\sigma} - \tanh^{-1}(1 - 2g_0/g_{\mathrm{cr}})\big)\right), \tag{1.22}$$

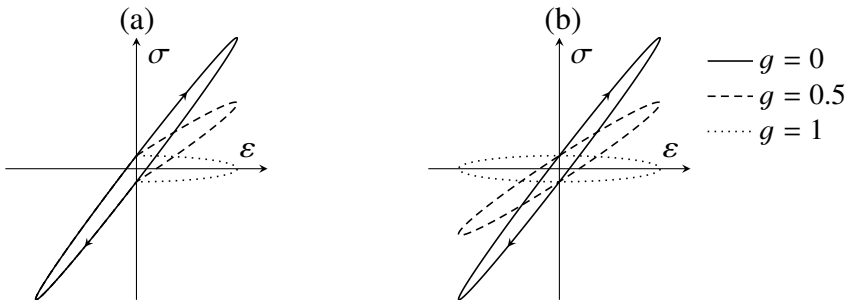

Figure 1.5. (a) Typical stress-strain relationship obtained with the damage-dependent viscoelastic bimodular law, for a sinusoidal strain evolution and constant damage [76]. (b) Similar curve deduced from the soft-ratchet model (1.20) where $g_{cr} = 1$. The arrows indicate how time increases along the curve.

in order to ensure $g < g_{cr}$. Moreover, a polynomial constitutive law is used instead of the Lennard–Jones potential, and a generalized Zener rheology is used instead of the Kelvin–Voigt rheology above (1.20). Without loss of generality, [38] assumes also that $g_{cr} = 1$. Using first-order finite-volume methods, qualitative agreement with dynamic acousto-elastic testing is obtained.

3. Outline

Let us summarize the literature overview by the fact that rocks and concrete are nonlinear dissipative solids, which peculiarities already arise at low strain levels $\varepsilon \sim 10^{-6}$. Quasistatic experiments show nonlinear hysteretic stress-strain relationships. Dynamic experiments highlight the generation of higher-order harmonics. Furthermore, the softening and the recovery of the material is observed, which occurs over large time scales.

On the modeling side, classical nonlinear viscoelasticity theories are able to reproduce many experimental observations besides the long-time relaxation. Despite their agreement with experiments and their relation to microscopic features (contacts at crack interfaces), hysteresis models raise practical questions. Indeed, very few works illustrate their use in a computational framework [22, 70, 88]. In counterpart, studies related to damage modeling (Lyakhovsky et al., Vakhnenko et al.) have lead to several numerical studies. As such, damage-like models provide a way to represent nonlinear softening and recovery processes in a self-consistent way. However, this type of approach does not provide a detailed look at the influence of the material's microstructure for now.

The present thesis follows [38] and is a continuation of the phenomenological approach resulting from continuum damage modeling. Since nonlinearity of stress-strain relationships is an important experimental feature, nonlinear elasticity is presented in the second chapter (p. 15). In particular, uniaxial constitutive laws with polynomial expressions (1.1) are examined, and finite-volume methods are presented.

The third chapter (p. 45) is devoted to the computation of an analytical solution. It has been obtained for a particular initial-value problem of nonlinear elastodynamics, where the initial data is discontinuous (Riemann problem). Moreover, the stress-strain relationship may have an inflection point, as is the

case of the cubic polynomial (1.1). This constitutive law is used as an example along the chapter, and the computation of the solution is detailed. This solution is used in Chapter 2 to assess the performances of finite-volume methods.

The next chapters concern the modeling of the slow dynamics, and its coupling with the previous numerical methods. The fourth chapter (p. 69) presents a continuum model, analogous to damage models. It is developed within the framework of the finite-strain theory and of thermodynamics. The model is designed to reproduce the slow dynamics observed in experiments, and is kept as simple as possible. The coupling of the slow dynamics with finite-volume methods is addressed, and the softening/recovery process is illustrated numerically.

Experimental evidence demonstrates the need of viscoelastic dissipation. This behavior is added to the softening model in the fifth chapter (p. 105) in the uniaxial case. Finite-volume methods are presented, as well as a numerical continuation method in the frequency domain for the computation of periodic vibrations. Qualitative agreement is obtained with the experimental observations. The conclusions and perspectives are detailed in the sixth chapter (p. 137).

Publications

Parts of the present dissertation have lead to publications. The corresponding bibliography references are listed below:

[1] H. Berjamin, N. Favrie, B. Lombard, G. Chiavassa: "Nonlinear waves in solids with slow dynamics: an internal-variable model", *Proc. R. Soc. A* **473**(2201) (2017), 20170024. DOI: 10.1098/rspa.2017.0024

[2] H. Berjamin, B. Lombard, G. Chiavassa, N. Favrie: "Analytical solution to 1D nonlinear elastodynamics with general constitutive laws", *Wave Motion* **74** (2017), 35–55. DOI: 10.1016/j.wavemoti.2017.06.006

[3] H. Berjamin, B. Lombard, G. Chiavassa, N. Favrie: "Modeling longitudinal wave propagation in nonlinear viscoelastic solids with softening", *Int. J. Solids Struct.* **141–142** (2018), 35–44. DOI: 10.1016/j.ijsolstr.2018.02.009

[4] H. Berjamin, B. Lombard, G. Chiavassa, N. Favrie: "A finite-volume approach to 1D nonlinear elastic waves: Application to slow dynamics", *Acta Acust. united Ac.* **104**(4) (2018), 561–570. DOI: 10.3813/AAA.919197

[5] H. Berjamin, G. Chiavassa, N. Favrie, B. Lombard, E. Sarrouy: "Internal-variable modeling of solids with slow dynamics: Wave propagation and resonance simulations", *Proc. Mtgs. Acoust.* **34**(1) (2018), 022001. DOI: 10.1121/2.0000844

[6] H. Berjamin, G. Chiavassa, N. Favrie, B. Lombard, C. Payan: "A unified treatment of nonlinear viscoelasticity and non-equilibrium dynamics". In: *Nonlinear Ultrasonic and Vibro-Acoustical Techniques for Nondestructive Evaluation*. Ed. by T. Kundu. Springer, 2019. Chap. 11, pp. 471–486. DOI: 10.1007/978-3-319-94476-0_11

[7] H. Berjamin, B. Lombard, G. Chiavassa, N. Favrie: “Plane-strain waves in nonlinear elastic solids with softening”, submitted (2018).

CHAPTER 2

Longitudinal waves in hyperelastic material

Nonlinear elasticity is the simplest model of nonlinear mechanical behavior. It is widely used to assess the nonlinearity of geomaterials experimentally, e.g. in nondestructive testing applications. In the present chapter, we investigate nonlinear stress-strain relationships with polynomial expressions.

In Section 1, we introduce the constitutive equations of Murnaghan's hyperelasticity, in the three-dimensional finite-strain framework (works published in [4]). This material model leads to polynomial stress-strain relationships under the uniaxial assumption. The equations of motion are rewritten as a nonlinear system of conservation laws, which resembles the p-system of gas dynamics.

Section 2 introduces finite-volume methods for nonlinear elastodynamics, such as the flux-limiter method. Based on Roe linearization [69], numerical methods of order up to two and higher-order methods are developed. The ability of the methods to capture discontinuous wave solutions is tested, as well as their ability to compute smooth waves accurately. Parts of this study can be found in the publication [4].

1. Governing equations

1.1. Lagrangian hyperelasticity

Let us consider an homogeneous continuum. A particle initially located at some position $\boldsymbol{x}_0$ of the reference configuration moves to a position $\boldsymbol{x}_t$ of the current deformed configuration. The deformation gradient is a second-order tensor defined by [35, 50, 97, 98]

$$\boldsymbol{F} = \mathbf{grad}\, \boldsymbol{x}_t = \boldsymbol{I} + \mathbf{grad}\, \boldsymbol{u}\,, \tag{2.1}$$

where $\boldsymbol{u} = \boldsymbol{x}_t - \boldsymbol{x}_0$ denotes the displacement field and **grad** is the gradient with respect to the material coordinates $\boldsymbol{x}_0$ (Lagrangian gradient). In the reference configuration, the deformation gradient (2.1) is equal to the metric tensor $\boldsymbol{I}$. Here, the Euclidean space is described by an orthonormal basis $(\boldsymbol{e}_1, \boldsymbol{e}_2, \boldsymbol{e}_3)$ and a Cartesian coordinate system (O, x, y, z), so that the matrix of the coordinates of $\boldsymbol{I}$ is the identity matrix.

The choice of a representation of motion — Eulerian or Lagrangian — does not affect the expressions of the constitutive laws and the evolution equations. However, it affects the expression of the material derivative and of the spatial differential operators. In particular, this choice affects the equations of motion. Here, the Lagrangian representation of motion is used (see Sec. 4.1 of the Appendix for elements of Eulerian hyperelasticity). Hence, the material derivative $\dot{\boldsymbol{\psi}}$ of any field $\boldsymbol{\psi}(\boldsymbol{x}_0, t)$ is $\dot{\boldsymbol{\psi}} = \partial_t \boldsymbol{\psi}$. In particular, the material derivative of the deformation gradient satisfies

$$\dot{\boldsymbol{F}} = \mathbf{grad}\, \boldsymbol{v}\,, \tag{2.2}$$

where $\boldsymbol{v}(\boldsymbol{x}_0, t)$ is the velocity field. The conservation of mass implies

$$\rho_0/\rho = \det \boldsymbol{F}\,, \tag{2.3}$$

where ρ denotes the mass density in the deformed configuration, and ρ_0 denotes the mass density in the reference configuration. The motion is also driven by the conservation of momentum. If self gravitation is neglected, the latter writes

$$\rho_0 \dot{\boldsymbol{v}} = \mathbf{div}\, \boldsymbol{P} + \boldsymbol{f}^v\,, \qquad \text{where} \qquad \boldsymbol{P} = (\det \boldsymbol{F})\, \boldsymbol{\sigma} \cdot \boldsymbol{F}^{-\top} \tag{2.4}$$

is the first Piola–Kirchhoff tensor. The divergence with respect to the material coordinates is denoted by **div**. The Cauchy stress tensor $\boldsymbol{\sigma} = (\det \boldsymbol{F})^{-1} \boldsymbol{P} \cdot \boldsymbol{F}^{\top} = \boldsymbol{\sigma}^{\top}$ is specified later on, through a specification of $\boldsymbol{P}$. The term $\boldsymbol{f}^v$ is an external volume force applied to the material.

In acoustics, the thermodynamic process is usually assumed to be adiabatic (no heat transfer). The first principle of thermodynamics introduces the specific internal energy e. The conservation of energy writes

$$\rho \dot{e} = \boldsymbol{\sigma} : \boldsymbol{D}\,, \tag{2.5}$$

where $\boldsymbol{D} = \frac{1}{2}(\dot{\boldsymbol{F}} \cdot \boldsymbol{F}^{-1} + \boldsymbol{F}^{-\top} \cdot \dot{\boldsymbol{F}}^{\top})$ is the strain rate tensor, and the double-dot product $\boldsymbol{\sigma} : \boldsymbol{D}$ is the double-contraction of tensors. The second principle of thermodynamics gives

$$\rho \dot{\eta} \geqslant 0\,, \tag{2.6}$$

where η is the specific entropy. In hyperelasticity, the only variables of state are the specific entropy η and a strain tensor $\boldsymbol{\chi}$. Hence, the Gibbs identity applied to $\dot{e}$ reads

$$\dot{e} = T\dot{\eta} + \left.\frac{\partial e}{\partial \boldsymbol{\chi}}\right|_{\eta} : \dot{\boldsymbol{\chi}}\,, \tag{2.7}$$

where $T = \partial e/\partial\eta|_{\boldsymbol{\chi}} > 0$ is the absolute temperature. Multiplying (2.7) by ρ, the local equations of thermodynamics (2.5) and (2.6) yield the Clausius–Duhem inequality

$$\mathcal{D} = \boldsymbol{\sigma} : \boldsymbol{D} - \rho \left.\frac{\partial e}{\partial \boldsymbol{\chi}}\right|_{\eta} : \dot{\boldsymbol{\chi}} \geqslant 0\,, \tag{2.8}$$

for all states $\{\eta, \boldsymbol{\chi}\}$ and all evolutions $\{\dot{\eta}, \dot{\boldsymbol{\chi}}\}$. The left-hand term in (2.8) is the dissipation $\mathcal{D} = \rho T\dot{\eta}$ per unit volume of material (W m^{-3}). In hyperelasticity, the dissipation in the material is zero, i.e. the thermodynamic process is isentropic ($\dot{\eta} = 0$).

Here, the deformation of the material is represented by the Green–Lagrange strain tensor $\boldsymbol{\chi} = \boldsymbol{E}$. The Green–Lagrange strain tensor is defined as $\boldsymbol{E} = \frac{1}{2}(\boldsymbol{C} - \boldsymbol{I})$ where $\boldsymbol{C} = \boldsymbol{F}^{\top}\cdot\boldsymbol{F}$ is the right Cauchy–Green strain tensor, or equivalently as a function of the displacement gradient tensor:

$$\boldsymbol{E} = \frac{1}{2}\left(\mathbf{grad}\,\boldsymbol{u} + \mathbf{grad}^{\top}\boldsymbol{u} + \mathbf{grad}^{\top}\boldsymbol{u}\cdot\mathbf{grad}\,\boldsymbol{u}\right). \tag{2.9}$$

The material derivative of the Green–Lagrange tensor is $\dot{\boldsymbol{\chi}} = \dot{\boldsymbol{E}} = \boldsymbol{F}^{\top}\cdot\boldsymbol{D}\cdot\boldsymbol{F}$, where $\boldsymbol{D}$ is the strain rate tensor. For any second-order tensors $\boldsymbol{T}$, $\boldsymbol{F}$ and $\boldsymbol{D}$, we recall that

$$\begin{aligned}
\boldsymbol{T} : \left(\boldsymbol{F}^{\top}\cdot\boldsymbol{D}\cdot\boldsymbol{F}\right) &= (\boldsymbol{D}\cdot\boldsymbol{F}) : (\boldsymbol{F}\cdot\boldsymbol{T}) \\
&= \mathrm{tr}\left(\boldsymbol{D}\cdot\boldsymbol{F}\cdot(\boldsymbol{F}\cdot\boldsymbol{T})^{\top}\right) \\
&= \mathrm{tr}\left(\boldsymbol{D}\cdot(\boldsymbol{F}\cdot\boldsymbol{T}\cdot\boldsymbol{F}^{\top})^{\top}\right) \\
&= \left(\boldsymbol{F}\cdot\boldsymbol{T}\cdot\boldsymbol{F}^{\top}\right) : \boldsymbol{D}\,.
\end{aligned} \tag{2.10}$$

Thus, defining the strain energy density function $W = \rho_0 e$, the dissipation (2.8) rewrites as

$$\begin{aligned}
\mathcal{D} &= \boldsymbol{\sigma} : \boldsymbol{D} - \rho \left.\frac{\partial e}{\partial \boldsymbol{E}}\right|_{\eta} : \dot{\boldsymbol{E}} \\
&= \boldsymbol{\sigma} : \boldsymbol{D} - \frac{\rho}{\rho_0}\left.\frac{\partial W}{\partial \boldsymbol{E}}\right|_{\eta} : \left(\boldsymbol{F}^{\top}\cdot\boldsymbol{D}\cdot\boldsymbol{F}\right) \\
&= \left(\boldsymbol{\sigma} - \frac{\rho}{\rho_0}\boldsymbol{F}\cdot\left.\frac{\partial W}{\partial \boldsymbol{E}}\right|_{\eta}\cdot\boldsymbol{F}^{\top}\right) : \boldsymbol{D}\,.
\end{aligned} \tag{2.11}$$

Since the dissipation $\mathcal{D}$ in (2.11) is zero for all strain rate $\boldsymbol{D}$, the Cauchy stress tensor satisfies

$$\boldsymbol{\sigma} = \frac{1}{\det\boldsymbol{F}}\,\boldsymbol{F}\cdot\left.\frac{\partial W}{\partial \boldsymbol{E}}\right|_{\eta}\cdot\boldsymbol{F}^{\top}, \tag{2.12}$$

where $\rho/\rho_0 = (\det\boldsymbol{F})^{-1}$ follows from the conservation of mass (2.3). Therefore, one substitutes the expression of the first Piola–Kirchhoff stress tensor

$$\boldsymbol{P} = \boldsymbol{F}\cdot\left.\frac{\partial W}{\partial \boldsymbol{E}}\right|_{\eta} \tag{2.13}$$

in the conservation of momentum (2.4).

In the isotropic case, the dependence on $\boldsymbol{E}$ can be replaced by a dependence on the invariants $E_{\mathrm{I}} = \operatorname{tr}\boldsymbol{E}$, $E_{\mathrm{II}} = \frac{1}{2}\big((\operatorname{tr}\boldsymbol{E})^2 - \operatorname{tr}(\boldsymbol{E}^2)\big)$, and $E_{\mathrm{III}} = \det\boldsymbol{E}$. Using the invariants' tensor derivatives $\partial E_{\mathrm{I}}/\partial\boldsymbol{E}$, $\partial E_{\mathrm{II}}/\partial\boldsymbol{E}$ and $\partial E_{\mathrm{III}}/\partial\boldsymbol{E}$ [50], the tensor derivative $\partial W/\partial\boldsymbol{E}$ rewrites as

$$\begin{aligned}\frac{\partial W}{\partial \boldsymbol{E}} &= \frac{\partial W}{\partial E_{\mathrm{I}}}\boldsymbol{I} + \frac{\partial W}{\partial E_{\mathrm{II}}}\left(E_{\mathrm{I}}\boldsymbol{I} - \boldsymbol{E}\right) + \frac{\partial W}{\partial E_{\mathrm{III}}}\left(E_{\mathrm{II}}\boldsymbol{I} - E_{\mathrm{I}}\boldsymbol{E} + \boldsymbol{E}^2\right),\\ &= \alpha_0\boldsymbol{I} + \alpha_1\boldsymbol{E} + \alpha_2\boldsymbol{E}^2,\end{aligned} \tag{2.14}$$

where

$$\begin{aligned}\alpha_0 &= \frac{\partial W}{\partial E_{\mathrm{I}}} + E_{\mathrm{I}}\frac{\partial W}{\partial E_{\mathrm{II}}} + E_{\mathrm{II}}\frac{\partial W}{\partial E_{\mathrm{III}}},\\ \alpha_1 &= -\frac{\partial W}{\partial E_{\mathrm{II}}} - E_{\mathrm{I}}\frac{\partial W}{\partial E_{\mathrm{III}}},\\ \alpha_2 &= \frac{\partial W}{\partial E_{\mathrm{III}}},\end{aligned} \tag{2.15}$$

are functions of the invariants. An example of strain energy density in terms of the invariants of $\boldsymbol{E}$ is Murnaghan's law [91]

$$W = \frac{\lambda + 2\mu}{2}{E_{\mathrm{I}}}^2 - 2\mu E_{\mathrm{II}} + \frac{\mathfrak{l} + 2\mathfrak{m}}{3}{E_{\mathrm{I}}}^3 - 2\mathfrak{m}E_{\mathrm{I}}E_{\mathrm{II}} + \mathfrak{n}E_{\mathrm{III}}, \tag{2.16}$$

where λ, μ are the Lamé parameters and $\mathfrak{l}$, $\mathfrak{m}$, $\mathfrak{n}$ are the Murnaghan coefficients. If the Murnaghan coefficients $\mathfrak{l}$, $\mathfrak{m}$, $\mathfrak{n}$ are zero, then the Saint Venant–Kirchhoff model is recovered. Another example is Landau's law with parameters $\mathcal{A}$, $\mathcal{B}$, C, and the relationship with Murnaghan's law (2.16) is specified in [97].

Sometimes, the strain energy density function is expressed in terms of the right Cauchy–Green strain tensor $\boldsymbol{C} = \boldsymbol{F}^{\top}\cdot\boldsymbol{F} = 2\boldsymbol{E} + \boldsymbol{I}$. An example of strain energy density in terms of the invariants of $\boldsymbol{C}$ is the compressible Mooney–Rivlin model [119]

$$W = \mathfrak{c}_1\left(C_{\mathrm{I}}{C_{\mathrm{III}}}^{-1/3} - 3\right) + \mathfrak{c}_2\left(C_{\mathrm{II}}{C_{\mathrm{III}}}^{-2/3} - 3\right) + \mathfrak{d}_1\left({C_{\mathrm{III}}}^{1/2} - 1\right)^2, \tag{2.17}$$

where $(\mathfrak{c}_1, \mathfrak{c}_2, \mathfrak{d}_1)$ are material parameters. This hyperelastic model (2.17) is classically used in mechanics of elastomers. For conversions, one has the following relations between the invariants of $\boldsymbol{E}$ and $\boldsymbol{C}$:

$$\begin{aligned}E_{\mathrm{I}} &= \frac{1}{2}\left(C_{\mathrm{I}} - 3\right) && C_{\mathrm{I}} = 3 + 2E_{\mathrm{I}}\\ E_{\mathrm{II}} &= \frac{1}{4}\left(3 - 2C_{\mathrm{I}} + C_{\mathrm{II}}\right) && \Leftrightarrow \quad C_{\mathrm{II}} = 3 + 4E_{\mathrm{I}} + 4E_{\mathrm{II}}\\ E_{\mathrm{III}} &= \frac{1}{8}\left(C_{\mathrm{I}} - C_{\mathrm{II}} + C_{\mathrm{III}} - 1\right) && C_{\mathrm{III}} = 1 + 2E_{\mathrm{I}} + 4E_{\mathrm{II}} + 8E_{\mathrm{III}}\,.\end{aligned} \tag{2.18}$$

1.2. Longitudinal plane waves

1.2.a. *The uniaxial strain assumption*

We assume that the displacement field $\boldsymbol{u}$ has no component along $\boldsymbol{e}_2$ and $\boldsymbol{e}_3$. Moreover, its component u along $\boldsymbol{e}_1$ is independent on y and z. Therefore, the

displacement gradient writes $\mathbf{grad}\,\boldsymbol{u} = \varepsilon\,(\boldsymbol{e}_1 \otimes \boldsymbol{e}_1)$, where $\varepsilon = \partial_x u > -1$ is the axial component of the displacement gradient. The invariants of the Green–Lagrange strain tensor are $E_{\mathrm{I}} = \varepsilon + \frac{1}{2}\varepsilon^2$ and $E_{\mathrm{II}} = E_{\mathrm{III}} = 0$. Thus, the strain energy W is now a function of ε only. In the longitudinal case, the $_{11}$-coordinate of the first Piola–Kirchhoff tensor (2.13) is equal to the $_{11}$-coordinate σ of the Cauchy stress tensor (2.12). Eqs. (2.14)-(2.15) and the expression of the invariants provide the stress-strain relationship

$$\begin{aligned}\sigma &= (1+\varepsilon)\big(\alpha_0 + \alpha_1 E_{\mathrm{I}} + \alpha_2 {E_{\mathrm{I}}}^2\big)\,,\\ &= \frac{\partial E_{\mathrm{I}}}{\partial \varepsilon}\frac{\partial W}{\partial E_{\mathrm{I}}}\,,\\ &= W'(\varepsilon)\,,\end{aligned} \tag{2.19}$$

where W' denotes the total derivative of W with respect to ε. Inversely, one can write $W = \int_0^{\varepsilon} \sigma(\epsilon)\,\mathrm{d}\epsilon$.

■ *Constitutive laws.* The Murnaghan model of hyperelasticity (2.16) with parameters λ, μ, $\mathfrak{l}$, $\mathfrak{m}$, $\mathfrak{n}$ is widely used in the communities of geophysics and nondestructive testing [25, 54, 85, 101, 106]. With this expression of the strain energy (2.16), the axial component of the Cauchy stress (2.19) is

$$\sigma = M_0\,\varepsilon\left(1 + \left(\frac{3}{2} + \kappa\right)\varepsilon + \left(\frac{1}{2} + 2\kappa\right)\varepsilon^2 + \frac{5\kappa}{4}\varepsilon^3 + \frac{\kappa}{4}\varepsilon^4\right), \tag{2.20}$$

where $M_0 = \lambda + 2\mu > 0$ is the elastic modulus, and $\kappa = (\mathfrak{l} + 2\mathfrak{m})/(\lambda + 2\mu)$. If the Murnaghan coefficients equal zero ($\kappa = 0$), only geometric nonlinearities remain, and the Saint Venant–Kirchhoff model of hyperelasticity is recovered. The later reduces to the classical Hooke's law in the case of infinitesimal strain $\varepsilon \simeq 0$.

When geometric nonlinearities are neglected (e.g., when the Murnaghan coefficients are very large), the Green–Lagrange strain tensor is linearized with respect to the components of $\mathbf{grad}\,\boldsymbol{u}$, so that the strain tensor (2.9) is replaced by the infinitesimal strain tensor: $\boldsymbol{E} \simeq \frac{1}{2}(\mathbf{grad}\,\boldsymbol{u} + \mathbf{grad}^{\top}\boldsymbol{u}) = \boldsymbol{\varepsilon}$. Doing this, the first invariant of the strain tensor is $E_{\mathrm{I}} \simeq \varepsilon$ in the longitudinal case. Moreover, the first Piola–Kirchhoff stress is linearized with respect to the components of $\mathbf{grad}\,\boldsymbol{u}$ as well, i.e. $\boldsymbol{P} \simeq \partial W/\partial \boldsymbol{\varepsilon}$ in (2.13). Doing this, the longitudinal constitutive law (2.19) reduces to $\sigma = \alpha_0 + \alpha_1\varepsilon + \alpha_2\varepsilon^2$, and (2.20) becomes

$$\sigma = M_0\,\varepsilon\,(1 + \kappa\varepsilon)\,. \tag{2.21}$$

This constitutive law corresponds to a quadratic polynomial $\sigma = M_0\,\varepsilon\,(1 - \beta\varepsilon)$, with $\beta = -\kappa$.

As written in the introduction (Eq. (1.1) p. 5), a cubic polynomial constitutive law

$$\sigma = M_0\,\varepsilon\left(1 - \beta\varepsilon - \delta\varepsilon^2\right) \tag{2.22}$$

is also widely used to describe nonlinear elasticity in solids [54, 70, 88, 139]. If the geometric nonlinearities are negligible (2.21), then the parameters $\beta = -\kappa$ and $\delta = 0$ correspond to Murnaghan's law. If the geometric nonlinearities are

taken into account (2.20), then the choice $-\beta = \frac{3}{2} + \kappa$ and $-\delta = \frac{1}{2} + 2\kappa$ makes the two models coincide up to the third order. Contrary to (2.20), orders 4 and 5 are not taken into account in (1.1), which shows that both models are not equivalent.

The major difference between the stress-strain relationships (2.20) and (2.22) is the number of independent parameters. In (2.22), the cubic term can be set independently of the quadratic term. In (2.20), the cubic term is not independent on the quadratic term: if (2.20) and (2.22) are assimilated, then $\delta = \frac{5}{2} + 2\beta$. However, experimental evidence shows that δ is larger than β by several orders of magnitude, so that a constitutive law of the Murnaghan type is not sufficient to represent accurately elastic nonlinearity in geomaterials [117]. Therefore, the polynomial law (2.22) is preferred in what follows.

1.2.b. *System of conservation laws*

The equations of motion (2.2)-(2.4) write as a non-homogeneous system of conservation laws with respect to the variables $\boldsymbol{q} = (\varepsilon, v)^\top$, where v is the particle velocity component along $\boldsymbol{e}_1$:

$$\partial_t \boldsymbol{q} + \partial_x \boldsymbol{f}(\boldsymbol{q}) = \boldsymbol{s}\,. \tag{2.23}$$

The flux function is $\boldsymbol{f}(\boldsymbol{q}) = -(v, \sigma(\varepsilon)/\rho_0)^\top$, and the source term is $\boldsymbol{s} = (0, (\boldsymbol{f}^v \cdot \boldsymbol{e}_1)/\rho_0)^\top$. We assume that the stress σ is a smooth function of ε, which is strictly increasing over an open interval $]\varepsilon_{\text{inf}}, \varepsilon_{sup}[$ with $\varepsilon_{\text{inf}} < 0$ and $\varepsilon_{\text{sup}} > 0$. These bounds ε_{inf} and ε_{sup} can be finite or infinite. Also, no prestress is applied, i.e. $\sigma(0) = 0$.

The Jacobian matrix of the flux is

$$\boldsymbol{f}'(\boldsymbol{q}) = -\begin{pmatrix} 0 & 1 \\ \sigma'(\varepsilon)/\rho_0 & 0 \end{pmatrix}, \tag{2.24}$$

where $\sigma' = W''$ is the derivative of σ with respect to ε. The eigenvalues of $\boldsymbol{f}'(\boldsymbol{q})$ are

$$\lambda_1(\boldsymbol{q}) = -c(\boldsymbol{q}), \qquad \lambda_2(\boldsymbol{q}) = c(\boldsymbol{q}), \tag{2.25}$$

where

$$c(\boldsymbol{q}) = c(\varepsilon) = \sqrt{\sigma'(\varepsilon)/\rho_0} \tag{2.26}$$

is the speed of sound. The right eigenvectors $\boldsymbol{r}_k$ and left eigenvectors $\boldsymbol{l}_k$ satisfy ($k = 1$ or $k = 2$)

$$\begin{aligned} \boldsymbol{f}'(\boldsymbol{q})\,\boldsymbol{r}_k(\boldsymbol{q}) &= \lambda_k(\boldsymbol{q})\,\boldsymbol{r}_k(\boldsymbol{q}), \\ \boldsymbol{l}_k(\boldsymbol{q})^\top \boldsymbol{f}'(\boldsymbol{q}) &= \lambda_k(\boldsymbol{q})\,\boldsymbol{l}_k(\boldsymbol{q})^\top. \end{aligned} \tag{2.27}$$

They can be normalized in such a way that $\boldsymbol{l}_k(\boldsymbol{q})^\top \boldsymbol{r}_k(\boldsymbol{q}) = 1$:

$$\begin{aligned} \boldsymbol{r}_1(\boldsymbol{q}) &= \begin{pmatrix} 1 \\ c(\boldsymbol{q}) \end{pmatrix}, & \boldsymbol{l}_1(\boldsymbol{q}) &= \frac{1}{2}\begin{pmatrix} 1 \\ 1/c(\boldsymbol{q}) \end{pmatrix}, \\ \boldsymbol{r}_2(\boldsymbol{q}) &= \begin{pmatrix} 1 \\ -c(\boldsymbol{q}) \end{pmatrix}, & \boldsymbol{l}_2(\boldsymbol{q}) &= \frac{1}{2}\begin{pmatrix} 1 \\ -1/c(\boldsymbol{q}) \end{pmatrix}. \end{aligned} \tag{2.28}$$

If the eigenvalues λ_k of a 2×2 system of conservation laws are real and distinct over an open set Ω of $\mathbb{R}^2$, then the system is *strictly hyperbolic* over Ω [40]. Here, the system (2.23) is strictly hyperbolic for $\Omega =]\varepsilon_{\text{inf}}, \varepsilon_{\text{sup}}[\times \mathbb{R}$.

If the kth characteristic field satisfies $\boldsymbol{\nabla}\lambda_k \cdot \boldsymbol{r}_k = 0$ for all states $\boldsymbol{q}$ in Ω, then it is *linearly degenerate*. Based on (2.25), linear degeneracy reduces to $\sigma(\varepsilon) = M_0\,\varepsilon$, where $M_0 > 0$ is Young's modulus. Therefore, linear degeneracy corresponds to the case of linear elasticity [8]. If linear degeneracy is not satisfied, the classical case is obtained when $\boldsymbol{\nabla}\lambda_k \cdot \boldsymbol{r}_k \neq 0$ for all states $\boldsymbol{q}$ in Ω. The kth characteristic field is then *genuinely nonlinear*. Here, this is equivalent to state

$$\sigma''(\varepsilon) \neq 0\,, \tag{2.29}$$

for all ε in $]\varepsilon_{\text{inf}}, \varepsilon_{\text{sup}}[$. Therefore, σ is either a strictly convex function or a strictly concave function. A less classical case is when both $\boldsymbol{\nabla}\lambda_k \cdot \boldsymbol{r}_k = 0$ and $\boldsymbol{\nabla}\lambda_k \cdot \boldsymbol{r}_k \neq 0$ can occur over Ω. This happens when σ'' has isolated zeros, where σ has an inflection point. The stress σ is therefore neither convex nor concave.

Remark 2.1. When setting $\boldsymbol{f}^v = \boldsymbol{0}$ and replacing ε by the specific volume v, $-\sigma/\rho_0$ by the pressure p and v by the particle velocity u in (2.23), the so-called "p-system" of gas dynamics is recovered [40, 146].

■ *Example (Murnaghan).* In the case of Murnaghan's law (2.20), strict hyperbolicity of (2.23) is ensured if $\kappa - 2 + 6\,(1-\kappa)\,(1+\varepsilon)^2 + 5\kappa\,(1+\varepsilon)^4 > 0$. Therefore, one must have

$$\varepsilon \in \begin{cases}]\varepsilon_+, \varepsilon_-[& \text{if } \kappa < 0\,, \\ ]\varepsilon_+, +\infty[& \text{if } 0 \leqslant \kappa < 2\,, \\ ]-1, \varepsilon_-[\,\cup\,]\varepsilon_+, +\infty[& \text{if } 2 \leqslant \kappa\,, \end{cases} \tag{2.30}$$

where

$$\varepsilon_\pm = -1 + \sqrt{\frac{3\,(\kappa-1) \pm \sqrt{4\,(\kappa-1)^2 + 5}}{5\kappa}}\,. \tag{2.31}$$

The constitutive law (2.20) is convex if $\sigma''(\varepsilon) \geqslant 0$, i.e.

$$3 + 2\kappa + (3 + 12\kappa)\,\varepsilon + 15\kappa\,\varepsilon^2 + 5\kappa\,\varepsilon^3 \geqslant 0\,. \tag{2.32}$$

Hence, Murnaghan's law is locally concave at small strains ($\varepsilon \simeq 0$) provided that $\kappa \leqslant -3/2$, otherwise it is locally convex at small strains. The inflection point

$$\varepsilon_0 = -1 + \sqrt{\frac{3\,(\kappa-1)}{5\kappa}} \tag{2.33}$$

where σ'' vanishes is represented in Figure 2.1, as well as the hyperbolicity domains (2.30) of Murnaghan's law.

■ *Example (polynomial).* The constitutive law $\sigma = M_0\,\varepsilon\left(1 - \beta\varepsilon - \delta\varepsilon^2\right)$ is a cubic polynomial function (2.22), where M_0 is Young's modulus and (β, δ) are positive. Figure 2.2 represents the constitutive law (2.22) and its sound speed

$$c(\varepsilon) = c_0\,\sqrt{1 - 2\beta\varepsilon - 3\delta\varepsilon^2}\,. \tag{2.34}$$

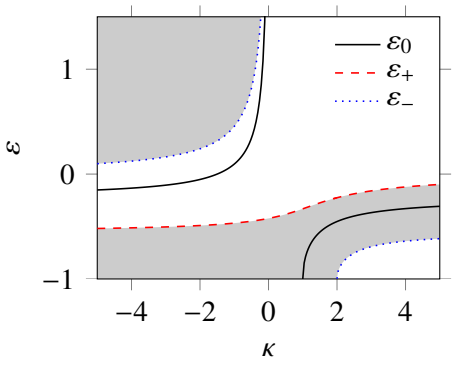

Figure 2.1. Sketch of the hyperbolicity domains (white) of Murnaghan's law (2.20) with respect to the parameter $\kappa = (\mathrm{l} + 2\mathrm{m})/(\lambda + 2\mu)$.

In the particular case where the nonlinearity in (2.22) is quadratic ($\delta = 0$), strict hyperbolicity is ensured for ε in $]\varepsilon_{\text{inf}}, \varepsilon_{\text{sup}}[=]-\infty, 1/(2\beta)[$. If the nonlinearity is cubic ($\delta \neq 0$), strict hyperbolicity is satisfied when ε belongs to

$$\left]\varepsilon_{\text{inf}}, \varepsilon_{\text{sup}}\right[= \left]\frac{1}{\beta - \sqrt{\beta^2 + 3\delta}}, \frac{1}{\beta + \sqrt{\beta^2 + 3\delta}}\right[. \tag{2.35}$$

At the bounds ε_{inf} and ε_{sup}, σ has a zero slope, i.e. the speed of sound is zero. The inflection point is defined by $\sigma''(\varepsilon_0) = 0$, which is satisfied at $\varepsilon_0 = -\beta/(3\delta)$. At the inflection point, the sound speed reaches its maximum value

$$c(\varepsilon_0) = c_0 \sqrt{1 + \frac{\beta^2}{3\delta}} > c_0 . \tag{2.36}$$

This example is used in Chapter 3, where an analytical solution is detailed.

In general, no analytical solution is known for the previous equations of motion. Thus, numerical methods are needed to compute wave solutions. The next section presents various finite-volume schemes, which have been adapted to the case of nonlinear elastodynamics. The performances of the methods are compared with respect to particular analytical solutions. Contrary to linear elastodynamics where a smooth acoustic perturbation remains smooth along its propagation, shock waves can develop in nonlinear elastodynamics (see the Appendix, Sec. 4.2). Therefore, it is important to test the ability of numerical methods to approximate discontinuous solutions.

2. Finite-volume methods

In this section, we describe finite-volume methods for the system of elastodynamics (2.23). We first present standard finite-volume methods of order up to two [69]. Then, we introduce higher-order methods. The performances of the methods are assessed on two test cases. The first test corresponds to a smooth initial-value problem of linear elastodynamics. The second test corresponds to a discontinuous initial-value problem — a Riemann problem — for a nonconvex constitutive law. The analytical solution of this problem is the subject of Chapter 3. The physical parameters are set according to the values in Table 2.1, which correspond to typical values in rocks. In all the numerical examples

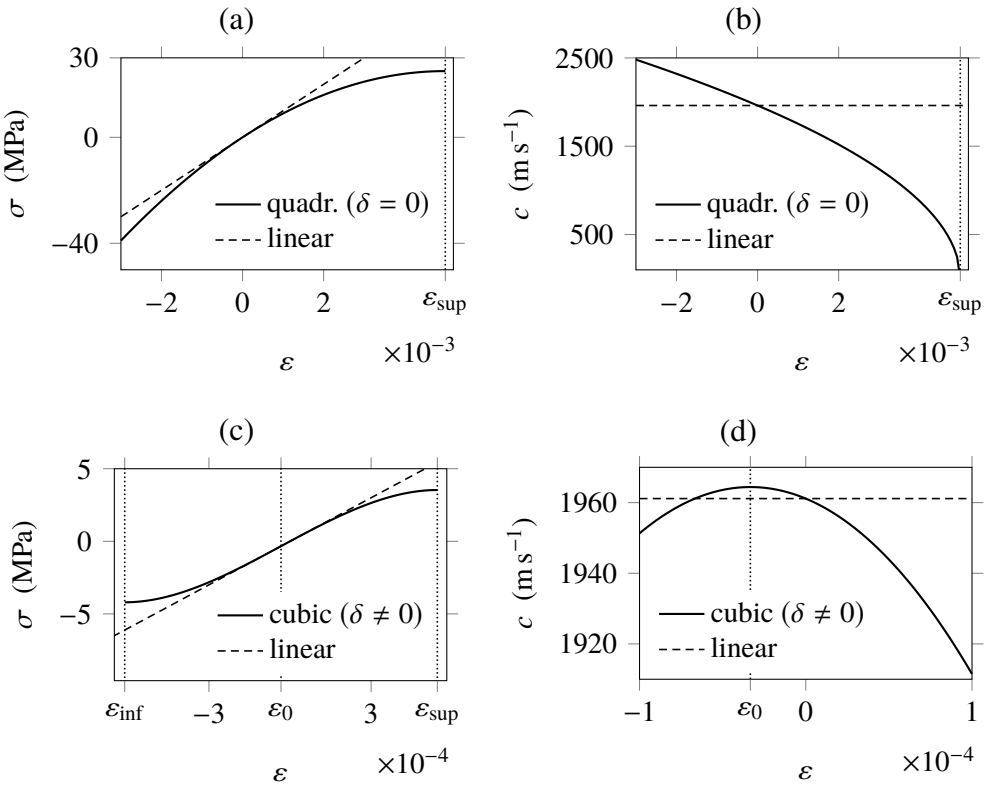

Figure 2.2. (a) Polynomial law (2.22) with a quadratic nonlinearity ($\delta = 0$) and (b) corresponding speed of sound (2.34). (c)-(d) Idem with a cubic nonlinearity ($\delta \neq 0$), zoom.

Table 2.1. Physical parameters.

ρ_0 (kg m^{-3})	M_0 (GPa)	β	δ
2600	10	10^2	10^6

of this chapter, computations are performed over the reduced spatial domain $x \in [x_0, x_{N_x}] = [-0.5, 0.5]$ m.

■ *Test 1 (linear elasticity).* In this case, $\sigma(\varepsilon) = M_0\,\varepsilon$ in (2.23) is linear, and the sound speed $c(\varepsilon) = \sqrt{\sigma'(\varepsilon)/\rho_0}$ is equal to the constant $c_0 = \sqrt{M_0/\rho_0}$. The solution to an initial value problem $\boldsymbol{q}(x,0) = \big(\varepsilon^\circ(x), v^\circ(x)\big)^\top = \boldsymbol{q}^\circ(x)$ is

$$\begin{cases} \varepsilon(x,t) = \dfrac{1}{2}\left(\varepsilon^\circ(x-c_0t) + \varepsilon^\circ(x+c_0t) + \dfrac{v^\circ(x+c_0t) - v^\circ(x-c_0t)}{c_0}\right), \\ v(x,t) = \dfrac{1}{2}\left(v^\circ(x-c_0t) + v^\circ(x+c_0t) + \dfrac{\varepsilon^\circ(x+c_0t) - \varepsilon^\circ(x-c_0t)}{1/c_0}\right). \end{cases} \tag{2.37}$$

This result can be obtained by diagonalization of the Jacobian matrix $\boldsymbol{f}'(\boldsymbol{q})$ [69]. Here, results are calculated for the case in which the initial particle velocity is

$v^\circ(x) = 0$. The initial strain is a C^6 wavelet with expression

$$\varepsilon^\circ(x) = \begin{cases} 2V \displaystyle\sum_{i=0}^{3} \frac{a_i}{a} \sin(-2^i k_c\, x) & \text{if } 0 < -x < \dfrac{2\pi}{k_c}, \\ 0 & \text{elsewhere}, \end{cases} \tag{2.38}$$

where $a_0 = 1$, $a_1 = -21/32$, $a_2 = 63/768$, $a_3 = -1/512$, and $a \approx 1.507$ is a normalization coefficient. According to (2.37), the initial data (2.38) induces the propagation of a left-going wave and a right-going wave at the absolute velocity c_0. The amplitude of each strain wave is V, and the amplitude of each velocity wave is Vc_0. In (2.38), the central frequency is $f_c = c_0 k_c/(2\pi) = 20$ kHz and the strain amplitude is $V = 10^{-5}$. The solution (2.37) is computed up to $t = 0.15$ ms and displayed in Figure 2.3a.

■ *Test 2 (cubic polynomial).* In this case, $\sigma(\varepsilon) = M_0\, \varepsilon \left(1 - \beta\varepsilon - \delta\varepsilon^2\right)$ is a cubic polynomial function (2.22), and the sound speed $c(\varepsilon)$ is not constant anymore. We consider piecewise constant initial data, with a single discontinuity at the abscissa $x = 0$, i.e. a Riemann problem. On the left side of the discontinuity, the initial data is $\boldsymbol{q}^\circ(x < 0) = \boldsymbol{q}_L$, where $\varepsilon_L = 1.8 \times 10^{-4}$ and $v_L = 0$. On the right side of the discontinuity, the initial data is $\boldsymbol{q}^\circ(x > 0) = \boldsymbol{q}_R$, where $\varepsilon_R = -1.8 \times 10^{-4}$ and $v_R = 0.4$ m/s. The analytical solution to this initial-value problem is detailed in Chapter 3, where the current configuration is denoted by $\mathcal{S}_1\mathcal{R}\mathcal{S}_2$. As shown in Fig. 2.3b, the left-going wave is a discontinuity (shock wave $\mathcal{S}_1$). The right-going wave is a compound wave, also known as semi-shock, made of a continuous part followed by a discontinuity (rarefaction-shock $\mathcal{R}\mathcal{S}_2$). Thus, the solution writes

$$\boldsymbol{q}(x,t) = \begin{cases} \boldsymbol{q}_L & \text{if } x < s_1 t, \\ \boldsymbol{q}_M & \text{if } s_1 t < x \leqslant c(\varepsilon_M)\, t, \\ \tilde{\boldsymbol{q}}_2(x/t) & \text{if } c(\varepsilon_M)\, t \leqslant x \leqslant c(\varepsilon_R^*)\, t, \\ \boldsymbol{q}_R & \text{if } c(\varepsilon_R^*)\, t \leqslant x, \end{cases} \tag{2.39}$$

where $\varepsilon_M \approx 1.014 \times 10^{-4}$ and $\varepsilon_R^* = 0.4 \times 10^{-4}$. The shape of the rarefaction and the shock speeds are specified in Chapter 3. The solution (2.39) is computed up to $t = 0.2$ ms and is displayed in Fig. 2.3b.

2.1. Basic principle

In the examples studied here, the physical domain is infinite. We consider a finite numerical domain $[x_0, x_{N_x}]$. It is discretized using a regular grid in space with step $\Delta x = (x_{N_x} - x_0)/N_x$. Also, a variable time step $\Delta t = t_{n+1} - t_n$ is introduced. Therefore, $\boldsymbol{q}(x_i, t_n)$ denotes the solution to (2.23) at the abscissa $x_i = x_0 + i\,\Delta x$ and the time t_n.

A cell, or finite volume, is associated to each node of the grid x_i. The cells are defined by $C_i = \left[x_{i-1/2}, x_{i+1/2}\right]$, where $x_{i\pm1/2} = x_i \pm \Delta x/2$ [69]. The system of partial differential equations $\partial_t \boldsymbol{q} + \partial_x \boldsymbol{f}(\boldsymbol{q}) = \boldsymbol{s}$ (2.23) is then integrated in

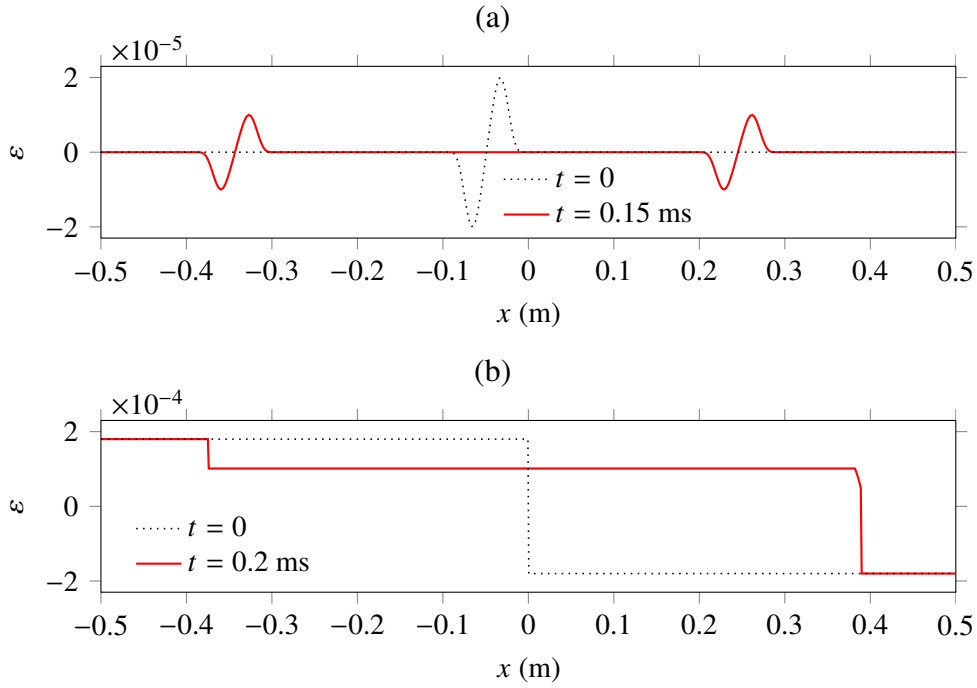

Figure 2.3. (a) Analytical solution of Test 1 where the initial data is smooth and the constitutive law is linear. (b) Analytical solution of Test 2 where a Riemann problem is solved. The constitutive law is nonlinear and nonconvex.

space over a cell C_i:

$$\frac{\mathrm{d}}{\mathrm{d}t}\int_{C_i} \boldsymbol{q}(x,t)\,\mathrm{d}x + \boldsymbol{f}(\boldsymbol{q}(x_{i+1/2},t)) - \boldsymbol{f}(\boldsymbol{q}(x_{i-1/2},t)) = \int_{C_i} \boldsymbol{s}(x,t)\,\mathrm{d}x\,. \tag{2.40}$$

Introducing the cell averages $\bar{\boldsymbol{q}}_i(t) = \frac{1}{\Delta x}\int_{C_i} \boldsymbol{q}(x,t)\,\mathrm{d}x$, Eq. (2.40) rewrites as

$$\frac{\mathrm{d}}{\mathrm{d}t}\bar{\boldsymbol{q}}_i(t) + \frac{\boldsymbol{f}_{i+1/2}(t) - \boldsymbol{f}_{i-1/2}(t)}{\Delta x} = \bar{\boldsymbol{s}}_i(t)\,, \tag{2.41}$$

where $\boldsymbol{f}_{i+1/2}(t) = \boldsymbol{f}(\boldsymbol{q}(x_{i+1/2},t))$. Now, we introduce the average in time of the physical flux over a time step: $\overline{\boldsymbol{f}}^n_{i+1/2} = \frac{1}{\Delta t}\int_{t_n}^{t_{n+1}} \boldsymbol{f}_{i+1/2}(\tau)\,\mathrm{d}\tau$. Integrating (2.41) over a time step $[t_n, t_{n+1}]$ yields

$$\bar{\boldsymbol{q}}_i(t_{n+1}) = \bar{\boldsymbol{q}}_i(t_n) - \frac{\Delta t}{\Delta x}\left(\overline{\boldsymbol{f}}^n_{i+1/2} - \overline{\boldsymbol{f}}^n_{i-1/2}\right) + \Delta t\,\overline{\boldsymbol{s}}^n_i\,. \tag{2.42}$$

This integrated version of (2.23) is the basis of finite volume methods.

In finite volume methods, the computational variables are the approximations $\boldsymbol{q}^n_i \simeq \bar{\boldsymbol{q}}_i(t_n)$, $\boldsymbol{f}^n_{i+1/2} \simeq \overline{\boldsymbol{f}}^n_{i+1/2}$ and $\boldsymbol{s}^n_i \simeq \overline{\boldsymbol{s}}^n_i$ of the averaged quantities defined above. Injecting these approximations in Eq. (2.42) yields

$$\boldsymbol{q}^{n+1}_i = \boldsymbol{q}^n_i - \frac{\Delta t}{\Delta x}\left(\boldsymbol{f}^n_{i+1/2} - \boldsymbol{f}^n_{i-1/2}\right) + \Delta t\,\boldsymbol{s}^n_i\,. \tag{2.43}$$

The average in time of the physical flux at a cell interface $\boldsymbol{f}^n_{i+1/2}$ is usually computed from the values of $\boldsymbol{q}^n_\bullet$ in the $2S$ neighbor cells. Therefore, an iteration

in time at one cell (2.43) requires $2S + 1$ values. As we will see in the next section, $S = 1$ for most of the methods (cf. Appendix, Sec. 4.3.c). A numerical method of the form (2.43) is in *conservation form*, since it mimics the property of the exact solution (2.42) [69].

In the linear elastic case, the stability analysis involves the Courant number $\mathrm{Co} = c_0 \Delta t / \Delta x$. The Courant–Friedrichs–Lewy (CFL) condition imposes that this dimensionless number does not exceed $\mathrm{Co}_{\max}$, which depends on the numerical method [69]. For a nonlinear hyperbolic system, no stability criterion is known in general. A classical approach consists in assuming that the CFL condition still holds with a modified Courant number:

$$\mathrm{Co} = \frac{\Delta t}{\Delta x} c^n_{\max} \leqslant \mathrm{Co}_{\max}, \tag{2.44}$$

where

$$c^n_{\max} = \max_{\varepsilon \in \left[\min_i \varepsilon^n_i, \max_i \varepsilon^n_i\right]} c(\varepsilon) \tag{2.45}$$

is the maximum absolute wave speed that is encountered at the time t_n (cf. Section 13.1.3 in [69]). The time step $\Delta t = \mathrm{Co}\, \Delta x / c^n_{\max}$ must be actualized at each iteration in time according to the value of $c^n_{\max}$. If the constitutive law $\varepsilon \mapsto \sigma(\varepsilon)$ is convex or concave, (2.45) reduces to $c^n_{\max} = \max_i c(\varepsilon^n_i)$. In the case of linear elasticity, $c^n_{\max} = c_0$ is constant, so that the time step Δt is constant too. Many numerical methods are stable under the CFL condition (2.44) with $\mathrm{Co}_{\max} = 1$. In practice, the Courant number is set to a value which is slightly lower than $\mathrm{Co}_{\max}$, so as to avoid instabilities due to round-off errors. If not specified, the Courant number is set to $\mathrm{Co} = 0.95$ in the numerical applications.

2.2. Classical finite-volume schemes

All the numerical methods presented hereinafter are in conservation form (2.43). Therefore, the method is defined by the expression of the numerical flux $\boldsymbol{f}^n_{i+1/2}$. In the present section, we detail the numerical flux of several finite-volume schemes of order up to two, so that these methods are ready to implement.

2.2.a. *Lax–Friedrichs*

The classical Lax–Friedrichs method is associated to the numerical flux

$$\boldsymbol{f}^n_{i+1/2} = \frac{1}{2}\left(\boldsymbol{f}(\boldsymbol{q}^n_i) + \boldsymbol{f}(\boldsymbol{q}^n_{i+1})\right) - \frac{\Delta x}{2\,\Delta t}\left(\boldsymbol{q}^n_{i+1} - \boldsymbol{q}^n_i\right). \tag{2.46}$$

For a linear system of conservation laws, this method is stable under the CFL condition (2.44) with $\mathrm{Co}_{\max} = 1$ [69]. Measurements of the L^2-error illustrate that the method (2.43)-(2.46) is first-order accurate (see Fig. 2.5). However, as displayed on Fig. 2.4, the Lax–Friedrichs method is very diffusive.

2.2.b. *Godunov*

The solution to the Riemann problem may be used to construct numerical schemes. Godunov's method consists in computing the exact solution over a

time step Δt, when the initial data at time t_n is piecewise constant. More precisely, the initial data is equal to $\boldsymbol{q}_i^n$ over each cell C_i. The numerical flux in (2.43) is set to $\boldsymbol{f}_{i+1/2}^n = \boldsymbol{f}(\boldsymbol{q}_{i+1/2}^\star)$, where $\boldsymbol{q}_{i+1/2}^\star$ is the solution to the Riemann problem at the cell interface $x_{i+1/2}$. Therefore, this method requires to know the value of the solution to any Riemann problem at the time Δt. For a linear system of conservation laws, Godunov's method reduces to the *upwind scheme*, which is stable under the CFL condition (2.44) with $\mathrm{Co}_{\max} = 1$ [69].

For a general constitutive law, solving the Riemann problem may be difficult or expensive, as seen in Chapter 3. Often, it is not required to compute the exact solution to the Riemann problem to get accurate results. A wide variety of *approximate Riemann solvers* has been proposed that can be applied much more cheaply than the exact Riemann solver [69]. One example is Roe's linearized Riemann solver. Here, the physical flux is approximated linearly at each cell interface. Thus, if $\boldsymbol{A}_{i+1/2}$ approximates the Jacobian matrix $\boldsymbol{f}'(\boldsymbol{q}_{i+1/2}^n)$, one has

$$\boldsymbol{f}(\boldsymbol{q}) \simeq \boldsymbol{f}'(\boldsymbol{q}_{i+1/2}^n)\,\boldsymbol{q} \simeq \boldsymbol{A}_{i+1/2}\,\boldsymbol{q}\,, \quad \text{if} \quad x \simeq x_{i+1/2}\,. \tag{2.47}$$

If $\boldsymbol{A}_{i+1/2}$ is diagonalizable, then $\boldsymbol{A}_{i+1/2} = \boldsymbol{R}\,\boldsymbol{\Lambda}\,\boldsymbol{R}^{-1}$, where $\boldsymbol{\Lambda}$ and $\boldsymbol{R}$ denote respectively the matrices of eigenvalues and right eigenvectors of $\boldsymbol{A}_{i+1/2}$. Furthermore, if $\boldsymbol{\Lambda}$ is real, then the linearized system (2.23)-(2.47) is hyperbolic. Locally, the classical upwind method for linear hyperbolic systems can be applied:

$$\boldsymbol{f}_{i+1/2}^n = \frac{1}{2}\left(\boldsymbol{f}(\boldsymbol{q}_i^n) + \boldsymbol{f}(\boldsymbol{q}_{i+1}^n)\right) - \frac{1}{2}\left|\boldsymbol{A}_{i+1/2}\right|\left(\boldsymbol{q}_{i+1}^n - \boldsymbol{q}_i^n\right), \tag{2.48}$$

where $\left|\boldsymbol{A}_{i+1/2}\right| = \boldsymbol{R}\,|\boldsymbol{\Lambda}|\,\boldsymbol{R}^{-1}$.

The Jacobian matrix $\boldsymbol{f}'(\boldsymbol{q}_{i+1/2}^n)$ in (2.47) can be approximated by using a linear average, e.g. $\boldsymbol{A}_{i+1/2} = \boldsymbol{f}'\left(\frac{1}{2}(\boldsymbol{q}_i^n + \boldsymbol{q}_{i+1}^n)\right)$ or $\boldsymbol{A}_{i+1/2} = \frac{1}{2}\left(\boldsymbol{f}'(\boldsymbol{q}_i^n) + \boldsymbol{f}'(\boldsymbol{q}_{i+1}^n)\right)$. In general, these approximations are not accurate near discontinuities, for which $\|\boldsymbol{q}_{i+1}^n - \boldsymbol{q}_i^n\|$ may be large. This issue can be solved by using a Roe's matrix such that

1. $\boldsymbol{A}_{i+1/2}$ is diagonalizable with real eigenvalues;
2. $\boldsymbol{A}_{i+1/2}\left(\boldsymbol{q}_{i+1}^n - \boldsymbol{q}_i^n\right) = \boldsymbol{f}(\boldsymbol{q}_{i+1}^n) - \boldsymbol{f}(\boldsymbol{q}_i^n)$;
3. $\lim\limits_{\boldsymbol{q}_{i+1}^n \to \boldsymbol{q}_i^n} \boldsymbol{A}_{i+1/2} = \boldsymbol{f}'(\boldsymbol{q}_i^n)$.

According to Section 15.3.2 of [69], such a matrix may be expressed by the formula

$$\boldsymbol{A}_{i+1/2} = \int_0^1 \boldsymbol{f}'\left(\boldsymbol{q}_i^n + \zeta\,(\boldsymbol{q}_{i+1}^n - \boldsymbol{q}_i^n)\right)\mathrm{d}\zeta\,, \tag{2.49}$$

which ensures that the properties 2 and 3 are satisfied. In the case of the system (2.23), which corresponds to Exercise 15.1.(a) p. 349 of [69], the following matrix is obtained:

$$\boldsymbol{A}_{i+1/2} = -\begin{pmatrix} 0 & 1 \\ a_{i+1/2}^n & 0 \end{pmatrix} \tag{2.50}$$

where

$$a_{i+1/2}^n = \frac{\sigma(\varepsilon_{i+1}^n) - \sigma(\varepsilon_i^n)}{\rho_0 \left(\varepsilon_{i+1}^n - \varepsilon_i^n\right)} . \tag{2.51}$$

To avoid divisions by zero when $\varepsilon_i^n = \varepsilon_{i+1}^n$, one computes

$$a_{i+1/2}^n = \frac{\sigma'(\varepsilon_i^n)}{\rho_0} \tag{2.52}$$

in this particular case. The eigenvalues of the matrix (2.50) are $\{-s_{i+1/2}^n, s_{i+1/2}^n\}$, where $s_{i+1/2}^n = \sqrt{a_{i+1/2}^n}$, and the corresponding eigenvectors are

$$\begin{aligned} \boldsymbol{r}_{i+1/2}^1 &= \begin{pmatrix} 1 \\ s_{i+1/2}^n \end{pmatrix}, \qquad \boldsymbol{l}_{i+1/2}^1 = \frac{1}{2}\begin{pmatrix} 1 \\ 1/s_{i+1/2}^n \end{pmatrix}, \\ \boldsymbol{r}_{i+1/2}^2 &= \begin{pmatrix} 1 \\ -s_{i+1/2}^n \end{pmatrix}, \qquad \boldsymbol{l}_{i+1/2}^2 = \frac{1}{2}\begin{pmatrix} 1 \\ -1/s_{i+1/2}^n \end{pmatrix}. \end{aligned} \tag{2.53}$$

Since the stress $\sigma(\varepsilon)$ is increasing over the hyperbolicity domain, the coefficient $a_{i+1/2}^n$ is positive. Therefore, the eigenvalue $s_{i+1/2}^n$ is real, and the property 1 is satisfied. The matrix (2.50) is a Roe matrix. Here, $\boldsymbol{R} = (\boldsymbol{r}_{i+1/2}^1 | \boldsymbol{r}_{i+1/2}^2)$, $|\boldsymbol{\Lambda}| = s_{i+1/2}^n \operatorname{diag}(1, 1)$ and $\boldsymbol{R}^{-1} = (\boldsymbol{l}_{i+1/2}^1 | \boldsymbol{l}_{i+1/2}^2)^\top$, so that the Roe flux (2.48) rewrites as

$$\boldsymbol{f}_{i+1/2}^n = \frac{1}{2}\left(\boldsymbol{f}(\boldsymbol{q}_i^n) + \boldsymbol{f}(\boldsymbol{q}_{i+1}^n)\right) - \frac{1}{2} s_{i+1/2}^n \left(\boldsymbol{q}_{i+1}^n - \boldsymbol{q}_i^n\right). \tag{2.54}$$

As shown in Fig. 2.5, this method is first-order accurate too, but less diffusive than the Lax–Friedrichs method (Fig. 2.4).

2.2.c. *Lax–Wendroff*

The Lax–Wendroff method is obtained through a second-order Taylor expansion of the solution $\boldsymbol{q}(x, t)$ over a time step. Then the differential system (2.23) is used to replace time derivatives by space derivatives which are approximated by centered finite differences. The Lax–Wendroff finite difference method is associated to the numerical flux [40]

$$\boldsymbol{f}_{i+1/2}^n = \frac{1}{2}\left(\boldsymbol{f}(\boldsymbol{q}_i^n) + \boldsymbol{f}(\boldsymbol{q}_{i+1}^n)\right) - \frac{\Delta t}{2\,\Delta x} \boldsymbol{A}_{i+1/2} \left(\boldsymbol{f}(\boldsymbol{q}_{i+1}^n) - \boldsymbol{f}(\boldsymbol{q}_i^n)\right), \tag{2.55}$$

where $\boldsymbol{A}_{i+1/2}$ is a local approximation of the Jacobian (2.47). If the Roe's matrix (2.50) is used, then (2.55) rewrites as

$$\boldsymbol{f}_{i+1/2}^n = \frac{1}{2}\left(\boldsymbol{f}(\boldsymbol{q}_i^n) + \boldsymbol{f}(\boldsymbol{q}_{i+1}^n)\right) - \frac{\Delta t}{2\,\Delta x} (s_{i+1/2}^n)^2 \left(\boldsymbol{q}_{i+1}^n - \boldsymbol{q}_i^n\right). \tag{2.56}$$

The Lax–Wendroff method (2.43)-(2.56) is stable under the CFL condition (2.44) with $\mathrm{Co}_{\max} = 1$ [69]. Measurements of the L^2-error illustrate that this method is second-order accurate (see Figure 2.5). However, as displayed on Figure 2.4, the Lax–Wendroff method has numerical dispersion, i.e. the spectral components of the solution do not propagate at the same speed c_0. Also, the Lax–Wendroff method introduces spurious oscillations near discontinuities (Fig. 2.6a$_{1,2}$).

2.2.d. *Flux limiter*

As displayed on Figure 2.5, the Lax–Wendroff method (2.43)-(2.56) gives much better accuracy on smooth solutions than the Roe method (2.43)-(2.54). However, both methods fail to resolve discontinuities accurately, either by smearing or by introducing spurious oscillations in the numerical solution (Figure 2.6a$_{1,2}$). High-resolution methods such as the flux limiters, MUSCL, WAF, PPM and high-resolution centered schemes are designed to increase the accuracy near discontinuities. Here a flux-limiter method from [69] is implemented, and the method is described hereinafter.

The Lax–Wendroff flux can be viewed as a correction of the Roe flux. Indeed, substracting and adding $\frac{1}{2}s^n_{i+1/2}\,(\boldsymbol{q}^n_{i+1}-\boldsymbol{q}^n_i)$ in the Lax–Wendroff flux (2.56), one rewrites the latter as $\boldsymbol{f}^n_{i+1/2}=\boldsymbol{f}^L_{i+1/2}+\boldsymbol{f}^C_{i+1/2}$, where $\boldsymbol{f}^L_{i+1/2}$ is the Roe flux (2.54) and

$$\boldsymbol{f}^C_{i+1/2}=\frac{1}{2}s^n_{i+1/2}\left(1-\frac{\Delta t}{\Delta x}s^n_{i+1/2}\right)(\boldsymbol{q}^n_{i+1}-\boldsymbol{q}^n_i) \tag{2.57}$$

is a second-order correction. The flux-limiter method consists in adding a certain amount $\boldsymbol{f}^H_{i+1/2}$ of the correction term $\boldsymbol{f}^C_{i+1/2}$ to the Roe flux, depending on the jump $\boldsymbol{q}^n_{i+1}-\boldsymbol{q}^n_i$ in the numerical solution. Hence, the flux-limiter method reads

$$\boldsymbol{f}^n_{i+1/2}=\boldsymbol{f}^L_{i+1/2}+\boldsymbol{f}^H_{i+1/2}, \tag{2.58}$$

where $\boldsymbol{f}^L_{i+1/2}$ is the Roe flux (2.54) and $\boldsymbol{f}^H_{i+1/2}\simeq\boldsymbol{f}^C_{i+1/2}$ is specified later on.

The classical high resolution method proposed in [69] consists in extending the flux-limiter method for scalar conservation laws to systems. One way is to decompose the correction term in the basis of right eigenvectors of $\boldsymbol{A}_{i+1/2}$ (2.53):

$$\boldsymbol{q}^n_{i+1}-\boldsymbol{q}^n_i=\sum_{k=1}^{2}\mathcal{W}^k_{i+1/2}, \tag{2.59}$$

where

$$\mathcal{W}^k_{i+1/2}=\frac{\boldsymbol{l}^k_{i+1/2}\cdot(\boldsymbol{q}^n_{i+1}-\boldsymbol{q}^n_i)}{\boldsymbol{l}^k_{i+1/2}\cdot\boldsymbol{r}^k_{i+1/2}}\boldsymbol{r}^k_{i+1/2}\,. \tag{2.60}$$

Then, a limiting procedure is applied. The jump $\boldsymbol{q}^n_{i+1}-\boldsymbol{q}^n_i$ (2.59) in the second-order correction term (2.57) is replaced by $\sum_k\phi(\theta^k_{i+1/2})\mathcal{W}^k_{i+1/2}$:

$$\begin{aligned}\boldsymbol{f}^H_{i+1/2}=\frac{1}{2}s^n_{i+1/2}\left(1-\frac{\Delta t}{\Delta x}s^n_{i+1/2}\right)\times\\ \times\left(\phi(\theta^1_{i+1/2})\mathcal{W}^1_{i+1/2}+\phi(\theta^2_{i+1/2})\mathcal{W}^2_{i+1/2}\right).\end{aligned} \tag{2.61}$$

The function ϕ is a *limiter function* and $\theta^k_{i+1/2}$ quantifies the variation of $\mathcal{W}^k_{i+1/2}$ over $[x_i, x_{i+1}]$. Here, $\theta^k_{i+1/2}$ is defined by

$$\theta^1_{i+1/2}=\frac{\mathcal{W}^1_{i+3/2}\cdot\mathcal{W}^1_{i+1/2}}{\mathcal{W}^1_{i+1/2}\cdot\mathcal{W}^1_{i+1/2}}\quad\text{and}\quad\theta^2_{i+1/2}=\frac{\mathcal{W}^2_{i-1/2}\cdot\mathcal{W}^2_{i+1/2}}{\mathcal{W}^2_{i+1/2}\cdot\mathcal{W}^2_{i+1/2}}\,. \tag{2.62}$$

The indices in $\theta^1_{i+1/2}$ and $\theta^2_{i+1/2}$ are not the same since the variation of $\boldsymbol{\mathcal{W}}^k_{i+1/2}$ is computed in the upwind direction (2.62) [69].

If the solution is smooth in the kth characteristic field over $[x_i, x_{i+1}]$, then $\theta^k_{i+1/2} \approx 1$. In this case, the Lax–Wendroff flux (2.56) has much better accuracy than the Roe flux (2.54). Therefore, we set $\phi(1) = 1$ in (2.61). If the solution has a sharp discontinuity in the kth characteristic field over $[x_i, x_{i+1}]$, then $\theta^k_{i+1/2} \approx 0$. In this case, the Roe flux (2.54) is preferred. Therefore, we set $\phi(0) = 0$ in (2.61). Many possible limiter functions can be found in the literature. A classical choice is the MC limiter (monotonized central), defined by [69]

$$\phi(\theta) = \max\{0, \min\{(1+\theta)/2, 2\theta, 2\}\}\,. \tag{2.63}$$

The minmod limiter defined by

$$\phi(\theta) = \max\{0, \min\{1, \theta\}\} \tag{2.64}$$

introduces a bit more numerical diffusion than the MC limiter.

The flux-limiter method (2.43)-(2.58) is stable under the CFL condition (2.44) with $\mathrm{Co}_{\max} = 1$ [69]. For a linear system of conservation laws, the MC limiter has shown higher accuracy than the minmod limiter. As displayed on Figure 2.4, the flux-limiter method reduces the numerical dispersion of the Lax–Wendroff method. However, the extrema of the solution have been clipped, since the flux-limiter method is slightly more diffusive. Measurements of the L^2-error illustrate that the flux-limiter method is not far from being second-order accurate (Fig. 2.5). As displayed on Figure 2.6b_1, this method can catch discontinuities more accurately than all the previous methods.

However, numerical methods with limiters may not converge towards the entropic solution in the case of nonconvex Riemann problems [60, 69, 145]. This is illustrated on Test 2. Indeed, the MC limiter (2.63) introduces a spurious step in the numerical solution of Figure 2.6b_2, which does not disappear when the number of points N_x is increased. This step is diminished by reducing the Courant number (Fig. 2.6c_2), which increases the numerical viscosity. This can also be viewed on the sharpness of the discontinuity from the Figures 2.6b_1 and 2.6c_1. The minmod limiter (2.64) does not seem to suffer such a limitation. Indeed, even for high Courant numbers ($\mathrm{Co} = 0.95$), the numerical solution converges towards the correct solution (Fig. 2.6b_2). Therefore, the minmod limiter is preferred to the MC limiter for the system of nonlinear elastodynamics.

2.3. Higher-order methods

The results obtained with classical finite-volume methods of order up to two suggest that the flux-limiter method is a good compromise between first-order and second-order methods. Indeed, if an adequate limiter function is chosen, the flux-limiter method is more accurate than first-order and second-order methods on both smooth and nonsmooth solutions (in the range of parameters tested). Several higher-order finite-volume schemes can be found in the literature [69]. Here, we present two higher-order methods. The first one, from the ADER family

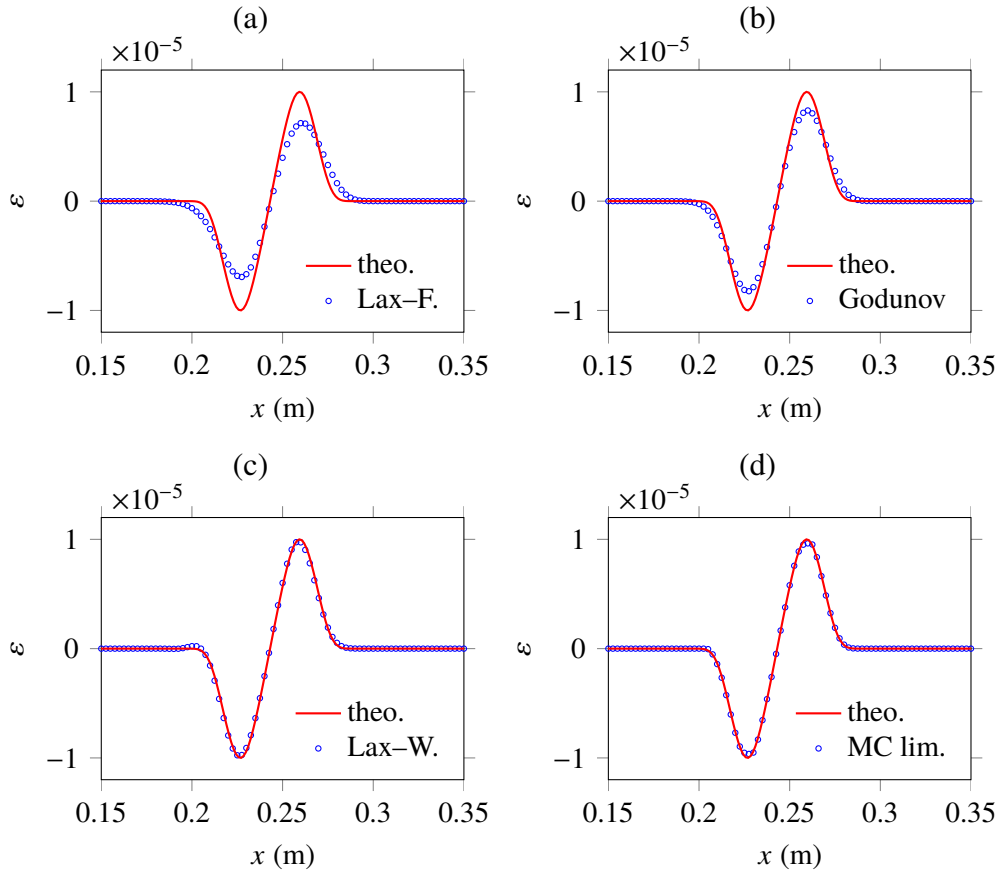

Figure 2.4. Test 1, zoom on the right-going wave. Numerical solutions obtained with finite-volume methods where $N_x = 400$. (a) Lax–Friedrichs, (b) Godunov, (c) Lax–Wendroff, (d) MC flux limiter.

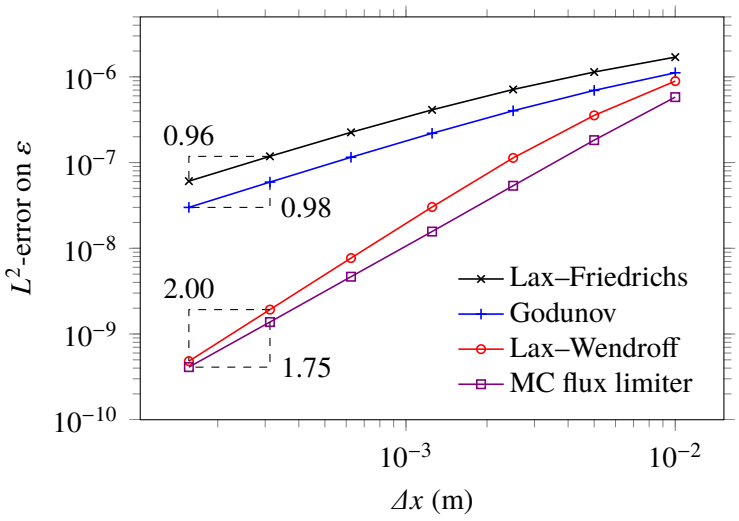

Figure 2.5. Test 1. Convergence measurement of finite-volume methods. The number of points varies from $N_x = 100$ to $N_x = 6400$, i.e. Δx varies in $[0.16, 10]$ mm.

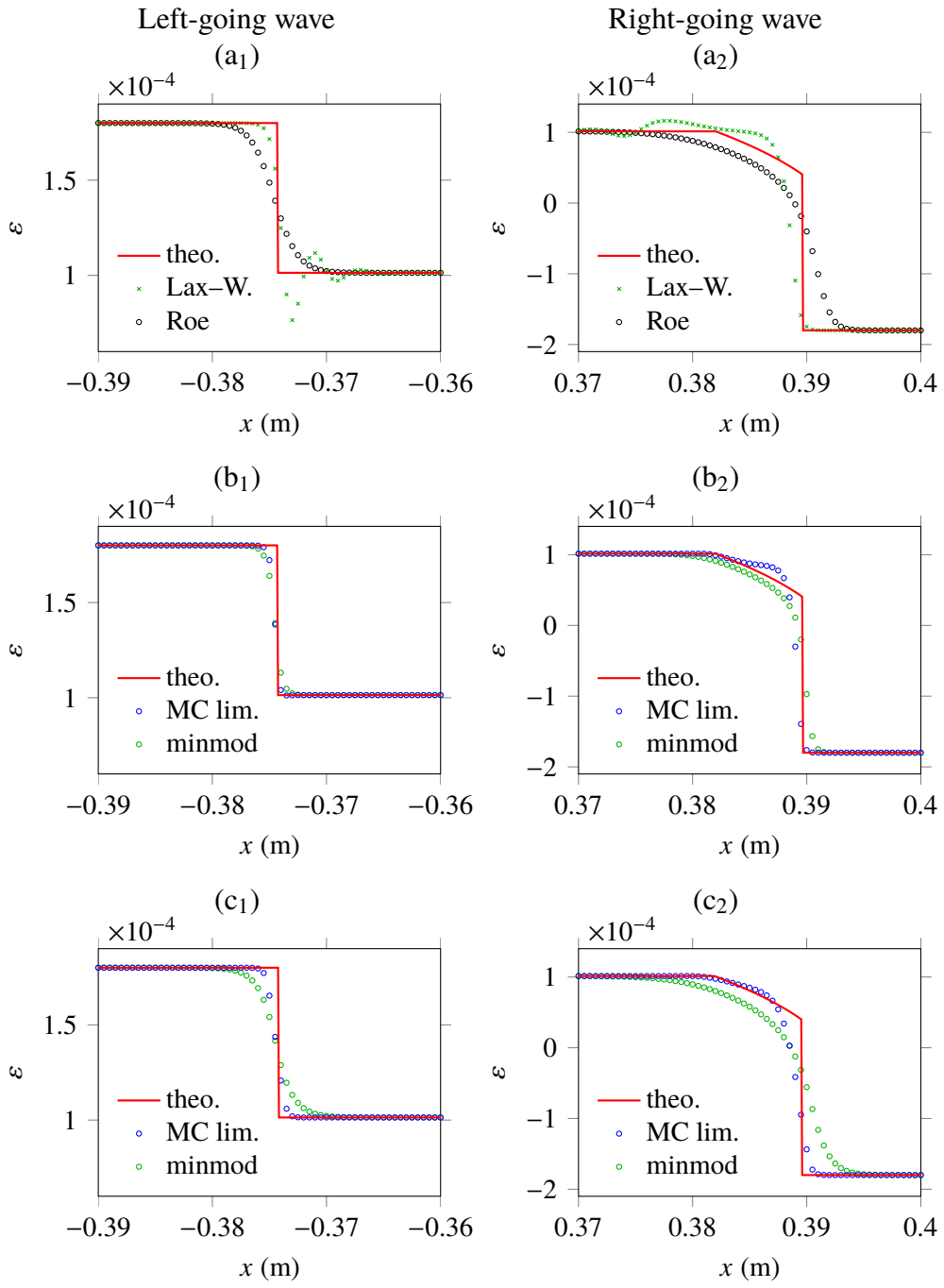

Figure 2.6. Test 2, zoom. Numerical solution obtained with the flux-limiter method where $N_x = 2000$. The first row (a_1)-(a_2) compares the Roe flux and the Lax–Wendroff flux. Then, the MC limiter and the minmod limiter are used. In (b_1)-(b_2), the Courant number is $\mathrm{Co} = 0.95$, whereas in (c_1)-(c_2), $\mathrm{Co} = 0.55$.

Table 2.2. Coefficients Υ_{jk} in the numerical flux $\boldsymbol{f}^n_{i+1/2}$ of the ADER scheme (2.65).

j	k			
	0	1	2	3
−1	−1/12	−1/24	1/12	1/24
0	7/12	5/8	−1/12	−1/8
1	7/12	−5/8	−1/12	1/8
2	−1/12	1/24	1/12	−1/24

(arbitrary high-order derivatives) [36, 124], is a higher-order version of the Lax–Wendroff method. The second one is a WENO finite-difference scheme (weighted essentially nonoscillatory) [128]. It is based on an interpolation procedure, and on high-order time integration.

2.3.a. *ADER*

The numerical flux of the fourth-order ADER scheme is obtained similarly to the flux of the Lax–Wendroff scheme (see Section 12.2 of [68] and (2.55)), but higher-order spatial finite differences are used. Thus,

$$\boldsymbol{f}^n_{i+1/2} = \sum_{j=-1}^{2} \sum_{k=0}^{3} \Upsilon_{jk} \left(\frac{\Delta t}{\Delta x} \boldsymbol{A}_{i+1/2} \right)^k \boldsymbol{f}(\boldsymbol{q}^n_{i+j}), \tag{2.65}$$

where the coefficients Υ_{jk} are given in Table 2.2. In practice, the ADER scheme (2.43)-(2.65) is stable under the CFL condition (2.44) with $\mathrm{Co}_{\max} = 1$. Figure 2.7a shows that the ADER scheme does not introduce visible artifacts in smooth solutions. Measurements of the L^2-error illustrate that this method is fourth-order accurate on smooth solutions (Fig. 2.8). However, the method introduces spurious oscillations near discontinuities, and is unable to capture compound waves (Figs. 2.9a$_{1,2}$).

2.3.b. *The WENO-Roe scheme*

In this subsection, we restrict ourselves to the homogeneous systems of conservation laws $\partial_t \boldsymbol{q} + \partial_x \boldsymbol{f}(\boldsymbol{q}) = \boldsymbol{0}$, for which a high-order numerical method is presented. It relies on WENO (weighted essentially nonoscillatory) interpolation — a nonlinear polynomial interpolation technique which avoids spurious oscillations — and on high-order explicit time-integration. This reconstruction procedure provides an approximation of the cell interface value $u(x_{i+1/2})$ of a scalar function u from the average cell values $\bar{u}_j$ (see the Appendix, Sec. 4.3.a). A review of such numerical methods can be found in [128].

Till now, the system of conservation laws has been discretized simultaneously in space and time (2.43). Here, a *method of lines* $\mathrm{d}\boldsymbol{q}_i/\mathrm{d}t = \boldsymbol{\mathcal{L}}_i(\boldsymbol{q})$ is used, which results from discretizing in space first. Then, a time discretization is introduced, and explicit time-integration of the differential equation is performed. One can

implement the fourth-order Runge–Kutta method

$$\begin{aligned}
\boldsymbol{q}_i^* &= \boldsymbol{q}_i^n + \frac{1}{2}\Delta t\, \boldsymbol{\mathcal{L}}_i(\boldsymbol{q}^n),\\
\boldsymbol{q}_i^{**} &= \boldsymbol{q}_i^n + \frac{1}{2}\Delta t\, \boldsymbol{\mathcal{L}}_i(\boldsymbol{q}^*),\\
\boldsymbol{q}_i^{***} &= \boldsymbol{q}_i^n + \Delta t\, \boldsymbol{\mathcal{L}}_i(\boldsymbol{q}^{**}),\\
\boldsymbol{q}_i^{n+1} &= -\frac{1}{3}\,\boldsymbol{q}_i^n + \frac{1}{3}\,\boldsymbol{q}_i^* + \frac{2}{3}\,\boldsymbol{q}_i^{**} + \frac{1}{3}\,\boldsymbol{q}_i^{***} + \frac{1}{6}\Delta t\, \boldsymbol{\mathcal{L}}_i(\boldsymbol{q}^{***}),
\end{aligned} \tag{2.66}$$

but other choices are possible. For instance, a third-order TVD (total variation diminishing) Runge–Kutta method is sometimes preferred [24, 39, 53, 127, 128]. The Runge–Kutta method (2.66) is not TVD. It is stable under the condition

$$\Delta t \leqslant 2/3\, \Delta t_{\mathrm{FE}}\,, \tag{2.67}$$

where Δt_{FE} is the stability limit $\Delta t \leqslant \Delta t_{\mathrm{FE}}$ of the forward Euler method $\boldsymbol{q}_i^{n+1} = \boldsymbol{q}_i^n + \Delta t\, \boldsymbol{\mathcal{L}}_i(\boldsymbol{q}^n)$ [126].

The difference between finite-difference and finite-volume WENO schemes is subtle on one-dimensional regular meshes [128]. In finite-volume schemes, WENO reconstruction is applied to the cell averages $\boldsymbol{q}_i^n \simeq \bar{\boldsymbol{q}}_i(t_n)$ of the conserved variables. Here, we present a finite-difference scheme, where WENO reconstruction is applied to the cell averages $\boldsymbol{f}_i^n \simeq \overline{(\boldsymbol{f} \circ \boldsymbol{q})}_i(t_n)$ of the flux. The method of lines reads

$$\frac{\mathrm{d}}{\mathrm{d}t}\boldsymbol{q}_i = \boldsymbol{\mathcal{L}}_i(\boldsymbol{q}) \simeq \frac{\boldsymbol{f}_{i-1/2} - \boldsymbol{f}_{i+1/2}}{\Delta x} \tag{2.68}$$

where $\boldsymbol{f}_{i\pm1/2}$ is obtained by WENO reconstruction.

The WENO reconstruction procedure in Sec. 4.3.a applies to scalar functions. For systems of conservation laws, it provides better accuracy to perform reconstruction in local characteristic variables rather than componentwise [128]. Therefore, $\boldsymbol{f}_{i+1/2}$ is computed as follows:

1. Compute an approximation $\boldsymbol{A}_{i+1/2}$ of the Jacobian matrix at a cell interface $x_{i+1/2}$, here Roe's matrix (2.50), and compute its left and right eigenvectors $\boldsymbol{l}_{i+1/2}^k$, $\boldsymbol{r}_{i+1/2}^k$ with $k = 1, \ldots, 2$;
2. Transform the physical flux to local characteristic fluxes

$$\vartheta_{i+1/2}^k(\boldsymbol{q}) = \frac{\boldsymbol{l}_{i+1/2}^k \cdot \boldsymbol{f}(\boldsymbol{q})}{\boldsymbol{l}_{i+1/2}^k \cdot \boldsymbol{r}_{i+1/2}^k}\,; \tag{2.69}$$

3. Perform WENO reconstruction of each characteristic flux $\vartheta_{i+1/2}^k$ to obtain the corresponding component of the numerical flux $\Theta_{i+1/2}^k$ at a cell interface $x_{i+1/2}$;
4. Transform back into physical space by using

$$\boldsymbol{f}_{i+1/2} = \sum_{k=1}^{2} \Theta_{i+1/2}^k\, \boldsymbol{r}_{i+1/2}^k\,. \tag{2.70}$$

These steps are performed at each stage of the time-stepping procedure (2.66).

For the stability of finite-difference WENO schemes, the reconstruction procedure in Sec. 4.3.a must be applied in an upwind fashion. Left-going characteristic fluxes use a biased stencil with one more point to the right, whereas right-going characteristic fluxes use a biased stencil with one more point to the left [128]. Here, the eigenvalues of the local Jacobian matrix are $\{-s_{i+1/2}, s_{i+1/2}\}$. Thus, we compute $\Theta^1_{i+1/2}$ by WENO reconstruction of the characteristic flux $\vartheta^1_{i+1/2}(\boldsymbol{q})$ over the stencils $S_1 = \{x_{i-2}, x_{i-1}, x_i\}$, $S_2 = \{x_{i-1}, x_i, x_{i+1}\}$ and $S_3 = \{x_i, x_{i+1}, x_{i+2}\}$. Similarly, $\Theta^2_{i+1/2}$ is obtained by WENO reconstruction of the characteristic flux $\vartheta^2_{i+1/2}(\boldsymbol{q})$ over the stencils $S_1 = \{x_{i-3}, x_{i-2}, x_{i-1}\}$, $S_2 = \{x_{i-2}, x_{i-1}, x_i\}$ and $S_3 = \{x_{i-1}, x_i, x_{i+1}\}$.

Since WENO interpolation is nonlinear with respect to the data, one must be careful to the orders of magnitude of the data, which must not be too large or too small. Ideally, one would like that the numerical results do not depend on the amplitude of the excitation. For this purpose, we apply the WENO scheme to the dimensionless data

$$\boldsymbol{q}_{\aleph} = \begin{pmatrix} \varepsilon_{\aleph} \\ v_{\aleph} \end{pmatrix} = \begin{pmatrix} \varepsilon/\varepsilon_{\max} \\ v/v_{\max} \end{pmatrix}, \tag{2.71}$$

where $\varepsilon_{\max}$ and $v_{\max}$ are constants. As shown in Appendix 4.3.b, the change of variables (2.71) amounts to divide the characteristic fluxes $\vartheta^k_{i+1/2}$ by $\varepsilon_{\max}$ in (2.69), and to multiply the numerical flux by $\varepsilon_{\max}$ in (2.70). Thus, the local characteristic fluxes are

$$\begin{aligned} \vartheta^1_{i+1/2}(\boldsymbol{q}) &= -\frac{1}{2}\left(v + \frac{\sigma(\varepsilon)}{\rho_0\, s_{i+1/2}}\right) \Big/ \varepsilon_{\max}\,, \\ \vartheta^2_{i+1/2}(\boldsymbol{q}) &= -\frac{1}{2}\left(v - \frac{\sigma(\varepsilon)}{\rho_0\, s_{i+1/2}}\right) \Big/ \varepsilon_{\max}\,, \end{aligned} \tag{2.72}$$

where $s_{i+1/2} = \sqrt{a_{i+1/2}}$ (2.51) is positive, and the numerical flux in (2.68) is given by

$$\boldsymbol{f}_{i+1/2} = \begin{pmatrix} \Theta^1_{i+1/2} + \Theta^2_{i+1/2} \\ s_{i+1/2}\,(\Theta^1_{i+1/2} - \Theta^2_{i+1/2}) \end{pmatrix} \varepsilon_{\max}\,. \tag{2.73}$$

The variables $\varepsilon_{\max}$ and $v_{\max}$ denote respectively the maximum absolute strain and the maximum absolute particle velocity, such that the components of $\boldsymbol{q}_{\aleph}$ in (2.71) have the order of magnitude of unity. Only the value of $\varepsilon_{\max}$ is required to perform WENO reconstruction in dimensionless variables (2.72)-(2.73). The maximum absolute strain $\varepsilon_{\max}$ can be estimated a priori by linearizing the stress-strain relationship $\sigma(\varepsilon) \simeq M_0\,\varepsilon$. In this case, the maximum amplitude of the analytical solution (2.37) can be deduced from the amplitude of the excitation. For example, one obtains $\varepsilon_{\max} = 10^{-5}$ in the case of Test 1, and $\varepsilon_{\max} = 1.8\times10^{-4}$ in the case of Test 2.

Figure 2.7 displays the results obtained with the WENO scheme on Test 1. Numerical dissipation is very low and the order of convergence is higher than four (Fig. 2.8). At the same Courant number Co = 0.66, the results obtained with the WENO method are much better than those obtained with the MC flux

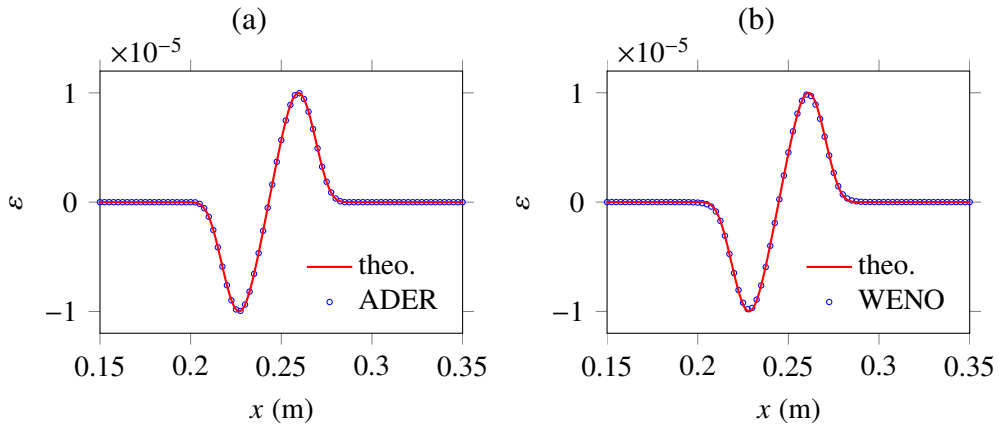

Figure 2.7. Test 1, zoom on the right-going wave. Numerical solution obtained with high-order methods where $N_x = 400$. (a) ADER scheme, where the Courant number is Co $= 0.95$; (b) WENO scheme, where Co $= 0.66$.

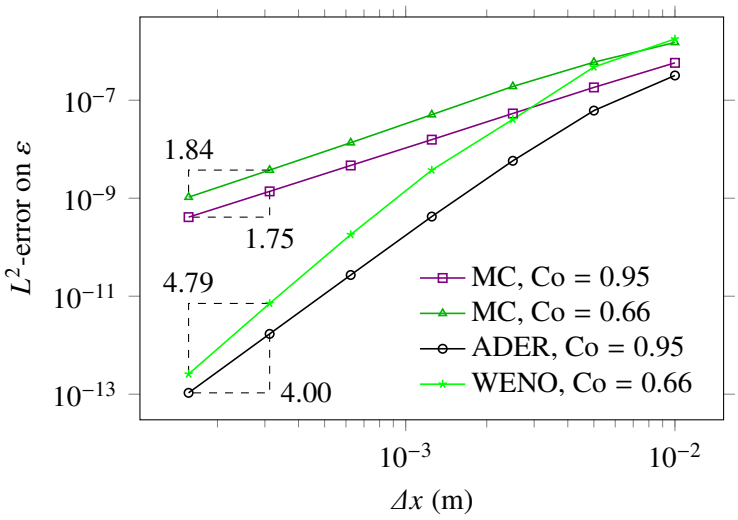

Figure 2.8. Test 1. Convergence measurement of high-order methods, compared to the second-order flux-limiter method. The number of points varies from $N_x = 100$ to $N_x = 6400$, i.e. Δx varies in $[0.16, 10]$ mm.

limiter. Figure 2.9 compares the WENO method to the minmod flux limiter on Test 2. Here too, the WENO method gives better results than the minmod flux limiter when Co $= 0.66$. However, for Co $= 0.95$, the results obtained with the flux-limiter method are similar to those obtained with the WENO method at Co $= 0.66$. Modified WENO finite-volume schemes and discontinuous Galerkin finite element methods have been proposed in [19, 113] to increase the performance of such methods in the case of nonconvex conservation laws.

■ *Discussion.* The choice of a numerical method depends on the computational time needed to solve a problem with a given accuracy. For this purpose, Figure 2.10 shows the time spent by a midrange laptop to compute the solution of Test 1 (Intel Core i3-2370M, 2.4 GHz, 4 Go, 2012), with the discretizations from Fig. 2.8. One observes that the flux-limiter method and the ADER scheme have comparable computational times for a given discretization. Nevertheless, the ADER scheme is much more accurate on smooth solutions, while the flux-limiter

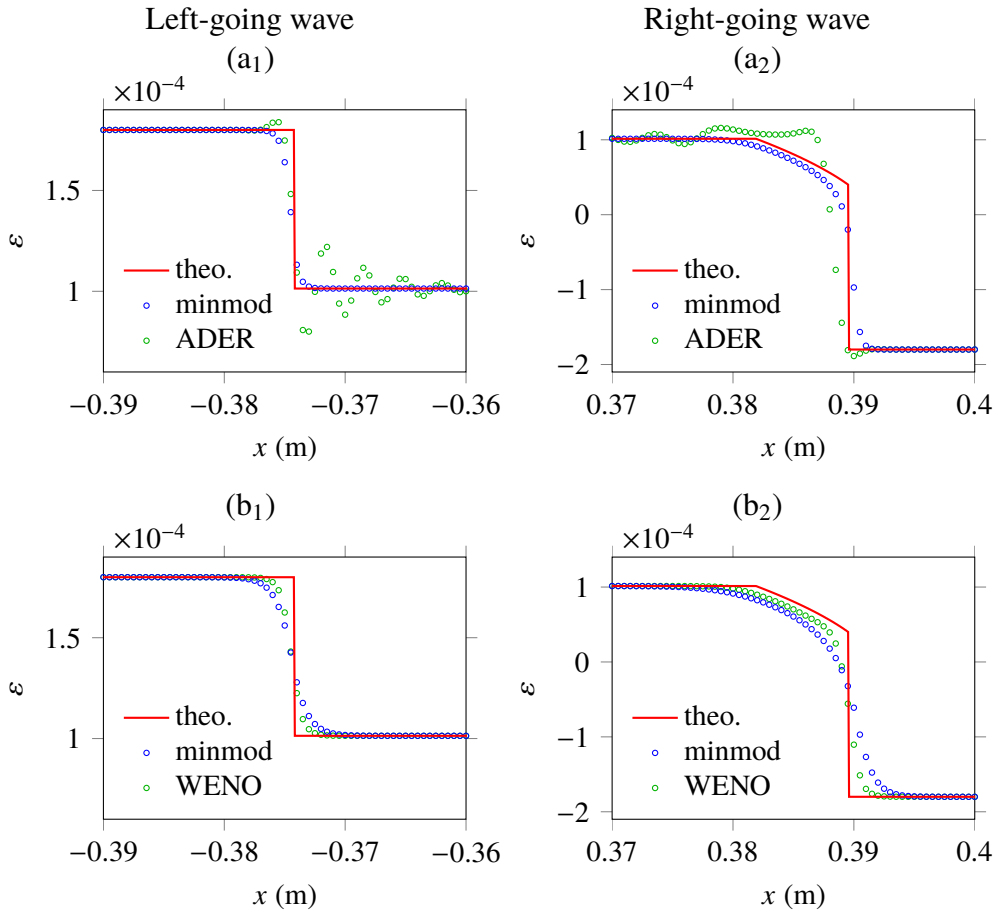

Figure 2.9. Test 2. Numerical solution obtained with high-order methods compared to the flux-limiter method, where $N_x = 2000$ (zoom). (a_1)-(a_2) Minmod flux limiter and ADER, where Co $= 0.95$; (b_1)-(b_2) Minmod flux limiter and WENO, where Co $= 0.66$.

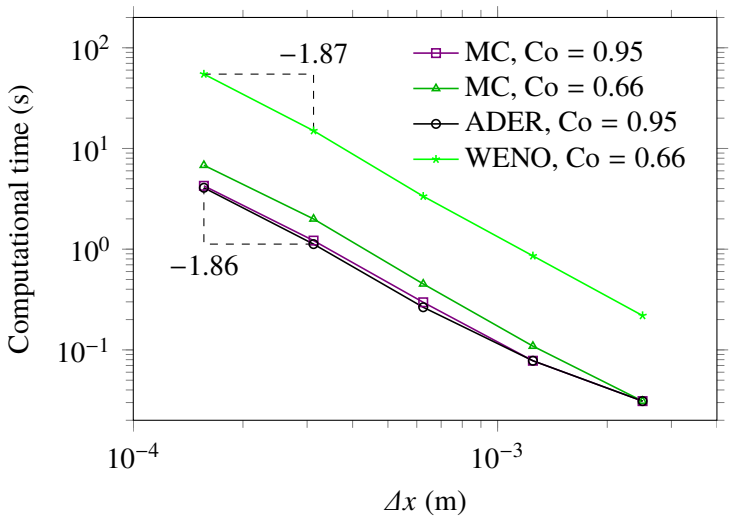

Figure 2.10. Test 1. Computational time needed to solve the problem with high-order methods and with the flux-limiter method (configuration from Fig. 2.8).

method is much more accurate on nonsmooth solutions (cf. Fig. 2.9). With the same discretization, the WENO scheme requires approximately ten times more computational time, but the WENO scheme is more flexible than the previous methods. Therefore, the ADER scheme is best suited for the computation of smooth solutions (high accuracy for a reasonable computational time). The flux-limiter method is best suited for the computation of nonsmooth solutions (high accuracy for a reasonable computational time). The WENO scheme is best suited for cases where the smoothness of the solution is not known (high accuracy, but large computational time).

3. Conclusion

In this chapter, the propagation of longitudinal waves in hyperelastic material has been investigated theoretically and numerically. The study concerns polynomial stress-strain relationships. Particular features of nonlinear wave propagation are illustrated numerically, and various finite-volume methods are presented.

The examples show that compound waves require particular attention when using numerical methods. As a result, a rationale behind the choice of well-suited numerical methods is given at the end of the chapter. The main benefit of using the WENO scheme instead of the flux-limiter scheme or the ADER scheme is its flexibility regarding the smoothness of the solution, but its computational costs are significant.

The present chapter is a necessary step in the study of nonlinear waves in geomaterials. Indeed, it is important to be aware of the peculiarities of nonlinear wave propagation when performing numerical experiments related to experimental observations. Chapter 3 details the analytical solution of the Riemann problem (such as Test 2). Then, the following chapters are dedicated to the modeling of slow dynamics and viscoelastic dissipation in solids. The corresponding models enter the same theoretical framework as the hyperelastic material model of Chapter 2. Also, the numerical methods presented in that chapter — flux-limiter method, ADER scheme — are used in the case of solids with slow dynamics, and in two space dimensions.

4. Appendix

4.1. Eulerian hyperelasticity

The Lagrangian representation of motion is used along the thesis. In the Eulerian representation of motion, the material derivative $\dot{\boldsymbol{\psi}}$ of any field $\boldsymbol{\psi}(\boldsymbol{x}_t, t)$ is $\dot{\boldsymbol{\psi}} = \mathbf{grad}\,\boldsymbol{\psi} \cdot \boldsymbol{v} + \partial_t \boldsymbol{\psi}$. Here, the gradient operator is defined with respect to the current position $\boldsymbol{x}_t$ (Eulerian gradient), as well as the other spatial differential operators. Using the relationship between the Lagrangian and the Eulerian gradient operators, the conservation of deformation gradient (2.2) becomes $\dot{\boldsymbol{F}} = \mathbf{grad}\,\boldsymbol{v} \cdot \boldsymbol{F}$. The conservation of mass implies $\dot{\rho}/\rho = -\mathrm{div}\,\boldsymbol{v}$, where ρ denotes the mass density in the deformed configuration. The motion is also driven by the conservation of momentum, which writes $\rho\dot{\boldsymbol{v}} = \mathbf{div}\,\boldsymbol{\sigma} + \boldsymbol{f}_E^v$, where $\boldsymbol{\sigma}$ is the Cauchy stress tensor. The force $\boldsymbol{f}_E^v$ is related to the force $\boldsymbol{f}^v$ in (2.4) through $\boldsymbol{f}^v = \boldsymbol{f}_E^v \det \boldsymbol{F}$.

As such, the equations of motion are not written as a system of conservation laws. Using the expression of the material derivative and vector calculus identities, the conservation of mass rewrites as

$$\partial_t \rho + \mathrm{div}(\rho \boldsymbol{v}) = 0\,, \tag{2.74}$$

which is a scalar conservation laws. Similarly, the conservation of momentum rewrites as

$$\partial_t(\rho \boldsymbol{v}) = \mathbf{div}(\boldsymbol{\sigma} - \rho \boldsymbol{v} \otimes \boldsymbol{v}) + \boldsymbol{f}_E^v\,. \tag{2.75}$$

In hyperelasticity, the stress tensor $\boldsymbol{\sigma}$ depends on a given strain tensor $\boldsymbol{\chi}$, which is defined as a function of the deformation gradient tensor $\boldsymbol{F}$. Following [37], one can obtain a conservative formulation by introducing the vectors $\boldsymbol{a}^n$, defined as the nth column of the tensor $\boldsymbol{F}^{-\top}$. These vectors satisfy

$$\partial_t \boldsymbol{a}^n + \mathbf{grad}(\boldsymbol{v} \cdot \boldsymbol{a}^n) = \boldsymbol{0}\,, \qquad \mathbf{curl}\,\boldsymbol{a}^n = \boldsymbol{0} \tag{2.76}$$

for $n = 1, 2, 3$, leading to a conservative formulation of the equations of motion.

4.2. Shock wave generation

In nonlinear acoustics, discontinuities may develop from smooth initial data $\boldsymbol{q}(x, 0) = \boldsymbol{q}^\circ(x)$ in finite time. The smallest such time is called *breaking time*. For $k = 1, 2$, we introduce the k-Riemann invariants $w_k = v + (-1)^k C(\varepsilon)$, where C is an antiderivative of the speed of sound c (2.26). According to [62, 63], the differential equation

$$\mathrm{D}(\zeta) + \kappa\zeta^2 = 0\,, \qquad \zeta(0) = \zeta^\circ(x_0) \tag{2.77}$$

is satisfied by $\zeta = e^h \partial_x w_2$, where h is defined as $\partial_{w_1} h = \partial_{w_1} c/(2c)$, e.g. $h = \frac{1}{2}\ln c$. The differential operator $\mathrm{D} = \partial_t + c\,\partial_x$ denotes the time derivative along the 2-characteristics. The Riemann invariant w_2 is constant along 2-characteristics,

which are the curves of the x-t plane defined by $\frac{\mathrm{d}}{\mathrm{d}t}x = c$. The coefficient in (2.77) is given by $\kappa = e^{-h}\partial_{w_2} c$. The solution of (2.77) blows up at the time t^* such that

$$\int_0^{t^*} \kappa(x(\tau), \tau)\, \mathrm{d}\tau = \frac{-1}{\zeta^\circ(x_0)}, \tag{2.78}$$

where integration is performed along the 2-characteristic curve starting at $x(0) = x_0$ [63]. In practice, it is difficult to deduce the exact value of the breaking time $t_B = \inf_{x_0} t^*$ from (2.78), but bounds and estimates can be found. If the quadratic constitutive law $\sigma = M_0\, \varepsilon \left(1 - \beta\varepsilon\right)$ is used and the initial data is $\varepsilon^\circ(x) = 2V \sin(k_c x)$, $v^\circ(x) = 0$ where $k_c = \omega/c_0$ is the wavenumber, one obtains the estimate $t_B \simeq 1/(\beta V \omega)$ [62].

4.3. Complements on finite volumes

4.3.a. *WENO reconstruction*

We present the WENO reconstruction procedure used in the WENO scheme of Sec. 2.3. If u denotes a function from which we know the averages $\bar{u}_j$ over the cells $C_j = [x_{j-1/2}, x_{j+1/2}]$, such a reconstruction procedure provides an approximation of the value $u(x_{i+1/2})$ at a cell interface. If U is a primitive function of u, then the cell averages $\bar{u}_j$ depend on $U(x_{j\pm1/2})$. Thus, the primitive function satisfies

$$U(x_{i+1/2}) = \Delta x \sum_{j=0}^{i} \bar{u}_j\,, \quad \text{where} \quad \bar{u}_j = \frac{U(x_{j+1/2}) - U(x_{j-1/2})}{\Delta x}\,. \tag{2.79}$$

Knowing all the values of U at the cell interfaces, one can obtain a polynomial interpolation of U. An approximation of u is obtained by differentiating this polynomial [128].

For example, there is a unique polynomial P_1 of degree at most three that interpolates U at the abscissas $\{x_{i-5/2}, x_{i-3/2}, x_{i-1/2}, x_{i+1/2}\}$. One can verify that the cell averages over the cells C_{i-2}, C_{i-1}, C_i of its derivative P_1' are exactly equal to $\bar{u}_{i-2}$, $\bar{u}_{i-1}$, $\bar{u}_i$. Therefore, P_1' reconstructs the data over the stencil $S_1 = \{x_{i-2}, x_{i-1}, x_i\}$. Similarly, one obtains the polynomials P_2' and P_3' that reconstruct the data over the stencils $S_2 = \{x_{i-1}, x_i, x_{i+1}\}$ and $S_3 = \{x_i, x_{i+1}, x_{i+2}\}$ respectively [128]. All three approximations

$$\begin{aligned}
P_1'(x_{i+1/2}) &= \frac{1}{3}\bar{u}_{i-2} - \frac{7}{6}\bar{u}_{i-1} + \frac{11}{6}\bar{u}_i\,,\\
P_2'(x_{i+1/2}) &= -\frac{1}{6}\bar{u}_{i-1} + \frac{5}{6}\bar{u}_i + \frac{1}{3}\bar{u}_{i+1}\,,\\
P_3'(x_{i+1/2}) &= \frac{1}{3}\bar{u}_i + \frac{5}{6}\bar{u}_{i+1} - \frac{1}{6}\bar{u}_{i+2}\,,
\end{aligned} \tag{2.80}$$

of $u(x_{i+1/2})$ are third-order accurate in Δx, if u is smooth over $[x_{i-5/2}, x_{i+5/2}]$. Moreover, the convex linear combination

$$\gamma_1\, P_1'(x_{i+1/2}) + \gamma_2\, P_2'(x_{i+1/2}) + \gamma_3\, P_3'(x_{i+1/2}) \tag{2.81}$$

with $\gamma_1 = 1/10$, $\gamma_2 = 3/5$ and $\gamma_3 = 3/10$ is a fifth-order approximation of $u(x_{i+1/2})$ [128].

If u is only piecewise smooth, we would like that the interpolation procedure introduces no spurious oscillations in the vicinity of a discontinuity. The classical ENO procedure consists in choosing one of the three approximations (2.80) according to the smoothness of u. The smoothness is measured by divided differences over the stencils S_1, S_2 and S_3 [39, 128]. The WENO procedure consists in constructing a convex linear combination

$$w_1\, P_1'(x_{i+1/2}) + w_2\, P_2'(x_{i+1/2}) + w_3\, P_3'(x_{i+1/2}), \tag{2.82}$$

of the three approximations (2.80), and in setting the nonlinear weights w_j so as to avoid oscillations. The choice of the nonlinear weights w_j relies on a *smoothness indicator*

$$\beta_j = \sum_{\ell=1}^{2} \Delta x^{2\ell-1} \int_{x_{i-1/2}}^{x_{i+1/2}} \left(\frac{\mathrm{d}^\ell}{\mathrm{d}x^\ell}\, P_j'(x) \right)^2 \mathrm{d}x, \tag{2.83}$$

defined as a scaled sum of the squared L^2-norm of the interpolation polynomial's derivatives (2.83). Here,

$$\begin{aligned}
\beta_1 &= \frac{13}{12}\left(\bar{u}_{i-2} - 2\bar{u}_{i-1} + \bar{u}_i\right)^2 + \frac{1}{4}\left(\bar{u}_{i-2} - 4\bar{u}_{i-1} + 3\bar{u}_i\right)^2, \\
\beta_2 &= \frac{13}{12}\left(\bar{u}_{i-1} - 2\bar{u}_i + \bar{u}_{i+1}\right)^2 + \frac{1}{4}\left(\bar{u}_{i-1} - \bar{u}_{i+1}\right)^2, \\
\beta_3 &= \frac{13}{12}\left(\bar{u}_i - 2\bar{u}_{i+1} + \bar{u}_{i+2}\right)^2 + \frac{1}{4}\left(3\bar{u}_i - 4\bar{u}_{i+1} + \bar{u}_{i+2}\right)^2.
\end{aligned} \tag{2.84}$$

The nonlinear weights in (2.82) are computed according to

$$w_j = \frac{\tilde{w}_j}{\tilde{w}_1 + \tilde{w}_2 + \tilde{w}_3}, \qquad \text{with} \qquad \tilde{w}_j = \frac{\gamma_j}{(10^{-6} + \beta_j)^2}. \tag{2.85}$$

If U is smooth in the stencil S_j, then β_j is small and $w_j \simeq \gamma_j$. Else, β_j is large and $w_j \simeq 0$. Therefore, WENO reconstruction is at least as accurate as ENO reconstruction, and higher-order accurate when u is smooth (2.81) [128].

If the stencils are $S_1 = \{x_{i+1}, x_{i+2}, x_{i+3}\}$, $S_2 = \{x_i, x_{i+1}, x_{i+2}\}$ and $S_3 = \{x_{i-1}, x_i, x_{i+1}\}$, then the corresponding polynomial approximations of $u(x_{i+1/2})$ are

$$\begin{aligned}
P_1'(x_{i+1/2}) &= \frac{11}{6}\bar{u}_{i+1} - \frac{7}{6}\bar{u}_{i+2} + \frac{1}{3}\bar{u}_{i+3}, \\
P_2'(x_{i+1/2}) &= \frac{1}{3}\bar{u}_i + \frac{5}{6}\bar{u}_{i+1} - \frac{1}{6}\bar{u}_{i+2}, \\
P_3'(x_{i+1/2}) &= -\frac{1}{6}\bar{u}_{i-1} + \frac{5}{6}\bar{u}_i + \frac{1}{3}\bar{u}_{i+1}.
\end{aligned} \tag{2.86}$$

Moreover, the convex linear combination (2.81) is a fifth-order approximation of $u(x_{i+1/2})$. The nonlinear weights in the WENO reconstruction (2.82) are given

by (2.85), with the smoothness indicators

$$\begin{aligned}
\beta_1 &= \frac{13}{12}\left(\bar{u}_{i+1} - 2\bar{u}_{i+2} + \bar{u}_{i+3}\right)^2 + \frac{1}{4}\left(3\bar{u}_{i+1} - 4\bar{u}_{i+2} + \bar{u}_{i+3}\right)^2 , \\
\beta_2 &= \frac{13}{12}\left(\bar{u}_{i} - 2\bar{u}_{i+1} + \bar{u}_{i+2}\right)^2 + \frac{1}{4}\left(\bar{u}_{i+2} - \bar{u}_{i}\right)^2 , \\
\beta_3 &= \frac{13}{12}\left(\bar{u}_{i-1} - 2\bar{u}_{i} + \bar{u}_{i+1}\right)^2 + \frac{1}{4}\left(\bar{u}_{i-1} - 4\bar{u}_{i} + 3\bar{u}_{i+1}\right)^2 .
\end{aligned} \tag{2.87}$$

This reconstruction is very similar to those for the stencils $S_1 = \{x_{i-2}, x_{i-1}, x_i\}$, $S_2 = \{x_{i-1}, x_i, x_{i+1}\}$ and $S_3 = \{x_i, x_{i+1}, x_{i+2}\}$, but it is biased with one more point to the right of the cell interface.

4.3.b. *Dimensionless variables*

Let us do the change of variables (2.71). The physical variables $\boldsymbol{q}$ still satisfy the system of conservation laws (2.23). The dimensionless variables (2.71) also satisfy a system of conservation laws $\partial_t \boldsymbol{q}_{\aleph} + \partial_x \boldsymbol{f}_{\aleph}(\boldsymbol{q}_{\aleph}) = \boldsymbol{0}$ with physical flux

$$\boldsymbol{f}_{\aleph}(\boldsymbol{q}_{\aleph}) = \begin{pmatrix} 1/\varepsilon_{\max} & 0 \\ 0 & 1/v_{\max} \end{pmatrix} \boldsymbol{f}(\boldsymbol{q}) . \tag{2.88}$$

The corresponding Roe's matrix is

$$\left(\boldsymbol{A}_{i+1/2}\right)_{\aleph} = \begin{pmatrix} 0 & r_{\max} \\ (s_{i+1/2})^2/r_{\max} & 0 \end{pmatrix}, \tag{2.89}$$

where $r_{\max} = v_{\max}/\varepsilon_{\max}$ and $s_{i+1/2} = \sqrt{a_{i+1/2}}$ satisfies (2.51). Roe's matrix in dimensionless variables (2.89) has the same eigenvalues than Roe's Matrix in physical variables (2.50). Its eigenvectors are

$$\begin{aligned}
\left(\boldsymbol{r}^1_{i+1/2}\right)_{\aleph} &= \begin{pmatrix} 1 \\ s_{i+1/2}/r_{\max} \end{pmatrix}, \qquad \left(\boldsymbol{l}^1_{i+1/2}\right)_{\aleph} = \frac{1}{2}\begin{pmatrix} 1 \\ r_{\max}/s_{i+1/2} \end{pmatrix}, \\
\left(\boldsymbol{r}^2_{i+1/2}\right)_{\aleph} &= \begin{pmatrix} 1 \\ -s_{i+1/2}/r_{\max} \end{pmatrix}, \qquad \left(\boldsymbol{l}^2_{i+1/2}\right)_{\aleph} = \frac{1}{2}\begin{pmatrix} 1 \\ -r_{\max}/s_{i+1/2} \end{pmatrix}.
\end{aligned} \tag{2.90}$$

Then, $\vartheta^k_{i+1/2}(\boldsymbol{q}_{\aleph}) = \left(\boldsymbol{l}^k_{i+1/2}\right)_{\aleph} \cdot \boldsymbol{f}_{\aleph}(\boldsymbol{q}_{\aleph})$ yields the expression of the characteristic fluxes in equation (2.69). When injecting (2.88) into the definition of $\boldsymbol{\mathcal{L}}_i(\boldsymbol{q})$ (2.68), one has

$$\boldsymbol{f}_{i+1/2} = \begin{pmatrix} \varepsilon_{\max} & 0 \\ 0 & v_{\max} \end{pmatrix} \left(\boldsymbol{f}_{i+1/2}\right)_{\aleph} , \tag{2.91}$$

where

$$\left(\boldsymbol{f}_{i+1/2}\right)_{\aleph} = \sum_{k=1}^{K} \Theta^k_{i+1/2} \left(\boldsymbol{r}^k_{i+1/2}\right)_{\aleph} . \tag{2.92}$$

Thus, the numerical flux (2.73) is obtained.

Table 2.3. Number of ghost cells S on both sides of the domain for each numerical method.

	Lax-Friedrichs Godunov Lax–Wendroff	Flux limiter ADER	WENO
S	1	2	3

4.3.c. *Boundary conditions*

To compute $\boldsymbol{q}_i^{n+1}$ when $0 \leqslant i \leqslant N_x$, the numerical methods presented here require S values to the left and S values to the right of $\boldsymbol{q}_i^n$ (see Table 2.3). Therefore, S "ghost cells" are added to both sides of the domain, such that the values $\{\boldsymbol{q}_{-1}^n, \ldots, \boldsymbol{q}_{-S}^n\}$ and $\{\boldsymbol{q}_{N_x+1}^n, \ldots, \boldsymbol{q}_{N_x+S}^n\}$ can be accessed. The content of the ghost cells depends on which type of boundary condition is applied. When the time-stepping procedure uses intermediate steps, e.g. when the fourth-order Runge–Kutta method (2.66) is used for time-integration, ghost cells must be added to the vectors of intermediate values. The boundary conditions must be applied at each intermediate time step, for example respectively on $\boldsymbol{q}^*$, $\boldsymbol{q}^{**}$ and $\boldsymbol{q}^{***}$.

■ *Outflow boundary conditions.* For instance, to represent an infinite physical domain, one can set

$$\boldsymbol{q}_{-i}^n = \boldsymbol{q}_0^n \qquad \text{and} \qquad \boldsymbol{q}_{N_x+i}^n = \boldsymbol{q}_{N_x}^n \qquad \text{for } i = 1, \ldots, S, \tag{2.93}$$

at each iteration in time [69].

■ *Periodic boundary conditions.* To represent a periodic physical domain, one can set

$$\boldsymbol{q}_{-i}^n = \boldsymbol{q}_{N_x+1-i}^n \qquad \text{and} \qquad \boldsymbol{q}_{N_x+i}^n = \boldsymbol{q}_{-1+i}^n \qquad \text{for } i = 1, \ldots, S, \tag{2.94}$$

at each iteration in time [69].

■ *Free edges.* A free edge is a boundary of the physical domain on which no contact force is applied. Here, it is equivalent to impose that the stress, and so the strain, is zero on the boundary. If the boundary $x = x_0$ is a free edge, then ε_0^n must be equal to zero for all n. One way to implement this boundary condition, is to use symmetry. Let $\boldsymbol{q}^\circ(x)$ denote the initial data over $[x_0, x_{N_x}]$. It is extended to the left by

$$\varepsilon^\circ(x_0 - \xi) = -\varepsilon^\circ(x_0 + \xi) \qquad \text{and} \qquad v^\circ(x_0 - \xi) = v^\circ(x_0 + \xi), \tag{2.95}$$

where $\xi > 0$. If we solve the Cauchy problem for a linear constitutive law (2.37), then $\varepsilon(x_0, t) = 0$, and $v(x_0, t)$ is not modified. Therefore, it is natural to set

$$\begin{aligned} \varepsilon_{-i}^n &= -\varepsilon_i^n \\ v_{-i}^n &= v_i^n \end{aligned} \qquad \text{and} \qquad \begin{aligned} \varepsilon_{N_x+i}^n &= -\varepsilon_{N_x-i}^n \\ v_{N_x+i}^n &= v_{N_x-i}^n \end{aligned} \qquad \text{for } i = 1, \ldots, S, \tag{2.96}$$

so as to model a free edge at the abscissas x_0 and x_{N_x} respectively (Section 7.3.3 in [69]).

■ *Clamped edges.* A clamped edge is a boundary of the physical domain on which the displacement is zero, and so the particle velocity. If the boundary $x = x_0$ is a clamped edge, then v_0^n must be equal to zero for all n. Similarly to the previous case of the free edge, it is natural to set

$$\begin{aligned} \varepsilon_{-i}^n &= \varepsilon_i^n \\ v_{-i}^n &= -v_i^n \end{aligned} \qquad \text{and} \qquad \begin{aligned} \varepsilon_{N_x+i}^n &= \varepsilon_{N_x-i}^n \\ v_{N_x+i}^n &= -v_{N_x-i}^n \end{aligned} \qquad \text{for } i = 1, \ldots, S, \tag{2.97}$$

so as to model a clamped edge at the abscissas x_0 and x_{N_x} respectively. This boundary condition can be modified to represent an oscillating edge [69].

CHAPTER 3

The Riemann problem of longitudinal elastodynamics

ANALYTICAL SOLUTIONS are known in the case of linear elastodynamics, where the stress is proportional to the strain. Indeed, the method of characteristics provides the solution to many initial-value problems. Moreover, Green's function makes it possible to solve the non-homogeneous system (2.23) analytically for various types of source terms $\boldsymbol{s}$.

In the nonlinear case, no general analytical solution is known. The present chapter is dedicated to the analytical solution of a particular initial-value problem: the Riemann problem (i.e., piecewise constant initial data). We restrict ourselves to the system of conservation laws (2.23) without any external volume force ($\boldsymbol{f}^v = \boldsymbol{0}$):

$$\partial_t \boldsymbol{q} + \partial_x \boldsymbol{f}(\boldsymbol{q}) = \boldsymbol{0} \tag{3.1}$$

with $\boldsymbol{q} = (\varepsilon, v)^\top$ and $\boldsymbol{f}(\boldsymbol{q}) = -(v, \sigma(\varepsilon)/\rho_0)^\top$. The Riemann problem for this system is defined by the initial condition

$$\boldsymbol{q}(x,0) = \begin{cases} \boldsymbol{q}_L & \text{if } x < 0, \\ \boldsymbol{q}_R & \text{elsewhere}, \end{cases} \tag{3.2}$$

with $\boldsymbol{q}_L = (\varepsilon_L, v_L)^\top$ and $\boldsymbol{q}_R = (\varepsilon_R, v_R)^\top$. Solving (2.23)-(3.2) with $\boldsymbol{s} = \boldsymbol{0}$ is the goal of the present chapter. In this study, we restrict ourselves to at most one inflection point ε_0 in the domain of hyperbolicity $]\varepsilon_{\text{inf}}, \varepsilon_{\text{sup}}[$, such that $\sigma''(\varepsilon_0) = 0$. The study has been published in [2].

Figure 3.1. (a) Structure of the solution to the Riemann problem. (b) Structure of an elementary solution in one characteristic field. If $k = 1$, then $(\boldsymbol{q}_\ell, \boldsymbol{q}_r) = (\boldsymbol{q}_L, \boldsymbol{q}_M)$. If $k = 2$, then $(\boldsymbol{q}_\ell, \boldsymbol{q}_r) = (\boldsymbol{q}_M, \boldsymbol{q}_R)$.

The solution to the Riemann problem involves two waves associated to each characteristic field (Figure 3.1a). In the linearly degenerate case where the stress is proportional to the strain, these elementary waves are contact discontinuities propagating at speed $\mp c_0$. In the genuinely nonlinear case (2.29) where σ is either strictly convex or strictly concave, each wave can be either a shock or a rarefaction wave [40, 129]. Thus, the resolution is similar to the case of the p-system of gas dynamics. As illustrated in the previous chapter, this is no longer true if the stress-strain relationship has an inflection point. Indeed, the elementary waves can combine continuous and discontinuous parts (compound waves). The underlying mathematical theory is well established [30, 65, 72, 146]. It has been applied to the previous system in [125], but for a constitutive law which is not relevant here (negative Young's modulus).

All these elementary solutions — discontinuities, rarefactions and compound waves — are examined separately in the next section. For this purpose, we study k-waves ($k = 1$ or $k = 2$) which connect a left state $\boldsymbol{q}_\ell$ and a right state $\boldsymbol{q}_r$ (see Figure 3.1b). The next section concerns the resolution of the Riemann problem (3.2), which involves two elementary waves. In particular, we state a condition which ensures the existence of the solution. Also, we show how to predict the nature of the physically admissible solution. Along the chapter, the polynomial constitutive law $\sigma = M_0\,\varepsilon\left(1 - \beta\varepsilon - \delta\varepsilon^2\right)$ (2.22) with the parameters given in Table 2.1 serves as an example, for which analytical expressions are detailed. A dedicated software tool can be found at `https://gchiavassa.perso.centrale-marseille.fr/RiemannElasto/`. In the publication [2], other constitutive laws are also considered.

1. Elementary solutions

1.1. Wave types

1.1.a. *Discontinuities*

We are looking for piecewise constant solutions to the Riemann problem (2.23)-(3.2) in one characteristic field ($k = 1$ or $k = 2$). They satisfy the Rankine–Hugoniot jump condition [40]

$$\boldsymbol{f}(\boldsymbol{q}_r) - \boldsymbol{f}(\boldsymbol{q}_\ell) = s_k\,(\boldsymbol{q}_r - \boldsymbol{q}_\ell), \tag{3.3}$$

from which one deduces $v_r = v_\ell - s_k\,(\varepsilon_r - \varepsilon_\ell)$, with the shock speeds

$$s_1 = -\sqrt{\frac{\sigma(\varepsilon_r) - \sigma(\varepsilon_\ell)}{\rho_0\,(\varepsilon_r - \varepsilon_\ell)}}\,, \qquad s_2 = \sqrt{\frac{\sigma(\varepsilon_r) - \sigma(\varepsilon_\ell)}{\rho_0\,(\varepsilon_r - \varepsilon_\ell)}}\,. \tag{3.4}$$

Hence, in the ε-σ plane, the quantity $\rho_0 {s_k}^2$ is the slope of the line connecting $(\varepsilon_\ell, \sigma(\varepsilon_\ell))$ and $(\varepsilon_r, \sigma(\varepsilon_r))$. A discontinuity wave is the piecewise constant function defined by

$$\boldsymbol{q}(x,t) = \begin{cases} \boldsymbol{q}_\ell & \text{if } x < s_k t\,, \\ \boldsymbol{q}_r & \text{if } x > s_k t\,. \end{cases} \tag{3.5}$$

It is a weak solution of the Riemann problem (2.23)-(3.2) [40].

Weak solutions of the Riemann problem are not unique. Therefore, the discontinuity (3.5) is not necessarily the physical (entropic) solution. To be admissible, a k-discontinuity must satisfy the *Liu entropy condition* (Eq. (E) in [72]). In the present case, the Liu entropy condition reads

$$s_1 \geqslant -\sqrt{\frac{\sigma(\varepsilon) - \sigma(\varepsilon_\ell)}{\rho_0\,(\varepsilon - \varepsilon_\ell)}} \ \text{ if } k = 1, \quad s_2 \leqslant \sqrt{\frac{\sigma(\varepsilon) - \sigma(\varepsilon_\ell)}{\rho_0\,(\varepsilon - \varepsilon_\ell)}} \ \text{ if } k = 2, \tag{3.6}$$

for all ε between ε_ℓ and ε_r. In (3.6), s_1 and s_2 are given by (3.4). A geometrical interpretation of (3.6) can be stated as follows (Section 8.4 in [30]):

- if $s_k\,(\varepsilon_r - \varepsilon_\ell) < 0$, the k-discontinuity that joins $\boldsymbol{q}_\ell$ and $\boldsymbol{q}_r$ is admissible if the graph of σ between ε_ℓ and ε_r lies below the chord that connects $(\varepsilon_\ell, \sigma(\varepsilon_\ell))$ to $(\varepsilon_r, \sigma(\varepsilon_r))$;
- if $s_k\,(\varepsilon_r - \varepsilon_\ell) > 0$, the k-discontinuity that joins $\boldsymbol{q}_\ell$ and $\boldsymbol{q}_r$ is admissible if the graph of σ between ε_ℓ and ε_r lies above the chord that connects $(\varepsilon_\ell, \sigma(\varepsilon_\ell))$ to $(\varepsilon_r, \sigma(\varepsilon_r))$.

Remark 3.1. Liu's entropy condition [72] generalizes the classical Lax entropy condition $\lambda_k(\boldsymbol{q}_\ell) > s_k > \lambda_k(\boldsymbol{q}_r)$ to nongenuinely nonlinear systems of conservation laws. Liu's condition is stricter than the Lax entropy condition in the general case, but both are equivalent in the genuinely nonlinear case (2.29). Indeed, if σ is concave, the graph of σ always lies above the chord. Thus, Liu's entropy condition reduces to the condition $s_k\,(\varepsilon_R - \varepsilon_L) > 0$, which is also a consequence of the Lax entropy condition.

Remark 3.2. Liu's entropy condition [72] generalizes the Oleinik entropy condition to 2×2 hyperbolic systems of conservation laws. In the case of a scalar conservation law with a flux function $f(q)$, Oleinik's entropy condition writes:

$$\frac{f(q) - f(q_L)}{q - q_L} \leqslant \frac{f(q_R) - f(q_L)}{q_R - q_L} \leqslant \frac{f(q_R) - f(q)}{q_R - q} \tag{3.7}$$

for all q between q_L and q_R (see Eq. (8.4.3) in [30]). In practice, the Riemann problem of scalar conservation laws can be solved graphically by using a geometrical interpretation of the Oleinik condition (3.7).

Let us apply the previous graphical method. To do so, we introduce the function F defined for $a \neq b$ by

$$F : (a, b) \mapsto \sigma'(a) - \frac{\sigma(a) - \sigma(b)}{a - b}\,. \tag{3.8}$$

Also, we denote by $a^\dagger$ and b^* the points such that

$$F(a, a^\dagger) = 0 \qquad \text{and} \qquad F(b^*, b) = 0\,. \tag{3.9}$$

By construction, one has $(a^\dagger)^* = (a^*)^\dagger = a$. The geometrical interpretation of Liu's entropy condition (3.6) is illustrated on Figure 3.2, where σ is convex for $\varepsilon < \varepsilon_0$ and concave for $\varepsilon > \varepsilon_0$. On this figure, ε_ℓ belongs to the concave part.

- When $k = 1$, then $s_k < 0$ (3.4). If $\varepsilon_r > \varepsilon_\ell$, the graph must lie below the chord, which is not possible due to the concavity. If $\varepsilon_r < \varepsilon_\ell$, the graph must lie above the chord, which is only possible if $\varepsilon_r \geqslant \varepsilon_\ell^*$ (3.9), such that the chord is tangent to the curve at $\varepsilon_r = \varepsilon_\ell^*$.
- When $k = 2$, then $s_k > 0$ (3.4). If $\varepsilon_r > \varepsilon_\ell$, the graph must lie above the chord, which is satisfied due to the concavity. If $\varepsilon_r < \varepsilon_\ell$, the graph must lie below the chord, which is only possible if $\varepsilon_r \leqslant \varepsilon_\ell{}^\dagger$ (3.9), such that the chord is tangent to the curve at ε_ℓ.

When ε_ℓ belongs to the convex part, one can carry out a similar analysis to describe the admissibility of k-discontinuities. The result is the same, but inequalities are of opposite sense. Finally, after multiplication by $(\varepsilon_\ell - \varepsilon_0)$, one obtains the inequalities ensuring that a k-discontinuity is admissible:

$$\begin{aligned}
&\text{if } k = 1, \quad (\varepsilon_\ell - \varepsilon_0)\,\varepsilon_\ell^* \leqslant (\varepsilon_\ell - \varepsilon_0)\,\varepsilon_r < (\varepsilon_\ell - \varepsilon_0)\,\varepsilon_\ell\,,\\
&\text{if } k = 2,\\
&\qquad (\varepsilon_\ell - \varepsilon_0)\,\varepsilon_\ell < (\varepsilon_\ell - \varepsilon_0)\,\varepsilon_r \quad \text{or} \quad (\varepsilon_\ell - \varepsilon_0)\,\varepsilon_r \leqslant (\varepsilon_\ell - \varepsilon_0)\,\varepsilon_\ell{}^\dagger.
\end{aligned} \tag{3.10}$$

For more than one inflection point, contact discontinuities satisfying $\lambda_k(\boldsymbol{q}_\ell) = s_k = \lambda_k(\boldsymbol{q}_r)$ may be admissible in the sense of Liu (3.6). Here, only one inflection point is considered, so that no contact discontinuity is admissible.

Now, we put $\boldsymbol{q}_\ell$ in the ε-v plane, and we construct the locus of right states $\boldsymbol{q}$ which can be connected to $\boldsymbol{q}_\ell$ through a k-discontinuity. The jump between $\boldsymbol{q}_\ell$ and $\boldsymbol{q}$ must satisfy the Rankine–Hugoniot condition (3.3). Thus, we obtain the curves $\mathcal{S}_k(\boldsymbol{q}_\ell)$ called k-Hugoniot loci and denote these by $\mathcal{S}_k^\ell$ for the sake of simplicity:

$$\begin{aligned}
v &= v_\ell + \operatorname{sgn}(\varepsilon - \varepsilon_\ell)\sqrt{(\sigma(\varepsilon) - \sigma(\varepsilon_\ell))(\varepsilon - \varepsilon_\ell)/\rho_0} \equiv \mathcal{S}_1^\ell(\varepsilon)\,,\\
v &= v_\ell - \operatorname{sgn}(\varepsilon - \varepsilon_\ell)\sqrt{(\sigma(\varepsilon) - \sigma(\varepsilon_\ell))(\varepsilon - \varepsilon_\ell)/\rho_0} \equiv \mathcal{S}_2^\ell(\varepsilon)\,.
\end{aligned} \tag{3.11}$$

A few properties of these curves are detailed in the Appendix (Section 4.1.a).

■ *Example (polynomial).* If $\delta = 0$ in (2.22), σ is concave. Therefore, a k-shock is admissible if $s_k\,(\varepsilon_r - \varepsilon_\ell) > 0$. Otherwise ($\delta \neq 0$), σ is neither convex nor concave. The stress σ is convex if $\varepsilon < \varepsilon_0$ and concave if $\varepsilon > \varepsilon_0$, with $\varepsilon_0 = -\beta/(3\delta)$. Therefore, Liu's entropy condition reduces to (3.10). An illustration is given on Figure 3.2 for a similar constitutive law, where $\varepsilon_\ell = 10^{-3} > \varepsilon_0$.

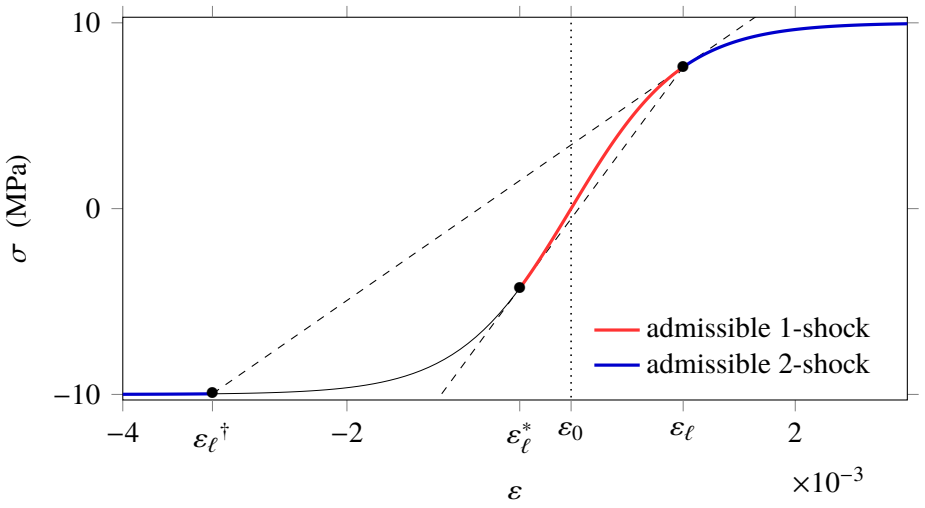

Figure 3.2. Admissibility of shocks in the sense of Liu (3.6). The admissibility regions mark the values of ε_r such that a k-shock connecting $(\varepsilon_\ell, \sigma(\varepsilon_\ell))$ to $(\varepsilon_r, \sigma(\varepsilon_r))$ is admissible, where $\varepsilon_\ell = 10^{-3}$. Here, a hyperbolic function $\sigma = M_0 \times 10^{-3} \tanh(\varepsilon/10^{-3})$ with the inflection point located at $\varepsilon_0 = 0$ is used instead of the cubic polynomial (2.22) for graphical reasons.

1.1.b. *Rarefaction waves*

We are looking for piecewise smooth continuous solutions of the Riemann problem (2.23)-(3.2) which connect $\boldsymbol{q}_\ell$ and $\boldsymbol{q}_r$. Since the system of conservation laws is invariant under uniform stretching of space and time coordinates $(x, t) \mapsto (\alpha x, \alpha t)$, we restrict ourselves to self-similar solutions of the form $\boldsymbol{q}(x, t) = \tilde{\boldsymbol{q}}(\xi)$, where $\xi = x/t$. Injecting this Ansatz in (2.23) gives two equations satisfied by $\tilde{\boldsymbol{q}}'(\xi)$. The trivial solution $\tilde{\boldsymbol{q}}'(\xi) = \boldsymbol{0}$ is eliminated. Differentiating the other equation implies that there exists $k \in \{1, 2\}$, such that (Section I.3.1 in [40])

$$\begin{cases} \lambda_k(\tilde{\boldsymbol{q}}(\xi)) = \xi\,, \\ \qquad \tilde{\boldsymbol{q}}'(\xi) = \dfrac{1}{\boldsymbol{\nabla}\lambda_k(\tilde{\boldsymbol{q}}(\xi)) \cdot \boldsymbol{r}_k(\tilde{\boldsymbol{q}}(\xi))}\, \boldsymbol{r}_k(\tilde{\boldsymbol{q}}(\xi))\ . \end{cases} \tag{3.12}$$

To connect left and right states, we impose that $\tilde{\boldsymbol{q}}(\lambda_k(\boldsymbol{q}_\ell)) = \boldsymbol{q}_\ell$ and $\tilde{\boldsymbol{q}}(\lambda_k(\boldsymbol{q}_r)) = \boldsymbol{q}_r$. The function

$$\boldsymbol{q}(x,t) = \begin{cases} \boldsymbol{q}_\ell & \text{if } x \leqslant \lambda_k(\boldsymbol{q}_\ell)\, t\,, \\ \tilde{\boldsymbol{q}}(x/t) & \text{if } \lambda_k(\boldsymbol{q}_\ell)\, t \leqslant x \leqslant \lambda_k(\boldsymbol{q}_r)\, t\,, \\ \boldsymbol{q}_r & \text{if } \lambda_k(\boldsymbol{q}_r)\, t \leqslant x\,, \end{cases} \tag{3.13}$$

is a self-similar weak solution of (2.23)-(3.2) connecting $\boldsymbol{q}_\ell$ and $\boldsymbol{q}_r$ [40]. Such a solution is called simple wave or rarefaction wave.

Let us achieve the computation of $\tilde{\boldsymbol{q}}(\xi)$ by defining a primitive $C : \varepsilon \mapsto \int^\varepsilon c(\epsilon)\, \mathrm{d}\epsilon$ of the sound speed c over $]\varepsilon_{\inf}, \varepsilon_{\sup}[$. The k-Riemann invariants w_k defined by

$$w_1(\boldsymbol{q}) = v - C(\varepsilon), \qquad w_2(\boldsymbol{q}) = v + C(\varepsilon), \tag{3.14}$$

are constant on k-rarefaction waves [40]. In practice, this property is used to

rewrite (3.12) as

$$\begin{cases} \lambda_k(\tilde{\boldsymbol{q}}(\xi)) = \xi\,, \\ w_k(\tilde{\boldsymbol{q}}(\xi)) = w_k(\boldsymbol{q}_\ell)\,. \end{cases} \tag{3.15}$$

Finally, using the expressions of the eigenvalues (2.25) and the Riemann invariants (3.14), one obtains

$$\begin{aligned} \tilde{\boldsymbol{q}}(\xi) &= \begin{pmatrix} c^{-1}(-\xi) \\ w_1(\boldsymbol{q}_\ell) + C \circ c^{-1}(-\xi) \end{pmatrix} \quad \text{if } k = 1, \\ \tilde{\boldsymbol{q}}(\xi) &= \begin{pmatrix} c^{-1}(\xi) \\ w_2(\boldsymbol{q}_\ell) - C \circ c^{-1}(\xi) \end{pmatrix} \quad \text{if } k = 2. \end{aligned} \tag{3.16}$$

In (3.15)-(3.16), $\boldsymbol{q}_\ell$ can be replaced by $\boldsymbol{q}_r$, or by any other state on the rarefaction wave.

Let us examine the admissibility of the rarefaction wave (3.16). Firstly, the eigenvalue $\lambda_k(\tilde{\boldsymbol{q}}(\xi))$ must be increasing from $\xi = \lambda_k(\boldsymbol{q}_\ell)$ to $\xi = \lambda_k(\boldsymbol{q}_r)$. In particular, we must have

$$\lambda_k(\boldsymbol{q}_\ell) \leqslant \lambda_k(\boldsymbol{q}_r)\,. \tag{3.17}$$

Secondly, Eq. (3.12) requires that $\boldsymbol{\nabla}\lambda_k \cdot \boldsymbol{r}_k$ does not vanish along the curve $\xi \mapsto \tilde{\boldsymbol{q}}(\xi)$. This is never satisfied when the characteristic fields are linearly degenerate, but it is always satisfied when the characteristic fields are genuinely nonlinear. In the nonconvex case, it implies that a rarefaction cannot cross the inflection point ε_0, i.e. the condition

$$(\varepsilon_\ell - \varepsilon_0)(\varepsilon_r - \varepsilon_0) \geqslant 0 \tag{3.18}$$

must be satisfied by the left state and the right state.

Now, we put $\boldsymbol{q}_\ell$ in the ε-v plane, and we construct the locus of right states $\boldsymbol{q}$ which can be connected to $\boldsymbol{q}_\ell$ through a k-rarefaction. The states $\boldsymbol{q}_\ell$ and $\boldsymbol{q}$ must satisfy $w_k(\boldsymbol{q}) = w_k(\boldsymbol{q}_\ell)$. Thus, we obtain the rarefaction curves $\mathcal{R}_k(\boldsymbol{q}_\ell)$ denoted by $\mathcal{R}_k^\ell$ for the sake of simplicity:

$$\begin{aligned} v &= v_\ell - C(\varepsilon_\ell) + C(\varepsilon) \equiv \mathcal{R}_1^\ell(\varepsilon), \\ v &= v_\ell + C(\varepsilon_\ell) - C(\varepsilon) \equiv \mathcal{R}_2^\ell(\varepsilon)\,. \end{aligned} \tag{3.19}$$

A few properties of these curves are detailed in the Appendix (Section 4.1.a).

■ *Example (polynomial).* To compute rarefaction waves, one needs the expressions of C and c^{-1} in (3.16). In the case of the quadratic nonlinearity ($\delta = 0$), a primitive of the sound speed (2.34) is

$$C(\varepsilon) = -c_0\,\frac{(1 - 2\beta\varepsilon)^{3/2}}{3\beta}\,, \tag{3.20}$$

and the inverse function of c is

$$c^{-1}(\xi) = \frac{1 - (\xi/c_0)^2}{2\beta}\,. \tag{3.21}$$

In the case of the cubic nonlinearity ($\delta \neq 0$), a primitive of the sound speed (2.34) is

$$C(\varepsilon) = c(\varepsilon)\,\frac{\beta + 3\delta\varepsilon}{6\delta} + c_0\,\frac{\beta^2 + 3\delta}{6\delta\sqrt{3\delta}}\,\arcsin\!\left(\frac{\beta + 3\delta\varepsilon}{\sqrt{\beta^2 + 3\delta}}\right). \tag{3.22}$$

Since c is not monotonous (Figure 2.2d), its inverse is not unique. The inverse over the range $[0, c(\varepsilon_0)]$ is made of two branches:

$$c^{-1}(\xi) \in \left\{ -\frac{\beta}{3\delta} - \sqrt{\frac{\beta^2}{9\delta^2} + \frac{1-(\xi/c_0)^2}{3\delta}}\,,\; -\frac{\beta}{3\delta} + \sqrt{\frac{\beta^2}{9\delta^2} + \frac{1-(\xi/c_0)^2}{3\delta}} \right\}. \tag{3.23}$$

The choice of the inverse (3.23) in (3.16) depends on ε_ℓ. Indeed, $\tilde{\boldsymbol{q}}(\xi)$ must satisfy $\tilde{\boldsymbol{q}}(\lambda_k(\boldsymbol{q}_\ell)) = \boldsymbol{q}_\ell$ and $\tilde{\boldsymbol{q}}(\lambda_k(\boldsymbol{q}_r)) = \boldsymbol{q}_r$, i.e. $\varepsilon_\ell = c^{-1} \circ c(\varepsilon_\ell)$ and $\varepsilon_r = c^{-1} \circ c(\varepsilon_r)$. Since ε_ℓ and ε_r are on the same side of the inflection point (3.18), the choice of the inverse in (3.23) relies only on ε_ℓ. If $\varepsilon_\ell < \varepsilon_0$, the inverse (3.23) must be smaller than $\varepsilon_0 = -\beta/(3\delta)$ (first expression). Else, it must be larger (second expression).

1.1.c. *Compound waves*

In this section, σ has an inflection point at ε_0, i.e. $\sigma''(\varepsilon_0) = 0$. The characteristic fields are thus not genuinely nonlinear over $]\varepsilon_{\text{inf}}, \varepsilon_{\text{sup}}[$. On the one hand, a k-discontinuity which crosses the line $\varepsilon = \varepsilon_0$ is not always admissible (3.10). On the other hand, a k-rarefaction cannot cross the line $\varepsilon = \varepsilon_0$ (3.18). When discontinuities and rarefactions are not admissible, one can start from $\boldsymbol{q}_\ell$ with an admissible k-discontinuity and connect it to $\boldsymbol{q}_r$ with an admissible k-rarefaction (shock-rarefaction). Alternatively, one can start from $\boldsymbol{q}_\ell$ with an admissible k-rarefaction and connect it to $\boldsymbol{q}_r$ with an admissible k-discontinuity (rarefaction-shock). These compound waves composed of one rarefaction and one discontinuity are now examined separately.

■ *Shock-rarefactions.* We consider a k-shock-rarefaction that connects $\boldsymbol{q}_\ell$ and $\boldsymbol{q}_r$. The rarefaction cannot cross the line $\varepsilon = \varepsilon_0$. It breaks when reaching ε_ℓ^* [146] such that $F(\varepsilon_\ell^*, \varepsilon_\ell) = 0$ (3.9). Therefore, a shock-rarefaction is defined by

$$\boldsymbol{q}(x,t) = \begin{cases} \boldsymbol{q}_\ell & \text{if } x < \lambda_k(\varepsilon_\ell^*)\,t\,, \\ \tilde{\boldsymbol{q}}(x/t) & \text{if } \lambda_k(\varepsilon_\ell^*)\,t < x \leqslant \lambda_k(\varepsilon_r)\,t\,, \\ \boldsymbol{q}_r & \text{if } \lambda_k(\varepsilon_r)\,t \leqslant x\,. \end{cases} \tag{3.24}$$

The rarefaction part $\tilde{\boldsymbol{q}}(\xi)$ is given by (3.16) where $\boldsymbol{q}_\ell$ has to be replaced by $\boldsymbol{q}_r$. An illustration is given on Figure 3.3a, where the parameters are the same as in Figure 3.9. If the shock-rarefaction (3.24) is a weak solution of (2.23)-(3.2), then both parts are weak solutions. On the one hand, the discontinuous part must satisfy the Rankine–Hugoniot condition (3.3) with left state $\boldsymbol{q}_\ell$ and right state $\boldsymbol{q}_\ell^* = (\varepsilon_\ell^*, v_\ell^*)^\top$:

$$v_\ell^* = v_\ell - s_k\,(\varepsilon_\ell^* - \varepsilon_\ell)\,. \tag{3.25}$$

Due to the relation (3.9) between ε_ℓ and ε_ℓ^*, the shock speed s_k (3.4) satisfies

$$\begin{aligned} s_1 &= -\sqrt{\frac{\sigma(\varepsilon_\ell^*)-\sigma(\varepsilon_\ell)}{\rho_0\,(\varepsilon_\ell^*-\varepsilon_\ell)}}, \\ &= -c(\varepsilon_\ell^*), \end{aligned} \qquad \text{and} \qquad \begin{aligned} s_2 &= \sqrt{\frac{\sigma(\varepsilon_\ell^*)-\sigma(\varepsilon_\ell)}{\rho_0\,(\varepsilon_\ell^*-\varepsilon_\ell)}}, \\ &= c(\varepsilon_\ell^*)\,. \end{aligned} \tag{3.26}$$

On the other hand, the Riemann invariants (3.14) must be constant on the continuous part:

$$w_k(\boldsymbol{q}_\ell^*) = w_k(\boldsymbol{q}_r)\,. \tag{3.27}$$

Finally, equations (3.25) and (3.27) yield

$$v_r = v_\ell - (-1)^k \left(C(\varepsilon_r) - C(\varepsilon_\ell^*) + c(\varepsilon_\ell^*)(\varepsilon_\ell^* - \varepsilon_\ell)\right). \tag{3.28}$$

Admissibility of shock-rarefactions is presented in Section 1.2.

Now, we put $\boldsymbol{q}_\ell$ in the ε-v plane, and we construct the locus of right states $\boldsymbol{q}$ which can be connected to $\boldsymbol{q}_\ell$ through a k-shock-rarefaction. The states $\boldsymbol{q}_\ell$ and $\boldsymbol{q}$ must satisfy (3.28). Thus, we obtain the shock-rarefaction curves $\mathcal{SR}_k(\boldsymbol{q}_\ell)$ and denote these by $\mathcal{SR}_k^\ell$ for the sake of simplicity:

$$\begin{aligned} v &= v_\ell + c(\varepsilon_\ell^*)(\varepsilon_\ell^* - \varepsilon_\ell) - C(\varepsilon_\ell^*) + C(\varepsilon) \equiv \mathcal{SR}_1^\ell(\varepsilon), \\ v &= v_\ell - c(\varepsilon_\ell^*)(\varepsilon_\ell^* - \varepsilon_\ell) + C(\varepsilon_\ell^*) - C(\varepsilon) \equiv \mathcal{SR}_2^\ell(\varepsilon)\,. \end{aligned} \tag{3.29}$$

A few properties of these curves are detailed in the Appendix (Section 4.1.a).

■ *Rarefaction-shocks.* We consider a k-rarefaction-shock that connects $\boldsymbol{q}_\ell$ and $\boldsymbol{q}_r$. The rupture of the rarefaction wave occurs when reaching ε_r^* [146] such that $F(\varepsilon_r^*, \varepsilon_r) = 0$ (3.9). Therefore, a rarefaction-shock is defined by

$$\boldsymbol{q}(x,t) = \begin{cases} \boldsymbol{q}_\ell & \text{if } x \leqslant \lambda_k(\varepsilon_\ell)\,t\,, \\ \tilde{\boldsymbol{q}}(x/t) & \text{if } \lambda_k(\varepsilon_\ell)\,t \leqslant x < \lambda_k(\varepsilon_r^*)\,t\,, \\ \boldsymbol{q}_r & \text{if } \lambda_k(\varepsilon_r^*)\,t < x\,, \end{cases} \tag{3.30}$$

where $\tilde{\boldsymbol{q}}(\xi)$ is given by (3.16). An illustration is given on Figure 3.3b, where the parameters are the same as in Figure 3.9. With similar arguments than for (3.25) and (3.27), one obtains

$$v_r = v_\ell + (-1)^k \left(C(\varepsilon_\ell) - C(\varepsilon_r^*) + c(\varepsilon_r^*)(\varepsilon_r^* - \varepsilon_r)\right). \tag{3.31}$$

Admissibility of rarefaction-shocks is presented in Section 1.2, where the computation of ε^* is also examined.

Now, we put $\boldsymbol{q}_\ell$ in the ε-v plane, and we construct the locus of right states $\boldsymbol{q}$ which can be connected to $\boldsymbol{q}_\ell$ through a k-rarefaction-shock. The states $\boldsymbol{q}_\ell$ and $\boldsymbol{q}$ must satisfy (3.31). Thus, we obtain the rarefaction-shock curves $\mathcal{RS}_k(\boldsymbol{q}_\ell)$ and denote these by $\mathcal{RS}_k^\ell$ for the sake of simplicity:

$$\begin{aligned} v &= v_\ell - C(\varepsilon_\ell) + C(\varepsilon^*) - c(\varepsilon^*)(\varepsilon^* - \varepsilon) \equiv \mathcal{RS}_1^\ell(\varepsilon), \\ v &= v_\ell + C(\varepsilon_\ell) - C(\varepsilon^*) + c(\varepsilon^*)(\varepsilon^* - \varepsilon) \equiv \mathcal{RS}_2^\ell(\varepsilon)\,. \end{aligned} \tag{3.32}$$

Again, a few properties of these curves are detailed in the Appendix (Section 4.1.a).

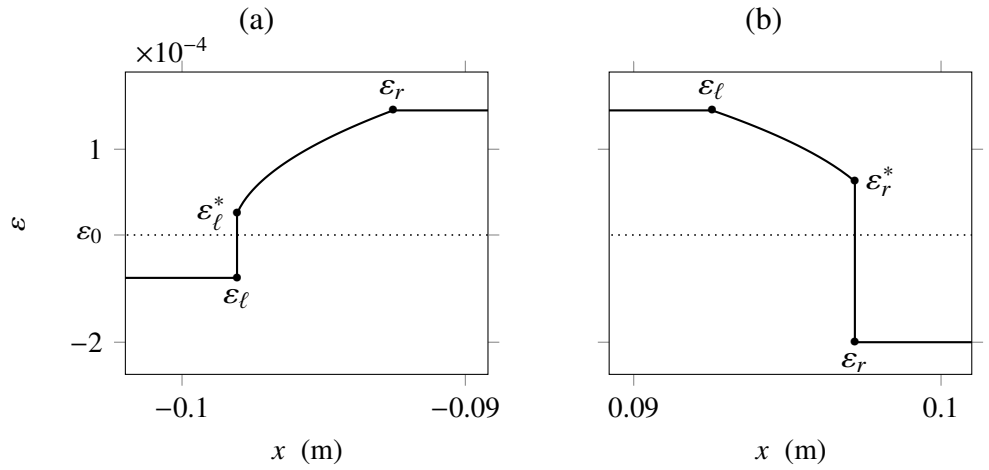

Figure 3.3. Compound waves obtained with the cubic polynomial law (2.22). Snapshot of ε in the case of (a) a 1-shock-rarefaction and (b) a 2-rarefaction-shock.

1.2. Graphical method

In practice, a graphical method can be applied to construct entropic elementary solutions to (2.23)-(3.2) based on discontinuities, rarefactions and compound waves. This method is very useful for nonconvex constitutive laws and can be stated as follows (Section 9.5 in [30]):

For 1-waves,

- if $\varepsilon_r < \varepsilon_\ell$, we construct the convex hull of σ over $[\varepsilon_r, \varepsilon_\ell]$, i.e. the largest convex fonction which is smaller or equal to σ;
- if $\varepsilon_r > \varepsilon_\ell$, we construct the concave hull of σ over $[\varepsilon_\ell, \varepsilon_r]$, i.e. the smallest concave fonction which is larger or equal to σ.

For 2-waves,

- if $\varepsilon_r < \varepsilon_\ell$, we construct the concave hull of σ over $[\varepsilon_r, \varepsilon_\ell]$;
- if $\varepsilon_r > \varepsilon_\ell$, we construct the convex hull of σ over $[\varepsilon_\ell, \varepsilon_r]$.

Between ε_ℓ and ε_r, the intervals where the slope of the hull is constant correspond to admissible discontinuities. The other intervals correspond to admissible rarefactions.

■ *Example (polynomial).* On Figure 3.4, we illustrate the method for the polynomial constitutive law (2.22), where the inflection point is $\varepsilon_0 = -\beta/(3\delta)$ (cf. Chapter 2). The stress σ is convex for $\varepsilon < \varepsilon_0$ and concave for $\varepsilon > \varepsilon_0$. Here, $\varepsilon_r = -4 \times 10^{-4}$ is smaller than $\varepsilon_\ell = 4.5 \times 10^{-4}$. If $k = 1$, we construct the convex hull of σ. If $k = 2$, we construct the concave hull of σ. The method predicts that the solution is made of two compound waves: a 1-shock-rarefaction wave and a 2-rarefaction-shock wave. In agreement with the definitions of such waves in the previous section, the 1-rarefaction breaks when reaching ε_ℓ^* and the 2-rarefaction

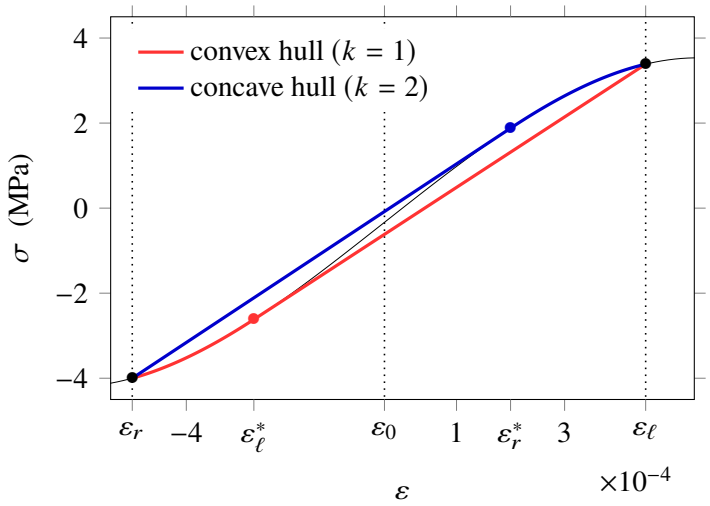

Figure 3.4. Graphical construction of the solution for $\varepsilon_r < \varepsilon_\ell$ and the cubic polynomial law (2.22). Here, we obtain a 1-shock-rarefaction (convex hull) and a 2-rarefaction-shock (concave hull).

Table 3.1. Admissible elementary waves for the cubic polynomial law (2.22) when $\varepsilon_\ell > \varepsilon_0$ and ε_r varies in $\mathbb{R}$ (increasing values of ε_r from the left to the right).

ε_r	ε_{inf}	$\varepsilon_\ell{}^\dagger$	ε_ℓ^*	$\varepsilon_0 = -\frac{\beta}{3\delta}$	ε_ℓ	ε_{sup}
$k = 1$	$\mathcal{SR}_1$	$\mathcal{SR}_1$	$\mathcal{S}_1$	$\mathcal{S}_1$	$\mathcal{R}_1$	
$k = 2$	$\mathcal{S}_2$	$\mathcal{RS}_2$	$\mathcal{RS}_2$	$\mathcal{R}_2$	$\mathcal{S}_2$	

breaks when reaching ε_r^*. Nevertheless, the reasoning on Fig. 3.4 was made for a constant value of $\varepsilon_r < \varepsilon_\ell$ between $\varepsilon_\ell^\dagger$ and ε_ℓ^*. When ε_r varies, the hulls on Fig. 3.4 vary. Depending on ε_r, one obtains different admissible waves. These possibilities are listed in Table 3.1.

If $\delta = 0$ in (2.22), σ is concave, and there are no compound waves. In the case $\delta > 0$, compound waves are possible. The computation of compound wave solutions (3.30)-(3.24) requires to solve (3.9). Here, (3.9) can be solved analytically: $\varepsilon^* = -\frac{1}{2}(\varepsilon + \beta/\delta)$, and inversely, $\varepsilon^\dagger = -2\varepsilon - \beta/\delta$.

2. Solution of the Riemann problem

2.1. General strategy

If (2.23) is a strictly hyperbolic system, the solution to the Riemann problem (2.23)-(3.2) has three constant states $\boldsymbol{q}_L, \boldsymbol{q}_M$ and $\boldsymbol{q}_R$ (see Figure 3.1a). Solving the Riemann problem amounts to find the admissible k-waves, and to compute the intermediate state $\boldsymbol{q}_M$. Here, every possible wave structure combining a 1-wave and a 2-wave must be examined. Since σ has only one inflection point at ε_0, compound waves can only be composed of one rarefaction and one discontinuity.

In order to find the intermediate state $\boldsymbol{q}_M$, we construct the forward wave curve Φ_p^L of right states $\boldsymbol{q}$ which can be connected to $\boldsymbol{q}_L$ through an admissible

k-wave (Sections 9.4-9.5 in [30]). It satisfies:

$$\Phi_k^L(\varepsilon) = \begin{cases} \mathcal{S}_k^L(\varepsilon) & \text{if admissible } k\text{-shock,} \\ \mathcal{R}_k^L(\varepsilon) & \text{if admissible } k\text{-rarefaction,} \\ \mathcal{RS}_k^L(\varepsilon) & \text{if admissible } k\text{-rarefaction-shock,} \\ \mathcal{SR}_k^L(\varepsilon) & \text{if admissible } k\text{-shock-rarefaction.} \end{cases} \tag{3.33}$$

According to equations (3.11), (3.19), (3.32) and (3.29), this curve is only translated vertically when v_L changes. Similarly, we construct the backward wave curve Ψ_k^R of left states $\boldsymbol{q}$ which can be connected to $\boldsymbol{q}_R$ through an admissible k-wave:

$$\Psi_k^R(\varepsilon) = \begin{cases} \mathcal{S}_k^R(\varepsilon) & \text{if admissible } k\text{-shock,} \\ \mathcal{R}_k^R(\varepsilon) & \text{if admissible } k\text{-rarefaction,} \\ \mathcal{SR}_k^R(\varepsilon) & \text{if admissible } k\text{-rarefaction-shock,} \\ \mathcal{RS}_k^R(\varepsilon) & \text{if admissible } k\text{-shock-rarefaction.} \end{cases} \tag{3.34}$$

Backward wave curves (3.34) are obtained by replacing the elementary forward wave curves in (3.33) by elementary backward wave curves. It amounts to replace rarefaction-shock curves by shock-rarefaction curves, and vice versa. Here too, the curve Ψ_k^R is only translated vertically when v_R changes. Also, one can remark that $v_R = \Phi_k^L(\varepsilon_R)$ is equivalent to $v_L = \Psi_k^R(\varepsilon_L)$.

The intermediate state $\boldsymbol{q}_M$ is connected to $\boldsymbol{q}_L$ through an admissible 1-wave and to $\boldsymbol{q}_R$ through an admissible 2-wave. Thus, it satisfies

$$v_M = \Phi_1^L(\varepsilon_M) = \Psi_2^R(\varepsilon_M), \tag{3.35}$$

or equivalently

$$\begin{cases} v_M = \Phi_1^L(\varepsilon_M), \\ v_R = \Phi_2^M(\varepsilon_R). \end{cases} \tag{3.36}$$

The existence of the solution to (3.35) is discussed in the next subsections. If the solution exists, one can find the intermediate state $\boldsymbol{q}_M$ numerically. To do so, the strain ε_M is computed by solving (3.35) with the Newton–Raphson method, and the velocity v_M is given by $v_M = \Phi_1^L(\varepsilon_M)$. The form of the solution $\boldsymbol{q}(x,t)$ is then deduced from the corresponding elementary solutions (3.5), (3.13), (3.24) or (3.30).

2.2. Concave constitutive laws

Let us assume that σ'' is strictly negative over $]\varepsilon_{\inf}, \varepsilon_{\sup}[$. Therefore, the characteristic fields are genuinely nonlinear and σ is strictly concave. In this case, compound waves are not admissible. Also, discontinuities and rarefactions have to satisfy the admissibility conditions (3.6) and (3.17) respectively. Thus, forward

and backward wave curves become

$$\Phi_1^L(\varepsilon) = \begin{cases} \mathcal{S}_1^L(\varepsilon) & \text{if } \varepsilon < \varepsilon_L\,, \\ \mathcal{R}_1^L(\varepsilon) & \text{if } \varepsilon \geqslant \varepsilon_L\,, \end{cases} \qquad \Phi_2^L(\varepsilon) = \begin{cases} \mathcal{S}_2^L(\varepsilon) & \text{if } \varepsilon > \varepsilon_L\,, \\ \mathcal{R}_2^L(\varepsilon) & \text{if } \varepsilon \leqslant \varepsilon_L\,, \end{cases}$$
$$\Psi_1^R(\varepsilon) = \begin{cases} \mathcal{S}_1^R(\varepsilon) & \text{if } \varepsilon > \varepsilon_R\,, \\ \mathcal{R}_1^R(\varepsilon) & \text{if } \varepsilon \leqslant \varepsilon_R\,, \end{cases} \qquad \Psi_2^R(\varepsilon) = \begin{cases} \mathcal{S}_2^R(\varepsilon) & \text{if } \varepsilon < \varepsilon_R\,, \\ \mathcal{R}_2^R(\varepsilon) & \text{if } \varepsilon \geqslant \varepsilon_R\,. \end{cases} \tag{3.37}$$

Since the characteristic fields are genuinely nonlinear, Φ_1^L and Ψ_2^R are of class C^2 (Section I.6 in [40]). From the properties of each elementary curve studied before, we deduce that Φ_1^L is an increasing bijection over $]\varepsilon_{\inf}, \varepsilon_{\sup}[$ and that Ψ_2^R is a decreasing bijection. Lastly, Theorem 6.1 in [40] states that for $\|\boldsymbol{q}_R - \boldsymbol{q}_L\|$ sufficiently small, the entropic solution of (2.23)-(3.2) is unique. Similarly to Theorem 7.1 in [40], we get a condition on the initial data which ensures the existence of the solution.

Theorem 3.1. *If the characteristic fields are genuinely nonlinear (2.29), then the entropic solution to the Riemann problem (2.23)-(3.2) exists and is unique, provided that*

$$\lim_{\varepsilon \to \varepsilon_{inf}+} \Psi_2^R(\varepsilon) - \Phi_1^L(\varepsilon) > 0 \qquad \textit{and} \qquad \lim_{\varepsilon \to \varepsilon_{sup}-} \Psi_2^R(\varepsilon) - \Phi_1^L(\varepsilon) < 0\,, \tag{3.38}$$

with Φ_1^L and Ψ_2^R given in (3.37).

Proof. To ensure that the solution described above exists, the forward and backward wave curves Φ_1^L and Ψ_2^R must intersect at a strain ε_M satisfying (3.35). The associated functions are continuous bijections over the interval $]\varepsilon_{\inf}, \varepsilon_{\sup}[$. Moreover, Φ_1^L is strictly increasing while Ψ_2^R is strictly decreasing. Therefore, they intersect once over $]\varepsilon_{\inf}, \varepsilon_{\sup}[$ if and only if their ranges intersect. The latter are respectively

$$\left]\lim_{\varepsilon \to \varepsilon_{\inf}+} \Phi_1^L(\varepsilon), \lim_{\varepsilon \to \varepsilon_{sup}-} \Phi_1^L(\varepsilon)\right[\quad \text{and} \quad \left]\lim_{\varepsilon \to \varepsilon_{\sup}-} \Psi_2^R(\varepsilon), \lim_{\varepsilon \to \varepsilon_{\inf}+} \Psi_2^R(\varepsilon)\right[.$$

A comparison between these bounds ends the proof (3.38). □

Theorem 3.1 can be written in terms of v_R. Indeed, (3.38) is equivalent to

$$\Phi_2^{\inf}(\varepsilon_R) < v_R < \Phi_2^{\sup}(\varepsilon_R)\,, \tag{3.39}$$

where

$$\Phi_2^{\inf}(\varepsilon_R) = \lim_{\varepsilon \to \varepsilon_{\inf}+} \Phi_1^L(\varepsilon) + v_R - \Psi_2^R(\varepsilon)\,,$$
$$\Phi_2^{\sup}(\varepsilon_R) = \lim_{\varepsilon \to \varepsilon_{\sup}-} \Phi_1^L(\varepsilon) + v_R - \Psi_2^R(\varepsilon)\,. \tag{3.40}$$

The functions $\Phi_2^{\inf}$ and $\Phi_2^{\sup}$ in (3.39) are the forward wave curves passing through the states $\boldsymbol{q}_{\inf}$ and $\boldsymbol{q}_{\sup}$ respectively, such that

$$\boldsymbol{q}_{\inf} = \lim_{\varepsilon \to \varepsilon_{\inf}+} \left(\varepsilon, \Phi_1^L(\varepsilon)\right)^\top \quad \text{and} \quad \boldsymbol{q}_{\sup} = \lim_{\varepsilon \to \varepsilon_{\sup}-} \left(\varepsilon, \Phi_1^L(\varepsilon)\right)^\top. \tag{3.41}$$

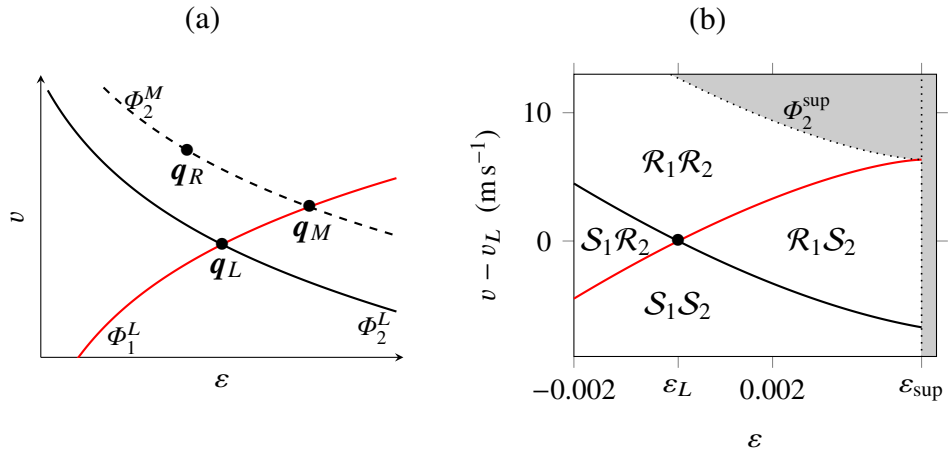

Figure 3.5. (a) Construction of the solution to (3.36). (b) Admissibility regions and hyperbolicity domain (white) for the polynomial law (2.22) with $\delta = 0$ and $\varepsilon_L = 10^{-4}$.

Graphically, $\Phi_2^{\inf}$ and $\Phi_2^{\sup}$ correspond to the dashed curve Φ_2^M on Figure 3.5a when ε_M tends towards $\varepsilon_{\inf}$ or $\varepsilon_{\sup}$ respectively. Since the curve Φ_1^L is only translated vertically when v_L varies, the condition (3.39)-(3.41) can be written in terms of the velocity jump $v_R - v_L$ by substracting v_L in (3.39). For analytical expressions and remarks, see (3.53) in the Appendix (Section 4.1.b).

In (3.39), $\Phi_2^{\inf}(\varepsilon_R)$ is infinite if $\varepsilon_{\inf} = -\infty$ or if $\sigma(\varepsilon)$ tends towards $-\infty$ when ε tends towards $\varepsilon_{\inf}+$. The value of $\Phi_2^{\sup}(\varepsilon_R)$ is infinite if $C(\varepsilon)$ tends towards $+\infty$ when ε tends towards $\varepsilon_{\sup}-$. If both are infinite, then Theorem 3.1 is satisfied for every initial data. Else, there exists a bound on $v_R - v_L$ which ensures the existence of the solution.

Now, we describe the admissibility regions, i.e. the regions of the ε-v plane where a given wave structure is admissible given $\boldsymbol{q}_L$. This is similar to the approach presented in Theorem 7.1 of [40]. Thus, we draw the forward wave curves Φ_1^L and Φ_2^L passing through $\boldsymbol{q}_L$. These curves divide the plane into four regions (Figure 3.5a). When $\boldsymbol{q}_M$ belongs to Φ_1^L, (3.37) states which kind of 1-wave connects $\boldsymbol{q}_M$ to $\boldsymbol{q}_L$. Then, we draw the forward wave curve Φ_2^M passing through $\boldsymbol{q}_M$. For any $\boldsymbol{q}_R$ belonging to Φ_2^M, we know which kind of 2-wave connects it to $\boldsymbol{q}_M$ (3.37). Finally, we obtain a map of the admissible combinations of 1-waves and 2-waves (Figure 3.5b). If (3.39) is satisfied, then four regions are distinguished:

- If $v_R \geqslant \Phi_1^L(\varepsilon_R)$ and $v_R \geqslant \Phi_2^L(\varepsilon_R)$, region $\mathcal{R}_1\mathcal{R}_2$,
- Else, if $v_R \geqslant \Phi_1^L(\varepsilon_R)$ and $v_R < \Phi_2^L(\varepsilon_R)$, region $\mathcal{S}_1\mathcal{R}_2$,
- Else, if $v_R \geqslant \Phi_2^L(\varepsilon_R)$ and $v_R < \Phi_1^L(\varepsilon_R)$, region $\mathcal{R}_1\mathcal{S}_2$,
- Else, region $\mathcal{S}_1\mathcal{S}_2$.

■ *Example (polynomial).* In the case of the constitutive law (2.22) with $\delta = 0$, $]\varepsilon_{\inf}, \varepsilon_{\sup}[=]-\infty, 1/(2\beta)[$. At the lower bound, $\varepsilon_{\inf} = -\infty$. But at the upper bound, $C(\varepsilon)$ vanishes when ε tends towards $1/(2\beta)$. Therefore, Theorem 3.1 is not satisfied for high values of the velocity jump. To illustrate, we take

$\varepsilon_L = -\varepsilon_R = 10^{-4}$ and the parameters issued from Table 2.1. Condition (3.53) then becomes $v_R - v_L \leqslant$ 13.07 m/s, which is shown graphically in Figure 3.5b.

2.3. Convex-concave constitutive laws

Let us assume that σ'' is strictly decreasing and equals zero at $\varepsilon = \varepsilon_0$. Therefore, the characteristic fields are neither linearly degenerate nor genuinely nonlinear. The constitutive law is strictly convex for $\varepsilon < \varepsilon_0$ and strictly concave for $\varepsilon > \varepsilon_0$. For any a and b, let us denote

$$\begin{aligned} a \underset{L}{\leqslant} b \qquad &\Leftrightarrow \qquad (\varepsilon_L - \varepsilon_0)\, a \leqslant (\varepsilon_L - \varepsilon_0)\, b\,, \\ a \underset{R}{<} b \qquad &\Leftrightarrow \qquad (\varepsilon_R - \varepsilon_0)\, a < (\varepsilon_R - \varepsilon_0)\, b\,. \end{aligned}$$

Similar notations are used for other kinds of inequalities, such as $a \underset{L}{>} b$, etc. From the graphical method in Section 1.2 based on convex hull constructions, forward and backward wave curves write

$$\begin{aligned} \Phi_1^L(\varepsilon) &= \begin{cases} \mathcal{S}_1^L(\varepsilon) & \text{if } \varepsilon_L^* \underset{L}{\leqslant} \varepsilon \underset{L}{<} \varepsilon_L\,, \\ \mathcal{R}_1^L(\varepsilon) & \text{if } \varepsilon \underset{L}{\geqslant} \varepsilon_L\,, \\ \mathcal{SR}_1^L(\varepsilon) & \text{if } \varepsilon \underset{L}{<} \varepsilon_L^*\,, \end{cases} \\ \Phi_2^L(\varepsilon) &= \begin{cases} \mathcal{S}_2^L(\varepsilon) & \text{if } \varepsilon \underset{L}{<} {\varepsilon_L}^\dagger \quad \text{or} \quad \varepsilon \underset{L}{>} \varepsilon_L\,, \\ \mathcal{R}_2^L(\varepsilon) & \text{if } \varepsilon_0 \underset{L}{\leqslant} \varepsilon \underset{L}{\leqslant} \varepsilon_L\,, \\ \mathcal{RS}_2^L(\varepsilon) & \text{if } {\varepsilon_L}^\dagger \underset{L}{\leqslant} \varepsilon \underset{L}{<} \varepsilon_0\,, \end{cases} \\ \Psi_1^R(\varepsilon) &= \begin{cases} \mathcal{S}_1^R(\varepsilon) & \text{if } \varepsilon \underset{R}{<} {\varepsilon_R}^\dagger \quad \text{or} \quad \varepsilon \underset{R}{>} \varepsilon_R\,, \\ \mathcal{R}_1^R(\varepsilon) & \text{if } \varepsilon_0 \underset{R}{\leqslant} \varepsilon \underset{R}{\leqslant} \varepsilon_R\,, \\ \mathcal{RS}_1^R(\varepsilon) & \text{if } {\varepsilon_R}^\dagger \underset{R}{\leqslant} \varepsilon \underset{R}{<} \varepsilon_0\,, \end{cases} \\ \Psi_2^R(\varepsilon) &= \begin{cases} \mathcal{S}_2^R(\varepsilon) & \text{if } \varepsilon_R^* \underset{R}{\leqslant} \varepsilon \underset{R}{<} \varepsilon_R\,, \\ \mathcal{R}_2^R(\varepsilon) & \text{if } \varepsilon \underset{R}{\geqslant} \varepsilon_R\,, \\ \mathcal{SR}_2^R(\varepsilon) & \text{if } \varepsilon \underset{R}{<} \varepsilon_R^*\,. \end{cases} \end{aligned} \tag{3.42}$$

When $\varepsilon_0 \to -\infty$, the constitutive law becomes strictly concave. In this case, ε, ε_L and ε_R are always larger than ε_0. Thus, $\underset{L}{<}$ can be replaced by $<$ in (3.42) (idem for similar notations). Moreover, ε_L^*, ε_R^*, ${\varepsilon_L}^\dagger$ and ${\varepsilon_R}^\dagger$ tend towards $-\infty$. Therefore, we recover the wave curves (3.37).

Forward and backward wave curves are Lipschitz continuous and they are C^2 in the vicinity of the states $\boldsymbol{q}_L$ or $\boldsymbol{q}_R$. Their regularity may be reduced to C^1 after the first crossing with the line $\varepsilon = \varepsilon_0$ (cf. Sections 9.3-9.5 of [30]). From the properties of each elementary curve studied before, we deduce that Φ_1^L is an increasing bijection over $]\varepsilon_{\inf}, \varepsilon_{\sup}[$ and Ψ_2^R a decreasing bijection. Lastly,

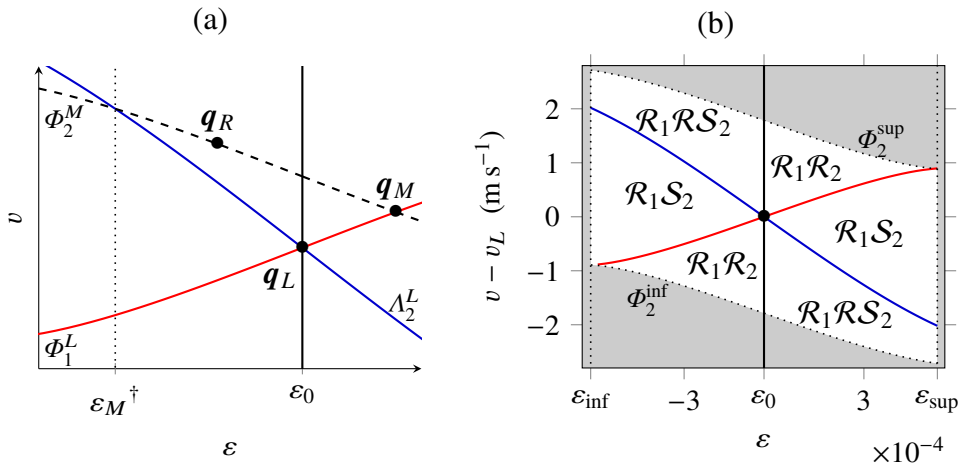

Figure 3.6. Case $\varepsilon_L = \varepsilon_0$. (a) Construction of the solution to (3.36). (b) Admissibility regions and hyperbolicity domain (white) for the polynomial law (2.22) with a cubic nonlinearity and parameters from Table 2.1.

Theorem 9.5.1 in [30] states that for $\|\boldsymbol{q}_R - \boldsymbol{q}_L\|$ sufficiently small, the entropic solution is unique. Similarly to Theorem 3.1, we deduce a condition which ensures the existence of the entropic solution for any initial data.

Theorem 3.2. *If the constitutive law is strictly convex for $\varepsilon < \varepsilon_0$ and strictly concave for $\varepsilon > \varepsilon_0$, then the entropic solution to the Riemann problem (2.23)-(3.2) exists and is unique, provided that*

$$\lim_{\varepsilon \to \varepsilon_{inf}+} \Psi_2^R(\varepsilon) - \Phi_1^L(\varepsilon) > 0 \qquad \textit{and} \qquad \lim_{\varepsilon \to \varepsilon_{sup}-} \Psi_2^R(\varepsilon) - \Phi_1^L(\varepsilon) < 0, \tag{3.43}$$

with Φ_1^L and Ψ_2^R given in (3.42).

Proof. Similarly to Theorem 3.1, we can reduce the existence criterion to a comparison between the ranges of Φ_1^L and Ψ_2^R. □

Theorem 3.2 can be written in terms of the velocity jump $v_R - v_L$. The analytical expressions (3.54)-(3.57) are given in the Appendix (Section 4.1.b). If both limits of $C(\varepsilon)$ are infinite when ε tends towards $\varepsilon_{\inf}+$ or $\varepsilon_{\sup}-$, then (3.43) is satisfied for every initial data. Else, there exists a bound on the velocity jump, which ensures the existence of the solution.

■ *Case $\varepsilon_L = \varepsilon_0$.* We describe the admissibility regions when the left state is on the inflection point. As we did for concave constitutive laws, we draw the forward wave curve Φ_1^L passing through $\boldsymbol{q}_L$ (Figure 3.6a). Let us consider an intermediate state $\boldsymbol{q}_M$ belonging to Φ_1^L. It is connected to $\boldsymbol{q}_L$ through a 1-rarefaction (3.42). Then, we draw the forward wave curve Φ_2^M passing through $\boldsymbol{q}_M$. For any $\boldsymbol{q}_R$ belonging to Φ_2^M, one knows which kind of 2-wave connects $\boldsymbol{q}_M$ to $\boldsymbol{q}_R$ (3.42). On Figure 3.6a, $\varepsilon_M > \varepsilon_0$. Therefore, we have a 2-shock if $\varepsilon_R < \varepsilon_M{}^\dagger$ or $\varepsilon_R > \varepsilon_M$, a 2-rarefaction if $\varepsilon_0 \leqslant \varepsilon_R \leqslant \varepsilon_M$ and a 2-rarefaction-shock else. On Figure 3.6a, the 2-wave is a rarefaction-shock.

To achieve the partition of the ε-v space into admissibility regions, we introduce the curve Λ_2^L which marks the equality case in Liu's entropy condition

for 2-shocks (3.6). The curve Λ_2^L marks the frontier between the admissibility regions of 2-shocks and 2-rarefaction-shocks. It is the set of right states $\boldsymbol{q}$ belonging to Φ_2^M such that $\varepsilon = {\varepsilon_M}^\dagger$, or equivalently $\varepsilon^* = \varepsilon_M$, when $\boldsymbol{q}_M$ varies along Φ_1^L (Figure 3.6a). Hence, $\boldsymbol{q}$ satisfies $v = \mathcal{RS}_2^M(\varepsilon)$, where $\boldsymbol{q}_M = (\varepsilon^*, \Phi_1^L(\varepsilon^*))^\top$:

$$v = \Phi_1^L(\varepsilon^*) + c(\varepsilon^*)(\varepsilon^* - \varepsilon) \equiv \Lambda_2^L(\varepsilon)\,. \tag{3.44}$$

Finally, we obtain a map of the admissible combinations of 1-waves and 2-waves (Figure 3.6b). If (3.39) is satisfied and $\varepsilon_L = \varepsilon_0$, then three regions are distinguished:

- If $v_R \underset{R}{\geqslant} \Phi_1^L(\varepsilon_R)$, region $\mathcal{R}_1\mathcal{R}_2$,
- Else, if $v_R \underset{R}{\geqslant} \Lambda_2^L(\varepsilon_R)$, region $\mathcal{R}_1\mathcal{S}_2$,
- Else, region $\mathcal{R}_1\mathcal{RS}_2$.

■ *Case* $\varepsilon_L \neq \varepsilon_0$. Figure 3.7 represents the admissibility regions for $\varepsilon_L > \varepsilon_0$. Similarly, Figure 3.8 shows the admissibility regions for $\varepsilon_L < \varepsilon_0$. In both cases, we draw the forward wave curves Φ_1^L and Φ_2^L passing through $\boldsymbol{q}_L$. For any intermediate state $\boldsymbol{q}_M$ belonging to Φ_1^L, Eq. (3.42) selects the 1-wave which connects $\boldsymbol{q}_M$ to $\boldsymbol{q}_L$: a 1-shock if $\varepsilon_L^* \leqslant \varepsilon_M < \varepsilon_L$, a 1-rarefaction if $\varepsilon_M \geqslant \varepsilon_L$ and a 1-shock-rarefaction else. Then, we draw the curve Λ_2^L marking Liu's condition for 2-shocks. Thus, we can already qualify six admissibility regions.

To achieve the partition of the ε-v space, we introduce the curve Λ_1^L which corresponds to the equality case in Liu's entropy condition for 1-shocks (3.6). The curve Λ_1^L marks the frontier between the admissibility regions of 1-shocks and 1-shock-rarefactions. It is the locus of right states $\boldsymbol{q}$ belonging to Φ_2^M, where the intermediate state is $\boldsymbol{q}_M = (\varepsilon_L^*, \Phi_1^L(\varepsilon_L^*))^\top$. Since $(\varepsilon_L^* - \varepsilon_0)(\varepsilon_L - \varepsilon_0) \leqslant 0$, the inequalities depending on $\varepsilon_M - \varepsilon_0$ in $\Phi_2^M(\varepsilon)$ (3.42) can be changed in inequalities depending on $\varepsilon_L - \varepsilon_0$. Hence,

$$v = \begin{cases} \mathcal{S}_2^M(\varepsilon) & \text{if } \varepsilon \underset{L}{\geqslant} \varepsilon_L \quad \text{or} \quad \varepsilon \underset{L}{\leqslant} \varepsilon_L^* \\ \mathcal{R}_2^M(\varepsilon) & \text{if } \varepsilon_0 \underset{L}{\geqslant} \varepsilon \underset{L}{\geqslant} \varepsilon_L^* \\ \mathcal{RS}_2^M(\varepsilon) & \text{if } \varepsilon_L \underset{L}{\geqslant} \varepsilon \underset{L}{\geqslant} \varepsilon_0 \end{cases} \equiv \Lambda_1^L(\varepsilon)\,. \tag{3.45}$$

Finally, if (3.39) is satisfied and $\varepsilon_L \neq \varepsilon_0$, then nine regions are distinguished:

- If $v_R \underset{L}{\geqslant} \Phi_2^L(\varepsilon_R)$, $v_R \underset{L}{\geqslant} \Phi_1^L(\varepsilon_R)$ and $\varepsilon_R \underset{L}{\geqslant} \varepsilon_0$, region $\mathcal{R}_1\mathcal{R}_2$,
- Else, if $v_R \underset{L}{\geqslant} \Phi_2^L(\varepsilon_R)$ and $\left[v_R \underset{L}{\leqslant} \Phi_1^L(\varepsilon_R) \text{ or } v_R \underset{L}{\leqslant} \Lambda_2^L(\varepsilon_R)\right]$, region $\mathcal{R}_1\mathcal{S}_2$,
- Else, if $v_R \underset{L}{\geqslant} \Phi_2^L(\varepsilon_R)$, $v_R \underset{L}{\geqslant} \Lambda_2^L(\varepsilon_R)$ and $\varepsilon_R \underset{L}{\leqslant} \varepsilon_0$, region $\mathcal{R}_1\mathcal{RS}_2$,
- Else, if $v_R \underset{L}{\leqslant} \Phi_2^L(\varepsilon_R)$, $v_R \underset{L}{\geqslant} \Lambda_1^L(\varepsilon_R)$ and $v_R \underset{R}{\geqslant} \Phi_1^L(\varepsilon_R)$, region $\mathcal{S}_1\mathcal{R}_2$,

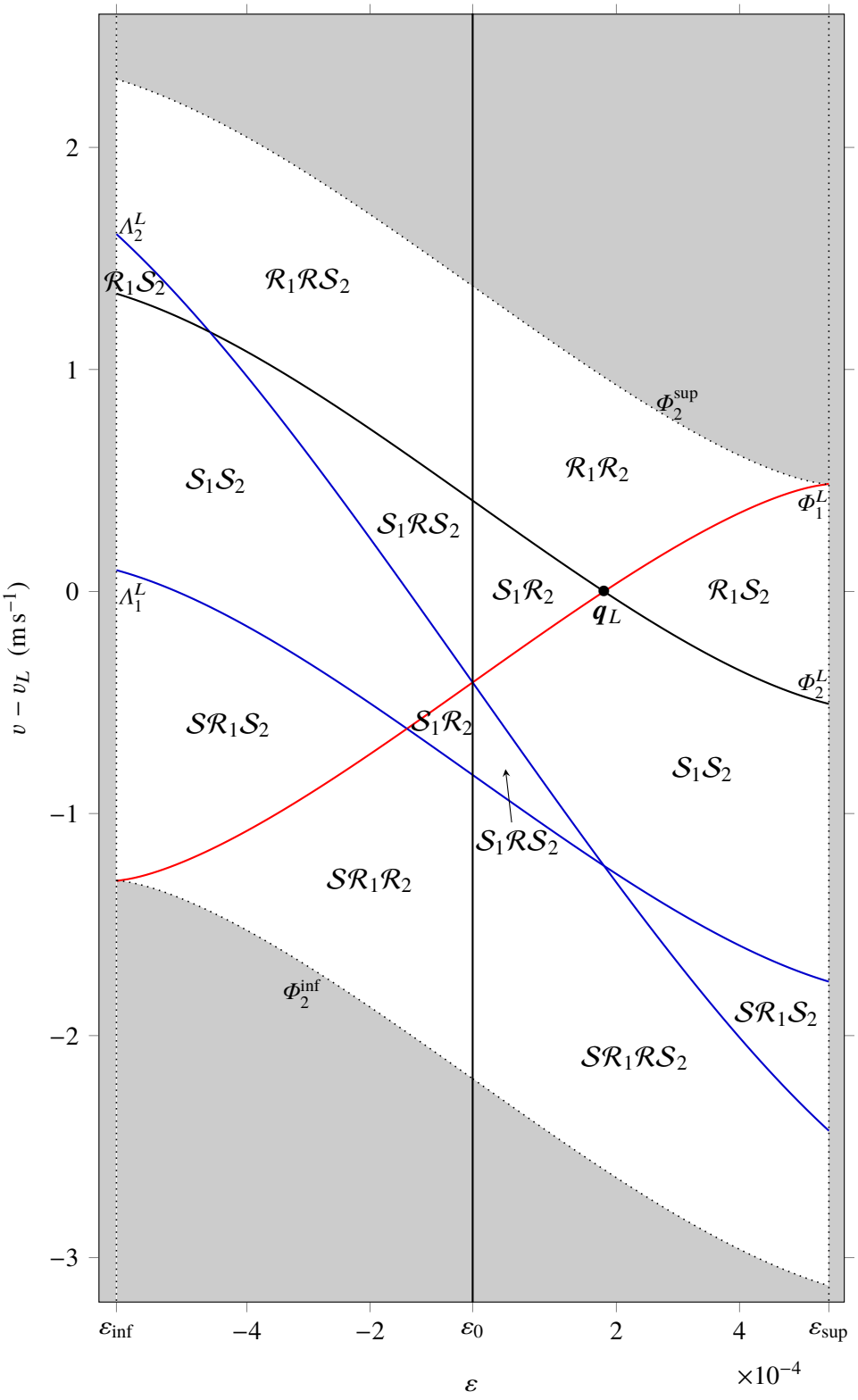

Figure 3.7. Case $\varepsilon_L > \varepsilon_0$. Admissibility regions and hyperbolicity domain (white) for the polynomial law (2.22) with a cubic nonlinearity and the parameters from Table 2.1. Here, $\varepsilon_L = 1.8 \times 10^{-4}$.

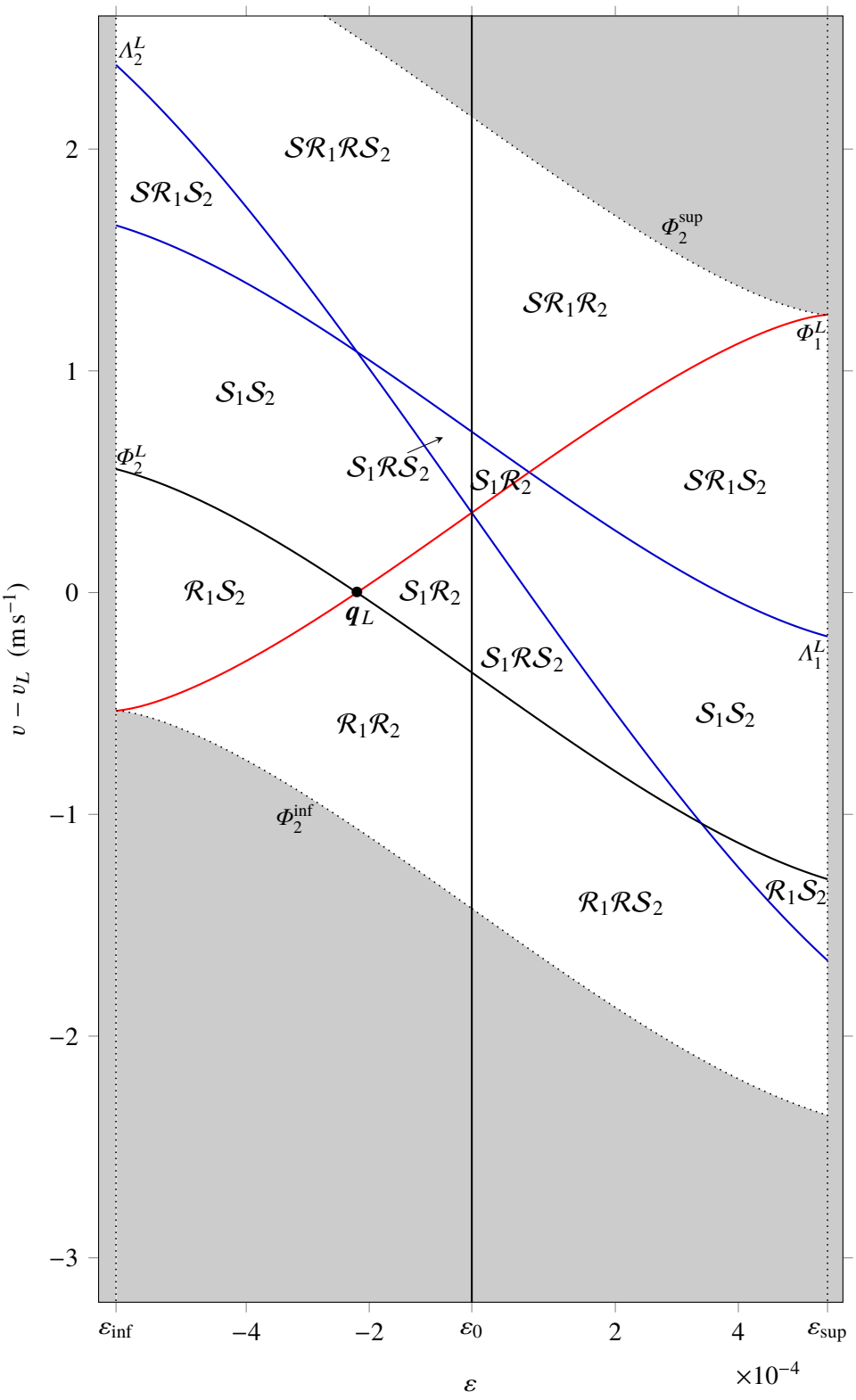

Figure 3.8. Case $\varepsilon_L < \varepsilon_0$. Same as Figure 3.7, but with $\varepsilon_L = -2.2 \times 10^{-4}$.

- Else, if $v_R \underset{L}{\leqslant} \Phi_2^L(\varepsilon_R)$, $v_R \underset{L}{\geqslant} \Lambda_1^L(\varepsilon_R)$ and $v_R \underset{R}{<} \Lambda_2^L(\varepsilon_R)$, region $\mathcal{S}_1\mathcal{R}\mathcal{S}_2$,
- Else, if $v_R \underset{L}{\leqslant} \Phi_1^L(\varepsilon_R)$, $v_R \underset{L}{\leqslant} \Lambda_1^L(\varepsilon_R)$ and $\varepsilon_R \underset{L}{\leqslant} \varepsilon_0$, region $\mathcal{S}\mathcal{R}_1\mathcal{R}_2$,
- Else, if $v_R \underset{L}{\leqslant} \Lambda_1^L(\varepsilon_R)$ and $\left[v_R \underset{L}{>} \Phi_1^L(\varepsilon_R) \text{ or } v_R \underset{L}{\geqslant} \Lambda_2^L(\varepsilon_R) \right]$, region $\mathcal{S}\mathcal{R}_1\mathcal{S}_2$,
- Else, if $v_R \underset{L}{<} \Lambda_1^L(\varepsilon_R)$, $v_R \underset{L}{<} \Lambda_2^L(\varepsilon_R)$ and $\varepsilon_R \underset{L}{>} \varepsilon_0$, region $\mathcal{S}\mathcal{R}_1\mathcal{R}\mathcal{S}_2$,
- Else, region $\mathcal{S}_1\mathcal{S}_2$.

■ *Example (polynomial).* In the case of the cubic polynomial law (2.22) where $\delta > 0$, $]\varepsilon_{\text{inf}}, \varepsilon_{\text{sup}}[$ is bounded (2.35). The limit of $C(\varepsilon)$ when ε tends towards ε_{sup} or ε_{inf} is equal to $\pm\frac{\pi}{2} c_0 \frac{\beta^2+3\delta}{6\delta\sqrt{3\delta}}$. Therefore, the velocity jump $v_R - v_L$ is also bounded, which is illustrated on Figure 3.6 and Figure 3.7. With the parameters from Table 2.1, it must belong to $[-1.91, 1.66]$ m s^{-1} if $\varepsilon_L = -\varepsilon_R = 10^{-4}$.

Let us detail the Riemann solution for a configuration with two compound waves and $\varepsilon < \varepsilon_0$. On Figure 3.9, we display the solution with initial data $\varepsilon_L = -10^{-4}$, $\varepsilon_R = -2 \times 10^{-4}$, $v_L = -0.6$ m s^{-1} and $v_R = 0.6$ m s^{-1}. It consists of two compound waves:

$$\boldsymbol{q}(x,t) = \begin{cases} \boldsymbol{q}_L & \text{if } x < -c(\varepsilon_L^*)\, t\,, \\ \tilde{\boldsymbol{q}}_1(x/t) & \text{if } -c(\varepsilon_L^*)\, t \leqslant x \leqslant -c(\varepsilon_M)\, t\,, \\ \boldsymbol{q}_M & \text{if } -c(\varepsilon_M)\, t \leqslant x \leqslant c(\varepsilon_M)\, t\,, \\ \tilde{\boldsymbol{q}}_2(x/t) & \text{if } c(\varepsilon_M)\, t \leqslant x < c(\varepsilon_R^*)\, t\,, \\ \boldsymbol{q}_R & \text{if } c(\varepsilon_R^*)\, t \leqslant x\,. \end{cases} \tag{3.46}$$

where $\tilde{\boldsymbol{q}}_1(\xi)$ and $\tilde{\boldsymbol{q}}_2(\xi)$ satisfy (3.16) with $k = 1$ and $k = 2$ respectively. Here, $\varepsilon_M \approx 1.604 \times 10^{-4}$. The rarefactions break at $\varepsilon_L^* = 0$ and $\varepsilon_R^* = 0.5 \times 10^{-4}$.

3. Conclusion

The analytical solution to the Riemann problem has been detailed for general stress-strain relationships, which have at most one inflection point. If the stress-strain relationship is convex or concave, then the study is similar to the p-system of gas dynamics, i.e., the entropic solution is made of shock waves and rarefaction waves. However, if the stress-strain relationship has an inflection point, compound waves must be considered.

For the polynomial law (2.22), an interactive application and a Matlab Toolbox which solve the problem have been developed, cf. https://gchiavassa.perso.centrale-marseille.fr/RiemannElasto. The previous analytical solution has been used as a validation test case for the numerical methods in Chapter 2. It is a challenging test due to the non-smoothness and the non-uniqueness of weak solutions, which is best highlighted in cases with compound waves. The Riemann solution may be used for the validation of other numerical methods, such as the methods used in seismology [114] or in NDE applications [25, 123].

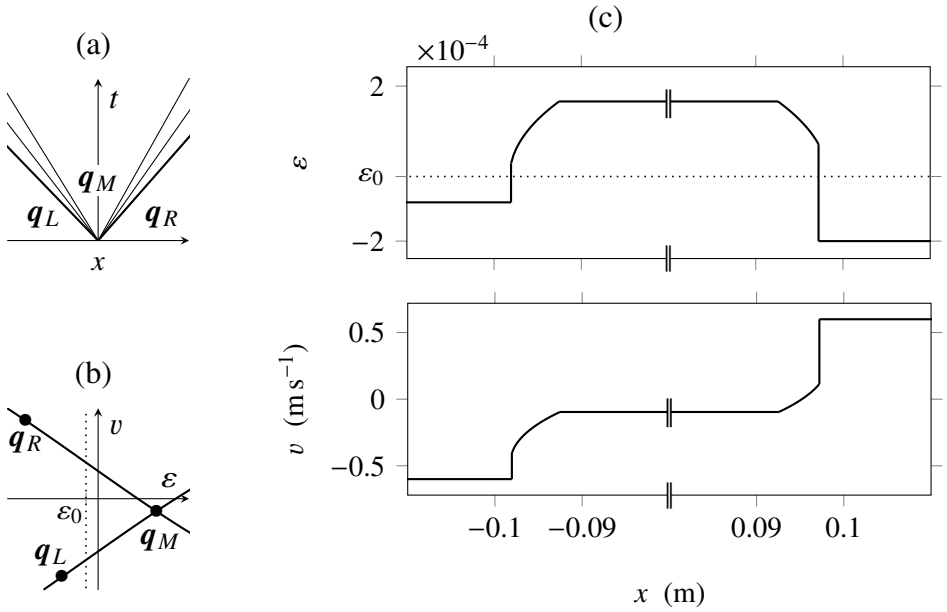

Figure 3.9. (a) Solution to the Riemann problem for the cubic polynomial law (2.22) with two compound waves. (b) 1-shock-rarefaction and 2-rarefaction-shock curves. (c) Analytical solution at $t = 0.05$ ms. The x-axis is broken from -0.08 to 0.08 m.

The mathematics and the approach presented here could be applied to more complicated constitutive laws, e.g. with a disjoint union of inflection points. Another prospect concerns the case of nonsmooth constitutive laws such as bimodular elasticity. In the case of the Euler equations, this point is addressed in [90].

4. Appendix

4.1. Details on the Riemann solution

4.1.a. *Elementary wave curves*

Here, we list some properties of the curves $\mathcal{S}_k^\ell$, $\mathcal{R}_k^\ell$, $\mathcal{SR}_k^\ell$ and $\mathcal{RS}_k^\ell$.

■ *Discontinuities.* Let us differentiate equation (3.11). We obtain

$$\begin{aligned}\frac{\mathrm{d}}{\mathrm{d}\varepsilon}\mathcal{S}_1^\ell(\varepsilon) &= \frac{1}{2}\sqrt{\frac{\sigma(\varepsilon)-\sigma(\varepsilon_\ell)}{\rho_0\,(\varepsilon-\varepsilon_\ell)}}\left(1+\sigma'(\varepsilon)\Big/\frac{\sigma(\varepsilon)-\sigma(\varepsilon_\ell)}{\varepsilon-\varepsilon_\ell}\right)\\ &= -\frac{\mathrm{d}}{\mathrm{d}\varepsilon}\mathcal{S}_2^\ell(\varepsilon) > 0\,.\end{aligned} \tag{3.47}$$

Therefore, $\mathcal{S}_1^\ell$ is an increasing bijection and $\mathcal{S}_2^\ell$ is a decreasing bijection.

■ *Rarefactions.* Since C is the primitive of a strictly positive continuous function, C is strictly increasing and continuous. Therefore, $\mathcal{R}_1^\ell$ is an increasing bijection and $\mathcal{R}_2^\ell$ is a decreasing bijection (3.19).

■ *Shock-rarefactions.* Shock-rarefaction curves (3.29) have the same properties as rarefaction curves (3.19). Indeed, they differ only by a constant, which equals zero if $\varepsilon_\ell = \varepsilon_\ell^* = \varepsilon_0$.

■ *Rarefaction-shocks.* Let use differentiate equation (3.32). We obtain

$$\frac{\mathrm{d}}{\mathrm{d}\varepsilon}\mathcal{RS}_1^\ell(\varepsilon) = c(\varepsilon^*) - \frac{\mathrm{d}\varepsilon^*}{\mathrm{d}\varepsilon}\,c'(\varepsilon^*)\,(\varepsilon^*-\varepsilon) = -\frac{\mathrm{d}}{\mathrm{d}\varepsilon}\mathcal{RS}_2^\ell(\varepsilon), \tag{3.48}$$

where

$$c(\varepsilon^*) = \sqrt{\frac{\sigma'(\varepsilon^*)}{\rho_0}} \qquad \text{and} \qquad c'(\varepsilon^*) = \frac{\sigma''(\varepsilon^*)}{2\sqrt{\rho_0\,\sigma'(\varepsilon^*)}}\,. \tag{3.49}$$

Applying the implicit functions theorem to $F(\varepsilon^*,\varepsilon)$ in (3.9) requires $\partial F/\partial a(\varepsilon^*,\varepsilon) \neq 0$. Since $\partial F/\partial a(\varepsilon^*,\varepsilon) = \sigma''(\varepsilon^*)$, the hypotheses of the theorem are satisfied if $\varepsilon^* \neq \varepsilon_0$, where ε_0 denotes the inflection point. Finally,

$$\frac{\mathrm{d}\varepsilon^*}{\mathrm{d}\varepsilon} = -\frac{\partial F/\partial b}{\partial F/\partial a}(\varepsilon^*,\varepsilon) = \frac{\sigma'(\varepsilon^*)-\sigma'(\varepsilon)}{\sigma''(\varepsilon^*)(\varepsilon^*-\varepsilon)}\,. \tag{3.50}$$

Thus,

$$\frac{\mathrm{d}}{\mathrm{d}\varepsilon}\mathcal{RS}_1^\ell(\varepsilon) = \frac{\sigma'(\varepsilon^*)+\sigma'(\varepsilon)}{2\sqrt{\rho_0\,\sigma'(\varepsilon^*)}} = -\frac{\mathrm{d}}{\mathrm{d}\varepsilon}\mathcal{RS}_2^\ell(\varepsilon) > 0\,. \tag{3.51}$$

Therefore, $\mathcal{RS}_1^\ell$ is an increasing bijection and $\mathcal{RS}_2^\ell$ is a decreasing bijection.

4.1.b. *Restriction on the velocity jump*

In this section, we provide analytical expressions deduced from Theorem 3.1 and Theorem 3.2.

■ *Concave constitutive laws.* We go back to the condition that must be satisfied by the initial data when the constitutive law is concave, i.e. Eq. (3.38) in Theorem 3.1. According to the expressions of Φ_1^L and Ψ_2^R in (3.37), one has

$$\lim_{\varepsilon\to\varepsilon_{\inf}+} \mathcal{S}_2^R(\varepsilon) - \mathcal{S}_1^L(\varepsilon) > 0 \qquad \text{and} \qquad \lim_{\varepsilon\to\varepsilon_{\sup}-} \mathcal{R}_2^R(\varepsilon) - \mathcal{R}_1^L(\varepsilon) < 0\,. \tag{3.52}$$

This can be expressed in terms of the velocity jump $v_R - v_L$. Based on (3.11) and (3.19), condition (3.52) becomes

$$\begin{cases} v_R - v_L > -\lim\limits_{\varepsilon\to\varepsilon_{\inf}+} \left(\sqrt{\dfrac{\sigma(\varepsilon)-\sigma(\varepsilon_L)}{\rho_0}(\varepsilon-\varepsilon_L)} + \sqrt{\dfrac{\sigma(\varepsilon)-\sigma(\varepsilon_R)}{\rho_0}(\varepsilon-\varepsilon_R)} \right), \\ v_R - v_L < \lim\limits_{\varepsilon\to\varepsilon_{\sup}-} 2C(\varepsilon) - C(\varepsilon_L) - C(\varepsilon_R)\,. \end{cases} \tag{3.53}$$

■ *Convex-concave constitutive laws.* The same condition (3.43) must be satisfied by the initial data when the constitutive law is strictly convex for $\varepsilon < \varepsilon_0$ and strictly concave for $\varepsilon > \varepsilon_0$ (Theorem 3.2). The expressions of Φ_1^L and Ψ_2^R are given by (3.42). For instance, when ε tends towards $\varepsilon_{\inf}$ in $\Phi_1^L(\varepsilon)$, one needs a comparison between ε_L^* and $\varepsilon_{\inf}$ to choose the correct elementary wave curve. Since $\sigma'(\varepsilon_L^*) > 0 = \sigma'(\varepsilon_{\inf})$, it is immediate that $\varepsilon_L^* > \varepsilon_{\inf}$. Similar comparisons can be written to select the correct elementary curve in $\Psi_2^R(\varepsilon)$ or when ε tends towards $\varepsilon_{\sup}$. Finally, (3.43) writes

- if $\varepsilon_L \geqslant \varepsilon_0$ and $\varepsilon_R \geqslant \varepsilon_0$

$$\lim_{\varepsilon\to\varepsilon_{\inf}+} \mathcal{SR}_2^R(\varepsilon) - \mathcal{SR}_1^L(\varepsilon) > 0 \quad \text{and} \quad \lim_{\varepsilon\to\varepsilon_{\sup}-} \mathcal{R}_1^L(\varepsilon) - \mathcal{R}_2^R(\varepsilon) > 0, \tag{3.54}$$

- if $\varepsilon_L \geqslant \varepsilon_0 > \varepsilon_R$

$$\lim_{\varepsilon\to\varepsilon_{\inf}+} \mathcal{R}_2^R(\varepsilon) - \mathcal{SR}_1^L(\varepsilon) > 0 \quad \text{and} \quad \lim_{\varepsilon\to\varepsilon_{\sup}-} \mathcal{R}_1^L(\varepsilon) - \mathcal{SR}_2^R(\varepsilon) > 0, \tag{3.55}$$

- if $\varepsilon_R \geqslant \varepsilon_0 > \varepsilon_L$

$$\lim_{\varepsilon\to\varepsilon_{\inf}+} \mathcal{SR}_2^R(\varepsilon) - \mathcal{R}_1^L(\varepsilon) > 0 \quad \text{and} \quad \lim_{\varepsilon\to\varepsilon_{\sup}-} \mathcal{SR}_1^L(\varepsilon) - \mathcal{R}_2^R(\varepsilon) > 0, \tag{3.56}$$

- if $\varepsilon_L < \varepsilon_0$ and $\varepsilon_R < \varepsilon_0$

$$\lim_{\varepsilon\to\varepsilon_{\inf}+} \mathcal{R}_2^R(\varepsilon) - \mathcal{R}_1^L(\varepsilon) > 0 \quad \text{and} \quad \lim_{\varepsilon\to\varepsilon_{\sup}-} \mathcal{SR}_1^L(\varepsilon) - \mathcal{SR}_2^R(\varepsilon) > 0\,. \tag{3.57}$$

Based on the expressions of the elementary wave curves (3.11), (3.19), (3.32) and (3.29), inequalities (3.54)-(3.57) become

- if $\varepsilon_L \geqslant \varepsilon_0$ and $\varepsilon_R \geqslant \varepsilon_0$

$$\begin{cases} v_R - v_L > \lim\limits_{\varepsilon\to\varepsilon_{\inf}+} 2C(\varepsilon) - C(\varepsilon_L^*) - c(\varepsilon_L^*)(\varepsilon_L - \varepsilon_L^*) \\ \qquad\qquad - C(\varepsilon_R^*) - c(\varepsilon_R^*)(\varepsilon_R - \varepsilon_R^*), \\ v_R - v_L < \lim\limits_{\varepsilon\to\varepsilon_{\sup}-} 2C(\varepsilon) - C(\varepsilon_L) - C(\varepsilon_R), \end{cases} \tag{3.58}$$

- if $\varepsilon_L \geqslant \varepsilon_0 > \varepsilon_R$

$$\begin{cases} v_R - v_L > \lim\limits_{\varepsilon \to \varepsilon_{\inf}+} 2C(\varepsilon) - C(\varepsilon_L^*) - c(\varepsilon_L^*)(\varepsilon_L - \varepsilon_L^*) - C(\varepsilon_R), \\ v_R - v_L < \lim\limits_{\varepsilon \to \varepsilon_{\sup}-} 2C(\varepsilon) - C(\varepsilon_L) - C(\varepsilon_R^*) - c(\varepsilon_R^*)(\varepsilon_R - \varepsilon_R^*), \end{cases} \tag{3.59}$$

- if $\varepsilon_R \geqslant \varepsilon_0 > \varepsilon_L$

$$\begin{cases} v_R - v_L > \lim\limits_{\varepsilon \to \varepsilon_{\inf}+} 2C(\varepsilon) - C(\varepsilon_L) - C(\varepsilon_R^*) - c(\varepsilon_R^*)(\varepsilon_R - \varepsilon_R^*), \\ v_R - v_L < \lim\limits_{\varepsilon \to \varepsilon_{\sup}-} 2C(\varepsilon) - C(\varepsilon_L^*) - c(\varepsilon_L^*)(\varepsilon_L - \varepsilon_L^*) - C(\varepsilon_R), \end{cases} \tag{3.60}$$

- if $\varepsilon_L < \varepsilon_0$ and $\varepsilon_R < \varepsilon_0$

$$\begin{cases} v_R - v_L > \lim\limits_{\varepsilon \to \varepsilon_{\inf}+} 2C(\varepsilon) - C(\varepsilon_L) - C(\varepsilon_R), \\ v_R - v_L < \lim\limits_{\varepsilon \to \varepsilon_{\sup}-} 2C(\varepsilon) - C(\varepsilon_L^*) - c(\varepsilon_L^*)(\varepsilon_L - \varepsilon_L^*) \\ \qquad\qquad - C(\varepsilon_R^*) - c(\varepsilon_R^*)(\varepsilon_R - \varepsilon_R^*)\,. \end{cases} \tag{3.61}$$

CHAPTER 4

Hyperelastic material with slow dynamics

SLOW DYNAMICS, i.e. non-instantaneous material softening under dynamic loadings, has been evidenced experimentally (cf. Chapter 1). This phenomenon is not reproduced by the previous hyperelastic material models, where the speed of sound is a function of the strain. Several models accounting for the slow dynamics can be found in the literature. Among them, the phenomenological model by Vakhnenko et al. [137, 138] is based on a variable that describes the softening of the material (see Chapter 1 Sec. 2). Numerical simulations show that the model is in qualitative agreement with dynamic acousto-elastic testing [38]. However, this model has been developed in a one-dimensional configuration, and a three-dimensional version is not known. Furthermore, we proved that this model is not thermodynamically admissible (see the Appendix, Section 5.1).

In Section 1, a three-dimensional phenomenological model is derived in the framework of the finite-strain theory. The notations are the same as in Sec. 1 of Chapter 2, where the equations of hyperelasticity are presented. Here, a supplementary internal variable of state is considered, which describes the softening of the material. A mechanical constitutive law is deduced from the

Clausius–Duhem inequality. Moreover, a family of evolution equations for the internal variable is proposed. This study has been published in [1].

Section 2 illustrates the propagation of longitudinal waves in nonlinear solids with slow dynamics. We show how to adapt the numerical methods from Chapter 2 to account for the slow dynamics. Then, numerical experiments in infinite domain are presented, which show qualitative agreement with experimental observations. The study is detailed in a publication [4].

Section 3 is devoted to the development of a similar numerical method in the plane-strain case (2D). The case of hyperelastic material of Murnaghan type is considered first. A numerical example illustrates the coupling between shear waves and compressional waves. Then, the slow dynamics is added in a similar fashion as in Section 2, and numerical experiments in unbounded domain are presented. These works have lead to an article submission [7].

1. Phenomenological material modeling

1.1. Construction of the model

1.1.a. *Preliminaries*

We choose the following variables of state: the specific entropy η, the strain tensor $\boldsymbol{\chi}$, and an additional scalar variable g, which is introduced to represent the softening/recovery of the material. Consequently, the Gibbs identity (2.7) becomes

$$\dot{e} = T\dot{\eta} + \left.\frac{\partial e}{\partial \boldsymbol{\chi}}\right|_{\eta,g} : \dot{\boldsymbol{\chi}} + \left.\frac{\partial e}{\partial g}\right|_{\eta,\boldsymbol{\chi}} \dot{g}\,. \tag{4.1}$$

Multiplying (4.1) by ρ, the local equations of thermodynamics (2.5)-(2.6) yield the Clausius–Duhem inequality

$$\mathscr{D} = \boldsymbol{\sigma} : \boldsymbol{D} - \rho \left.\frac{\partial e}{\partial \boldsymbol{\chi}}\right|_{\eta,g} : \dot{\boldsymbol{\chi}} - \rho \left.\frac{\partial e}{\partial g}\right|_{\eta,\boldsymbol{\chi}} \dot{g} \geqslant 0\,, \tag{4.2}$$

for all state $\{\eta, \boldsymbol{\chi}, g\}$ and all evolution $\{\dot{\eta}, \dot{\boldsymbol{\chi}}, \dot{g}\}$, where (4.2) is the dissipation $\mathscr{D}$ per unit volume of material (W/m^3). If g is constant over time, the hyperelastic case (2.8) is recovered.

The main ingredient of the model is an expression of the internal energy per unit volume of the form

$$\rho_0 e = \phi_1(g) W(\boldsymbol{\chi}) + \phi_2(g)\,, \tag{4.3}$$

where W is the strain energy density function, expressed in terms of the strain tensor $\boldsymbol{\chi}$. The function ϕ_1 has dimensionless values, and ϕ_2 is a storage energy. If $\phi_1(g) = 1$ and $\phi_2(g) = 0$ for all g, then the classical case of hyperelasticity is recovered, where $\rho_0 e = W(\boldsymbol{\chi})$ (cf. Chapter 2 Section 1). The expression of the internal energy (4.3) is analogous to the Ogden–Roxburgh model of filled rubber [99]. It is also formally analogous to a model of wet sticking fibers [112].

These similarities are detailed in Section 5.1. With the assumption (4.3), the following substitutions are made in the inequality (4.2):

$$\begin{aligned} \rho \left.\frac{\partial e}{\partial \boldsymbol{\chi}}\right|_{\eta,g} : \dot{\boldsymbol{\chi}} &= \phi_1 \frac{\rho}{\rho_0} \frac{\partial W}{\partial \boldsymbol{\chi}} : \dot{\boldsymbol{\chi}}, \\ \rho \left.\frac{\partial e}{\partial g}\right|_{\eta,\boldsymbol{\chi}} \dot{g} &= \frac{\rho}{\rho_0} \left(\phi_1' W + \phi_2'\right) \dot{g}, \end{aligned} \tag{4.4}$$

where ϕ_1' and ϕ_2' denote the derivatives of ϕ_1 and ϕ_2, respectively. The final constitutive laws are obtained for a given choice of strain tensor $\boldsymbol{\chi}$. Similarly to Chapter 2, the Green–Lagrange strain tensor $\boldsymbol{E}$ is used (2.9). For other strain tensors, the constitutive laws can be deduced from $\boldsymbol{E}$, and similar derivations can be carried out.

1.1.b. *Constitutive laws*

We choose the Green–Lagrange strain tensor $\boldsymbol{\chi} = \boldsymbol{E} = \frac{1}{2}\left(\boldsymbol{F}^\top \cdot \boldsymbol{F} - \boldsymbol{I}\right)$. Similarly to Chapter 2, the Clausius–Duhem inequality (4.2) with the substitutions (2.11)-(4.4) reduces to

$$\mathscr{D} = \underbrace{\left(\boldsymbol{\sigma} - \phi_1 \bar{\boldsymbol{\sigma}}\right) : \boldsymbol{D}}_{\mathscr{D}_{\text{el}}} \underbrace{-\rho/\rho_0 \left(\phi_1' W + \phi_2'\right) \dot{g}}_{\mathscr{D}_{\text{inel}}} \geqslant 0, \tag{4.5}$$

where the hyperelastic Cauchy stress tensor

$$\bar{\boldsymbol{\sigma}} = \frac{1}{\det \boldsymbol{F}} \boldsymbol{F} \cdot \left.\frac{\partial W}{\partial \boldsymbol{E}}\right|_{\eta} \cdot \boldsymbol{F}^\top \tag{4.6}$$

depends on $\boldsymbol{F}$ (2.12).

The stress $\boldsymbol{\sigma}$ is a state function: it does not dependent on $\boldsymbol{D}$, which is not a variable of state. Thus, the term $\mathscr{D}_{\text{el}}$ in the dissipation (4.5) is a scalar product between $\boldsymbol{D}$ and a tensor which does not depend on $\boldsymbol{D}$. Moreover, the term $\mathscr{D}_{\text{inel}}$ does not depend on $\boldsymbol{D}$. Therefore, the Clausius–Duhem inequality (4.5) for all $\boldsymbol{D}$ yields the constitutive law

$$\boldsymbol{\sigma} = \phi_1(g)\, \bar{\boldsymbol{\sigma}}(\boldsymbol{F}), \tag{4.7}$$

where the hyperelastic stress $\bar{\boldsymbol{\sigma}}$ is defined in (4.6).

Now, the Clausius–Duhem inequality (4.5) reduces to $\mathscr{D}_{\text{inel}} \geqslant 0$, for all state and all $\dot{g}$. Therefore, $\phi_1' W + \phi_2'$ is either dependent on $\dot{g}$ or equal to zero. We choose the simplest nontrivial dependence:

$$\phi_1' W + \phi_2' = -\alpha \dot{g}, \tag{4.8}$$

where $\alpha \geqslant 0$ is expressed in $\mathrm{J\,m^{-3}\,s}$. The parameter α may be variable, e.g. dependent on the sign of $\dot{g}$, temperature, or any desired parameter. If $\alpha \neq 0$, Eq. (4.8) gives the evolution equation

$$\dot{g} = -\frac{1}{\alpha} \left(\phi_1'(g)\, W(\boldsymbol{\chi}) + \phi_2'(g)\right). \tag{4.9}$$

Otherwise ($\alpha = 0$), the internal variable g satisfies $\phi_1' W + \phi_2' = 0$, i.e. $g = g_{\text{eq}}(\chi)$ where

$$g_{\text{eq}}(\chi) = \left(\phi_2'/\phi_1'\right)^{-1} \left(-W(\chi)\right). \tag{4.10}$$

In this case, the internal variable is instantaneously modified when the strain varies: no slow dynamics occurs.

The previous choice ensures that the Clausius–Duhem inequality is satisfied, independently of the sign of $\dot{g}$. Indeed, with the assumption (4.8), the dissipation per unit volume in the material (4.5) is

$$0 \leqslant \mathscr{D} = \begin{cases} 0 & \text{if } \alpha = 0, \\ \dfrac{\rho}{\rho_0} \dfrac{\left(\phi_1' W + \phi_2'\right)^2}{\alpha} & \text{if } \alpha > 0. \end{cases} \tag{4.11}$$

If $\alpha = 0$ or $\alpha \longrightarrow +\infty$, then no dissipation occurs: the thermodynamic process is reversible. If $0 < \alpha < +\infty$, the thermodynamic process is irreversible, which is the origin of hysteresis curves under a dynamic loading.

The effect of g on the stress (4.7) is specified through ϕ_1. If $\phi_1(g) = 1$ for all g, then no stress softening occurs. Indeed, classical hyperelasticity is recovered. If $\phi_1(g) = 0$ for all g, then the stress does not depend on the strain any more: the material is destroyed. For the physical relevance of the constitutive law (4.7), we assume that $\phi_1 > 0$. Moreover, we assume that $g = 0$ entails no stress softening: $\phi_1(0) = 1$. A natural choice satisfying these requirements is

$$\phi_1(g) = 1 - g, \tag{4.12}$$

where $g < 1$.

We require that $g = 0$ is an equilibrium point (4.10) if no strain is applied. Hence, one must have $\phi_2'(0) = 0$. If the softening function (4.12) is chosen, the convexity of ϕ_2 ensures that the equilibrium point (4.10) is unique. Simple choices for ϕ_2 are

$$\phi_2(g) = \frac{1}{2}\gamma g^2, \tag{4.13}$$

$$\phi_2(g) = -\frac{1}{2}\gamma \ln(1 - g^2), \tag{4.14}$$

where $\gamma > 0$ is an energy per unit volume. The model equations (4.12)-(4.14) are chosen to avoid that g reaches 1. In the vicinity of $g = 0$, both expressions (4.13) and (4.14) are equivalent.

To summarize, the Lagrangian equations of motion are given by the conservation of deformation gradient (2.2), the conservation of momentum (2.4), and the evolution equation of g (4.9):

$$\begin{cases} \dot{\boldsymbol{F}} = \mathbf{grad}\, \boldsymbol{v}, \\ \rho_0 \dot{\boldsymbol{v}} = \mathbf{div}\, \boldsymbol{P} + \boldsymbol{f}^v, \\ -\alpha \dot{g} = \phi_1' W + \phi_2'. \end{cases} \tag{4.15}$$

The functions ϕ_1 and ϕ_2 are specified by (4.12) and (4.13)-(4.14), respectively. If the right Cauchy–Green tensor $\boldsymbol{\chi} = \boldsymbol{E}$ is used, then the first Piola–Kirchhoff stress tensor $\boldsymbol{P} = (\det \boldsymbol{F})\, \boldsymbol{\sigma} \cdot \boldsymbol{F}^{-\top}$ in the conservation of momentum is deduced from the constitutive law (4.6)-(4.7):

$$\boldsymbol{P} = \phi_1(g)\, \boldsymbol{F} \cdot \left.\frac{\partial W}{\partial \boldsymbol{E}}\right|_{\eta} . \tag{4.16}$$

Otherwise, tensor algebra yields the expression of the Piola–Kirchhoff stress tensor. In the next subsection, a few particular cases of (4.15)-(4.16) are detailed: the isotropic case, the case of infinitesimal strain and the case of uniaxial strain.

1.1.c. *Particular cases*

■ *Isotropic case.* The dependence to $\boldsymbol{E}$ of the internal energy can be replaced by a dependence to the invariants $E_{\mathrm{I}}, E_{\mathrm{II}}, E_{\mathrm{III}}$. In particular, the conservation of mass (2.3) rewrites as $\rho_0/\rho = \det \boldsymbol{F} = \sqrt{1 + 2E_{\mathrm{I}} + 4E_{\mathrm{II}} + 8E_{\mathrm{III}}}$. The Piola–Kirchhoff stress tensor $\boldsymbol{P}$ satisfies (4.16), where $\partial W/\partial \boldsymbol{E} = \alpha_0 \boldsymbol{I} + \alpha_1 \boldsymbol{E} + \alpha_2 \boldsymbol{E}^2$ is given in (2.14). In the literature, several strain energy density functions W can be found. In terms of the invariants of $\boldsymbol{E}$, a classical example is Murnaghan's law (2.16) (see e.g. [97]). Murnaghan hyperelasticity is recovered if $\alpha \longrightarrow +\infty$ in (4.9).

■ *Infinitesimal strain.* The Green–Lagrange strain tensor $\boldsymbol{E}$ in (2.9) is linearized with respect to the displacement gradient, i.e. $\boldsymbol{E} \simeq \frac{1}{2}\big(\mathbf{grad}\, \boldsymbol{u} + \mathbf{grad}^{\top} \boldsymbol{u}\big) = \boldsymbol{\varepsilon}$ reduces to the infinitesimal strain tensor $\boldsymbol{\varepsilon}$. The first Piola–Kirchhoff stress tensor (4.16) is linearized with respect to the coordinates of the displacement gradient too, i.e. $\boldsymbol{F} \cdot \partial W/\partial \boldsymbol{E} \simeq \partial W/\partial \boldsymbol{\varepsilon}$. In (4.15), the conservation of deformation gradient $\dot{\boldsymbol{F}} = \mathbf{grad}\, \boldsymbol{v}$ is replaced by the conservation of infinitesimal strain $\dot{\boldsymbol{\varepsilon}} = \frac{1}{2}\big(\mathbf{grad}\, \boldsymbol{v} + \mathbf{grad}^{\top} \boldsymbol{v}\big)$. If the strain energy W is compatible with Hooke's law in the infinitesimal strain limit (e.g., the strain energy of Murnaghan's law (2.16) is used), then linear elastodynamics are recovered when passing to the limit $\alpha \longrightarrow +\infty$ in (4.9).

■ *Uniaxial strain.* In this case, only the component of the displacement field along $\boldsymbol{e}_1$ remains (cf. Sec. 1.2 of Chapter 2). Moreover, this coordinate u is assumed to be invariant with respect to the other coordinates. The conservation of momentum $\rho_0 \dot{v} = \partial_x \sigma + \boldsymbol{f}^v \cdot \boldsymbol{e}_1$ involves the particle velocity $v = \dot{u}$, and the $_{11}$-component σ of the first Piola–Kirchhoff tensor $\boldsymbol{P}$. According to (2.19) and (4.16), this stress component satisfies $\sigma = \phi_1(g)\, \bar{\sigma}(\varepsilon)$, where $\bar{\sigma} = W'$ is the derivative of the strain energy density function with respect to $\varepsilon = \partial_x u$. In (4.15), the conservation of deformation gradient $\dot{\boldsymbol{F}} = \mathbf{grad}\, \boldsymbol{v}$ reduces to the scalar conservation law $\dot{\varepsilon} = \partial_x v$, so that (4.15) becomes

$$\begin{cases} \dot{\varepsilon} = \partial_x\, v\,, \\ \rho_0 \dot{v} = \partial_x \sigma + \boldsymbol{f}^v \cdot \boldsymbol{e}_1\,, \\ -\alpha \dot{g} = \phi_1'\, W + \phi_2'\,. \end{cases} \tag{4.17}$$

An example of strain energy density function is issued from the cubic polynomial law (2.22), where $W = \big(\frac{1}{2} - \frac{1}{3}\beta - \frac{1}{4}\delta\varepsilon^2\big) M_0\, \varepsilon^2$ is expressed in terms of Young's

modulus M_0 and the higher-order elastic constants β, δ. The relationship between the polynomial law and Murnaghan's law (2.16) is specified in Chapter 2. A similar analysis can be performed with the Mooney–Rivlin model (2.17) using Taylor series approximations.

1.2. Qualitative properties

In this subsection, some properties of the model related to the softening are detailed. In particular, the effect of the model parameters is illustrated, which is useful for quantitative validations.

1.2.a. *Analytical results*

From now on, the softening function (4.12) is used, i.e. $\phi_1(g) = 1 - g$. If a strain step is applied locally, then g is driven by (4.9), where the strain energy W is a constant. With the quadratic expression (4.13) of ϕ_2, the internal variable g evolves exponentially in time towards $g_{\text{eq}}(\chi)$, which is defined in (4.10). The corresponding relaxation time is $\tau_g = \alpha/\gamma$.

Now, the case of uniaxial strain is considered. A sinusoidal strain with frequency $f_c = \omega_c/2\pi = 1$ kHz and amplitude V is applied locally. With the quadratic expression (4.13) of ϕ_2, the evolution equation (4.9) writes

$$\begin{aligned} \dot{g}(t) + \frac{g(t)}{\tau_g} &= \frac{1}{\tau_\varepsilon} \frac{W(V\sin(\omega_c t))}{M_0 V^2}, \\ &= \frac{1}{\tau_\varepsilon} \left(\frac{a_0}{2} + \sum_{n=1}^{+\infty} a_n \cos(n\omega_c t) + b_n \sin(n\omega_c t) \right), \end{aligned} \tag{4.18}$$

where $\tau_\varepsilon = \alpha/(M_0 V^2)$ is a time constant and a_n, b_n are the Fourier coefficients of the normalized strain energy $W/(M_0 V^2)$. The solution of the ordinary differential equation (4.18) is

$$\begin{aligned} g(t) = &\left(g(0) - \frac{\tau_g}{\tau_\varepsilon} \left(\frac{a_0}{2} + \sum_{n=1}^{+\infty} \frac{a_n - n\omega_c \tau_g b_n}{1 + (n\omega_c \tau_g)^2} \right) \right) \exp(-t/\tau_g) \\ &+ \frac{\tau_g}{\tau_\varepsilon} \left(\frac{a_0}{2} + \sum_{n=1}^{+\infty} \frac{a_n - n\omega_c \tau_g b_n}{1 + (n\omega_c \tau_g)^2} \cos(n\omega_c t) + \frac{b_n + n\omega_c \tau_g a_n}{1 + (n\omega_c \tau_g)^2} \sin(n\omega_c t) \right). \end{aligned} \tag{4.19}$$

The first term in (4.19) decreases exponentially in time with constant τ_g. The second term is the steady-state term, which oscillates at the frequency f_c around its average value

$$\langle g \rangle_{t \gg \tau_g} = \frac{\tau_g}{\tau_\varepsilon} \frac{a_0}{2}, \tag{4.20}$$

where $\tau_g/\tau_\varepsilon = M_0 V^2/\gamma$. In the case of the polynomial law (2.22) with parameters β and δ, the nonzero Fourier coefficients are given in Table 4.1. The average of g (4.20) is

$$\langle g \rangle_{t \gg \tau_g} = \frac{M_0}{4\gamma} V^2 + O(V^4). \tag{4.21}$$

Table 4.1. Nonzero Fourier coefficients (4.18) in the case of the cubic polynomial law (2.22).

n	0	1	2	3	4
a_n	$\frac{1}{2} - \frac{3}{16}\delta V^2$		$-\frac{1}{4} + \frac{1}{8}\delta V^2$		$-\frac{1}{32}\delta V^2$
b_n		$-\frac{1}{4}\beta V$		$\frac{1}{12}\beta V$	

Table 4.2. Physical parameters.

ρ_0 (kg/m^3)	M_0 (GPa)	β	δ	γ (J/m^3)	α (J m^{-3} s)
2200	14	50	10^8	1.0	0.01

From a practical point of view, if the Young's modulus M_0 is known and the constants τ_g and $\langle g \rangle_{t \gg \tau_g}$ are deduced from measurements at small sinusoidal loadings, then the parameters α and γ of the model can be estimated.

As shown later on (Section 2), the speed of sound c satisfies $\rho_0 c^2 = (1 - g)\,\bar{\sigma}'(\varepsilon)$ in the case of uniaxial strain (1D). If the material is linear-elastic without slow dynamics, then $g = 0$ and $\bar{\sigma}'(\varepsilon) = M_0$, so that the speed of sound reduces to $c_0 = \sqrt{M_0/\rho_0}$. The relative variation of the effective elastic modulus $\rho_0 c^2$ with respect to the linear elastic case writes

$$\frac{\Delta M}{M} = \frac{\rho_0 c^2 - M_0}{M_0} = (1 - g)\,\frac{\bar{\sigma}'(\varepsilon)}{M_0} - 1\,. \tag{4.22}$$

Sometimes, the relative variation of the speed of sound $\Delta c/c = (c - c_0)/c_0$ is introduced instead (as is the case in Figure 1.2). From Taylor series approximations, one shows that the latter is related to (4.22) through $\Delta c/c \simeq \frac{1}{2}\Delta M/M$. If the cubic polynomial law (2.22) is used, then the relative variation of the elastic modulus is

$$\frac{\Delta M}{M} = (1 - g)\,(1 - 2\beta\varepsilon - 3\delta\varepsilon^2) - 1\,, \tag{4.23}$$

which reduces to $-g$ if β and δ equal zero. The average of $\Delta M/M$ over a period of forcing is deduced from (4.19) and (4.23):

$$\left\langle \frac{\Delta M}{M} \right\rangle_{t \gg \tau_g} = -\frac{M_0 + 6\delta\gamma}{4\gamma} V^2 + O(V^4)\,. \tag{4.24}$$

The diminution of the elastic modulus with the square of the strain amplitude is similar to the *Payne effect* of filled rubber [23, 103, 108].

On Figure 4.1a, $\Delta M/M$ is represented in the case of Hooke's law with the parameters from Table 4.2. In this softening phase, $\Delta M/M$ decreases and reaches the steady state. At $t = 50$ ms, the excitation is stopped. Thus, τ_ε goes to infinity in (4.19). During the recovery, $\Delta M/M$ increases exponentially in time towards zero with time constant $\tau_g = 10$ ms.

Figures 4.1b and 4.1c show the steady-state solution. On Figure 4.1b, $\Delta M/M$ is represented with respect to the strain for several forcing amplitudes, according to Equation (4.23) with $\beta = \delta = 0$. A hysteretic behavior caused by the dissipation

is observed. Figure 4.1c is an alternative representation of the phenomenon for several strain amplitudes. Here, the effect of increasing strain levels on the stress-strain relationship is outlined.

On Figure 4.2, the behavior of the model with the polynomial law (2.22) and $\beta = 50, \delta = 10^8$ is compared to the previous case of Hooke's law. On Figure 4.2a, the softening phases are compared. Figure 4.2b represents the hysteresis curves. More important variations of $\Delta M/M$ are observed in the case of the cubic polynomial law, as well as a loss of symmetry in the hysteresis curves. These phenomena are due to the dependence (4.23) of $\Delta M/M$ with the strain, when β and δ are nonzero. The contribution of β and δ in the Fourier coefficients is not significant at strain amplitudes $V \approx 10^{-6}$ (Table 4.1).

Supplementary analytical results can be obtained in the case of Hooke's law. In this case, the relative variation of the elastic modulus (4.23) is $\Delta M/M = -g$, and the only nonzero Fourier coefficients in Table 4.1 are a_0 and a_2. The surface area of the hysteresis loops in Figure 4.1b is

$$S_{\bowtie} = \frac{2}{3}\frac{\tau_g}{\tau_\varepsilon}\frac{2\omega_c\tau_g}{1+(2\omega_c\tau_g)^2}V = \frac{2}{3}\frac{2\omega_c\alpha}{\gamma^2+(2\omega_c\alpha)^2}M_0V^3, \tag{4.25}$$

which vanishes at high γ, low and high frequency f_c, and low and high α. This result was obtained by piecewise integration of the hysteresis curves. The maximum value reached by the steady-state solution is

$$g_{\max} = \frac{\tau_g}{4\tau_\varepsilon}\left(1+\frac{1}{\sqrt{1+(2\omega_c\tau_g)^2}}\right). \tag{4.26}$$

The strain amplitude $V_{\max}$ for which the material is destroyed satisfies $g_{\max} = 1$:

$$V_{\max} = \sqrt{\frac{2\gamma}{M_0}}\sqrt{\frac{2\sqrt{1+(2\omega_c\tau_g)^2}}{1+\sqrt{1+(2\omega_c\tau_g)^2}}}. \tag{4.27}$$

In the present configuration, $V_{\max} \approx 1.7\times10^{-5}$. Thus, if the quadratic expression (4.13) of the storage energy ϕ_2 is chosen, the model is only valid for small strains. Note that algebra mistakes have been found in the publication [1] and they are corrected here (4.25)-(4.26).

1.2.b. *Internal energy*

According to Eq. (4.3), the internal energy per unit volume is separated into two terms. One term corresponds to the strain energy $\phi_1 W$, the other term corresponds to the storage energy ϕ_2. When $g = 0$, the internal energy is only elastic. As g increases at constant strain, the strain energy decreases and the storage energy increases. Therefore, the internal energy is transferred from the strain to ϕ_2 when g increases, and inversely.

Let us assume that $\alpha = 0$. The internal variable satisfies $g = g_{\text{eq}}(\chi)$ (4.10). With the quadratic expression (4.13) of ϕ_2, the internal variable is equal to

$$g_{\text{eq}}(\chi) = \frac{W(\chi)}{\gamma}. \tag{4.28}$$

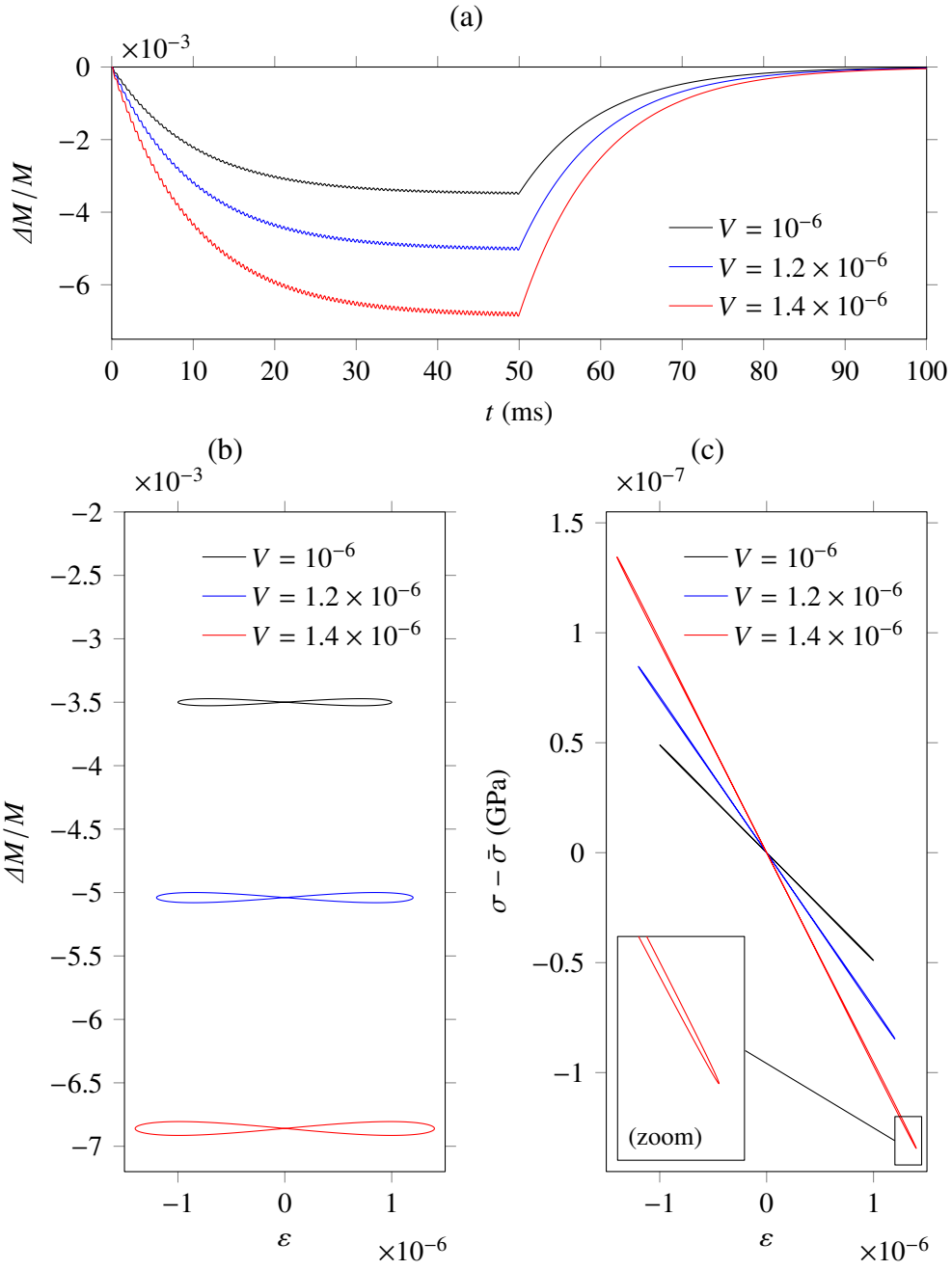

Figure 4.1. Analytical computation in the case of Hooke's law. (a) Evolution of the relative variation of the elastic modulus $\Delta M/M = -g$ with respect to its initial value, when a sinusoidal strain $\varepsilon = V \sin(\omega_c t)$ is applied until $t = 50$ ms (4.19). (b) Hysteresis curves $\Delta M/M$ versus ε in steady state ($\tau_g \ll t < 50$ ms); (c) Effect on the stress-strain relationship, where $\sigma - \bar{\sigma}$ is represented with respect to the strain ε.

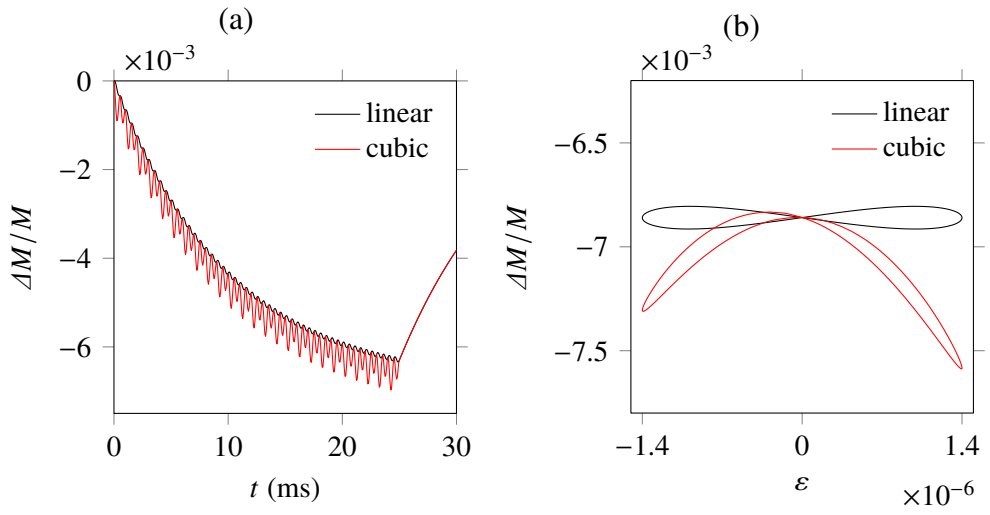

Figure 4.2. Comparison of the analytical computations in the cases of Hooke's law of linear elasticity and the cubic polynomial law. (a) Evolution of the relative variation $\Delta M/M$ of the elastic modulus when a sinusoidal strain with amplitude $V = 1.4 \times 10^{-6}$ is applied until $t = 25$ ms (4.19)-(4.23). (b) Hysteresis curves $\Delta M/M$ versus ε in steady state.

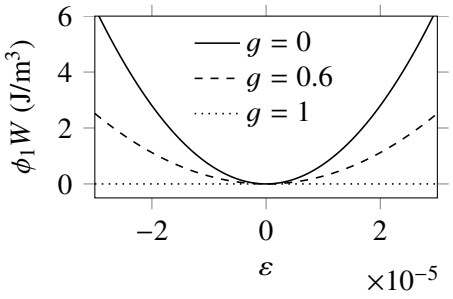

Figure 4.3. Sketch of the strain energy per unit volume $\phi_1 W = (1-g)\frac{1}{2}M_0\varepsilon^2$ with respect to the strain ε, for several values of the internal variable g.

The value $g = 1$, which corresponds to a destructed material, is reached for strain energies $W \geqslant \gamma$. In the case of Hooke's law with the parameters from Table 4.2, the maximum admissible strain is $\sqrt{2\gamma/M_0} \approx 1.2\times10^{-5}$. This value is recovered by setting $\tau_g = 0$ in Equation (4.27). The logarithmic expression (4.14) of ϕ_2 yields

$$g_{\text{eq}}(\chi) = \frac{2W(\chi)}{\gamma + \sqrt{\gamma^2 + 4W(\chi)^2}}, \tag{4.29}$$

which is always between zero and one. Therefore, there is no strain limit in this case.

Figure 4.3 represents the strain energy per unit volume $\phi_1 W$ when the geometry is 1D. The strain energy density function is issued from Hooke's law and the softening function (4.12) is used (parameters from Table 4.2). One can observe that the strain energy decreases as g increases. If $g = 1$, the strain energy does not depend on the strain anymore, which illustrates the destruction of the material.

On Figures 4.4a and 4.4b, the internal energy is represented with respect to g, where the quadratic expression (4.13) of the storage energy ϕ_2 is used. The values of g_{eq} correspond to the abscissas of the local minima of the curves (4.28). On Figure 4.4a, one can observe an increase in g_{eq} when the strain increases.

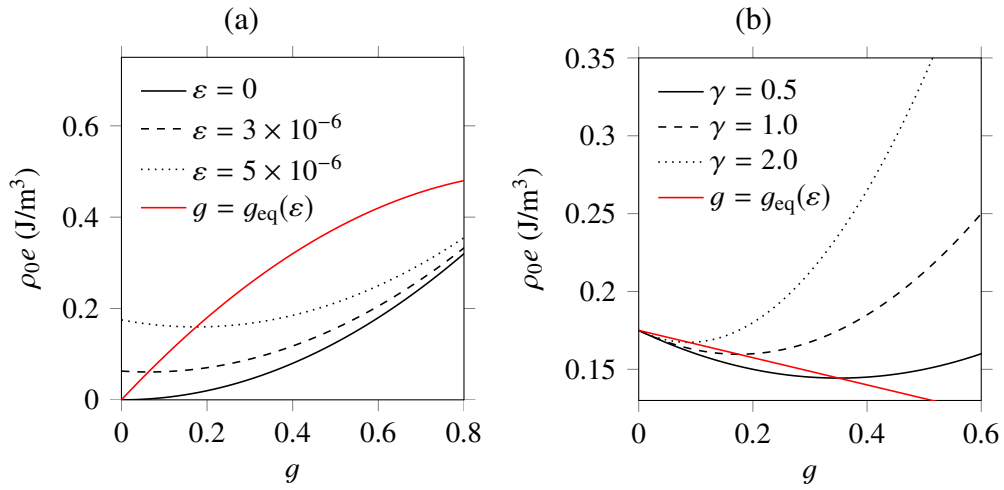

Figure 4.4. Sketch of the internal energy per unit volume $\rho_0 e$ with respect to g (4.3). It is represented (a) for several values of ε when $\gamma = 1.0$ J/m^3; (b) for several values of γ (J/m^3) when $\varepsilon = 5 \times 10^{-6}$.

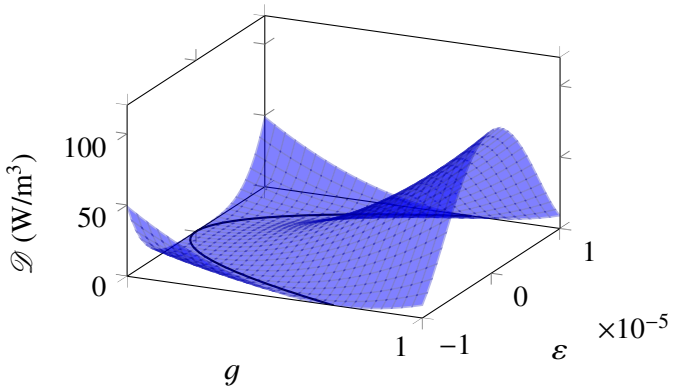

Figure 4.5. View of the dissipation $\mathscr{D}$ in ε-g coordinates (4.11). The black line marks the curve $g = g_{\text{eq}}(\varepsilon)$, i.e. the locus $\alpha = 0$ where no dissipation occurs (4.10).

No asymptote avoids to reach the value $g = 1$, which destroys the material. On Figure 4.4b, one can observe an increase in g_{eq} when γ decreases. Again, no asymptote avoids to reach the value $g = 1$, which destroys the material.

1.2.c. *Dissipation*

In one space dimension and small strain, $\mathscr{D}$ depends on ε and g. The dissipation per unit volume (4.11) is a surface in ε-g coordinates (Fig. 4.5). The expression of $\mathscr{D}$ is deduced from the softening function (4.12), the quadratic storage energy (4.13), Hooke's law and the conservation of mass $\rho_0/\rho = 1 + \varepsilon$. This figure illustrates that the dissipation is positive, in agreement with the Clausius–Duhem inequality. Also, one can observe that no dissipation occurs if $\alpha = 0$, which corresponds to the curve $g = g_{\text{eq}}(\varepsilon) = M_0\varepsilon^2/(2\gamma)$.

A new model for the dynamic behavior of solids has been proposed. The above analytical study shows that the model reproduces qualitatively the main features of real experiments. However, these computations have been carried out in a non-realistic configuration. To get closer to experimental configurations, we

develop 1D finite-volume methods with flux limiters, in a similar fashion as in Chapter 2.

2. Longitudinal waves

2.1. Governing equations

This section refers to the equations of motion in the uniaxial case (4.17). The variable g is added to the vector of unknowns $\boldsymbol{q}$, so that $\boldsymbol{q} = (\varepsilon, v, g)^\top$. The system of conservation laws (2.23) becomes a system of balance laws

$$\partial_t \boldsymbol{q} + \partial_x \boldsymbol{f}(\boldsymbol{q}) = \boldsymbol{r}(\boldsymbol{q}) + \boldsymbol{s}\,, \tag{4.30}$$

where

$$\begin{aligned} \boldsymbol{f}(\boldsymbol{q}) &= -\left(v, \sigma/\rho_0, 0\right)^\top, \\ \boldsymbol{r}(\boldsymbol{q}) &= -\frac{1}{\alpha}\left(0, 0, \phi_1'(g)W(\varepsilon) + \phi_2'(g)\right)^\top, \\ \boldsymbol{s} &= \frac{1}{\rho_0}\left(0, \boldsymbol{f}^v \cdot \boldsymbol{e}_1, 0\right)^\top, \end{aligned} \tag{4.31}$$

where the stress satisfies $\sigma = \phi_1(g)W'(\varepsilon)$. The Jacobian matrix $\boldsymbol{f}'(\boldsymbol{q})$ of $\boldsymbol{f}$ has the eigenvalues $\{-c(\boldsymbol{q}), c(\boldsymbol{q}), 0\}$, where

$$c(\boldsymbol{q}) = \sqrt{\phi_1(g)W''(\varepsilon)/\rho_0} \tag{4.32}$$

is the speed of sound. The speed of sound (4.32) is real and nonzero — in other words, the system (4.30) is strictly hyperbolic — provided that $\phi_1(g) > 0$ and $W''(\varepsilon) > 0$. The first condition implies that $g < 1$ in the case $\phi_1(g) = 1 - g$ (4.12). The second condition is already required in the elastic case (2.23), where the speed of sound (2.26) is equal to $\sqrt{W''(\varepsilon)/\rho_0}$.

Now let us examine the spectrum of the relaxation function in (4.30). The Jacobian matrix $\boldsymbol{r}'(\boldsymbol{q})$ of $\boldsymbol{r}$ has the eigenvalues $\{0, 0, -(\phi_1''(g)W(\varepsilon) + \phi_2''(g))/\alpha\}$. Therefore, if we follow (4.12)-(4.14) by setting $\phi_1(g) = 1 - g$ and by choosing a convex function for $\phi_2(g)$, then the Jacobian matrix $\boldsymbol{r}'(\boldsymbol{q})$ is negative semi-definite. Moreover, its spectral radius is

$$\Upsilon = \frac{\left|\phi_1''(g)W(\varepsilon) + \phi_2''(g)\right|}{\alpha}, \tag{4.33}$$

which reduces to $\Upsilon = \gamma/\alpha + O(g^2)$ in the case of (4.12)-(4.14). One recognizes the inverse of the relaxation time $\tau_g = \alpha/\gamma$, which is characteristic of the slow dynamics [1] (cf. Section 1.2).

2.2. Numerical resolution

2.2.a. *Finite-volume method*

It is now assumed that $\phi_1(g) = 1 - g$ (4.12). Applying the same explicit time-stepping formula as (2.43) to (4.30) yields

$$\boldsymbol{q}_i^{n+1} = \boldsymbol{q}_i^n - \frac{\Delta t}{\Delta x}\left(\boldsymbol{f}_{i+1/2}^n - \boldsymbol{f}_{i-1/2}^n\right) + \Delta t\left(\boldsymbol{r}(\boldsymbol{q}_i^n) + \boldsymbol{s}_i^n\right), \tag{4.34}$$

where the numerical flux $\boldsymbol{f}_{i+1/2}^n$ is specified later on. Numerical stability imposes a bound of the form

$$\Delta t \leqslant \min\left\{\frac{\Delta x}{c_{\max}^n}, \frac{2}{\Upsilon_{\max}^n}\right\}, \tag{4.35}$$

where $c_{\max}^n$ is the maximum sound velocity (4.32) that is encountered at time t_n, and $\Upsilon_{\max}^n$ is the maximum spectral radius of the relaxation function (4.33). Since the relaxation time of the slow dynamics is much larger than the period of exciting signals, the condition (4.35) reduces to the classical CFL condition $\mathrm{Co} \leqslant 1$ (2.44) with the Courant number $\mathrm{Co} = c_{\max}^n \Delta t/\Delta x$.

If the constitutive law $\varepsilon \mapsto W'(\varepsilon)$ is convex or concave, then the maximum sound speed at time t_n is given by $c_{\max}^n = \max_{0\leqslant i\leqslant N_x} c(\boldsymbol{q}_i^n)$, with the sound speed (4.32). If the constitutive law is neither convex nor concave, then the maximum sound speed becomes

$$c_{\max}^n = \max_{0\leqslant i<N_x} \sqrt{\frac{1 - \min\{g_i^n, g_{i+1}^n\}}{\rho_0} \max_{\varepsilon\in\mathcal{D}_i} W''(\varepsilon)}\,, \tag{4.36}$$

where $\mathcal{D}_i$ is the interval with bounds ε_i^n and ε_{i+1}^n. One can remark that the expression (2.45) of the elastic case is recovered if $g \equiv 0$.

■ *Roe linearization.* In this subsection, we derive the flux-limiter method with Roe linearization, in a similar fashion as in Section 2 of Chapter 2. For the system (4.30) with $\phi_1(g) = 1 - g$, the following matrix is obtained from (2.49):

$$\boldsymbol{A}_{i+1/2} = \begin{pmatrix} 0 & -1 & 0 \\ -a_{i+1/2}^n & 0 & b_{i+1/2}^n \\ 0 & 0 & 0 \end{pmatrix}, \tag{4.37}$$

where

$$\begin{aligned} a_{i+1/2}^n &= \frac{\sigma_{i+1}^n - \sigma_i^n}{\rho_0\,(\varepsilon_{i+1}^n - \varepsilon_i^n)} + \frac{g_{i+1}^n - g_i^n}{\varepsilon_{i+1}^n - \varepsilon_i^n} b_{i+1/2}^n, \\ b_{i+1/2}^n &= \frac{W(\varepsilon_{i+1}^n) - W(\varepsilon_i^n)}{\rho_0\,(\varepsilon_{i+1}^n - \varepsilon_i^n)}, \end{aligned} \tag{4.38}$$

and the stresses are $\sigma_i^n = (1 - g_i^n)\,W'(\varepsilon_i^n)$. To avoid divisions by zero when $\varepsilon_i^n = \varepsilon_{i+1}^n$, one computes

$$\begin{aligned} a_{i+1/2}^n &= \left(1 - \frac{g_i^n + g_{i+1}^n}{2}\right)\frac{W''(\varepsilon_i^n)}{\rho_0}, \\ b_{i+1/2}^n &= \frac{W'(\varepsilon_i^n)}{\rho_0}, \end{aligned} \tag{4.39}$$

in this particular case.

The eigenvalues of the matrix (4.37) with the coefficients (4.38)-(4.39) are $\{-s^n_{i+1/2}, s^n_{i+1/2}, 0\}$, where $s^n_{i+1/2} = \sqrt{a^n_{i+1/2}}$. We rewrite the coefficient $a^n_{i+1/2}$ from (4.38) as

$$a^n_{i+1/2} = \frac{W'(\varepsilon^n_{i+1}) - W'(\varepsilon^n_i)}{\rho_0\,(\varepsilon^n_{i+1} - \varepsilon^n_i)} - g^n_i \frac{W(\varepsilon^n_{i+1}) - W(\varepsilon^n_i) - W'(\varepsilon^n_i)(\varepsilon^n_{i+1} - \varepsilon^n_i)}{\rho_0\,(\varepsilon^n_{i+1} - \varepsilon^n_i)^2} - g^n_{i+1} \frac{W(\varepsilon^n_i) - W(\varepsilon^n_{i+1}) - W'(\varepsilon^n_{i+1})(\varepsilon^n_i - \varepsilon^n_{i+1})}{\rho_0\,(\varepsilon^n_{i+1} - \varepsilon^n_i)^2}. \tag{4.40}$$

One can note that the first term in (4.40) corresponds to the elastic case. Moreover, the next terms vanish when $g^n_i = 0 = g^n_{i+1}$, i.e. when no softening occurs. Since the strain energy function W is convex and $g < 1$ over the hyperbolicity domain, the coefficient $a^n_{i+1/2}$ in (4.40) is positive. Finally, the eigenvalue $s^n_{i+1/2}$ is real, and the matrix (4.37) is a Roe matrix for the system (4.30).

Similarly to the elastic case (2.53), we introduce the left and right eigenvectors of the matrix $\boldsymbol{A}_{i+1/2}$

$$\begin{aligned}
\boldsymbol{r}^1_{i+1/2} &= \begin{pmatrix} 1 \\ s^n_{i+1/2} \\ 0 \end{pmatrix}, & \boldsymbol{l}^1_{i+1/2} &= \frac{1}{2}\begin{pmatrix} 1 \\ 1/s^n_{i+1/2} \\ -b^n_{i+1/2}/a^n_{i+1/2} \end{pmatrix}, \\
\boldsymbol{r}^2_{i+1/2} &= \begin{pmatrix} 1 \\ -s^n_{i+1/2} \\ 0 \end{pmatrix}, & \boldsymbol{l}^2_{i+1/2} &= \frac{1}{2}\begin{pmatrix} 1 \\ -1/s^n_{i+1/2} \\ -b^n_{i+1/2}/a^n_{i+1/2} \end{pmatrix}, \\
\boldsymbol{r}^3_{i+1/2} &= \begin{pmatrix} b^n_{i+1/2}/a^n_{i+1/2} \\ 0 \\ 1 \end{pmatrix}, & \boldsymbol{l}^3_{i+1/2} &= \begin{pmatrix} 0 \\ 0 \\ 1 \end{pmatrix}.
\end{aligned} \tag{4.41}$$

Note that there may be numerical issues with the eigenvectors in [4] (divisions by possibly small numbers), thus it is recommended to use (4.41). Now, the jump $\boldsymbol{q}^n_{i+1} - \boldsymbol{q}^n_i$ is decomposed in the basis of right eigenvectors of the Roe matrix in a similar manner as (2.59). Since the eigenvalue corresponding to $k = 3$ in the decomposition is zero, the vector $\boldsymbol{\mathcal{W}}^3_{i+1/2}$ defined in (2.60) does not appear in the numerical flux $\boldsymbol{f}^n_{i+1/2}$ of the flux-limiter method (2.58). Therefore, the formulas (2.58) to (2.64) can be applied without modification to compute $\boldsymbol{f}^n_{i+1/2}$, using the vectors $\boldsymbol{\mathcal{W}}^1_{i+1/2}$ and $\boldsymbol{\mathcal{W}}^2_{i+1/2}$ deduced from (2.60)-(4.41), and the eigenvalue $s^n_{i+1/2}$ deduced from (4.38)-(4.39). The data is then updated according to (4.34).

2.3. Numerical experiments

In the following examples, we have $\phi_1(g) = 1 - g$, $\phi_2(g) = -\frac{1}{2}\gamma \ln(1 - g^2)$, and $W(\varepsilon) = \left(\frac{1}{2} - \frac{1}{3}\beta\varepsilon - \frac{1}{4}\delta\varepsilon^2\right) M_0\,\varepsilon^2$. The Courant number is set to Co = 0.95. The numerical domain is defined by $[x_0, x_{N_x}] = [-0.5, 0.5]$ m. The physical parameters of the model are given in Table 4.2.

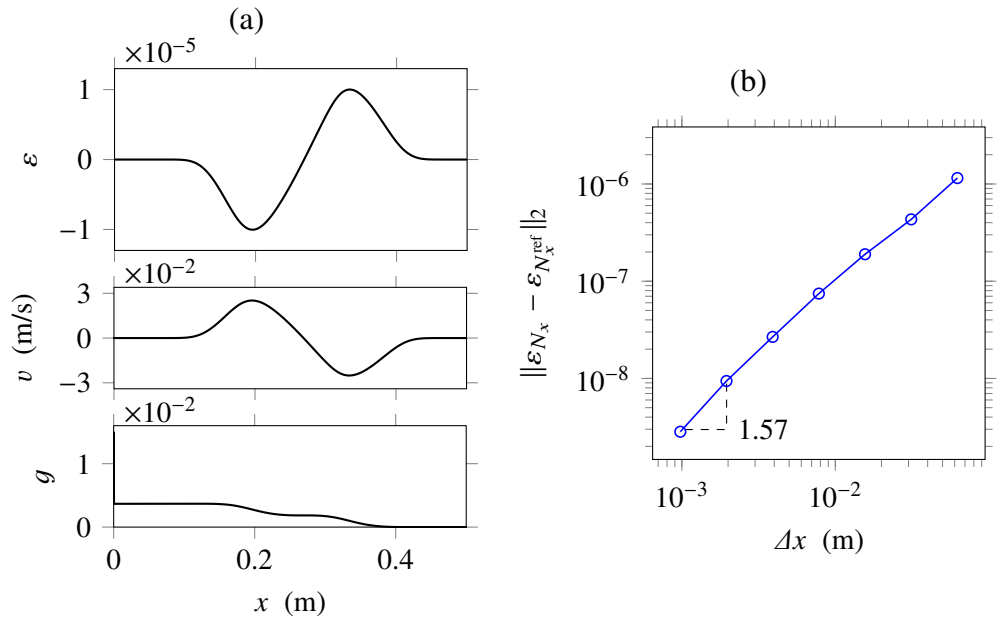

Figure 4.6. Assessment of the numerical method's convergence on the propagation of a smooth pulse. (a) Reference solution at $t = 0.19$ ms: strain, particle velocity, and softening variable. (b) Error measurement.

2.3.a. *Pulse propagation*

The initial data is zero, and a point load $\boldsymbol{f}^v = \delta_s(x)\varphi(t)\,\boldsymbol{e}_1$ located at the abscissa $x_s = 0$ generates a smooth pulse with angular frequency $\omega_c = 2\pi f_c$, with $f_c = 6$ kHz. The source signal in (4.30) satisfies

$$\varphi(t) = 2M_0V \sum_{i=0}^{3} \frac{a_i}{a} \sin(2^i \omega_c t), \tag{4.42}$$

where $V = 10^{-5}$, $a_0 = 1$, $a_1 = -21/32$, $a_2 = 63/768$, $a_3 = -1/512$, and $a \simeq 1.507$ is a normalization coefficient. It is turned on from $t = 0$ to $t = 1/f_c$, which corresponds to one fundamental period. Chosen for the smoothness of its time-evolution (4.42), the point source generates left-going and right-going waves with strain amplitude V.

The reference solution is an oversampled numerical solution (4.34) computed at $t = 0.19$ ms on a grid with $N_x^{\text{ref}} = 2^{15}$ points (Figure 4.6a). The pulse injected at $x_s = 0$ has propagated towards both increasing and decreasing x. By symmetry, only the right-going part is displayed here. No shock wave is observed: the waveform is slightly distorted but keeps smooth. Figure 4.6b illustrates the convergence of the numerical method. For a given coarse spatial discretization where $N_x \ll N_x^{\text{ref}}$, the numerical solution is computed up to $t \approx 0.19$ ms, and is compared to the reference numerical solution at the same final time. The evolution of the L^2 global error between both strain waveforms is represented in Figure 4.6b with respect to $\Delta x = 1/N_x$. One can observe that the order of convergence is between one and two.

2.3.b. *Dynamic acousto-elasticity*

The setup is the same as in the previous section, but here, the point load generates a sinusoidal strain with amplitude $V \approx 10^{-6}$ and angular frequency $\omega_c = 2\pi f_c$, with $f_c = 5$ kHz:

$$\varphi(t) = 2M_0 V \sin(\omega_c t)\,. \tag{4.43}$$

The source (4.43) is turned on from $t = 0$ to $t = 40$ ms, which corresponds to 200 periods of signal. A receiver records the numerical solution at the abscissa $x_r = 0.3$ m.

The numerical solution (4.34) is computed up to $t = 80$ ms on a grid with $N_x = 80$ points, which corresponds to 40 points per wavelength at the angular frequency ω_c. The computations are performed in C++. Each simulation lasts around 1.5 s, when a recent desktop computer is used (Intel Core i5-4690, 3.5 GHz, 16 Go, 2015). Figure 4.7a displays the strain ε and the variation of the elastic modulus $\Delta M/M$ (4.22) deduced from the sound speed (4.32), which are recorded at the position x_r of the receiver. A slow decrease of the elastic modulus combined with fast oscillations is observed until the source is stopped. Simultaneously, the strain signals are smooth sinusoids, so that $N_x = 80$ is sufficient. After the source is stopped, the elastic modulus recovers slowly its initial value, while the strain is equal to zero.

Figure 4.7b focuses on the steady-state solution. Here, the last 80 numerical values before $t = 40$ ms are used, which corresponds to two periods of signal at the frequency f_c. When $\Delta M/M$ from (4.22) is represented with respect to the strain recorded at the position of the receiver x_r, a hysteresis curve is obtained. The orders of magnitude of these phenomena — duration of the transients, magnitude of the softening, size and shape of the hysteresis curves — are very similar to those reported in [117] for Berea sandstone. In particular, one can note that the average softening $\langle \Delta M/M \rangle$ is proportional to V^2, as predicted in [1]. However, only qualitative agreement with Figure 5a of [117] is obtained.

We have shown how to include the slow dynamics in finite-volume methods under the uniaxial strain assumption (1D). The next section is devoted to the plane-strain case (2D). Here, finite-volume methods are implemented dimension by dimension using dimensional splitting. As in the one-dimensional case, the numerical method is well-suited to the computation of nonlinear waves in the Lagrangian framework. Moreover, it can be used for various hyperelastic material models (see e.g. the related study [17] and references therein).

3. Plane-strain waves

3.1. Governing equations

To derive the equations of plane-strain elastodynamics with softening, we go back to the isotropic case detailed in Section 1. The equations of motion are specified in (4.15), and the Piola–Kirchhoff stress tensor $\boldsymbol{P} = \phi_1(g)\,\boldsymbol{F} \cdot \partial W/\partial \boldsymbol{E}$ is given in (4.16). Here, the strain energy density function of Murnaghan's law

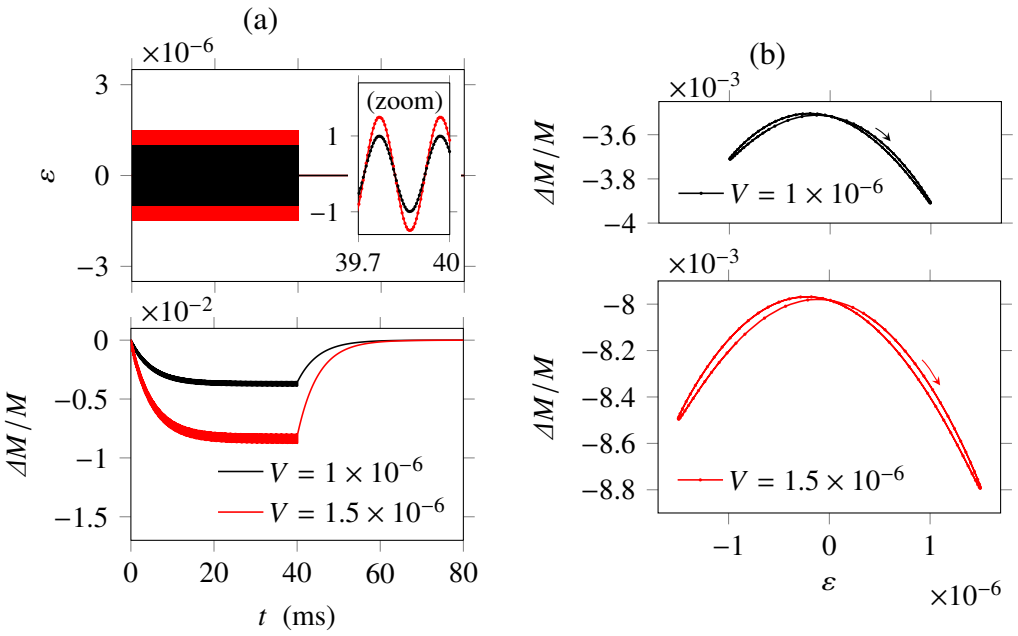

Figure 4.7. (a) Strain signal and softening of the material, as recorded by the receiver at the abscissa $x_r = 0.3$ m. (b) Hysteresis curves in steady-state. The arrow indicates how time increases along the curve.

(2.16) is used [91], which is expressed as a function of the strain invariants $E_{\mathrm{I}} = \operatorname{tr} \boldsymbol{E}$, $E_{\mathrm{II}} = \frac{1}{2}\big((\operatorname{tr} \boldsymbol{E})^2 - \operatorname{tr}(\boldsymbol{E}^2)\big)$, $E_{\mathrm{III}} = \det \boldsymbol{E}$ of the Green–Lagrange strain tensor $\boldsymbol{E}$. The model has five elastic constants: the Lamé parameters λ, μ, and the Murnaghan coefficients $\mathfrak{l}$, $\mathfrak{m}$, $\mathfrak{n}$.

3.1.a. *The plane-strain assumption*

The displacement field $\boldsymbol{u}$ is independent on z, and its component u_3 along $\boldsymbol{e}_3$ is zero. In the basis of unit tensors $(\boldsymbol{e}_i \otimes \boldsymbol{e}_j)_{1 \leqslant i,j \leqslant 3}$, the matrix of coordinates of the displacement gradient $\mathbf{grad}\, \boldsymbol{u}$ is therefore

$$\big(u_{i,j}\big) = \begin{pmatrix} u_{1,1} & u_{1,2} & 0 \\ u_{2,1} & u_{2,2} & 0 \\ 0 & 0 & 0 \end{pmatrix}. \tag{4.44}$$

Using the Einstein notation with indices in $\{1, 2\}$, the coordinates of the Green–Lagrange tensor (2.9) write $E_{ij} = \frac{1}{2}\big(u_{i,j} + u_{j,i} + u_{p,i}u_{p,j}\big)$. Its invariants are $E_{\mathrm{I}} = E_{nn}$, $E_{\mathrm{II}} = \frac{1}{2}\big({E_{\mathrm{I}}}^2 - E_{ij}E_{ij}\big) = \epsilon_{ij}E_{1i}E_{2j}$ and $E_{\mathrm{III}} = 0$, where ϵ_{ij} is the Levi-Civita symbol of $\mathbb{R}^2$. The Cayley–Hamilton theorem applied to the restriction of $\boldsymbol{E}$ to $\mathbb{R}^2 \times \mathbb{R}^2$ reads $E_{im}E_{mj} - E_{\mathrm{I}}E_{ij} + E_{\mathrm{II}}\delta_{ij} = 0$, where δ_{ij} is the Kronecker delta. Hence, the expression $\partial W/\partial \boldsymbol{E} = \alpha_0 \boldsymbol{I} + \alpha_1 \boldsymbol{E} + \alpha_2 \boldsymbol{E}^2$ of the strain energy's tensor derivative (2.14) becomes

$$\frac{\partial W}{\partial E_{ij}} = \tilde{\alpha}_0 \delta_{ij} + \tilde{\alpha}_1 E_{ij} \tag{4.45}$$

in the basis of unit tensors $(\boldsymbol{e}_i \otimes \boldsymbol{e}_j)_{1\leqslant i,j\leqslant 2}$. The corresponding coefficients deduced from (2.16) are

$$\begin{aligned} \tilde{\alpha}_0 &= \alpha_0 - \alpha_2 E_{\mathrm{II}} \quad &&= \lambda E_{\mathrm{I}} + \mathfrak{l} {E_{\mathrm{I}}}^2 - 2\mathfrak{m} E_{\mathrm{II}}\,, \\ \tilde{\alpha}_1 &= \alpha_1 + \alpha_2 E_{\mathrm{I}} \quad &&= 2\,(\mu + \mathfrak{m} E_{\mathrm{I}})\,. \end{aligned} \tag{4.46}$$

The coordinates P_{ij} of the first Piola–Kirchhoff stress tensor $\boldsymbol{P}$ in (4.16) are therefore

$$P_{ij} = \phi_1(g)\left(\delta_{im} + u_{i,m}\right)\left(\tilde{\alpha}_0 \delta_{mj} + \tilde{\alpha}_1 E_{mj}\right) \tag{4.47}$$

under the plane strain assumption, which does not depend upon the third Murnaghan coefficient $\mathfrak{n}$.

When the geometric nonlinearities are negligible, the coordinates E_{ij} of $\boldsymbol{E}$ are replaced by the coordinates $\varepsilon_{ij} = \frac{1}{2}\left(u_{i,j} + u_{j,i}\right)$ of $\boldsymbol{\varepsilon}$. Moreover, the first Piola–Kirchhoff stress tensor $\boldsymbol{P}$ is linearized with respect to $\mathbf{grad}\,\boldsymbol{u}$ too, i.e. $\boldsymbol{F}\cdot\partial W/\partial \boldsymbol{E} \simeq \partial W/\partial \boldsymbol{\varepsilon}$. Hence, the equation $P_{ij} = \phi_1(g)\left(\tilde{\alpha}_0\delta_{ij} + \tilde{\alpha}_1\varepsilon_{ij}\right)$ replaces (4.47). Under this assumption, linear elastodynamics is recovered if $g \equiv 0$ (i.e., $\alpha \longrightarrow +\infty$ in the evolution of g (4.9)), and if the Murnaghan coefficients $\mathfrak{l}$, $\mathfrak{m}$ in (4.46) are zero (see Appendix, Sec. 5.2 for details).

3.1.b. *System of balance laws*

Under the plane-strain assumption, the equations of motion (4.15) write as a two-dimensional system of balance laws

$$\partial_t \boldsymbol{q} + \partial_x \boldsymbol{f}(\boldsymbol{q}) + \partial_y \boldsymbol{g}(\boldsymbol{q}) = \boldsymbol{r}(\boldsymbol{q}) + \boldsymbol{s}\,, \tag{4.48}$$

where $\boldsymbol{q} = (u_{1,1}, u_{1,2}, u_{2,1}, u_{2,2}, v_1, v_2, g)^\top$ is the vector of unknowns. The expressions of the flux functions, the relaxation function and the source term are

$$\begin{aligned} \boldsymbol{f}(\boldsymbol{q}) &= -\Big(v_1, 0, v_2, 0, P_{11}/\rho_0, P_{21}/\rho_0, 0\Big)^\top, \\ \boldsymbol{g}(\boldsymbol{q}) &= -\Big(0, v_1, 0, v_2, P_{12}/\rho_0, P_{22}/\rho_0, 0\Big)^\top, \\ \boldsymbol{r}(\boldsymbol{q}) &= -\frac{1}{\alpha}\Big(0, 0, 0, 0, 0, 0, \phi_1'(g)W + \phi_2'(g)\Big)^\top, \\ \boldsymbol{s} &= \frac{1}{\rho_0}\Big(0, 0, 0, 0, \boldsymbol{f}^v\cdot\boldsymbol{e}_1, \boldsymbol{f}^v\cdot\boldsymbol{e}_2, 0\Big)^\top. \end{aligned} \tag{4.49}$$

In (4.49), the Piola–Kirchhoff stress components $(P_{ij})_{1\leqslant i,j\leqslant 2}$ depend on $(u_{i,j})_{1\leqslant i,j\leqslant 2}$ and g according to (4.47). The strain energy W depends on $(u_{i,j})_{1\leqslant i,j\leqslant 2}$ according to (2.16).

The Jacobian matrix of the flux component $\boldsymbol{f}$ along the x-axis is

$$\boldsymbol{f}'(\boldsymbol{q}) = -\begin{pmatrix} & & & & 1 & 0 & 0 \\ & & & & 0 & 0 & 0 \\ & & & & 0 & 1 & 0 \\ & & & & 0 & 0 & 0 \\ Q_{1111} & Q_{1112} & Q_{1121} & Q_{1122} & 0 & 0 & G_{11} \\ Q_{2111} & Q_{2112} & Q_{2121} & Q_{2122} & 0 & 0 & G_{21} \\ 0 & 0 & 0 & 0 & 0 & 0 & 0 \end{pmatrix}, \tag{4.50}$$

Table 4.3. Physical parameters of concrete.

ρ_0 (kg m^{-3})	λ (GPa)	μ (GPa)	l (GPa)	m (GPa)	γ (J m^{-3})	α (J m^{-3} s)
2400	12.7	17.5	−3007	−2283	4.0×10^{-2}	2.0×10^{-6}

where only three strips are displayed (everywhere else, the coefficients in the matrix are zero). The expression of the coefficients $Q_{ijk\ell}$ in (4.50) defined by $\rho_0 Q_{ijk\ell} = \partial P_{ij}/\partial u_{k,\ell}$ is detailed in the Appendix, Sec. 5.2, as well as the expression of the coefficients G_{ij} defined by $\rho_0 G_{ij} = \partial P_{ij}/\partial g$. A similar Jacobian matrix $\boldsymbol{g}'(\boldsymbol{q})$ is obtained for the flux component $\boldsymbol{g}$ along the y-axis. These matrices are diagonalized in the Appendix 5.2. The spectrum of both matrices has the form $\{-c_P, c_P, -c_S, c_S, 0, 0, 0\}$. In the case of Murnaghan hyperelasticity, the eigenvalues c_P, c_S can be complex [4], so that the system (4.48)-(4.49) is only conditionally hyperbolic (see e.g. [96] for discussions on hyperbolicity in hyperelasticity). Here, we restrict ourselves to configurations where the eigenvalues $c_P > c_S > 0$ are real. Thus, c_P and c_S correspond to the velocities of compression waves and shear waves, respectively.

■ *Plane waves.* We assume furthermore that the displacement field is invariant along a direction, say $\boldsymbol{e}_2$, so that $\boldsymbol{u}$ does not depend on y. In this case, the vector of unknown reduces to $\boldsymbol{q} = (u_{1,1}, u_{2,1}, v_1, v_2, g)^\top$ — the second and fourth rows of (4.48)-(4.49) are zero — and the flux $\boldsymbol{g}$ along y is zero. The Jacobian matrix $\boldsymbol{f}'(\boldsymbol{q})$ is obtained from (4.50) by removing the second and fourth rows, as well as the second and fourth columns. Doing so, two zero eigenvalues are removed from the spectrum, which reduces to $\{-c_P, c_P, -c_S, c_S, 0\}$.

We consider the case of Murnaghan material $g \equiv 0$, with the parameters in Table 4.3. The latter, found in [106], have been measured on concrete. Let us introduce the relative variation $\Delta c/c$ of the sound velocities c_P and c_S with respect to the case of Hooke's law, where $c_P = \sqrt{(\lambda + 2\mu)/\rho_0} \approx 4458$ m/s and $c_S = \sqrt{\mu/\rho_0} \approx 2700$ m/s. Fig. 4.8 displays the evolution of $\Delta c/c$ with respect to the compression strain $u_{1,1}$, when the shear strain $u_{2,1}$ is set to zero. One observes that the variations of c_P with respect to $u_{1,1}$ are much larger than the variations of c_S. This is confirmed by the Taylor series approximations

$$\begin{aligned}(\Delta c/c)_P &= \left(\frac{3}{2} + \frac{\mathrm{l} + 2\mathrm{m}}{\lambda + 2\mu}\right) u_{1,1} + O({u_{1,1}}^2) + O({u_{2,1}}^2) \approx -157\, u_{1,1}\,,\\ (\Delta c/c)_S &= \left(\frac{\lambda + 2\mu}{2\mu} + \frac{\mathrm{m}}{2\mu}\right) u_{1,1} + O({u_{1,1}}^2) + O({u_{2,1}}^2) \approx -63.8\, u_{1,1}\,,\end{aligned} \tag{4.51}$$

represented as dotted lines in Fig. 4.8. These approximations show also that the shear strain $u_{2,1}$ has much less influence than the compression strain $u_{1,1}$ on the variations of the sound velocities.

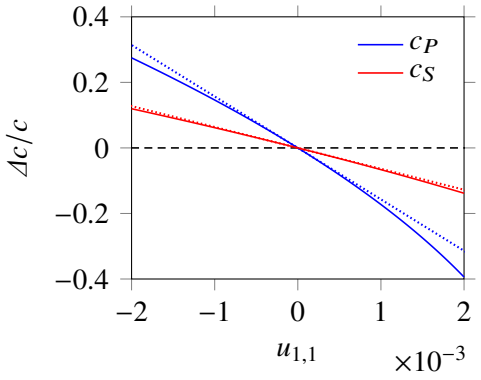

Figure 4.8. Murnaghan hyperelasticity ($g \equiv 0$). Relative variation $\Delta c/c$ of the speeds c_P and c_S of compressional and shear waves with respect to the case of Hooke's law. The variation $\Delta c/c$ is represented with respect to the compression strain $u_{1,1}$, and the shear strain is $u_{2,1} = 0$. The dotted lines mark Taylor series approximations (4.51).

3.2. Numerical resolution

3.2.a. *Numerical strategy*

We consider a finite numerical domain $[0, L_x] \times [0, L_y]$. It is discretized using a regular grid in space with mesh size Δx in the x direction, and Δy in the y direction. The coordinates of the nodes are $(x_i, y_j) = (i\,\Delta x, j\,\Delta y)$, where $0 \leqslant i \leqslant N_x$ and $0 \leqslant j \leqslant N_y$. The total number of nodes is $(N_x + 1) \times (N_y + 1)$, where $N_x = L_x/\Delta x$ and $N_y = L_y/\Delta y$. A variable time step $\Delta t = t_{n+1} - t_n$ is introduced. Therefore, $\boldsymbol{q}(x_i, y_j, t_n)$ denotes the solution to (4.48) at the grid node (i, j) and at the nth time step. Numerical approximations of the solution are denoted by $\boldsymbol{q}^n_{i,j} \simeq \boldsymbol{q}(x_i, y_j, t_n)$.

The non-homogeneous system of balance laws (4.48) is integrated explicitly in time:

$$\boldsymbol{q}^{n+1}_{i,j} = \boldsymbol{q}^n_{i,j} + \Delta \boldsymbol{q}^n_{\mathrm{FV}} + \Delta t \left(\boldsymbol{r}(\boldsymbol{q}^n_{i,j}) + \boldsymbol{s}^n_{i,j} \right), \tag{4.52}$$

where the approximation $\boldsymbol{s}^n_{i,j}$ of the source term $\boldsymbol{s}$ is specified later on. The increment $\Delta \boldsymbol{q}^n_{\mathrm{FV}}$ is deduced from the integration of $\partial_t \boldsymbol{q} + \partial_x \boldsymbol{f}(\boldsymbol{q}) + \partial_y \boldsymbol{g}(\boldsymbol{q}) = \boldsymbol{0}$ over one time step. Usually, one has $\Delta \boldsymbol{q}^n_{\mathrm{FV}} = (\mathcal{H}_x + \mathcal{H}_y - 2)\, \boldsymbol{q}^n_{i,j}$, where the discrete operators

$$\begin{aligned} \mathcal{H}_x \boldsymbol{q}^n_{i,j} &= \boldsymbol{q}^n_{i,j} - \frac{\Delta t}{\Delta x} \left(\boldsymbol{f}^n_{i+1/2,j} - \boldsymbol{f}^n_{i-1/2,j} \right), \\ \mathcal{H}_y \boldsymbol{q}^n_{i,j} &= \boldsymbol{q}^n_{i,j} - \frac{\Delta t}{\Delta y} \left(\boldsymbol{g}^n_{i,j+1/2} - \boldsymbol{g}^n_{i,j-1/2} \right), \end{aligned} \tag{4.53}$$

involve the fluxes $\boldsymbol{f}^n_{i+1/2,j}$, $\boldsymbol{g}^n_{i+1/2,j}$ of a 2D finite-volume scheme [69] (cf. Appendix, Sec. 5.2). Here, a second-order symmetric dimensional splitting [130] is used instead. That is to say, $\mathcal{H}_x$ and $\mathcal{H}_y$ correspond to the integration of $\partial_t \boldsymbol{q} + \partial_x \boldsymbol{f}(\boldsymbol{q}) = \boldsymbol{0}$ and $\partial_t \boldsymbol{q} + \partial_y \boldsymbol{g}(\boldsymbol{q}) = \boldsymbol{0}$ over one time step, so that (4.53) involves the fluxes $\boldsymbol{f}^n_{i+1/2,j}$, $\boldsymbol{g}^n_{i+1/2,j}$ of a 1D finite-volume scheme. The increment $\Delta \boldsymbol{q}^n_{\mathrm{FV}}$ is computed according to

$$\Delta \boldsymbol{q}^n_{\mathrm{FV}} = \frac{1}{2} \left(\mathcal{H}_x \mathcal{H}_y + \mathcal{H}_y \mathcal{H}_x - 2 \right) \boldsymbol{q}^n_{i,j}, \tag{4.54}$$

where $\mathcal{H}_x \mathcal{H}_y$ denotes the composition of the operators $\mathcal{H}_x$ and $\mathcal{H}_y$.

The numerical fluxes in (4.53)-(4.54) are computed according to the flux-limiter method [4, 69] described in the next subsection. This finite-volume

scheme is well-suited for nonlinear wave propagation and second-order accurate. The operators $\mathcal{H}_x$ and $\mathcal{H}_y$ are stable under the Courant–Friedrichs–Lewy (CFL) condition

$$\mathrm{Co} = \max_{\substack{0\leqslant i\leqslant N_x\\ 0\leqslant j\leqslant N_y}} \max\left\{\varrho_{f'}(\boldsymbol{q}^n_{i,j})\frac{\Delta t}{\Delta x},\ \varrho_{g'}(\boldsymbol{q}^n_{i,j})\frac{\Delta t}{\Delta y}\right\} \leqslant 1\,, \tag{4.55}$$

where Co is the maximum Courant number in the x and y directions. The spectral radius $\varrho_{f'}(\boldsymbol{q})$ of $\boldsymbol{f}'(\boldsymbol{q})$ corresponds to c_P (expression detailed in the Appendix 5.2), ditto the spectral radius $\varrho_{g'}(\boldsymbol{q})$ of $\boldsymbol{g}'(\boldsymbol{q})$. The stability of the scheme (4.52) is also restricted by the spectral radius of the Jacobian matrix $\boldsymbol{r}'(\boldsymbol{q})$. As in the uniaxial case (4.35) [4], the stability limits imply that the scheme (4.52) is stable under the classical CFL condition (4.55). Hence, given a spatial discretization and a Courant number $\mathrm{Co} \leqslant 1$, the value of the time step Δt is imposed by (4.55).

3.2.b. *Flux-limiter scheme*

We describe now the flux-limiter scheme [4, 69]. Since the computation of the numerical fluxes in the x and y directions is similar, only the numerical flux $\boldsymbol{f}^n_{i+1/2,j}$ in the x direction is detailed here. To do so, we introduce the Jacobian matrix

$$\boldsymbol{A}_{i+1/2,j} = \boldsymbol{f}'\big(\tfrac{1}{2}(\boldsymbol{q}^n_{i,j} + \boldsymbol{q}^n_{i+1,j})\big) \tag{4.56}$$

at the arithmetic mean of the grid node values in the x direction. The jump of the numerical solution $\boldsymbol{q}^n_{i+1,j} - \boldsymbol{q}^n_{i,j}$ along x is decomposed in the basis of right eigenvectors $\{\boldsymbol{p}^k_{i+1/2,j}, k = 1,\dots,7\}$ of $\boldsymbol{A}_{i+1/2,j}$,

$$\boldsymbol{q}^n_{i+1,j} - \boldsymbol{q}^n_{i,j} = \sum_{k=1}^{7} \alpha^k_{i+1/2,j}\,\boldsymbol{p}^k_{i+1/2,j} = \sum_{k=1}^{7} \boldsymbol{\mathcal{W}}^k_{i+1/2,j}\,, \tag{4.57}$$

which correspond to the eigenvalues $\{-c_P, c_P, -c_S, c_S, 0, 0, 0\}$ (cf. detailed expressions in the Appendix 5.2).

The numerical flux in (4.53) is the sum of a first-order flux and a second-order limited correction, $\boldsymbol{f}^n_{i+1/2,j} = \boldsymbol{f}^L_{i+1/2,j} + \boldsymbol{f}^H_{i+1/2,j}$, where

$$\begin{aligned}
\boldsymbol{f}^L_{i+1/2,j} &= \frac{1}{2}\Big(\boldsymbol{f}(\boldsymbol{q}^n_{i,j}) + \boldsymbol{f}(\boldsymbol{q}^n_{i+1,j})\Big) - \frac{1}{2}c_P\Big(\boldsymbol{\mathcal{W}}^1_{i+1/2,j} + \boldsymbol{\mathcal{W}}^2_{i+1/2,j}\Big)\\
&\quad - \frac{1}{2}c_S\Big(\boldsymbol{\mathcal{W}}^3_{i+1/2,j} + \boldsymbol{\mathcal{W}}^4_{i+1/2,j}\Big),\\
\boldsymbol{f}^H_{i+1/2,j} &= \frac{1}{2}c_P\left(1 - \frac{\Delta t}{\Delta x}c_P\right)\Big(\phi(\theta^1_{i+1/2,j})\boldsymbol{\mathcal{W}}^1_{i+1/2,j} + \phi(\theta^2_{i+1/2,j})\boldsymbol{\mathcal{W}}^2_{i+1/2,j}\Big)\\
&\quad + \frac{1}{2}c_S\left(1 - \frac{\Delta t}{\Delta x}c_S\right)\Big(\phi(\theta^3_{i+1/2,j})\boldsymbol{\mathcal{W}}^3_{i+1/2,j} + \phi(\theta^4_{i+1/2,j})\boldsymbol{\mathcal{W}}^4_{i+1/2,j}\Big)\,.
\end{aligned} \tag{4.58}$$

The coefficients $\theta^k_{i+1/2,j}$ where $k = 1,\dots,4$ express the upwind variation of the

jump (4.57) in the kth characteristic field,

$$\theta^{1,3}_{i+1/2,j} = \frac{\boldsymbol{\mathcal{W}}^{1,3}_{i+3/2,j} \cdot \boldsymbol{\mathcal{W}}^{1,3}_{i+1/2,j}}{\boldsymbol{\mathcal{W}}^{1,3}_{i+1/2,j} \cdot \boldsymbol{\mathcal{W}}^{1,3}_{i+1/2,j}}, \qquad \theta^{2,4}_{i+1/2,j} = \frac{\boldsymbol{\mathcal{W}}^{2,4}_{i-1/2,j} \cdot \boldsymbol{\mathcal{W}}^{2,4}_{i+1/2,j}}{\boldsymbol{\mathcal{W}}^{2,4}_{i+1/2,j} \cdot \boldsymbol{\mathcal{W}}^{2,4}_{i+1/2,j}}, \tag{4.59}$$

and ϕ denotes the minmod limiter function $\phi(\theta) = \max\{0, \min\{1, \theta\}\}$. As such, the weights $\phi(\theta^k_{i+1/2,j})$ are designed to avoid spurious oscillations in the numerical solution. Since the eigenvalues indexed by $k = 5, \ldots, 7$ in the decomposition of the jump (4.57) are zero, the corresponding terms $\boldsymbol{\mathcal{W}}^k_{i+1/2,j}$ do not appear in the numerical flux (4.58).

To carry out one iteration in time (4.52)-(4.54) at some grid node (i, j), the numerical values of $\boldsymbol{q}$ at the grid nodes $(i-2, \ldots, i+2) \times (j-2, \ldots, j+2)$ are required (4.58). Therefore, two columns and two rows of "ghost cells" are added on the left, the right, the top, and the bottom of the numerical domain. Then, a zero-order extrapolation of the numerical values is used to update the ghost cell values at each step of (4.54), similarly to the "outflow boundary condition" in Sec. 4.3.c of Chapter 2. This procedure is detailed in Section 21.8 of [69], and is used here to simulate an infinite physical domain.

3.3. Numerical experiments

In the following examples, the softening function is $\phi_1(g) = 1 - g$, and the storage energy is $\phi_2(g) = -\frac{1}{2}\gamma \ln(1 - g^2)$. The Courant number in (4.55) is set to $\mathrm{Co} = 0.9$. If not specified differently, the physical parameters are given in Table 4.3. The parameters γ, α have been chosen so as to obtain significant effects of the softening at the scale of the simulation. The numerical domain is defined by $L_x = L_y = 0.4$ m, and is discretized using $N_x = N_y = 800$ points in each direction.

3.3.a. *Murnaghan hyperelasticity*

The first example focuses on nonlinear elastodynamics, i.e., no softening occurs in the material. In (4.48)-(4.49), the source term and the relaxation function are removed ($\boldsymbol{s} = \boldsymbol{0}$, $\alpha \to +\infty$). We consider a Riemann problem with initial data $\boldsymbol{q}(x, y, 0)$, where the material is initially undeformed and opposite transverse velocities with amplitude V are applied:

$$\boldsymbol{q}(x, y, 0) = \begin{cases} V\,(0, 0, 0, 0, \quad \sin\varphi, -\cos\varphi, 0)^\top & \text{if } x_\varphi < 0\,, \\ V\,(0, 0, 0, 0, -\sin\varphi, \quad \cos\varphi, 0)^\top & \text{if } x_\varphi > 0\,. \end{cases} \tag{4.60}$$

The variable $x_\varphi = (x - x_s)\cos\varphi + (y - y_s)\sin\varphi$ is the x-abscissa of a new coordinate system, corresponding to a rotation by an angle φ and a translation by (x_s, y_s) of the original one. Here, the origin is set at $(x_s, y_s) = (L_x, L_y)/2$, the rotation angle is $\varphi = 15°$, and the velocity amplitude is $V = 1.0$ m/s. To reduce discretization artifacts due to the oblique discontinuity, the average value of (4.60) over the cell $[x_{i-1/2}, x_{i+1/2}] \times [y_{j-1/2}, y_{j+1/2}]$ is initially set at the grid node (i, j).

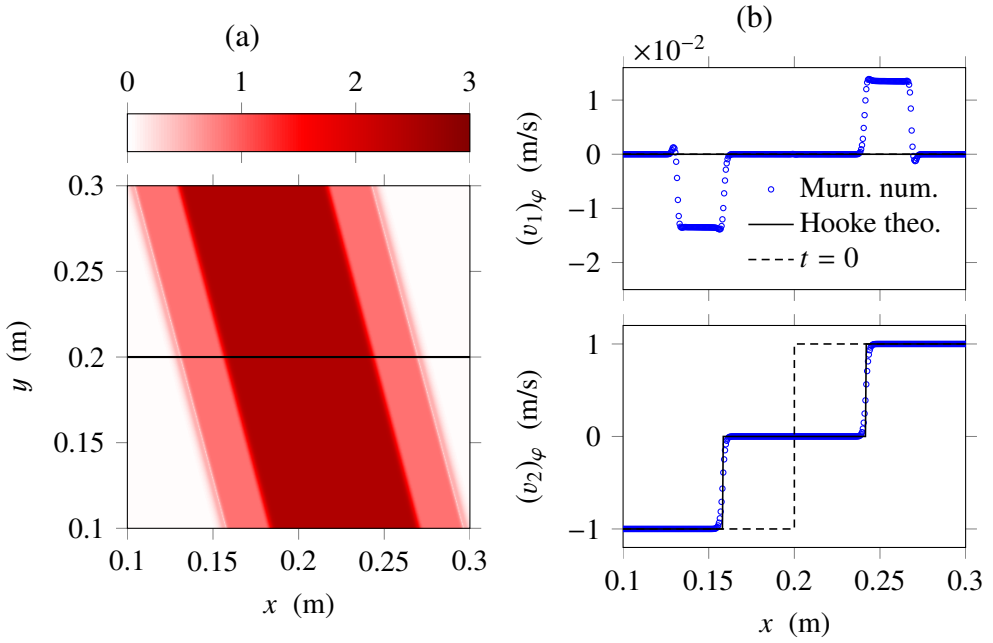

Figure 4.9. Generation of compression waves from pure shear initial data in Murnaghan hyperelasticity ($g \equiv 0$). (a) Map of $W^{1/8}$ at $t = 0.015$ ms, where W is the strain energy density (J/m^3). (b) Rotated longitudinal and transverse velocities $(v_1)_\varphi$, $(v_2)_\varphi$ along the horizontal line in the map, in the linear and nonlinear cases.

Figure 4.9 illustrates the coupling between plane shear waves and plane compression waves in hyperelasticity [37, 97], contrary to linear elasticity where both types of waves are decoupled. Fig. 4.9a displays a map of $W^{1/8}$ at $t = 0.015$ ms, where W is the strain energy (2.16) obtained numerically with the above method. Fig. 4.9b displays the evolution of the rotated longitudinal velocity $(v_1)_\varphi = v_1 \cos\varphi + v_2 \sin\varphi$ and the rotated transverse velocity $(v_2)_\varphi = -v_1 \sin\varphi + v_2 \cos\varphi$, along the solid line displayed in Fig. 4.9a. In the case of Hooke's law of linear elasticity, the solution to the initial-value problem (4.60) writes

$$\boldsymbol{q}(x,y,t) = \begin{cases} V\,(0,0,0,0,\ \ \sin\varphi, -\cos\varphi, 0)^\top & \text{if } x_\varphi < -c_S t\,, \\ \dfrac{V}{c_S}\big(-\sin\varphi\cos\varphi, -\sin^2\varphi, \cos^2\varphi, \sin\varphi\cos\varphi, 0, 0, 0\big)^\top & \\ \qquad\qquad\qquad\qquad\qquad\qquad \text{if } -c_S t < x_\varphi < c_S t\,, & \\ V\,(0,0,0,0,-\sin\varphi,\ \ \cos\varphi, 0)^\top & \text{if } c_S t < x_\varphi\,, \end{cases} \tag{4.61}$$

with $c_S = \sqrt{\mu/\rho_0}$, and only shear waves propagate. In the hyperelastic case, Fig. 4.9b shows that shear waves are generated from the initial data (4.60), but faster compression waves are also generated. The small-amplitude perturbations in the numerical solution are caused by the discretization of the oblique discontinuity (4.60).

3.3.b. *Softening*

In this second example, we consider the full system (4.48)-(4.49). The material is initially undeformed and at rest, $\boldsymbol{q}(x,y,0) = \mathbf{0}$, and a volume force $\boldsymbol{f}^v$ is used

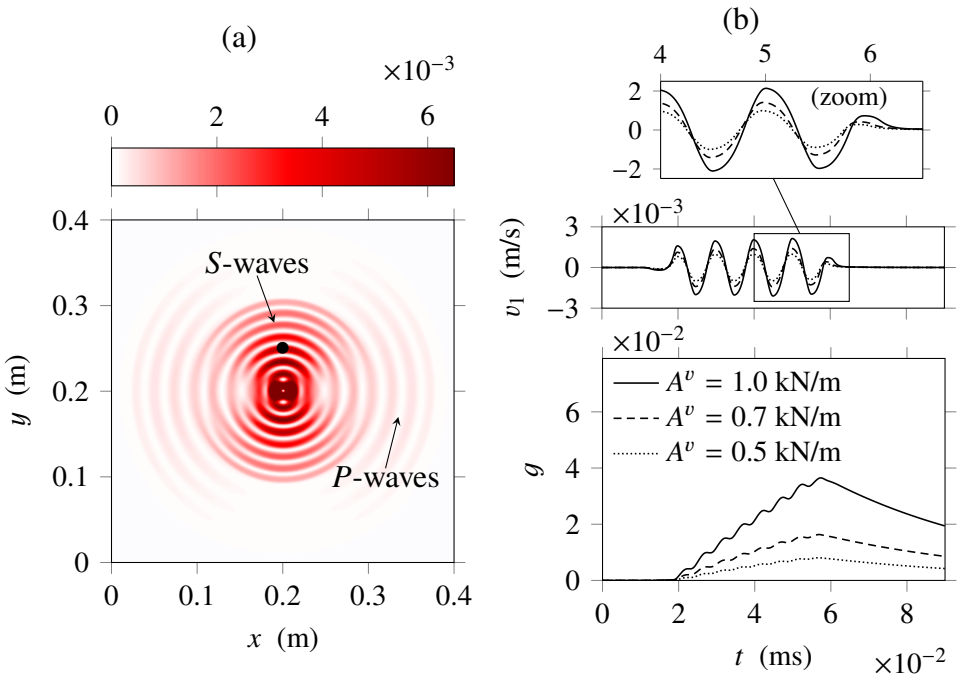

Figure 4.10. Softening induced by an acoustic point source (4.62). (a) Map of the strain energy $(1-g)\,W$ in J/m^3 at $t = 0.04$ ms, where the forcing amplitude is $A^v = 1.0$ kN/m. (b) Time histories of the velocity component v_1 at the position of the receiver (bullet point on the map) for several forcing amplitudes (top); Same for the softening variable g (bottom).

for the forcing $\boldsymbol{s}$. The volume force is an acoustic point source along x with expression $\boldsymbol{f}^v = A^v \sin(2\pi f_c t)\,\delta(x-x_s)\,\delta(y-y_s)\,\boldsymbol{e}_1$, where δ is the Dirac delta function, A^v is the amplitude, and f_c is the characteristic frequency. Usually, the increment $\boldsymbol{s}^n_{i,j}$ in (4.52) is obtained by averaging the source term $\boldsymbol{s}|_{t=t_n}$ of (4.48)-(4.49) over the cell $[x_{i-1/2}, x_{i+1/2}]\times[y_{j-1/2}, y_{j+1/2}]$. Here, we approximate the Dirac deltas by a truncated Gaussian function to avoid strain concentration at the source. Thus,

$$\boldsymbol{s}^n_{i,j} = \frac{A^v}{\rho_0}\sin(2\pi f_c t_n)\,\frac{\exp\!\left(-(d_{ij}/\sigma_c)^2\right)}{\pi\sigma_c{}^2\left(1-\exp\!\left(-(R/\sigma_c)^2\right)\right)}\mathbf{1}_{d_{ij}\leqslant R}\,(0,0,0,0,1,0,0)^\top, \tag{4.62}$$

where d_{ij} is the distance between (x_i, y_j) and (x_s, y_s). Denoted by the indicator function $\mathbf{1}_{d_{ij}\leqslant R}$, the function's support is a disk with radius $R = c_P/(7.5\,f_c)$, where $c_P = \sqrt{(\lambda+2\mu)/\rho_0}$ is the speed of linear compression waves. The width parameter of the Gaussian function is chosen such that $\sigma_c = R/2$. The point load has amplitude $A^v = 1.0$ kN/m, frequency $f_c = 100$ kHz, and it is located at the nearest grid node of the domain's center: $(x_s, y_s) \simeq (L_x, L_y)/2$. The source (4.62) is switched on at $t = 0$, and switched off at $t = 0.04$ ms. A receiver located at $(x_r, y_r) = (0.2, 0.25)$ m records the numerical solution during the simulation.

Figure 4.10 illustrates the effect of the softening on the wave propagation. Fig. 4.10a displays a map of the strain energy $(1-g)\,W$ at the time $t = 0.04$ ms, which shows the propagation of cylindrical waves. Denoted by a bullet point, the receiver is located in a region of the plane where mainly shear waves propagate. Fig. 4.10b shows the effect of the softening at the position of the

receiver for several forcing amplitudes A^v. One observes that g increases while the wave passes by the receiver, and that it relaxes towards zero afterwards. This softening/recovery process is all the more important as the forcing amplitude is large. The characteristic time of the slow dynamics $\tau_g = \alpha/\gamma \approx 0.05$ ms corresponds to the characteristic time of the recovery [1, 4]. In Fig. 4.10b, one observes the delay of the velocity signal due to the increase of g. The recorded signal is similar to experimental ones obtained in a longitudinal configuration [116] (Fig. 1.3).

4. Conclusion

A new model for the dynamic behavior of solids has been proposed. The following features are common with the soft-ratchet model of Vakhnenko et al. [137, 138]:

- a variable g describes the softening of the material;
- an evolution equation for g with a relaxation time is given;
- a low number of extra parameters for the non-classical effects is required (two parameters).

In comparison with the soft-ratchet model, several differences can be outlined. The new model

(i) satisfies the second principle of thermodynamics;

(ii) does not require an expression of the equilibrium value $g_{\text{eq}}(\sigma)$ of g, but an expression of the storage energy $\phi_2(g)$;

(iii) generalizes naturally to higher space dimensions.

Point (i) is a major difference with the soft-ratchet model (see the Appendix, Sec. 5.1). As shown in Section 1, the model reproduces qualitatively the macroscopic behavior of real media. The effect of the parameters γ and α on the softening is shown analytically.

In the present work, the modeling approach is purely phenomenological. No physical interpretation of g at the microscopic scale is known. To go further, some similarities to other materials are pointed out in Section 5.1, in particular with filled rubber. It seems that the dynamic response of rocks is similar to the Payne effect [108] and that the quasi-static response of rocks is similar to the Mullins effect [33, 81]. In the mechanics of elastomers, existing quasi-static models have a very similar structure to our dynamic model [34, 99]. By analogy, the coupling of nonlinear viscoelasticity and heat conduction could be a key for physical modeling [49]. Lastly, from a microscopic point of view, both materials are made approximately of a matrix with particles inside. These similarities may be used for future micromechanical modeling.

The model is well-adapted to finite-volume numerical methods, since the equations of motion write as a nonlinear system of balance laws. In the longitudinal case, the main features of dynamic acousto-elasticity have been reproduced

numerically, using a numerical method with flux limiters. This type of method can be generalized to higher space dimensions, as done here in the plane-strain case (2D) by using dimensional splitting. Thus, similar methods could be developed in the full 3D case.

Nevertheless, one limitation of the present study needs to be mentioned. The model amounts to linear elasticity in the small perturbation limit, where resonance peaks are of infinite height. This property is not in agreement with resonance experiments. To explore more realistic configurations (dissipative small perturbation limit), one should at least incorporate viscoelastic attenuation in the model. This aspect, which is crucial for prospective experimental validation, is addressed in the next chapter.

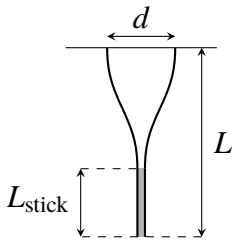

Figure 4.11. Sketch of two sticking fibers of length L with initial spacing d, when withdrawn from a wetting liquid (grey). The height of fluid between the fibers is L_{stick}.

5. Appendix

5.1. Other models

5.1.a. *Analogies*

■ *Quasistatic loading of filled rubber.* In the case of a quasistatic process, equilibrium is satisfied over the transformation. This is equivalent to have $\dot{g} \simeq 0$ in the model equation (4.9). The internal variable is then deduced from the strain through $g = g_{\text{eq}}(\chi)$ (4.10). Due to the constitutive relation (4.7), the stress depends explicitly on the strain. Therefore, no hysteresis occurs in the stress-strain relationship.

Pseudo-elastic models are designed to incorporate hysteresis and memory effects. Additional variables which are stored along the loading path can be used in the storage energy ϕ_2. For example, $W_{\max} = \max_t W(\chi)$ is used in [99] to describe the *Mullins effect*, which is an hysteresis phenomenon observed in cyclic loading of filled rubber. An expression of the form

$$\phi_2'(g) = W_{\max} + \frac{2\gamma}{\sqrt{\pi}} \operatorname{erf}^{-1}(-g), \tag{4.63}$$

is proposed in [99]. From (4.10), one deduces the expression of the internal variable

$$g_{\text{eq}}(\chi) = \operatorname{erf}\left(\frac{W_{\max} - W(\chi)}{2\gamma/\sqrt{\pi}}\right). \tag{4.64}$$

This expression satisfies $g_{\text{eq}} = 0$ if $W(\chi) = W_{\max}$. In particular, $g_{\text{eq}} = 0$ along the primary loading path. In the case of the *end-point memory* phenomenon which is observed in rocks [43], the pseudo-elastic model [99] can be adapted as described in Section 4 of [34]. For further reading, constitutive models for rubber can be found in [31, 33, 81, 104].

■ *System of wet fibers.* A formal analogy with a system of two partially-immersed fibers of length L can be made (Figure 4.11). Initially, their spacing is d. Then, the fibers are immersed in a fluid with surface tension Υ. When withdrawn quasi-statically, they stick together. The internal energy of this system is the sum of the bending energy in the fibers and the energy due to the surface tension of the fluid. Thus, [112]

$$\mathcal{E}_{\text{int}} = \phi_1(g)\,\mathcal{E}_{\text{el}} + \phi_2(g), \qquad g = \frac{L_{\text{stick}}}{L} \in [0, 1[, \tag{4.65}$$

where L_{stick} is the wet length of the fibers. In the case of a system of cylindrical elastic fibers with radius r and Young's modulus M_0, the expressions in (4.65) are

$$\begin{aligned} \phi_1(g) &= (1-g)^{-3}\,, \\ \mathcal{E}_{\text{el}} &= \frac{3M_0 I d^2}{L^3} \qquad \text{with} \qquad I = \frac{\pi r^4}{4}\,, \\ \phi_2(g) &= -4\Upsilon r L \int_0^g \left(\theta - \left(\frac{\pi}{2} - \theta\right)\left(\frac{1}{\cos\theta} - 1\right)\right) \mathrm{d}\zeta\,, \end{aligned} \tag{4.66}$$

Due to the geometry of the meniscus and the law of hydrostatics, one has

$$\cos\theta = \frac{\rho_{\text{f}}\, g_{\text{n}} \zeta r L}{\Upsilon + \rho_{\text{f}}\, g_{\text{n}} \zeta r L} \qquad \text{with} \qquad \zeta = \frac{z}{L}\,, \tag{4.67}$$

where z is the altitude in the fluid, ρ_{f} is the mass density of the fluid and g_{n} is the standard gravity. A sign mistake has been found in equation (2) of [112]. Equations (4.66)-(4.67) are taken from equations (3)-(4) of [112], where the sign is correct. Formally, the energy (4.65) is similar to the energy (4.3).

5.1.b. *Limitations of the soft-ratchet model*

■ *Thermodynamical analysis.* The soft-ratchet model by Vakhnenko et al. is a particular case of 1D model with internal variable of state [137, 138] (see Chapter 1). Thus, we carry out the thermodynamical analysis from Section 1. The soft-ratchet model introduces a concentration of activated defects g, which modifies the stress according to

$$\sigma = (1-g)\,\bar{\sigma}(\varepsilon)\,. \tag{4.68}$$

This constitutive law is the same as (4.7) with the softening function (4.12). In one space dimension, the strain rate satisfies $D = \dot{\varepsilon}/F$, where $F = 1 + \varepsilon$. The Clausius–Duhem inequality (4.2) rewrites as

$$\mathscr{D} = \left(\sigma - \rho_0 \frac{\partial e}{\partial \varepsilon}\right) D - \rho \frac{\partial e}{\partial g}\,\dot{g} \geqslant 0\,, \tag{4.69}$$

for all state and all evolution. Due to the constitutive law (4.68), the specific internal energy must satisfy

$$\rho_0 \frac{\partial e}{\partial \varepsilon} = (1-g)\,\bar{\sigma}(\varepsilon)\,. \tag{4.70}$$

When integrating (4.70) with respect to the strain ε, an integration constant appears, which we denote by $\phi_2(g)$. Thus, the internal energy per unit volume (4.3) is recovered, where $W'(\varepsilon) = \bar{\sigma}(\varepsilon)$. The Clausius–Duhem inequality (4.69) implies

$$\big(W(\varepsilon) - \phi_2'(g)\big)\,\dot{g} \geqslant 0 \tag{4.71}$$

for all $\{\varepsilon, g\}$ and all $\dot{g}$.

In the soft-ratchet model, the evolution equation for g has the form

$$\dot{g} = \big(g_{\text{eq}}(\sigma) - g\big)/\tau_g\,, \tag{4.72}$$

where $\tau_g > 0$ is a variable relaxation time and $g_{\text{eq}}(\sigma)$ is the value of g at equilibrium for a given stress. Various expressions of g_{eq} are proposed in the literature. In [137], g_{eq} reads

$$g_{\text{eq}}(\sigma) = g_0 \exp\left(\sigma/\tilde{\sigma}\right), \tag{4.73}$$

where $\tilde{\sigma}$ is a stress and g_0 is the value of g_{eq} at zero stress. This expression is modified in [38] to ensure $g_{\text{eq}} < 1$:

$$g_{\text{eq}}(\sigma) = \frac{1}{2}\left(1 + \tanh\left(\sigma/\tilde{\sigma} - \tanh^{-1}(1 - 2g_0)\right)\right). \tag{4.74}$$

Injecting (4.72) in (4.71) yields the condition

$$\left(\phi_2'(g) - W(\varepsilon)\right)\left(g - g_{\text{eq}}(\sigma)\right) \geqslant 0 \quad \text{with} \quad \sigma = (1-g)\,\bar{\sigma}(\varepsilon), \tag{4.75}$$

for all ε in $]-1, +\infty[$ and all g in $[0, 1]$.

In particular, (4.75) must hold for all g when $\varepsilon = 0$. In this case, the condition (4.75) reduces to $g \geqslant g_0$ for all g such that $\phi_2'(g) > 0$. We deduce that g_0 must be negative or zero, i.e. $g_0 = 0$. The expressions (4.73)-(4.74) of g_{eq} imply that g_{eq} is always equal to zero, which is not physically relevant. Something must be modified in the soft-ratchet model to satisfy Eq. (4.75). Here, we propose to seek thermodynamically admissible expressions of g_{eq}.

■ *Modified model.* Expressions of g_{eq} must be chosen carefully. The condition (4.75) imposes that $\phi_2'(g) - W(\varepsilon)$ and $g - g_{\text{eq}}(\sigma)$ have the same sign. Both functions of ε and g are smooth. Hence, they equal zero with a change in sign or with a gradient equal to zero. Since the gradient of both functions is nonzero, it implies that $\phi_2'(g) - W(\varepsilon)$ and $g - g_{\text{eq}}(\sigma)$ equal zero for the same values of ε and g. Combining both equalities, the condition

$$\phi_2'(g_{\text{eq}}(\sigma)) = W\left(\bar{\sigma}^{-1}\left(\frac{\sigma}{1 - g_{\text{eq}}(\sigma)}\right)\right) \tag{4.76}$$

is deduced from the constitutive law (4.68). An expression of g_{eq} which satisfies (4.76) is not necessarily thermodynamically admissible. Moreover, one can note that such an expression depends on the strain energy density W and on the storage energy ϕ_2.

Now, we examine the existence of a thermodynamically admissible expression of g_{eq} in a particular case. To do so, the strain energy density from Hooke's law $W : \varepsilon \mapsto \frac{1}{2} M_0\, \varepsilon^2$ is chosen. We select the quadratic expression (4.13) of the storage energy ϕ_2. The necessary condition (4.76) writes

$$\gamma g_{\text{eq}}(\sigma) = \frac{1}{2} M_0 \left(\frac{\sigma/M_0}{1 - g_{\text{eq}}(\sigma)}\right)^2. \tag{4.77}$$

It rewrites as a cubic equation:

$$\left(g_{\text{eq}}(\sigma) - \frac{2}{3}\right)^3 - \frac{1}{3}\left(g_{\text{eq}}(\sigma) - \frac{2}{3}\right) + \frac{2}{27} - \frac{\sigma^2}{2M_0\gamma} = 0, \tag{4.78}$$

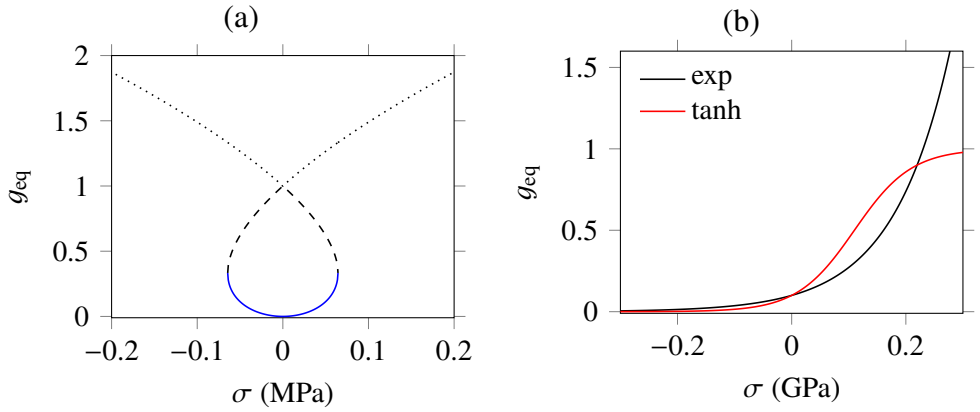

Figure 4.12. Graph of the equilibrium value $g_{eq}(\sigma)$ in the soft-ratchet model. (a) Roots of (4.78). The solid line corresponds to a thermodynamically admissible expression of g_{eq}. (b) Classical expressions "exp" (4.73) and "tanh" (4.74) of g_{eq}.

which may have multiple solutions.

When using Cardano's method, the discriminant

$$\Delta = \frac{27\,\sigma^2}{4M_0^2\gamma^2}\left(\frac{8M_0\gamma}{27} - \sigma^2\right) \tag{4.79}$$

of the cubic function in (4.78) is positive if $|\sigma| < \sqrt{8M_0\gamma/27}$. In this case, the three roots of (4.78) are real. On Figure 4.12a, the three real roots are represented, where the parameters are issued from Table 4.2. For comparison, the classical expressions (4.73) and (4.74) of $g_{eq}(\sigma)$ are displayed in Figure 4.12b, where $g_0 = 0.1$ and $\tilde{\sigma} = 0.1$ GPa. Among the three real roots of (4.78), only one satisfies $g_{eq}(0) = 0$ (solid line on Figure 4.12a):

$$g_{eq}(\sigma) = \frac{4}{3}\sin^2\left(\frac{1}{6}\arccos\left(1 - \frac{27\sigma^2}{4M_0\gamma}\right)\right). \tag{4.80}$$

This thermodynamically admissible expression of g_{eq} is only defined when the discriminant (4.79) is positive, i.e. for strains smaller than $\sqrt{8\gamma/(27M_0)} \approx 4.6 \times 10^{-6}$. This bound has nearly the same order of magnitude as (4.27).

To summarize, we have shown that the soft-ratchet model is not thermodynamically relevant. A modification of this model has been examined, which results in an implicit definition of g_{eq} (4.76). The expression of g_{eq} is dependent on the choice of a strain energy density function and a storage energy. Furthermore, Eq. (4.76) may be difficult to solve analytically in some cases. Lastly, the domain of validity of the model is restricted.

5.2. Complements on plane-strain finite volumes

5.2.a. *Coefficients of the Jacobian matrices*

We use the Einstein summation convention with indices in $\{1, 2\}$. To encompass both cases with and without geometric nonlinearity in a single equation,

we introduce a parameter $\Theta \in \{0, 1\}$ such that $\Theta = 1$ corresponds to finite strain case and $\Theta = 0$ corresponds to infinitesimal strain. Hence, the coordinates of the strain tensor (2.9) are written $E_{ij} = \varepsilon_{ij} + \frac{1}{2}\Theta\, u_{p,i}u_{p,j}$, where $\varepsilon_{ij} = \frac{1}{2}(u_{i,j} + u_{j,i})$ are the coordinates of the infinitesimal strain tensor. Moreover, the components of the Piola–Kirchhoff stress tensor (4.47) are written $P_{ij} = \phi_1(g)\left(\delta_{im} + \Theta\, u_{i,m}\right)\left(\tilde{\alpha}_0\delta_{mj} + \tilde{\alpha}_1 E_{mj}\right)$, i.e.

$$P_{ij} = \phi_1(g)\left(\tilde{\alpha}_0\delta_{ij} + \tilde{\alpha}_1 E_{ij} + \Theta\left(\tilde{\alpha}_0 u_{i,j} + \tilde{\alpha}_1 u_{i,m}E_{mj}\right)\right), \tag{4.81}$$

where $\tilde{\alpha}_0, \tilde{\alpha}_1$ are given in (4.46). The coefficients (4.50) of the Jacobian matrices $\boldsymbol{f}'(\boldsymbol{q})$ and $\boldsymbol{g}'(\boldsymbol{q})$ satisfy $\rho_0 Q_{ijk\ell} = \partial P_{ij}/\partial u_{k,\ell}$ and $\rho_0 G_{ij} = \partial P_{ij}/\partial g$. In the present case of Murnaghan material with softening (4.81) with the softening function $\phi_1(g) = 1 - g$, one has

$$\begin{aligned}
\rho_0 Q_{ijk\ell} &= \phi_1(g)\left(\delta_{ij}\frac{\partial\tilde{\alpha}_0}{\partial u_{k,\ell}} + E_{ij}\frac{\partial\tilde{\alpha}_1}{\partial u_{k,\ell}} + \tilde{\alpha}_1\frac{\partial E_{ij}}{\partial u_{k,\ell}}\right)\\
&+ \Theta\,\phi_1(g)\left(u_{i,j}\frac{\partial\tilde{\alpha}_0}{\partial u_{k,\ell}} + \tilde{\alpha}_0\delta_{ik}\delta_{j\ell} + u_{i,m}E_{mj}\frac{\partial\tilde{\alpha}_1}{\partial u_{k,\ell}} + \tilde{\alpha}_1\left(\delta_{ik}E_{j\ell} + u_{i,m}\frac{\partial E_{mj}}{\partial u_{k,\ell}}\right)\right),\\
\rho_0 G_{ij} &= \phi_1'(g)\left(\tilde{\alpha}_0\delta_{ij} + \tilde{\alpha}_1 E_{ij} + \Theta\left(\tilde{\alpha}_0 u_{i,j} + \tilde{\alpha}_1 u_{i,m}E_{mj}\right)\right),
\end{aligned} \tag{4.82}$$

where

$$\begin{aligned}
\frac{\partial E_{ij}}{\partial u_{k,\ell}} &= \frac{1}{2}\left(\delta_{ik}\delta_{j\ell} + \delta_{jk}\delta_{i\ell}\right) + \frac{1}{2}\Theta\left(u_{k,i}\delta_{j\ell} + u_{k,j}\delta_{i\ell}\right),\\
\frac{\partial E_{nn}}{\partial u_{k,\ell}} &= \delta_{k\ell} + \Theta\, u_{k,\ell},\\
\frac{\partial\tilde{\alpha}_0}{\partial u_{k,\ell}} &= (\lambda + 2(\mathfrak{l} - \mathfrak{m})E_{mm})\frac{\partial E_{nn}}{\partial u_{k,\ell}} + 2\mathfrak{m}E_{ij}\frac{\partial E_{ij}}{\partial u_{k,\ell}},\\
\frac{\partial\tilde{\alpha}_1}{\partial u_{k,\ell}} &= 2\mathfrak{m}\frac{\partial E_{nn}}{\partial u_{k,\ell}}.
\end{aligned}$$

The case of Hookean solids is recovered if $\phi_1(g) \equiv 1$, geometric nonlinearity is neglected ($\Theta = 0$), and the Murnaghan coefficients $\mathfrak{l}$, $\mathfrak{m}$ are zero. In this case, Eq. (4.82) gives $\rho_0 Q_{ijk\ell} = \lambda\delta_{ij}\delta_{k\ell} + \mu(\delta_{ik}\delta_{j\ell} + \delta_{jk}\delta_{i\ell})$ and $\rho_0 G_{ij} = 0$.

5.2.b. *Eigendecomposition of the Jacobian matrices*

We provide an eigendecomposition of the Jacobian matrices $\boldsymbol{f}'(\boldsymbol{q})$ and $\boldsymbol{g}'(\boldsymbol{q})$ of the fluxes. The hyperelastic case without softening is recovered by removing the last row and the last column of each matrix in the following paragraphs.

■ *Flux along the x-axis.* The Jacobian matrix (4.50) of $\boldsymbol{f}$ at the linear average (4.56) is diagonalized. Let us write $\boldsymbol{A}_{i+1/2,j} = \boldsymbol{R}\boldsymbol{\Lambda}\boldsymbol{R}^{-1}$ where $\boldsymbol{R}$ is an invertible real matrix, and $\boldsymbol{\Lambda}$ is a diagonal real matrix. The matrix of eigenvalues $\boldsymbol{\Lambda} = \mathrm{diag}(-c_P, c_P, -c_S, c_S, 0, 0, 0)$ satisfies

$$c_{P,S} = \frac{1}{\sqrt{2}}\sqrt{Q_{1111} + Q_{2121} \pm \sqrt{(Q_{1111} - Q_{2121})^2 + 4\,Q_{1121}Q_{2111}}}\,, \tag{4.83}$$

where the plus sign gives the expression of c_P (compressional waves), and the minus sign gives the expression of c_S (shear waves). The first four right eigenvectors $\boldsymbol{p}^k_{i+1/2,j}$ of $\boldsymbol{A}_{i+1/2,j}$ used in (4.57)-(4.58) are the first four columns of $\boldsymbol{R}$, where

$$\boldsymbol{R} = \begin{pmatrix} p_{11} & -p_{11} & p_{13} & -p_{13} & p_{15} & p_{16} & p_{17} \\ 0 & 0 & 0 & 0 & p_{25} & p_{26} & p_{27} \\ p_{31} & -p_{31} & p_{33} & -p_{33} & 1 & 0 & 0 \\ 0 & 0 & 0 & 0 & 0 & 1 & 0 \\ 1 & 1 & p_{13}/p_{33} & p_{13}/p_{33} & 0 & 0 & 0 \\ p_{31}/p_{11} & p_{31}/p_{11} & 1 & 1 & 0 & 0 & 0 \\ 0 & 0 & 0 & 0 & 0 & 0 & 1 \end{pmatrix}, \tag{4.84}$$

with the coefficients

$$p_{11} = 1/c_P\,, \qquad p_{31} = \frac{Q_{2111}/c_P}{(c_P)^2 - Q_{2121}}\,,$$

$$p_{13} = -\frac{(c_P)^2\, Q_{1121}/c_S}{\left((c_P)^2 - Q_{2121}\right) Q_{1111} + Q_{1121}Q_{2111}}\,, \qquad p_{33} = 1/c_S\,,$$

$$p_{15} = \frac{Q_{1112}Q_{2121} - Q_{1121}Q_{2112}}{Q_{1111}Q_{2112} - Q_{1112}Q_{2111}}\,, \qquad p_{25} = \frac{Q_{1121}Q_{2111} - Q_{1111}Q_{2121}}{Q_{1111}Q_{2112} - Q_{1112}Q_{2111}}\,,$$

$$p_{16} = \frac{Q_{1112}Q_{2122} - Q_{1122}Q_{2112}}{Q_{1111}Q_{2112} - Q_{1112}Q_{2111}}\,, \qquad p_{26} = \frac{Q_{1122}Q_{2111} - Q_{1111}Q_{2122}}{Q_{1111}Q_{2112} - Q_{1112}Q_{2111}}\,,$$

$$p_{17} = \frac{G_{21}Q_{1112} - G_{11}Q_{2112}}{Q_{1111}Q_{2112} - Q_{1112}Q_{2111}}\,, \qquad p_{27} = \frac{G_{11}Q_{2111} - G_{21}Q_{1111}}{Q_{1111}Q_{2112} - Q_{1112}Q_{2111}}\,.$$

The matrix $\boldsymbol{R}$ is invertible provided that its determinant is nonzero, which imposes that $Q_{1121}Q_{2111} \neq Q_{1111}Q_{2121}$ and $Q_{1121}Q_{2111} \neq -\frac{1}{4}(Q_{1111} - Q_{2121})^2$. Let us consider each equality case:

- if $Q_{1121}Q_{2111} = Q_{1111}Q_{2121}$, then the eigenvalues of $\boldsymbol{f}'(\boldsymbol{q})$ satisfy $c_S = 0$. Therefore, the reduced system of conservation laws for plane waves propagating along x is not strictly hyperbolic (eigenvalues $\{-c_P, c_P, -c_S, c_S, 0\}$);
- if $Q_{1121}Q_{2111} = -\frac{1}{4}(Q_{1111} - Q_{2121})^2$, then the eigenvalues of $\boldsymbol{f}'(\boldsymbol{q})$ satisfy $c_P = c_S$, which is impossible for the same reason.

Therefore, the previous eigendecomposition is valid over the domain of strict hyperbolicity. The first four left eigenvectors $\boldsymbol{l}^k_{i+1/2,j}$ of $\boldsymbol{A}_{i+1/2,j}$ are the first four rows of $\boldsymbol{R}^{-1}$, where

$$\boldsymbol{R}^{-1} = \begin{pmatrix} q_{11} & q_{12} & q_{13} & q_{14} & q_{15} & q_{16} & q_{17} \\ -q_{11} & -q_{12} & -q_{13} & -q_{14} & q_{15} & q_{16} & -q_{17} \\ -q_{41} & -q_{42} & -q_{43} & -q_{44} & q_{45} & q_{46} & -q_{47} \\ q_{41} & q_{42} & q_{43} & q_{44} & q_{45} & q_{46} & q_{47} \\ 0 & 1/p_{25} & 0 & -p_{26}/p_{25} & 0 & 0 & -p_{27}/p_{25} \\ 0 & 0 & 0 & 1 & 0 & 0 & 0 \\ 0 & 0 & 0 & 0 & 0 & 0 & 1 \end{pmatrix}, \tag{4.85}$$

with the coefficients

$$q_{11} = \frac{1}{2}\frac{p_{33}}{p_{11}p_{33} - p_{13}p_{31}}, \qquad q_{41} = \frac{1}{2}\frac{p_{31}}{p_{11}p_{33} - p_{13}p_{31}},$$
$$q_{12} = \frac{p_{13} - p_{15}p_{33}}{2\,p_{25}\,(p_{11}p_{33} - p_{13}p_{31})}, \qquad q_{42} = \frac{p_{11} - p_{15}p_{31}}{2\,p_{25}\,(p_{11}p_{33} - p_{13}p_{31})},$$
$$q_{13} = -\frac{1}{2}\frac{p_{13}}{p_{11}p_{33} - p_{13}p_{31}}, \qquad q_{43} = -\frac{1}{2}\frac{p_{11}}{p_{11}p_{33} - p_{13}p_{31}},$$
$$q_{14} = \frac{(p_{15}p_{26} - p_{16}p_{25})\,p_{33} - p_{13}p_{26}}{2\,p_{25}\,(p_{11}p_{33} - p_{13}p_{31})}, \qquad q_{44} = \frac{(p_{15}p_{26} - p_{16}p_{25})\,p_{31} - p_{11}p_{26}}{2\,p_{25}\,(p_{11}p_{33} - p_{13}p_{31})},$$
$$q_{15} = \frac{1}{2}\frac{p_{11}p_{33}}{p_{11}p_{33} - p_{13}p_{31}}, \qquad q_{45} = -\frac{1}{2}\frac{p_{31}p_{33}}{p_{11}p_{33} - p_{13}p_{31}},$$
$$q_{16} = -\frac{1}{2}\frac{p_{13}p_{11}}{p_{11}p_{33} - p_{13}p_{31}}, \qquad q_{46} = \frac{1}{2}\frac{p_{11}p_{33}}{p_{11}p_{33} - p_{13}p_{31}},$$
$$q_{17} = \frac{(p_{15}p_{27} - p_{17}p_{25})\,p_{33} - p_{13}p_{27}}{2\,p_{25}\,(p_{11}p_{33} - p_{13}p_{31})}, \qquad q_{47} = \frac{(p_{15}p_{27} - p_{17}p_{25})\,p_{31} - p_{11}p_{27}}{2\,p_{25}\,(p_{11}p_{33} - p_{13}p_{31})}.$$

The coefficients $\alpha^k_{i+1/2,j}$ in (4.57) are equal to the scalar products $\alpha^k_{i+1/2,j} = \boldsymbol{l}^k_{i+1/2,j} \cdot (\boldsymbol{q}^n_{i+1,j} - \boldsymbol{q}^n_{i,j})$.

■ *Flux along the y-axis.* Similarly to (4.56), we introduce the Jacobian matrix $\boldsymbol{g}'(\boldsymbol{q})$ of $\boldsymbol{g}$ at the linear average $\boldsymbol{B}_{i,j+1/2} = \boldsymbol{g}'\big(\frac{1}{2}(\boldsymbol{q}^n_{i,j} + \boldsymbol{q}^n_{i,j+1})\big)$, and provide an eigendecomposition $\boldsymbol{B}_{i,j+1/2} = \boldsymbol{R}\boldsymbol{\Lambda}\boldsymbol{R}^{-1}$. The matrix of eigenvalues $\boldsymbol{\Lambda} = \mathrm{diag}(-c_P, c_P, -c_S, c_S, 0, 0, 0)$ satisfies

$$c_{P,S} = \frac{1}{\sqrt{2}}\sqrt{Q_{2222} + Q_{1212} \pm \sqrt{(Q_{2222} - Q_{1212})^2 + 4\,Q_{2212}Q_{1222}}}\,, \tag{4.86}$$

where the plus and minus signs give the expressions of c_P and c_S, respectively. With similar notations as (4.84), we have

$$\boldsymbol{R} = \begin{pmatrix} 0 & 0 & 0 & 0 & p_{15} & p_{16} & p_{17} \\ p_{21} & -p_{21} & p_{23} & -p_{23} & p_{25} & p_{26} & p_{27} \\ 0 & 0 & 0 & 0 & 0 & 1 & 0 \\ p_{41} & -p_{41} & p_{43} & -p_{43} & 1 & 0 & 0 \\ p_{21}/p_{41} & p_{21}/p_{41} & 1 & 1 & 0 & 0 & 0 \\ 1 & 1 & p_{43}/p_{23} & p_{43}/p_{23} & 0 & 0 & 0 \\ 0 & 0 & 0 & 0 & 0 & 0 & 1 \end{pmatrix}, \tag{4.87}$$

with the coefficients

$$p_{21} = \frac{(c_S)^2\,Q_{1222}/c_P}{\big((c_P)^2 - Q_{1212}\big)\,Q_{1212} - Q_{1222}Q_{2212}}, \qquad p_{41} = 1/c_P,$$
$$p_{23} = 1/c_S, \qquad p_{43} = -\frac{Q_{2212}/c_S}{(c_P)^2 - Q_{1212}},$$
$$p_{15} = \frac{Q_{1212}Q_{2222} - Q_{1222}Q_{2212}}{Q_{1211}Q_{2212} - Q_{1212}Q_{2211}}, \qquad p_{25} = \frac{Q_{1222}Q_{2211} - Q_{1211}Q_{2222}}{Q_{1211}Q_{2212} - Q_{1212}Q_{2211}},$$

$$p_{16} = \frac{Q_{1212}Q_{2221} - Q_{1221}Q_{2212}}{Q_{1211}Q_{2212} - Q_{1212}Q_{2211}}, \qquad p_{26} = \frac{Q_{1221}Q_{2211} - Q_{1211}Q_{2221}}{Q_{1211}Q_{2212} - Q_{1212}Q_{2211}},$$
$$p_{17} = \frac{G_{22}Q_{1212} - G_{12}Q_{2212}}{Q_{1211}Q_{2212} - Q_{1212}Q_{2211}}, \qquad p_{27} = \frac{G_{12}Q_{2211} - G_{22}Q_{1211}}{Q_{1211}Q_{2212} - Q_{1212}Q_{2211}}.$$

A similar analysis shows that $\boldsymbol{R}$ is invertible over the domain of strict hyperbolicity:

$$\boldsymbol{R}^{-1} = \begin{pmatrix} q_{11} & q_{12} & q_{13} & q_{14} & q_{15} & q_{16} & q_{17} \\ -q_{11} & -q_{12} & -q_{13} & -q_{14} & q_{15} & q_{16} & -q_{17} \\ -q_{41} & -q_{42} & -q_{43} & -q_{44} & q_{45} & q_{46} & -q_{47} \\ q_{41} & q_{42} & q_{43} & q_{44} & q_{45} & q_{46} & q_{47} \\ 1/p_{25} & 0 & -p_{16}/p_{15} & 0 & 0 & 0 & -p_{17}/p_{15} \\ 0 & 0 & 1 & 0 & 0 & 0 & 0 \\ 0 & 0 & 0 & 0 & 0 & 0 & 1 \end{pmatrix}, \tag{4.88}$$

with the coefficients

$$q_{11} = \frac{p_{23} - p_{25}p_{43}}{2\,p_{15}\,(p_{21}p_{43} - p_{23}p_{41})}, \qquad q_{41} = \frac{p_{21} - p_{25}p_{41}}{2\,p_{15}\,(p_{21}p_{43} - p_{23}p_{41})},$$
$$q_{12} = \frac{1}{2}\frac{p_{43}}{p_{21}p_{43} - p_{23}p_{41}}, \qquad q_{42} = \frac{1}{2}\frac{p_{41}}{p_{21}p_{43} - p_{23}p_{41}},$$
$$q_{13} = \frac{(p_{16}p_{25} - p_{15}p_{26})\,p_{43} - p_{16}p_{23}}{2\,p_{15}\,(p_{21}p_{43} - p_{23}p_{41})}, \qquad q_{43} = \frac{(p_{16}p_{25} - p_{15}p_{26})\,p_{41} - p_{16}p_{21}}{2\,p_{15}\,(p_{21}p_{43} - p_{23}p_{41})},$$
$$q_{14} = -\frac{1}{2}\frac{p_{23}}{p_{21}p_{43} - p_{23}p_{41}}, \qquad q_{44} = -\frac{1}{2}\frac{p_{21}}{p_{21}p_{43} - p_{23}p_{41}},$$
$$q_{15} = \frac{1}{2}\frac{p_{43}p_{41}}{p_{21}p_{43} - p_{23}p_{41}}, \qquad q_{45} = -\frac{1}{2}\frac{p_{41}p_{23}}{p_{21}p_{43} - p_{23}p_{41}},$$
$$q_{16} = -\frac{1}{2}\frac{p_{41}p_{23}}{p_{21}p_{43} - p_{23}p_{41}}, \qquad q_{46} = \frac{1}{2}\frac{p_{23}p_{21}}{p_{21}p_{43} - p_{23}p_{41}},$$
$$q_{17} = \frac{(p_{17}p_{25} - p_{15}p_{27})\,p_{43} - p_{17}p_{23}}{2\,p_{15}\,(p_{21}p_{43} - p_{23}p_{41})}, \qquad q_{47} = \frac{(p_{17}p_{25} - p_{15}p_{27})\,p_{41} - p_{17}p_{21}}{2\,p_{15}\,(p_{21}p_{43} - p_{23}p_{41})}.$$

5.2.c. *Classical (unsplit) 2D finite-volume methods*

Here, we present briefly finite-volume methods for 2D systems of conservation laws. The properties of these methods illustrate the benefits of implementing dimensional splitting, which is used in the present chapter to construct a flux-limiter scheme.

■ *Lax–Friedrichs.* The numerical method is written in conservation form

$$\boldsymbol{q}_{i,j}^{n+1} = \boldsymbol{q}_{i,j}^{n} - \frac{\Delta t}{\Delta x}\left(\boldsymbol{f}_{i+1/2,j}^{n} - \boldsymbol{f}_{i-1/2,j}^{n}\right) - \frac{\Delta t}{\Delta y}\left(\boldsymbol{g}_{i,j+1/2}^{n} - \boldsymbol{g}_{i,j-1/2}^{n}\right). \tag{4.89}$$

The numerical fluxes $\boldsymbol{f}^n_{i+1/2,j}$ and $\boldsymbol{g}^n_{i,j+1/2}$ are deduced from the Lax–Friedrichs method, which writes as follows in two space dimensions:

$$\begin{aligned}
\boldsymbol{f}^n_{i+1/2,j} &= \frac{1}{2}\left(\boldsymbol{f}(\boldsymbol{q}^n_{i,j}) + \boldsymbol{f}(\boldsymbol{q}^n_{i+1,j})\right) - \frac{\Delta x}{4\,\Delta t}\left(\boldsymbol{q}^n_{i+1,j} - \boldsymbol{q}^n_{i,j}\right),\\
\boldsymbol{g}^n_{i,j+1/2} &= \frac{1}{2}\left(\boldsymbol{g}(\boldsymbol{q}^n_{i,j}) + \boldsymbol{g}(\boldsymbol{q}^n_{i,j+1})\right) - \frac{\Delta y}{4\,\Delta t}\left(\boldsymbol{q}^n_{i,j+1} - \boldsymbol{q}^n_{i,j}\right).
\end{aligned} \tag{4.90}$$

This method is table under the CFL condition $\mathrm{Co} < 1/\sqrt{2} \approx 0.707$, where Co is the Courant number. Note that this scheme does not amount to the one-dimensional Lax–Friedrichs method when the data is invariant by translation along x or y.

■ *Lax–Wendroff.* We introduce the Jacobian matrices $\boldsymbol{A}_{i+1/2,j}$, $\boldsymbol{B}_{i,j+1/2}$ at the arithmetic means of the grid node values in the x and y directions, respectively. The numerical fluxes $\boldsymbol{f}^n_{i+1/2,j}$ and $\boldsymbol{g}^n_{i,j+1/2}$ are deduced from the Lax–Wendroff method, which writes as follows in two space dimensions:

$$\begin{aligned}
\boldsymbol{f}^n_{i+1/2,j} &= \frac{1}{2}\left(\boldsymbol{f}(\boldsymbol{q}^n_{i,j}) + \boldsymbol{f}(\boldsymbol{q}^n_{i+1,j})\right) - \frac{\Delta t}{2\,\Delta x}\boldsymbol{A}_{i+1/2,j}\left(\boldsymbol{f}(\boldsymbol{q}^n_{i+1,j}) - \boldsymbol{f}(\boldsymbol{q}^n_{i,j})\right)\\
&\quad - \frac{\Delta t}{8\,\Delta y}\boldsymbol{A}_{i+1/2,j}\left(\boldsymbol{g}(\boldsymbol{q}^n_{i+1,j+1}) + \boldsymbol{g}(\boldsymbol{q}^n_{i,j+1}) - \boldsymbol{g}(\boldsymbol{q}^n_{i+1,j-1}) - \boldsymbol{g}(\boldsymbol{q}^n_{i,j-1})\right),\\
\boldsymbol{g}^n_{i,j+1/2} &= \frac{1}{2}\left(\boldsymbol{g}(\boldsymbol{q}^n_{i,j}) + \boldsymbol{g}(\boldsymbol{q}^n_{i,j+1})\right) - \frac{\Delta t}{2\,\Delta y}\boldsymbol{B}_{i,j+1/2}\left(\boldsymbol{g}(\boldsymbol{q}^n_{i,j+1}) - \boldsymbol{g}(\boldsymbol{q}^n_{i,j})\right)\\
&\quad - \frac{\Delta t}{8\,\Delta x}\boldsymbol{B}_{i,j+1/2}\left(\boldsymbol{f}(\boldsymbol{q}^n_{i+1,j+1}) + \boldsymbol{f}(\boldsymbol{q}^n_{i+1,j}) - \boldsymbol{f}(\boldsymbol{q}^n_{i-1,j+1}) - \boldsymbol{f}(\boldsymbol{q}^n_{i-1,j})\right).
\end{aligned} \tag{4.91}$$

This method is stable under the CFL condition $\mathrm{Co} < 1/\sqrt{2} \approx 0.707$, where Co is the Courant number. This scheme amounts to the one-dimensional Lax–Wendroff method when the data is invariant by translation along x or y.

CHAPTER 5

Slow dynamics of a viscoelastic bar

Viscoelastic attenuation is a key feature to reproduce the vibrations of real media. In particular, resonance experiments demonstrate the need of attenuation to describe accurately forced periodic oscillations [55, 135]. In the framework of linear elasticity, several rheological models based on a combination of springs and dashpots can be found in the literature. The standard linear solid, also known as generalized Maxwell or Zener body, is commonly used for the description of seismic wave propagation [16, 20, 89]. It consists in the combination of N_v elementary Zener elements with $3N_v$ parameters in total. The latter are obtained by optimization, so that a given quality factor is reached over a frequency range of interests (cf. Sec. 5.1 of the Appendix and [16, 38]).

Section 1 shows how viscoelasticity of Zener type can be coupled with the softening model from the previous chapter. In a first step, Zener viscoelasticity is generalized to nonlinear constitutive laws as proposed in [38], using internal variables of state (viscous strains) [83]. In a second step, the variable g accounting for the softening is added to the list of variables of state. Finally, the constitutive equations are chosen in agreement with the Clausius–Duhem inequality.

The equations of motion are written as a nonlinear system of balance laws. Similarly to the previous chapter, finite-volume methods are developed to solve

numerically the equations of motion (Section 2). Here, boundary conditions are introduced to simulate the forced vibrations of a longitudinal sample. The method is validated in the linear viscoelastic case. The full model shows qualitative agreement with resonance experiments and with dynamic acousto-elasticity. This study has been published in [3, 6].

Time-domain methods are useful to reproduce the material's softening (transient regime), but are not well-suited for the computation of resonance curves. The aim of Section 3 is to introduce a frequency-domain tool dedicated to resonance simulations. It is based on a finite-element semi-discretization of the equations of motion, and on the harmonic balance method. The periodic solution is followed while varying the exciting frequency by using a continuation method [27]. This framework may be useful for prospective experimental validations. Preliminary results have been communicated in [5].

1. Phenomenological material modeling

Let us consider a solid continuum in the Lagrangian representation of motion, which length L along the x-axis is very large compared to its other dimensions. No heat transfer occurs in the material, self-gravitation is neglected, and no external body force is applied. Only longitudinal vibrations are considered, and the displacement field is described by its component $u(x,t)$ along the x-axis. On one hand, kinematics reads $\partial_t \varepsilon = \partial_x v$, where $\varepsilon = \partial_x u > -1$ denotes the strain, and $v = \partial_t u$ denotes the particle velocity. On the other hand, the conservation of momentum writes $\rho_0 \partial_t v = \partial_x \sigma$, where ρ_0 is the density in the reference configuration (2.23). According to the conservation of mass (2.3), the density ρ in the deformed configuration satisfies $\rho_0/\rho = 1 + \varepsilon$. The expression of the stress σ is specified later on.

1.1. Construction of the model

1.1.a. *Nonlinear viscoelasticity*

Experimental evidence shows that elasticity is not sufficient to model geomaterials. In geophysics, the standard linear solid model is widely used to describe viscoelastic attenuation [16, 20, 89]. It consists in the combination of N_v elementary Zener mechanisms with elastic constants $M_\ell > 0$, $K_\ell > 0$ and damping constants $\nu_\ell > 0$, where $\ell = 1, \ldots, N_v$. Here, a generalization of the standard linear solid to nonlinear constitutive laws proposed in [38] is used. The corresponding schematic representation in terms of springs and dashpots is given in Figure 5.1. In the infinitesimal strain limit, i.e. when the springs with constant M_ℓ are linear, the standard linear solid model is recovered. Furthermore, inviscid nonlinear elasticity is recovered when the viscous effects are null, in the sense that $\nu_\ell \longrightarrow +\infty$ for $\ell = 1, \ldots, N_v$.

The parameters of the model M_ℓ, K_ℓ, ν_ℓ are deduced from the quality factor Q of the material over a frequency range of interest [16, 38]. To do so, the relaxation

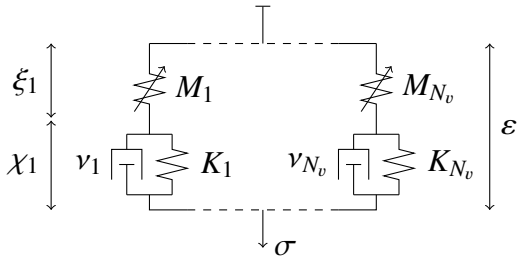

Figure 5.1. Rheological model of a nonlinear generalized Zener material.

times $\tau_{\sigma\ell}$, $\tau_{\varepsilon\ell}$ and the relaxed elastic modulus M_{rel} are introduced:

$$\tau_{\sigma\ell} = \frac{\nu_\ell}{M_\ell + K_\ell}, \qquad \tau_{\varepsilon\ell} = \frac{\nu_\ell}{K_\ell}, \qquad \frac{M_{\text{rel}}}{N_v} = \frac{M_\ell K_\ell}{M_\ell + K_\ell}. \tag{5.1}$$

In the numerical experiments of Section 2, $N_v = 5$ Zener mechanisms are used, and the quality factor is optimized over the frequency range $[f_{\min}, f_{\max}] = [1, 100]$ kHz towards the value $Q = 20$. The relaxation times $\tau_{\sigma\ell}$, $\tau_{\varepsilon\ell}$ are deduced from a nonlinear optimization procedure described in the Appendix, Sec. 5.1.

In the case of nonlinear Zener materials [38], the springs with constant M_ℓ are nonlinear (Figure 5.1). Their state of deformation is described by the variables ξ_ℓ, and their strain energy density W_ℓ is expressed by using a suitable strain energy density function. For example, W_ℓ may be expressed as a polynomial function of the strain ξ_ℓ:

$$W_\ell : \xi_\ell \mapsto \left(\frac{1}{2} - \frac{\beta}{3}\xi_\ell - \frac{\delta}{4}{\xi_\ell}^2\right) M_\ell \, {\xi_\ell}^2 . \tag{5.2}$$

Hooke's law $W_\ell = \frac{1}{2} M_\ell {\xi_\ell}^2$ is recovered in the case of small strains $\xi_\ell \to 0$, and also by setting the higher-order elastic constants β, δ to zero.

In counterpart, the parts with spring constant K_ℓ and damping constant ν_ℓ are still considered as linear, but one could make different choices. Their state of deformation is described by the variables $\chi_\ell = \varepsilon - \xi_\ell$, which are internal variables of state accounting for viscoelastic attenuation [83]. The strain energy density in each mechanism is $\frac{1}{2} K_\ell {\chi_\ell}^2$. Thus, the total strain energy W in the material is the sum of the strain energies in all the springs:

$$W = \sum_{\ell=1}^{N_v} W_\ell(\varepsilon - \chi_\ell) + \frac{1}{2} K_\ell {\chi_\ell}^2 . \tag{5.3}$$

According to the diagram in Figure 5.1, the stress σ_ℓ in the ℓth Zener mechanism is expressed by $\sigma_\ell = W'_\ell(\varepsilon - \chi_\ell)$ and $\sigma_\ell = K_\ell \chi_\ell + \nu_\ell \partial_t \chi_\ell$, where W'_ℓ is the derivative of the function W_ℓ. Combining both expressions of σ_ℓ, the evolution equations

$$\partial_t \chi_\ell = \frac{1}{\nu_\ell} \left(W'_\ell(\varepsilon - \chi_\ell) - K_\ell \chi_\ell \right) \tag{5.4}$$

are obtained. The relation $\sigma = \sum_{\ell=1}^{N_v} \sigma_\ell$ leads to the constitutive law

$$\sigma = \sum_{\ell=1}^{N_v} W'_\ell(\varepsilon - \chi_\ell) . \tag{5.5}$$

1.1.b. *Softening*

To describe the softening of the nonlinear viscoelastic material, we introduce a scalar variable g, which value in $[0, 1[$ modifies the stiffness of the material. This variable is modified along the time following an evolution equation. Similarly to Chapter 4 [1], the derivation of a softening model is based on continuum thermodynamics with internal variables [82, 84]. As usual in acoustics, the process is assumed adiabatic. The first principle of thermodynamics introduces the internal energy e per unit mass. The conservation of total energy (2.5) writes $\rho\dot{e} = \sigma D$, where $D = \dot{\varepsilon}/(1+\varepsilon)$ is the strain rate. The second principle of thermodynamics (2.6) gives $\rho\dot{\eta} \geqslant 0$, where η is the specific entropy. The system is described by the variables of state $\{\varepsilon, \eta, \chi_1, \ldots, \chi_{N_v}, g\}$, leading to the Gibbs identity (4.1)

$$\dot{e} = T\dot{\eta} + \frac{\partial e}{\partial \varepsilon}\dot{\varepsilon} + \frac{\partial e}{\partial \boldsymbol{p}} \cdot \dot{\boldsymbol{p}}\,, \tag{5.6}$$

where $T = \partial e/\partial \eta > 0$ is the absolute temperature. The vector $\boldsymbol{p} = (\chi_1, \ldots, \chi_{N_v}, g)^\top$ is a vector of internal variables, which evolution $\dot{\boldsymbol{p}}$ depends only on the state of the system. Combining the local equations of thermodynamics, the Gibbs equation (5.6) and the conservation of mass $\rho_0/\rho = 1 + \varepsilon$ (2.3), the Clausius–Duhem inequality is obtained:

$$\mathcal{D}_0 = \left(\sigma - \rho_0 \frac{\partial e}{\partial \varepsilon}\right)\dot{\varepsilon} - \rho_0 \frac{\partial e}{\partial \boldsymbol{p}} \cdot \dot{\boldsymbol{p}} \geqslant 0\,, \tag{5.7}$$

for all state $\{\varepsilon, \boldsymbol{p}\}$ and all evolution $\dot{\varepsilon}$. The left-hand term in (5.7) is the dissipation $\mathcal{D}_0$ per initial volume of material ($\mathrm{W\,m^{-3}}$).

Similarly to Eq. (4.3) of Chapter 4, we assume an internal energy per unit of initial volume of the following form:

$$\rho_0 e = \phi_1(g) W + \phi_2(g)\,, \tag{5.8}$$

with W given in (5.3). The softening of the material is expressed by the functions ϕ_1 and ϕ_2 of the previous chapter (4.12)-(4.14). Both the internal energy e and the stress σ are state functions. Thus, the Clausius–Duhem inequality (5.7) rewrites as $A(\varepsilon, \boldsymbol{p})\,\dot{\varepsilon} + B(\varepsilon, \boldsymbol{p}) \geqslant 0$, where $A = \sigma - \rho_0 \partial e/\partial \varepsilon$ and $B = -\rho_0 \partial e/\partial \boldsymbol{p} \cdot \dot{\boldsymbol{p}}$. To ensure a positive dissipation for all $\dot{\varepsilon}$, one must have $A = 0$ and $B \geqslant 0$. The condition $A = 0$ leads to the constitutive law $\sigma = \rho_0 \partial e/\partial \varepsilon$, i.e.

$$\sigma = \phi_1(g) \sum_{\ell=1}^{N_v} W'_\ell(\varepsilon - \chi_\ell)\,. \tag{5.9}$$

The expression of the stress is the same as in the viscoelastic case (5.5), but multiplied by $\phi_1(g)$. The condition $B \geqslant 0$ yields the possible choice

$$\dot{\boldsymbol{p}} = -\operatorname{diag}\left(\frac{1}{\phi_1(g)\nu_1}, \ldots, \frac{1}{\phi_1(g)\nu_{N_v}}, \frac{1}{\alpha}\right) \rho_0 \frac{\partial e}{\partial \boldsymbol{p}}\,, \tag{5.10}$$

where $\alpha > 0$ is a constant expressed in $\mathrm{J\,m^{-3}\,s}$. Thus, the evolution equations (5.4) of the viscous strains χ_ℓ are unchanged, and the evolution of the softening variable g is governed by

$$-\alpha \dot{g} = \phi'_1(g) W + \phi'_2(g)\,, \tag{5.11}$$

where ϕ_1', ϕ_2' are the derivatives of ϕ_1, ϕ_2, and the strain energy W is given in (5.3). Finally, the dissipation $\mathcal{D}_0$ per unit of initial volume is equal to $B = -\rho_0 \partial e/\partial \boldsymbol{p} \cdot \dot{\boldsymbol{p}}$, i.e.

$$\mathcal{D}_0 = \alpha \dot{g}^2 + \phi_1(g) \sum_{\ell=1}^{N_v} \nu_\ell \, (\dot{\chi}_\ell)^2 , \tag{5.12}$$

which is positive. If $\alpha \to +\infty$, then no softening occurs: the viscoelastic case from Section 1.1.a is recovered. Conversely, if $\alpha \to 0$, the material softens instantaneously. As shown in [1] and Chapter 4, the constant $\tau_g = \alpha/\gamma$ is the relaxation time of the slow dynamics.

To summarize, the equations of motion are the usual equations of longitudinal elastodynamics with the constitutive law (5.9), and the evolution equations (5.10). For convenience, we use now the relation $\chi_\ell = \varepsilon - \xi_\ell$ to eliminate the variables χ_ℓ. The evolution of the variables ξ_ℓ is governed by $\dot{\xi}_\ell = \dot{\varepsilon} - \dot{\chi}_\ell$, where $\dot{\chi}_\ell$ is specified in (5.4). Thus, a system of $N_v + 3$ partial differential equations in space and time is obtained,

$$\begin{cases} \partial_t \varepsilon = \partial_x v \,, \\ \rho_0 \partial_t v = \partial_x \sigma \qquad \text{with} \qquad \sigma = \phi_1(g) \displaystyle\sum_{\ell=1}^{N_v} W_\ell'(\xi_\ell) \,, \\ \partial_t \xi_\ell = \partial_x v + \dfrac{1}{\nu_\ell} \left(K_\ell \, (\varepsilon - \xi_\ell) - W_\ell'(\xi_\ell) \right) , \qquad \ell = 1, \ldots, N_v \,, \\ -\alpha \partial_t g = \phi_1'(g) \left(\displaystyle\sum_{\ell=1}^{N_v} W_\ell(\xi_\ell) + \frac{1}{2} K_\ell \, (\varepsilon - \xi_\ell)^2 \right) + \phi_2'(g) \,, \end{cases} \tag{5.13}$$

with $N_v + 3$ unknowns. The system (5.13) rewrites as a system of balance laws $\partial_t \boldsymbol{q} + \partial_x \boldsymbol{f}(\boldsymbol{q}) = \boldsymbol{r}(\boldsymbol{q})$ similar to (4.30), where $\boldsymbol{q} = \left(\varepsilon, v, \xi_1, \ldots, \xi_{N_v}, g\right)^\top$ is the vector of unknowns. The physical flux $\boldsymbol{f}(\boldsymbol{q})$ and the relaxation function $\boldsymbol{r}(\boldsymbol{q})$ are

$$\begin{aligned} \boldsymbol{f}(\boldsymbol{q}) &= -\left(v, \sigma/\rho_0, v, \ldots, v, 0\right)^\top , \\ \boldsymbol{r}(\boldsymbol{q}) &= \left(0, 0, \frac{K_1 \, (\varepsilon - \xi_1) - W_1'(\xi_1)}{\nu_1}, \ldots, \right. \\ &\qquad \left. \ldots, \frac{K_{N_v} \left(\varepsilon - \xi_{N_v}\right) - W_{N_v}'(\xi_{N_v})}{\nu_{N_v}}, -\frac{\phi_1'(g) W + \phi_2'(g)}{\alpha} \right)^\top , \end{aligned} \tag{5.14}$$

where the stress σ is deduced from the constitutive law (5.9), and the strain energy W is defined in (5.3).

Remark 5.1. In related works [76, 137, 138], a Kelvin–Voigt rheology is often used instead of the standard linear solid model. This rheology is simpler than the generalized Zener model, but is only valid on small frequency ranges. The coupling of a nonlinear Kelvin–Voigt model with the softening is described by the variables of state $\{\eta, \varepsilon, \dot{\varepsilon}, g\}$. The strain energy $W(\varepsilon)$ does not depend on $\dot{\varepsilon}$, and so does the internal energy (5.8). Therefore, the vector of internal variables reduces to $\boldsymbol{p} = (g)^\top$ in the Clausius–Duhem inequality (5.7). By setting

$$\begin{aligned} \sigma &= \phi_1(g) \left(W'(\varepsilon) + \nu \dot{\varepsilon} \right) , \\ -\alpha \dot{g} &= \phi_1'(g) W(\varepsilon) + \phi_2'(g) , \end{aligned} \tag{5.15}$$

Table 5.1. Physical parameters.

ρ_0 (kg m^{-3})	M_0 (GPa)	β	δ	Q	γ (J m^{-3})	α (J m^{-3} s)
2.6×10^3	10	200	10^8	20	1.0	10^{-3}

where $\nu > 0$ is the viscosity, the dissipation $\mathcal{D}_0 = \alpha \dot{g}^2 + \phi_1(g)\, \nu \dot{\varepsilon}^2$ is obtained, which is analogous to (5.12).

1.2. Properties

1.2.a. *Mathematical properties*

■ *Hyperbolic system of conservation laws.* Some properties of the system (5.13) without relaxation are listed below without proof (cf. Chapter 2). The Jacobian matrix $\boldsymbol{f}'(\boldsymbol{q})$ of the physical flux has the eigenvalues $\{-c(\boldsymbol{q}), 0, \ldots, 0, +c(\boldsymbol{q})\}$, where the speed of sound $c(\boldsymbol{q})$ satisfies

$$\rho_0 c(\boldsymbol{q})^2 = \phi_1(g) \sum_{\ell=1}^{N_v} W_\ell''(\xi_\ell)\,. \tag{5.16}$$

The hyperbolicity of the system (5.13) amounts to the fact that $c(\boldsymbol{q})$ is real and positive. A sufficient condition is that $\phi_1(g)$ is positive, and that ξ_ℓ satisfies $W_\ell''(\xi_\ell) \geqslant 0$ for all ℓ.

■ *Relaxation spectrum.* Now, we examine the spectrum of the relaxation function $\boldsymbol{r}$ in (5.14). In the small perturbation limit, $W_\ell(\xi_\ell) \simeq \frac{1}{2} M_\ell \xi_\ell^2$ amounts to the strain energy of Hooke's law and $\phi_2(g) \simeq \frac{1}{2}\gamma g^2$. The eigenvalues of the Jacobian matrix $\boldsymbol{r}'(\boldsymbol{q})$ are then $\{-1/\tau_{\sigma N_v}, \ldots, -1/\tau_{\sigma 1}, -1/\tau_g, 0, 0\}$, where the relaxation times are defined by (5.1) and $\tau_g = \alpha/\gamma$. As discussed in the Appendix (Section 5.1), the relaxation frequencies $1/\tau_{\sigma\ell}$ belong to a frequency range $[f_{\min}, f_{\max}]$ surrounding the excitation frequency. If the relaxation times $\tau_{\sigma\ell}$ are sorted in descending order, then $f_{\min} \approx 1/\tau_{\sigma 1} < 1/\tau_{\sigma N_v} \approx f_{\max}$. Using the numerical values in Table 5.1, one shows that the characteristic frequency $1/\tau_g$ of the slow dynamics is smaller than the exciting frequency. Therefore, the spectral radius of $\boldsymbol{r}'(\boldsymbol{q})$ is equal to $1/\tau_{\sigma N_v}$ in this case.

1.2.b. *Qualitative properties*

■ *Sinusoidal strain forcing.* To illustrate the decrease of the elastic modulus, we consider that a sinusoidal strain with frequency $f_c = 2$ kHz and amplitude $V \approx 10^{-6}$ is applied locally to the material. The evolution equations (5.4) and (5.11) for the variables $\chi_1, \ldots, \chi_{N_v}$ and g are now ordinary differential equations, which parameters are given in the Tables 5.1 and 5.4. The softening function is $\phi_1(g) = 1 - g$ and the storage energy is $\phi_2(g) = -\frac{1}{2}\gamma \ln(1-g^2)$. The Matlab solver "ode15s" for stiff differential equations is used for the numerical integration of (5.4)-(5.11), with at least 80 points per period at the frequency f_c. The effective elastic modulus is $M = \rho_0 c^2$, where c is the speed of sound (5.16). In Figure 5.2a,

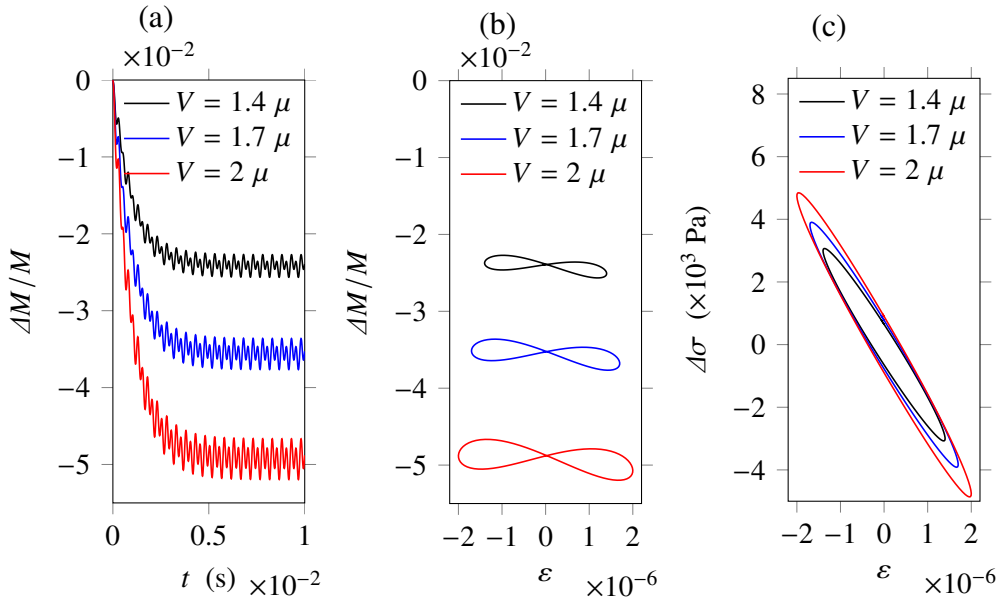

Figure 5.2. Softening in the case of a sinusoidal strain forcing $\varepsilon = V \sin(2\pi f_c t)$. (a) Time evolution of the relative variation $\Delta M/M$ of the effective elastic modulus (5.17). (b) Hysteresis curves $\Delta M/M$ versus ε in steady state ($t \gg \tau_g$); (c) Effect of the hysteresis on the stress-strain relationship. The stress variation $\Delta\sigma$ defined in (5.18) is represented with respect to ε.

the time evolution of its relative variation

$$\frac{\Delta M}{M} = \rho_0 c^2 \Big/ \left(\sum_{\ell=1}^{N_v} M_\ell \right) - 1 \tag{5.17}$$

is represented for increasing strain amplitudes V. A diminution of the effective elastic modulus is observed, until a steady state is reached. Figure 5.2b represents the relative variation of the effective elastic modulus with respect to the strain in steady state ($t \gg \tau_g$). Hysteresis curves are obtained, which size increases with the strain amplitude. In Figure 5.2c, the hysteresis in the stress-strain relationship (5.9) is displayed. Here, the variation of the stress

$$\Delta\sigma = \sigma - \sum_{\ell=1}^{N_v} M_\ell \varepsilon \tag{5.18}$$

is represented with respect to the strain. The hysteresis curves have the shape of ellipses. The slope of their major axis diminishes with increasing strain amplitudes, which illustrates the softening of the material.

■ *Strain step.* Now, we consider that a strain step of amplitude ε is applied locally to the material. The variable χ_ℓ evolves in time towards its equilibrium value $(\chi_\ell)_{\text{eq}}$, and the corresponding relaxation time is $\tau_{\sigma\ell}$. The equilibrium value of χ_ℓ is implicitly defined as a function of ε by the relation

$$W_\ell' \left(\varepsilon - (\chi_\ell)_{\text{eq}} \right) = K_\ell \, (\chi_\ell)_{\text{eq}}, \tag{5.19}$$

i.e. $(\chi_\ell)_{\text{eq}} = \frac{M_\ell}{M_\ell + K_\ell} \varepsilon$ in the case of Hooke's law ($\beta = 0$ and $\delta = 0$). The variable g evolves in time towards its equilibrium value

$$g_{\text{eq}} = \left(\phi_2' / \phi_1' \right)^{-1} (-W_{\text{eq}}), \tag{5.20}$$

where W_{eq} is the strain energy (5.3) at equilibrium. Assuming the separation of time scales $\tau_{\sigma 1} \ll \tau_g$, the corresponding relaxation time is τ_g. With the logarithmic expression $\phi_2(g) = -\frac{1}{2}\gamma \ln(1-g^2)$ of the storage energy, the equilibrium value (5.20) is

$$g_{\text{eq}} = \frac{2W_{\text{eq}}}{\gamma + \sqrt{\gamma^2 + 4W_{\text{eq}}}}, \tag{5.21}$$

which is bounded by 1 for all $W_{\text{eq}} \geqslant 0$. In the case of Hooke's law, the strain energy at equilibrium $W_{\text{eq}} = \frac{1}{2} M_{\text{rel}}\, \varepsilon^2$ is deduced from the expression of $(\chi_\ell)_{\text{eq}}$ and from the definition (5.1) of M_{rel}. Thus,

$$g_{\text{eq}} = \frac{M_{\text{rel}}\, \varepsilon^2}{\gamma + \sqrt{\gamma^2 + 2M_{\text{rel}}\, \varepsilon^2}} \underset{(\varepsilon \to 0)}{\simeq} \frac{M_{\text{rel}}\, \varepsilon^2}{2\gamma}. \tag{5.22}$$

Similar results have been obtained in the elastic case [1] (Chapter 4).

The addition of viscoelastic attenuation in the model changes its properties significantly. In the elastic case from Chapter 4, the only nonzero eigenvalue of $\boldsymbol{r}'(\boldsymbol{q})$ is related to the characteristic time $\tau_g = \alpha/\gamma$ of the slow dynamics. If attenuation is taken into account, then N_v characteristic times of the Zener model belong to the spectrum of $\boldsymbol{r}'(\boldsymbol{q})$. Also, one observes that the dissipation in the material is augmented by N_v positive terms. If we compare the hysteresis loops from Fig. 5.2c with the hysteresis loops from Fig. 4.1c p. 77, one can see notable differences. In particular, the curves in Fig. 4.1c pass through the origin of the diagram, which is not the case of the ellipses in Fig. 5.2c. As shown in the next section, the coupling with viscoelasticity has substantial implications on the development of finite-volume methods.

2. Time-domain numerical method

2.1. Numerical resolution

2.1.a. *Splitting strategy*

As in the previous chapter, the softening function is $\phi_1(g) = 1 - g$. We consider a finite domain $[0, L]$. It is discretized using a regular grid in space with mesh size Δx. The abscissas of the nodes are $x_i = i\,\Delta x$, where $0 \leqslant i \leqslant N_x$ and the number of nodes is $N_x = L/\Delta x$. A variable time step $\Delta t = t_{n+1} - t_n$ is introduced. Therefore, $\boldsymbol{q}(x_i, t_n)$ is the solution to (5.13) at the ith grid node and at the nth time step. Numerical approximations of the solution are denoted by $\boldsymbol{q}_i^n \simeq \boldsymbol{q}(x_i, t_n)$.

As discussed in [38], an efficient and flexible numerical strategy results from splitting the system (5.13) in a propagation part (or hyperbolic part)

$$\partial_t \boldsymbol{q} + \partial_x \boldsymbol{f}(\boldsymbol{q}) = \boldsymbol{0} \tag{5.23}$$

and a relaxation part

$$\partial_t \boldsymbol{q} = \boldsymbol{r}(\boldsymbol{q}). \tag{5.24}$$

The discrete operators corresponding to the integration of (5.23) and (5.24) are denoted $\mathcal{H}_a$ and $\mathcal{H}_b$, respectively. Numerically, both parts are integrated in time at each time step, with dedicated numerical methods. Here, a second-order accurate Strang splitting scheme [69]

$$\boldsymbol{q}_i^{n+1} = \mathcal{H}_b^{\Delta t/2}\, \mathcal{H}_a^{\Delta t}\, \mathcal{H}_b^{\Delta t/2} \boldsymbol{q}_i^n \tag{5.25}$$

is used, where $\mathcal{H}_a \mathcal{H}_b$ denotes the composition of $\mathcal{H}_a$ and $\mathcal{H}_b$. Hence, one iteration in time is obtained by integrating the relaxation part over a half time step, then the propagation part over a full time step, and again the relaxation part over a half time step.

As described in the next subsections, both $\mathcal{H}_a$ and $\mathcal{H}_b$ are fourth-order accurate operators. The operator $\mathcal{H}_a$ is stable under the CFL condition (2.44), whereas the operator $\mathcal{H}_b$ is made unconditionally stable using an adaptive Rosenbrock method. Thus, the coupled scheme (5.25) is stable under the CFL condition. A second-order error is introduced by the splitting [69], which penalizes the fourth-order accuracy of each operator. Nevertheless, the global accuracy observed practically is much larger than with second-order schemes. This choice reduces significantly numerical diffusion, which is crucial in the simulation of resonance experiments.

2.1.b. *Propagation part*

As discussed in Chapter 2, the numerical resolution of nonlinear systems of conservation laws (5.23) is usually performed using nonlinear conservative schemes such as finite-volume schemes with flux limiters or WENO schemes [69, 128]. Such methods are designed to capture discontinuities arising in the solution without introducing spurious oscillations. Here, the presence of viscoelasticity prevents the occurence of shocks. Therefore, this approach would be either too expensive from a computational point of view, or it would introduce too much numerical diffusion. A fourth-order conservative ADER scheme [36, 124] defined in Chapter 2 is preferred.

■ *ADER scheme.* The homogeneous system of conservation laws (5.23) is integrated numerically in space and time according to

$$\mathcal{H}_a^{\Delta t} \boldsymbol{q}_i^n = \boldsymbol{q}_i^n - \frac{\Delta t}{\Delta x} \left(\boldsymbol{f}_{i+1/2}^n - \boldsymbol{f}_{i-1/2}^n \right), \tag{5.26}$$

where $\boldsymbol{f}_{i+1/2}^n$ is the ADER flux (2.65) computed from the data $\boldsymbol{q}_i^n$. The latter is based on the linear approximation of the physical flux $\boldsymbol{f}(\boldsymbol{q}) \simeq \boldsymbol{A}_{i+1/2}\, \boldsymbol{q}$ at each time step, where $\boldsymbol{A}_{i+1/2}$ approximates the Jacobian $\boldsymbol{f}'(\boldsymbol{q})$ at the midpoint of $[x_i, x_{i+1}]$ and the time t_n.

In practice, the numerical scheme (5.26) with the numerical flux (2.65) is stable under the classical CFL condition $\mathrm{Co} \leqslant 1$ (2.44), where $\mathrm{Co} = c_{\max}^n \Delta t / \Delta x$ is the Courant number and $c_{\max}^n$ denotes the maximum sound speed (5.16) that is encountered at time t_n. If the stress-strain relationship $\xi_\ell \mapsto W_\ell'(\xi_\ell)$ is convex or concave, then $c_{\max}^n = \max_i c(\boldsymbol{U}_i^n)$. Otherwise, larger sound speeds may be reached between grid nodes (see e.g. Section 16.1 in [69]). The more general

expression is

$$\rho_0 \left(c_{\max}^n\right)^2 = \max_{0 \leqslant i < N_x} \left\{ (1 - \min\{g_i^n, g_{i+1}^n\}) \sum_{\ell=1}^{N_v} \max_{\xi_\ell \in (\mathcal{D}_\ell)_i} W_\ell''(\xi_\ell) \right\}, \tag{5.27}$$

where $(\mathcal{D}_\ell)_i$ is the interval with bounds $(\xi_\ell)_i^n$ and $(\xi_\ell)_{i+1}^n$.

■ *Roe linearization.* The matrix $\boldsymbol{A}_{i+1/2}$ in the ADER flux (2.65) is obtained by Roe linearization. The Roe matrix is defined by the three statements before Eq. (2.49). In the case of the system (5.13), the following $(N_v+3)\times(N_v+3)$-matrix is obtained by using (2.49):

$$\boldsymbol{A}_{i+1/2} = \begin{pmatrix} 0 & -1 & 0 & \cdots & 0 & 0 \\ & 0 & -a_1 & \cdots & -a_{N_v} & a_{N_v+1} \\ \vdots & -1 & 0 & \cdots & 0 & 0 \\ & \vdots & \vdots & \vdots & \vdots & \vdots \\ 0 & -1 & 0 & \cdots & 0 & 0 \\ 0 & 0 & 0 & \cdots & 0 & 0 \end{pmatrix}. \tag{5.28}$$

The coefficients deduced from (2.49) are for $\ell = 1, \ldots, N_v$,

$$\begin{aligned} a_\ell &= \frac{(1 - g_{i+1}^n) W_\ell'\big((\xi_\ell)_{i+1}^n\big) - (1 - g_i^n) W_\ell'\big((\xi_\ell)_i^n\big)}{\rho_0 \left((\xi_\ell)_{i+1}^n - (\xi_\ell)_i^n\right)} \\ &\quad + (g_{i+1}^n - g_i^n) \frac{W_\ell\big((\xi_\ell)_{i+1}^n\big) - W_\ell\big((\xi_\ell)_i^n\big)}{\rho_0 \big((\xi_\ell)_{i+1}^n - (\xi_\ell)_i^n\big)^2}, \\ a_{N_v+1} &= \sum_{\ell=1}^{N_v} \frac{W_\ell\big((\xi_\ell)_{i+1}^n\big) - W_\ell\big((\xi_\ell)_i^n\big)}{\rho_0 \big((\xi_\ell)_{i+1}^n - (\xi_\ell)_i^n\big)}. \end{aligned} \tag{5.29}$$

To avoid divisions by zero when $(\xi_{\ell^\star})_i^n = (\xi_{\ell^\star})_{i+1}^n$ for some $\ell^\star$ between 1 and N_v, the coefficients (5.29) are modified as follows (see Section 5.2):

$$\begin{aligned} a_{\ell^\star} &= \left(1 - \frac{g_i^n + g_{i+1}^n}{2}\right) \frac{W_{\ell^\star}''\big((\xi_{\ell^\star})_i^n\big)}{\rho_0}, \\ a_{N_v+1} &= \frac{W_{\ell^\star}'\big((\xi_{\ell^\star})_i^n\big)}{\rho_0} + \sum_{\substack{\ell=1 \\ \ell \neq \ell^\star}}^{N_v} \frac{W_\ell\big((\xi_\ell)_{i+1}^n\big) - W_\ell\big((\xi_\ell)_i^n\big)}{\rho_0 \big((\xi_\ell)_{i+1}^n - (\xi_\ell)_i^n\big)}. \end{aligned} \tag{5.30}$$

The eigenvalues of $\boldsymbol{A}_{i+1/2}$ are $\{-s_{i+1/2}^n, 0, \ldots, 0, +s_{i+1/2}^n\}$, where

$$s_{i+1/2}^n = \sqrt{\sum_{\ell=1}^{N_v} a_\ell}. \tag{5.31}$$

In the Section 5.2, we prove that $s_{i+1/2}^n$ is real in the hyperbolicity domain. Therefore, the matrix (5.28) is a Roe matrix.

2.1.c. *Relaxation part*

The relaxation equation (5.14)-(5.24) writes as a nonlinear system of first-order differential equations in time:

$$\begin{cases} \partial_t \xi_\ell = \dfrac{1}{\nu_\ell} \left(K_\ell \left(\varepsilon - \xi_\ell \right) - W'_\ell(\xi_\ell) \right), & \ell = 1, \ldots, N_v, \\ \partial_t g = \dfrac{1}{\alpha} \left(\displaystyle\sum_{\ell=1}^{N_v} W_\ell(\xi_\ell) + \frac{1}{2} K_\ell \left(\varepsilon - \xi_\ell \right)^2 \right) - \dfrac{\phi'_2(g)}{\alpha}, \end{cases} \tag{5.32}$$

where ε is constant. Due to the various orders of magnitude of the time constants $\tau_{\sigma\ell}, \tau_g$ in the relaxation spectrum, this differential system is stiff. To avoid stability and accuracy issues, the operator $\mathcal{H}_b$ in (5.25) is deduced from the adaptive Rosenbrock method of the Odeint C++ library [11]. For the numerical integration of (5.32) over a duration $\Delta t/2$, the maximum time step of the Rosenbrock method is set to $\Delta t/2$, and the tolerances are 10^{-4} (relative) and 10^{-5} (absolute). Finally, the numerical method (5.25) is stable under the CFL condition (2.44). Even if nothing avoids the condition $g < 1$ to be broken numerically, this unwanted event happens only at very high exciting amplitudes, where other phenomena must be taken into account (plasticity, failure).

2.2. Numerical experiments

2.2.a. *Configuration*

In the upcoming examples, we assume that the material is initially undeformed and at rest. Hence, the initial data $\boldsymbol{q}(x, 0)$ is zero for all x in the physical domain. To carry out one iteration in time at some grid node i, the numerical values of $\boldsymbol{q}$ at the grid nodes $i-2, \ldots, i+2$ are required (the stencil of the ADER scheme is $S = 2$). Therefore, two "ghost cells" must be added on the left and on the right of the numerical domain, which can account for various types of boundary conditions [69] (cf. Appendix of Chapter 2, Section 4.3). Here:

- A piston condition imposes a particle velocity $\dot{u}_d(t)$ at the abscissa $x = 0$. For compatibility with the initial conditions, one must have $\dot{u}_d(0) = 0$. By construction of the rheological model, the same boundary conditions apply to the variables $\xi_1, \ldots, \xi_N$ as to the strain ε. Such a boundary condition is represented numerically by setting for k in $\{1, 2\}$ at each time step

$$\begin{aligned} \varepsilon^n_{-k} &= \varepsilon^n_k, \\ v^n_{-k} &= -v^n_k + 2\dot{u}_d(t_{n+1}), \\ (\xi_\ell)^n_{-k} &= (\xi_\ell)^n_k, \qquad \ell = 1, \ldots, N_v, \\ g^n_{-k} &= g^n_0 . \end{aligned} \tag{5.33}$$

- A free edge is located at the abscissa $x = L$, which corresponds to a zero-strain condition. Therefore, one has also $\xi_\ell = 0$ for all ℓ at $x = L$.

Such a condition is represented by setting for k in $\{1, 2\}$ at each time step

$$\begin{aligned} \varepsilon^n_{N_x+k} &= -\varepsilon^n_{N_x-k}\,, \\ v^n_{N_x+k} &= v^n_{N_x-k}\,, \\ (\xi_\ell)^n_{N_x+k} &= -(\xi_\ell)^n_{N_x-k}\,, \qquad \ell = 1, \ldots, N_v, \\ g^n_{N_x+k} &= g^n_{N_x}\,. \end{aligned} \tag{5.34}$$

Now, several experiments are carried out with the numerical method described above. The Courant number is set to Co = 0.95. If not specified differently, the material parameters are given in Table 5.1 and Table 5.4. The physical domain is bounded, with length $L = 30$ cm. A particle velocity $\dot{u}_d(t)$ is imposed at the abscissa $x = 0$ using the piston condition (5.33). A free edge (5.34) is located at the abscissa $x = L$, as is the case in several experimental setups [117, 118].

2.2.b. *Resonance*

■ *Linear viscoelasticity.* We consider a linear Zener material ($\beta = 0$, $\delta = 0$, no softening). By definition, the frequency-response function of a linear system is the ratio of the output spectrum ($x = L$) to the input spectrum ($x = 0$), i.e.

$$FRF(\omega) = \frac{\hat{u}|_{x=L}(\omega)}{\hat{u}_d(\omega)} = \frac{\hat{v}|_{x=L}(\omega)}{\hat{\dot{u}}_d(\omega)}\,, \tag{5.35}$$

where the hat denotes the Fourier transform in time. A Fourier transform in space and time of (5.13) with $\alpha \to +\infty$ gives the following relation between the wavenumber k and the angular frequency ω,

$$k = \omega \left(\frac{M_{\text{rel}}}{\rho_0} \frac{1}{N_v} \sum_{\ell=1}^{N_v} \frac{1 + \mathrm{i}\omega\tau_{\varepsilon\ell}}{1 + \mathrm{i}\omega\tau_{\sigma\ell}} \right)^{-1/2}\,, \tag{5.36}$$

where i denotes the imaginary unit. For a harmonic excitation $u_d(t) = \exp(\mathrm{i}\omega t)$, we write the displacement field as a superposition of left-going and right-going monochromatic plane waves. Thus, $u(x,t) = \left(A\,\mathrm{e}^{\mathrm{i}kx} + B\,\mathrm{e}^{-\mathrm{i}kx}\right)\mathrm{e}^{\mathrm{i}\omega t}$, where the wavenumber k satisfies the dispersion relation (5.36). The coefficients A and B are deduced from the boundary conditions $u(0,t) = u_d(t)$ and $\partial_x u\,(L,t) = 0$. Finally, the ratio of the spectra (5.35) at the frequency ω yields

$$FRF(\omega) = \frac{2}{\exp(\mathrm{i}kL) + \exp(-\mathrm{i}kL)} = \frac{1}{\cos(kL)}\,, \tag{5.37}$$

where k is complex and frequency-dependent (5.36). Note that the expression (5.37) is not restricted to the dispersion relation (5.36) of Zener material.

To assess the quality of the numerical method, the frequency response is simulated numerically. For this purpose, a broadband chirp signal is used:

$$\dot{u}_d(t) = V \sin\left(2\pi \left(f_{\text{inf}} + \frac{{f_{\text{sup}}}^2 - {f_{\text{inf}}}^2}{4n} t\right) t\right) \mathbf{1}_{0 \leqslant t \leqslant 2n/(f_{\text{inf}} + f_{\text{sup}})}\,. \tag{5.38}$$

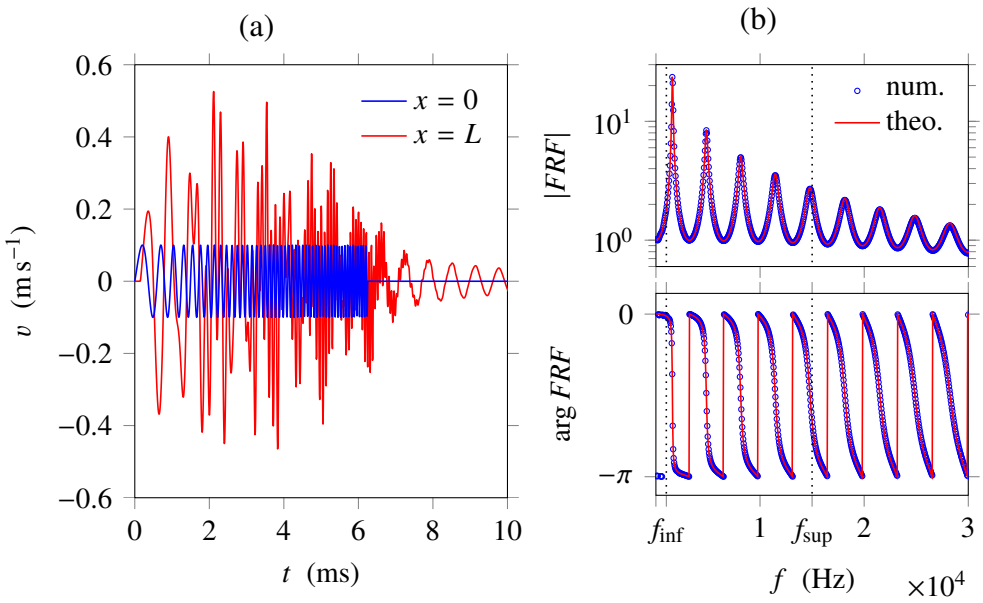

Figure 5.3. Computation of the frequency response of a linear Zener solid. (a) Time-domain signals at the abscissas $x = 0$ and $x = L$. (b) Numerical estimation (5.35) of the frequency response compared to the analytical expression (5.37), modulus (top) and phase (bottom). The vertical dotted lines mark the bandwidth of the exciting signal (5.38).

Here, the bandwidth is $[f_{\text{inf}}, f_{\text{sup}}] = [1, 15]$ kHz, the velocity amplitude is $V = 0.1$ m/s, and the number of arches is $n = 50$. The numerical solution is computed up to $t = 20$ ms, on a grid with $N_x = 100$ points. During the simulation, the particle velocity at the abscissas $x = 0$ and $x = L$ is recorded (Figure 5.3a). Then, a discrete time-domain Fourier transform of the signals is computed. Figure 5.3b displays the ratio of the spectra (5.35) so-obtained. Since the spatial discretization is fine enough — the signals have 43 points per wavelength at the frequency $f_{\text{sup}} = 15$ kHz — the numerical estimation of the frequency response function is very close to the analytical result (5.37) over the frequency range of the figure. The frequency response is made of resonance peaks, with a quasi-constant quality factor Q (see Appendix, Section 5.1). In the viscoelastic case, the resonance frequencies differ slightly from the elastic case, where they are odd multiples of $c/(4L)$.

■ *Full model.* Let us focus on the first mode of vibration which resonance frequency is 1585 Hz. The frequency range of interests reduces to $[f_{\text{inf}}, f_{\text{sup}}] = [1.4, 1.7]$ kHz. In the nonlinear case, defining the frequency response for broadband signals as (5.35) does not make any sense, due to the generation of harmonics. However, one can still define the frequency response for monochromatic signals. To do so, a sine function $\dot{u}_d(t) = V \sin(2\pi f_c t)$ of frequency f_c is used. In the linear case, the value of $FRF(\omega)$ is also given by the ratio

$$FRF(\omega) = \frac{c_1(v|_{x=L})}{c_1(\dot{u}_d)}, \tag{5.39}$$

where c_1 denotes the first complex Fourier coefficient at the angular frequency $\omega = 2\pi f_c$. This definition can still be used in the nonlinear case, where harmonic

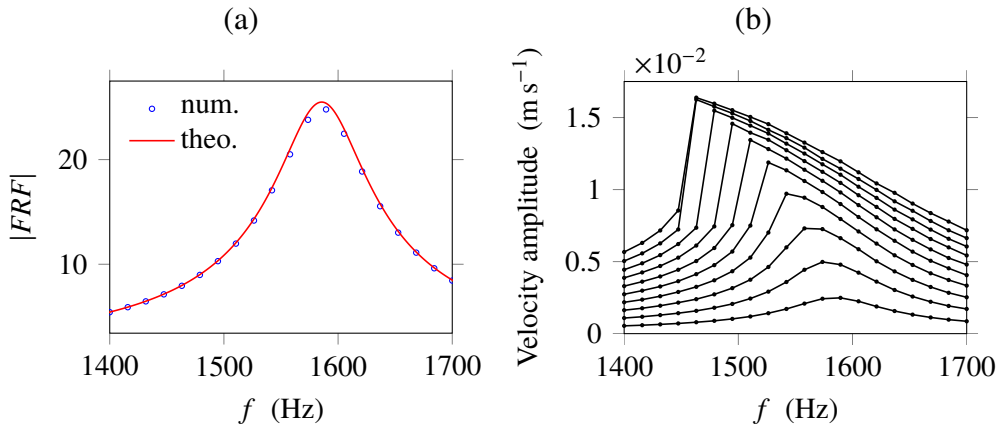

Figure 5.4. Computation of the frequency response (5.39) of nonlinear solids. (a) Validation on a linear viscoelastic material, by comparison with the analytical expression (5.37). (b) Numerical estimation of the output velocity amplitude ($x = L$) in the nonlinear case for increasing exciting amplitudes.

generation occurs. Since the frequency response is computed at the exciting frequency, the latter must be varied over the range $[f_{\text{inf}}, f_{\text{sup}}]$ to obtain a resonance curve.

For validation purposes, we compute the frequency response of the linear viscoelastic solid from the previous paragraph, but according to the formula (5.39). The numerical solution is computed on a grid with $N_x = 30$ points, which corresponds to 115 points per wavelength at the frequency f_{sup}. The input velocity amplitude is $V = 0.1$ mm/s. The exciting frequency f_c is increased by $\Delta f_c = (f_{\text{sup}} - f_{\text{inf}})/n$ every 50 ms, which is long enough to consider that the solution has reached the steady state. This increase is performed $n = 19$ times during the simulation. Two receivers record the numerical solution at the abscissas $x = 0$ and $x = L$. The Fourier coefficients c_1 are computed by numerical integration over the last period of signal at each exciting frequency f_c. To do so, the velocity signals are interpolated by a cubic spline over their last period, and the midpoint rule is used for numerical integration. As illustrated in Figure 5.4a, a large number of points per wavelength is required to compute accurately the frequency response in the vicinity of the resonance peak, where the modulus is slightly underestimated. This issue is due to the amplification of numerical errors near the resonance, and to the duration of the simulation until the steady-state is reached.

Now, the full model is considered. The forcing amplitude V is ranging from 0.1 mm/s to 1 mm/s by steps of 0.1 mm/s, and the exciting frequency is increased by Δf_c every 100 ms. Figure 5.4b displays the frequency-evolution of the output velocity amplitude $2\,|c_1(v|_{x=L})|$. According to (5.39), this quantity is equal to $V\,|FRF(\omega)|$ in the linear case. In the present nonlinear case, the velocity amplitude is not proportional to V anymore. In particular, one can note the frequency-shift of resonance peaks towards lower frequencies as V increases. At low values of V, the linear frequency response from Figure 5.4a is recovered. At high values of V, one can note the occurrence of a jump in the resonance curve. These features are typical of the experimental observations made on rock samples [55, 135].

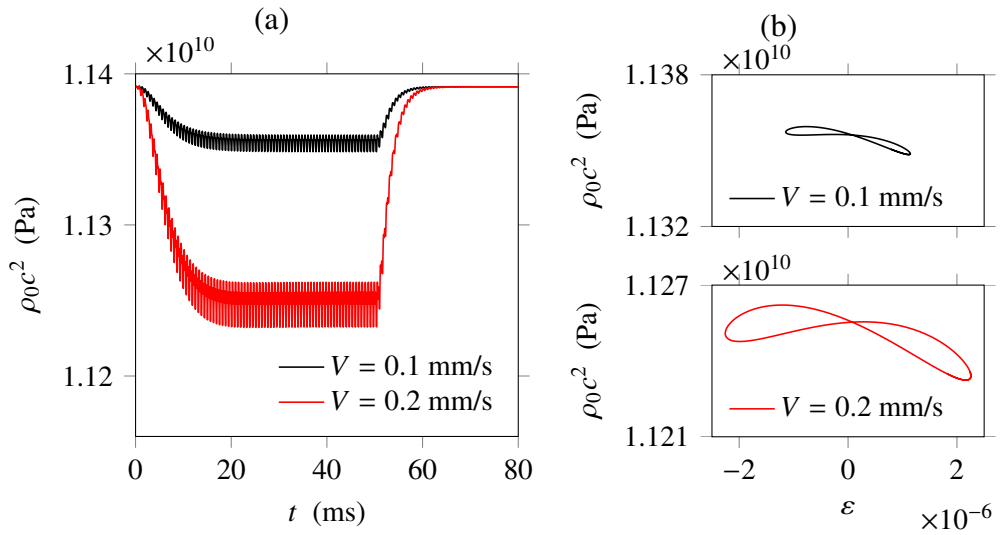

Figure 5.5. Dynamic acousto-elasticity. (a) Softening of the material, as recorded by the receiver at the abscissa $x = 0.1$ m. (b) Hysteresis curves in steady-state ($t \approx 50$ ms).

2.2.c. *Dynamic acoustoelasticity*

In dynamic acousto-elastic testing, the setup is similar. The parameters of the discretization are the same as in the previous case. A resonance frequency is chosen, so as to maximize the strain levels. The sinusoidal source with frequency $f_c = 1585$ Hz and velocity amplitude V is turned on from $t = 0$ to $t \approx 50.4$ ms. Now, the receiver records the numerical solution at the abscissa $x = 0.1$ m, up to $t = 80$ ms.

Figure 5.5a displays the effective elastic modulus $\rho_0 c^2$ (5.16), which is recorded at the position of the receiver. A slow decrease of the elastic modulus combined with fast oscillations is observed. The frequency of the fast oscillations is the frequency f_c of the source signal. When the source is stopped ($t \approx 50.4$ ms), the amplitude of the fast oscillations diminishes, and the elastic modulus recovers gradually its initial value. The duration of the softening is related to the characteristic time $\tau_g = \alpha/\gamma$ of the slow dynamics, and to the quality factor Q. As observed experimentally, the softening phenomenon is accentuated when the amplitude of forcing V is increased.

Figure 5.5b focuses on the steady-state solution. Here, the last period of signal before the end of excitation is used. When the effective elastic modulus is represented with respect to the strain at the position of the receiver, a hysteresis curve is obtained. The shape of the hysteresis curve is related to the coefficients β and δ of the polynomial law (5.2), and to the dissipation in the material (see Figure 5.2 and [1]).

Up to this point, we have adapted the works presented in Chapter 4 to viscoelastic material with softening (1D) [4]. The finite-volume tool is now able to perform more realistic simulations than in the elastic case. In particular, resonance experiments are reproduced numerically with a qualitative agreement. However, the computational time needed to produce the curves in Fig. 5.4b is large, for a small number of points on the curve (20 frequencies). In facts, for each

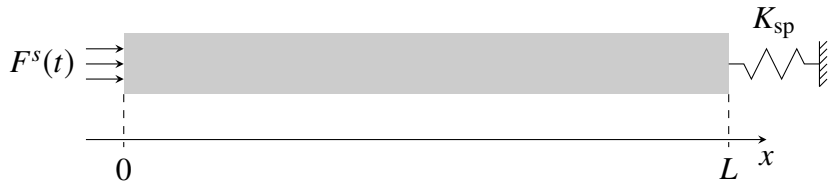

Figure 5.6. Mechanical model. The stress $F^s(t)$ is applied at one end of the bar, and a spring with stiffness K_{sp} is attached at the other end.

forcing amplitude V, the computation lasts around 35 min on a recent desktop computer (Intel Core i5-4690, 3.5 GHz, 16 Go, 2015). The next section is devoted to the development of a frequency-domain tool, which reduces drastically the computational time needed for resonance simulations.

3. Frequency-domain numerical method

In this section, a configuration related to real experiments is considered [115]. A cylindrical sample of Berea sandstone is suspended on strings, and longitudinal motion is induced by a piezoelectric disc glued onto one of its ends. The piezoelectric disk is assumed to impose a uniform sinusoidal force by unit surface $F^s(t)$ on the forced end, say at $x = 0$. The specific contribution of the transducer to the dynamics is neglected. The action of the strings is modeled by a spring with stiffness K_{sp}, which is assumed to impose a small uniform force by unit surface on the free edge of the sample ($x = L$). Including such a spring in the model avoids the occurrence of rigid-body motion, and is consistent with the action of suspending strings in the small perturbation limit. A schematic representation of the configuration is shown in Fig. 5.6. The boundary conditions are

$$\sigma(0,t) = F^s(t), \qquad \sigma(L,t) = -\frac{K_{\text{sp}}}{S_{\text{sp}}}\, u(L,t), \tag{5.40}$$

where u is the displacement field and S_{sp} denotes the cross-section area of the cylinder. In [115], the latter is $S_{\text{sp}} = 5.23\ \text{cm}^2$, and the sample's length is $L = 305.5$ mm. In what follows, the spring's stiffness is set to $K_{\text{sp}} = 10^3$ N/m.

3.1. Numerical resolution

3.1.a. *Semidiscrete weak form*

The material behavior is represented by the previous viscoelastic model with softening (Section 1). The softening function is $\phi_1(g) = 1 - g$, and the storage energy is $\phi_2(g) = \frac{1}{2}\gamma g^2$. Using the relation $v = \partial_t u$, the conservation of momentum $\rho_0 \partial_t v = \partial_x \sigma$ in (5.13) is rewritten as $\rho_0 \partial_{tt} u = \partial_x \sigma$. The expression of σ and the evolution equations of ξ_ℓ, g in (5.13) are unchanged, besides that ε, v are replaced by $\partial_x u$, $\partial_t u$.

We follow the mixed finite element approach, in a displacement-stress formulation [14, 21]. Thus, the conservation of momentum $\rho_0 \partial_{tt} u = \partial_x \sigma$ is multiplied

by the test function $\tilde{u} \in H^1$, while the expression of σ in (5.13) is multiplied by the test function $\tilde{\sigma} \in L^2$. The evolution equations of ξ_ℓ, g are multiplied by the test functions $\tilde{\xi}_\ell$, $\tilde{g}$ from L^2, respectively. Each equation is integrated over $x \in [0, L]$, leading to a weak formulation of the equations of motion. Integrating $\int_0^L \partial_x \sigma\, \tilde{u}\, \mathrm{d}x$ by parts, one obtains

$$\begin{cases} \rho_0 \langle \partial_{tt} u, \tilde{u} \rangle = (\sigma\, \tilde{u})|_{x=L} - (\sigma\, \tilde{u})|_{x=0} - \langle \sigma, \partial_x \tilde{u} \rangle\,, \\ \langle \sigma, \tilde{\sigma} \rangle = \displaystyle\sum_{\ell=1}^{N_v} \langle (1-g) W'_\ell(\xi_\ell), \tilde{\sigma} \rangle\,, \\ \langle \partial_t \xi_\ell, \tilde{\xi}_\ell \rangle = \langle \partial_{tx} u, \tilde{\xi}_\ell \rangle + \dfrac{1}{\nu_\ell} \left(K_\ell \langle (\partial_x u - \xi_\ell), \tilde{\xi}_\ell \rangle - \langle W'_\ell(\xi_\ell), \tilde{\xi}_\ell \rangle \right), \\ \alpha \langle \partial_t g, \tilde{g} \rangle = \left(\displaystyle\sum_{\ell=1}^{N_v} \langle W_\ell(\xi_\ell), \tilde{g} \rangle + \frac{1}{2} K_\ell \langle (\partial_x u - \xi_\ell)^2, \tilde{g} \rangle \right) - \gamma \langle g, \tilde{g} \rangle\,, \end{cases} \tag{5.41}$$

where $\langle h_1, h_2 \rangle = \int_0^L h_1\, h_2\, \mathrm{d}x$ for any functions h_1, h_2. These equations must be satisfied by the unknown fields u, σ, ξ_ℓ, g for arbitrary test functions $\tilde{u}$, $\tilde{\sigma}$, $\tilde{\xi}_\ell$, $\tilde{g}$.

For computational purposes, the system (5.41) is rewritten in finite-dimensional spaces. We denote by P^k the vector space of polynomials with degree k or less. The displacements $u, \tilde{u}$ are chosen in the polynomial space P^1 while the variables σ, $\tilde{\sigma}$, ξ_ℓ, $\tilde{\xi}_\ell$, g, $\tilde{g}$ belong to the polynomial space P^0, resulting in P^1-P^0 mixed elements. The finite element discretization is carried out using the Galerkin method based on Lagrange finite elements. For this purpose, a regular spatial discretization $x_i = (i-1)\, L_e$ is introduced, where $L_e = L/N_e$ is the element size and $i = 1, \ldots, N_e + 1$. Interior nodes have abscissas $x_{i+1/2} = (i - \frac{1}{2})\, L_e$ for $i = 1, \ldots, N_e$.

According to the previous choices, both the unknown displacement field u and the test function $\tilde{u}$ belong to the span of the P^1 basis functions $\{\psi_1, \ldots, \psi_{N_e+1}\}$ defined by

$$\psi_i(x) = \begin{cases} 1 - \zeta_i(x) & \text{if} \quad \zeta_i(x) \leqslant 1\,, \\ 0 & \text{elsewhere,} \end{cases} \tag{5.42}$$

where $\zeta_i(x) = |x - x_i|/L_e$. The unknown fields σ, ξ_ℓ, g and the test functions $\tilde{\sigma}$, $\tilde{\xi}_\ell$, $\tilde{g}$ belong to the span of the P^0 basis functions $\{\varphi_1, \ldots, \varphi_{N_e}\}$ defined by

$$\varphi_p(x) = \begin{cases} 1 & \text{if} \quad \zeta_{p+1/2}(x) \leqslant 1/2\,, \\ 0 & \text{elsewhere.} \end{cases} \tag{5.43}$$

Using Einstein's convention, we decompose the unknown fields as $u(x,t) = u_j(t)\, \psi_j(x), \sigma(x,t) = \sigma_q(t)\, \varphi_q(x)$, etc., where $u_j(t), \sigma_q(t)$, etc., are time-dependent grid-node unknowns. The fact that (5.41) must hold for arbitrary test functions amounts to test each basis function of the finite-dimensional spaces P^1 and P^0, i.e. $\tilde{u} = \psi_i$, $\tilde{\sigma} = \varphi_p$, etc. Thus, the following set of ordinary differential equations

is obtained:

$$\begin{cases} \rho_0 \langle \psi_i, \psi_j \rangle \ddot{u}_j = -\dfrac{K_{\rm sp}}{S_{\rm sp}} \delta_i^{N_e+1} \delta_j^{N_e+1} u_j - F^s \delta_i^1 - \langle \psi_i', \varphi_q \rangle \sigma_q \,, \\ \sigma_q = \displaystyle\sum_{\ell=1}^{N_v} \big((1-g) W_\ell'(\xi_\ell) \big)_q \,, \\ (\dot{\xi}_\ell)_q = \dot{\varepsilon}_q + \dfrac{1}{\nu_\ell} \big(K_\ell \, (\varepsilon - \xi_\ell)_q - W_\ell'(\xi_\ell)_q \big) \,, \\ \alpha \dot{g}_q = \left(\displaystyle\sum_{\ell=1}^{N_v} W_\ell(\xi_\ell)_q + \frac{1}{2} K_\ell \big((\varepsilon - \xi_\ell)^2 \big)_q \right) - \gamma g_q \,, \end{cases} \tag{5.44}$$

where $\delta_\bullet^\bullet$ denotes the Kronecker delta, the dot denotes the time derivative, and

$$\varepsilon_q = T_{qj} \, u_j \qquad \text{with} \qquad (T_{qj}) = \left(\langle \varphi_q, \varphi_p \rangle \right)^{-1} \left(\langle \varphi_p, \psi_j' \rangle \right) . \tag{5.45}$$

The scalar products of the basis functions ψ_i, ψ_i', φ_p in (5.44)-(5.45) are detailed in the Appendix, Sec. 5.3.

In time-domain finite-element methods, the differential system (5.44) is integrated numerically using a finite-difference method [14]. Doing so, the transient regime is captured, followed by the steady-state periodic solution (similarly to the results obtained with the finite-volume method of Sec. 2). Here, we follow a frequency-domain approach, aimed at computing long-time periodic solutions. As described in the next subsection, the system (5.44) is solved numerically using a Fourier series Ansatz.

3.1.b. *Continuation method*

We describe the numerical continuation method [27] hereinafter. The method applies to generic first-order quadratic differential-algebraic systems

$$\boldsymbol{A} \cdot \dot{\boldsymbol{q}} = \boldsymbol{c} + \boldsymbol{L} \cdot \boldsymbol{q} + \boldsymbol{Q} : (\boldsymbol{q} \otimes \boldsymbol{q}) , \tag{5.46}$$

or $A_{ab} \dot{q}_b = c_a + L_{ab} q_b + Q_{abc} q_b q_c$ with index notation, which are dependent on a parameter. This *continuation parameter* is the exciting angular frequency ω in the case of resonance simulations. The formulation (5.46) can account for many types of nonlinearity by introducing intermediate variables in the column vector $\boldsymbol{q}$ of length $N_{\boldsymbol{q}}$.

As such, the harmonic balance method (HBM) is aimed at computing periodic solutions of (5.46) using truncated Fourier series with H harmonics. Thus, $\boldsymbol{q}$ is expanded as truncated Fourier series with angular frequency ω, and this Ansatz is injected in (5.46). An algebraic system of $(2H+1) \times N_{\boldsymbol{q}}$ equations with respect to the Fourier coefficients of $\boldsymbol{q}$ is obtained, which can be solved numerically using Newton's method. As shown later, resonance curves are deduced from the set of Fourier coefficients so-obtained.

Computing the resonance curves using HBM and Newton's method for various frequencies is not convenient, in particular when solutions are not

Table 5.2. Linear viscoelastic parameters of Berea sandstone.

ρ_0 (kg m^{-3})	M_{rel} (GPa)	Q	f_Q (kHz)	τ_ε (ms)	τ_σ (ms)
2054	7.44	55	3.137	5.1666×10^{-2}	4.9821×10^{-2}

unique. Continuation methods provide an efficient way of following solutions while varying the frequency [27, 121]. Based on a series expansion of the solution with respect to a pseudo-arc length parameter, the asymptotic numerical method (ANM) provides continuous branches of the resonance curve, which length — frequency step — is adaptively set. The method is implemented in the ManLab and Diamanlab software tools, of which a recent version is used here.

3.2. Results

3.2.a. *Linear viscoelasticity*

We consider a linear viscoelastic material ($\beta = 0, \delta = 0$, no softening). Since the present study is focused on a small frequency range, a single-degree-of-freedom Zener rheology is assumed ($N_v = 1$), so that all indexes ℓ can be removed. In such materials, the wavenumber k of a harmonic plane wave satisfies the dispersion relation (5.36) (cf. Chapter 2 of [20]). The frequency-evolution of the quality factor Q is given by (5.59). As illustrated in Figure 5.7, the quality factor Q is minimum at the angular frequency $\omega_Q = 2\pi f_Q = (\tau_\varepsilon \tau_\sigma)^{-1/2}$. Given the minimum value of the quality factor $Q(\omega_Q)$, one deduces [20]

$$\tau_\varepsilon = \frac{\sqrt{Q(\omega_Q)^2 + 1} + 1}{Q(\omega_Q)\,\omega_Q}, \qquad \tau_\sigma = \frac{\sqrt{Q(\omega_Q)^2 + 1} - 1}{Q(\omega_Q)\,\omega_Q}. \tag{5.47}$$

One can note that $\tau_\varepsilon > \tau_\sigma$, which is necessary for thermodynamical reasons. In Table 5.2, the values of τ_ε, τ_σ are deduced from $Q(\omega_Q)$ according to (5.47).

The frequency-response function of the linear system is defined as the ratio of the output spectrum (particle velocity at $x = L$) to the input spectrum (stress at $x = 0$), i.e.

$$FRF(\omega) = \frac{\hat{v}|_{x=L}(\omega)}{\hat{\sigma}|_{x=0}(\omega)}, \tag{5.48}$$

where the hat denotes the Fourier transform in time. For a harmonic excitation $F^s(t) = \exp(\mathrm{i}\omega t)$, we write the displacement field as a superposition of left-going and right-going monochromatic plane waves. Thus, $u(x,t) = \left(A\,\mathrm{e}^{\mathrm{i}kx} + B\,\mathrm{e}^{-\mathrm{i}kx}\right)\mathrm{e}^{\mathrm{i}\omega t}$ and $\sigma(x,t) = \rho_0(\omega/k)^2\,\partial_x u(x,t)$, where the wavenumber k satisfies the dispersion relation (5.36). The coefficients A and B are deduced from the boundary conditions (5.40). Finally, the following expression of the frequency-response function (5.48) is obtained:

$$FRF(\omega) = \frac{\mathrm{i}\omega}{\rho_0 \frac{\omega^2}{k}\sin(kL) - \frac{K_{\text{sp}}}{S_{\text{sp}}}\cos(kL)}, \tag{5.49}$$

where the wavenumber k is complex and frequency-dependent. Note that the

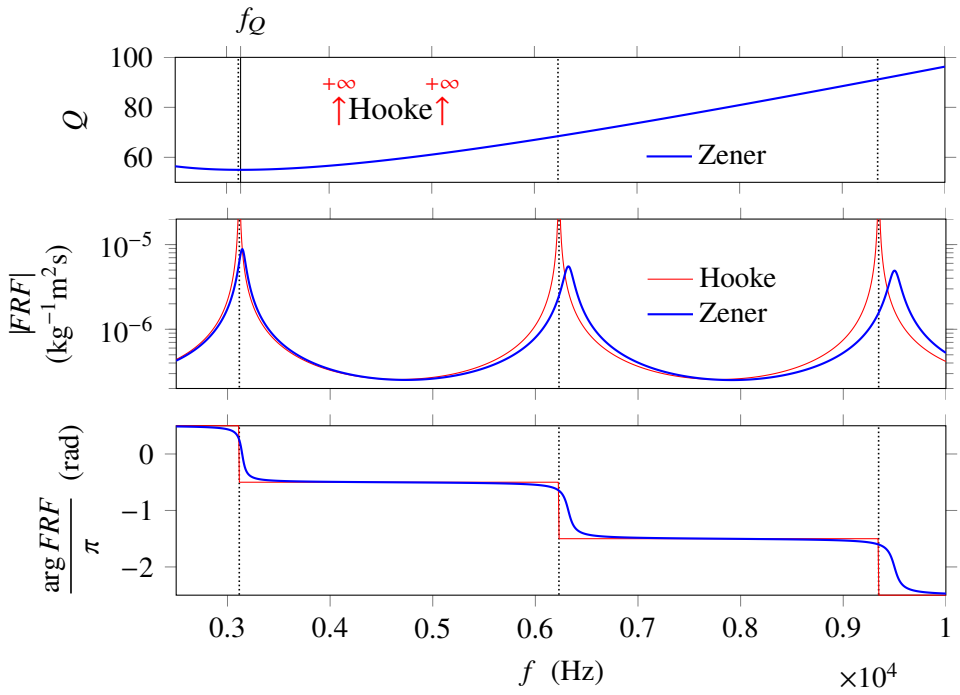

Figure 5.7. Hooke elasticity and Zener viscoelasticity (parameters in Table 5.2). Top: quality factor. The vertical solid line marks the frequency f_Q where $Q = 55$. Bottom: frequency-response function (5.49), modulus and phase. The dotted lines mark the resonance frequencies of the elastic system without spring.

expression (5.49) is not restricted to the dispersion relation (5.36) of Zener material.

Figure 5.7 shows the frequency-response function (5.49) in the viscoelastic case and in the elastic case up to the third mode. The parameters are given in Table 5.2 and in the description of the boundary conditions (5.40). Fig. 5.7 illustrates the finite height of the resonance peaks and their frequency shift due to viscoelastic attenuation. If no spring is attached ($K_{\mathrm{sp}} = 0$), then $|FRF(\omega)| = k\,(\rho_0\omega\sin(kL))^{-1}$. In this case, the resonance frequencies of the linear elastic system are multiples of $\frac{1}{2L}\sqrt{M_{\mathrm{rel}}/\rho_0} \approx 3.115$ kHz (vertical dotted lines in Fig. 5.7). One notes that the influence of the spring constant $K_{\mathrm{sp}} = 10^3$ N/m on the resonance frequencies is negligible.

The semidiscrete weak formulation of the equations of motion (5.44) becomes

$$\begin{cases} \rho_0\langle\psi_i,\psi_j\rangle\ddot{u}_j = -\dfrac{K_{\mathrm{sp}}}{S_{\mathrm{sp}}}\delta_i^{N_e+1}\delta_j^{N_e+1}u_j - F^s\delta_i^1 - M\langle\psi_i',\varphi_q\rangle\xi_q\,, \\ \dot{\xi}_q = \dot{\varepsilon}_q + \dfrac{K}{\nu}\varepsilon_q - \dfrac{M+K}{\nu}\xi_q\,. \end{cases} \tag{5.50}$$

The corresponding first-order DAE system (5.46) is linear ($\boldsymbol{Q} = \boldsymbol{0}$), which arrays $\boldsymbol{A}, \boldsymbol{c}, \boldsymbol{L}$ are given in the Appendix 5.3. The vector of unknowns

$$\boldsymbol{q} = (u_1, \ldots, u_{N_e+1}, \dot{u}_1, \ldots, \dot{u}_{N_e+1}, \xi_1, \ldots, \xi_{N_e})^\top \tag{5.51}$$

has length $N_{\boldsymbol{q}} = 3N_e+2$. In case of a time-periodic forcing with angular frequency

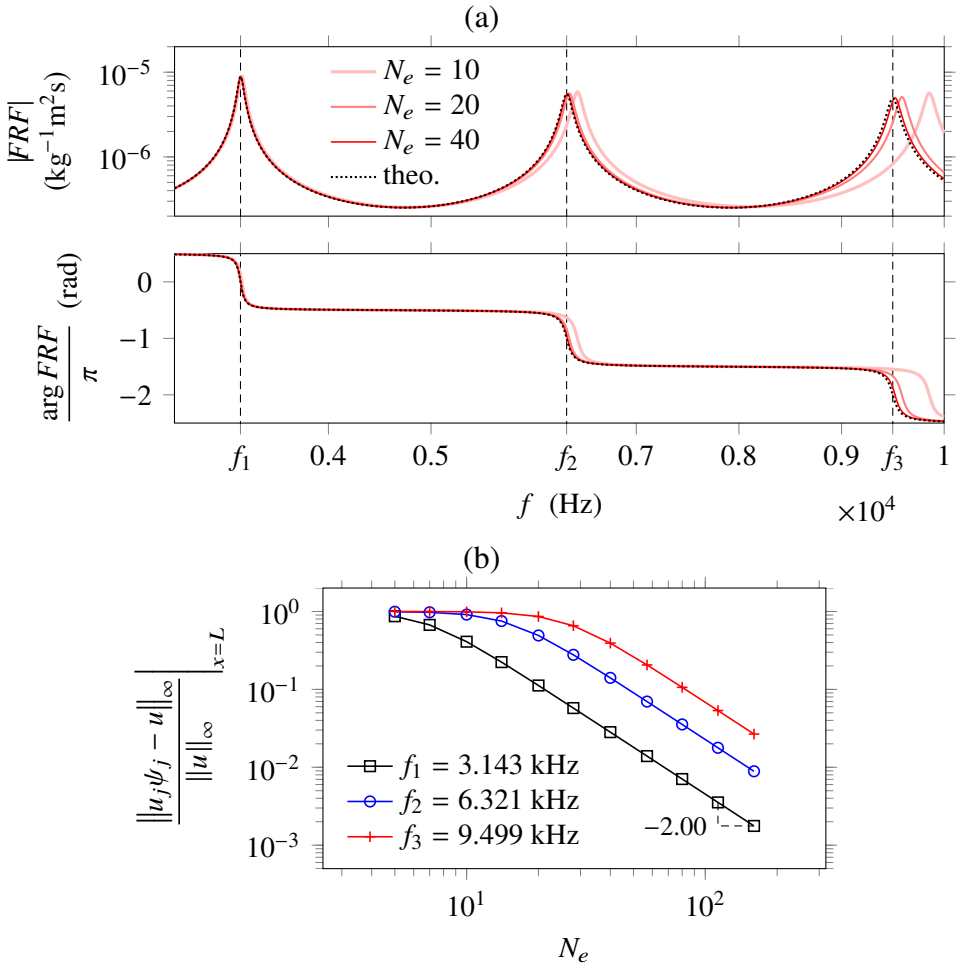

Figure 5.8. Convergence of the semidiscrete weak formulation (5.50) for linear Zener material. (a) Frequency-response functions. (b) L^∞ relative error of the HBM displacement $u_j\psi_j|_{x=L}$ with respect to the exact long-time displacement $u|_{x=L}$.

$\omega = 2\pi f$, the frequency-response (5.48) is the ratio

$$FRF(\omega) = \frac{c_1(v|_{x=L})}{c_1(\sigma|_{x=0})}, \tag{5.52}$$

where $c_1 = \frac{1}{2}(a_1 - \mathrm{i}b_1)$ denotes the first complex Fourier coefficient at the angular frequency ω, and (a_1, b_1) are the first real cosine and sine Fourier coefficients.

Since the ODE system (5.50) is linear, no harmonic generation occurs, and one can set $H = 1$ in the harmonic balance. No continuation algorithm is used here, and the HBM is applied straightforwardly. The forcing $F^s(t) = V\sin(2\pi ft)$ has amplitude $V = 1$ N/m^2 and frequency $f = \omega/(2\pi)$. With the same parameters as in Figure 5.7, the frequency response of the discretized system deduced from harmonic balance is computed according to (5.52) for various numbers of elements N_e (Figure 5.8). The resonance curves are shown in Fig. 5.8a, which illustrates the convergence of the method. Error measurements in uniform L^∞ norm are shown in Fig. 5.8b, performed on the displacement field at the abscissa $x = L$. The exciting frequency f belongs to the first three resonance frequencies f_1, f_2, f_3 of the forced system. Second-order accuracy is obtained as the grid is

refined. Subsequently, we set $N_e = 30$ elements, which corresponds to twenty P^1-P^0 mixed elements per wavelength at the frequency f_3.

3.2.b. *Nonlinear viscoelasticity*

We consider a nonlinear Zener material (no softening). In the small strain limit, it reduces to a linear Zener body, with the parameters in Table 5.2. The influence of higher-order elastic constants β, δ accounting for material nonlinearity is examined here, around the first resonance peak. The semidiscrete weak formulation of the equations of motion (5.44) reads

$$\begin{cases} \rho_0 \langle \psi_i, \psi_j \rangle \ddot{u}_j = -\dfrac{K_{\text{sp}}}{S_{\text{sp}}} \delta_i^{N_e+1} \delta_j^{N_e+1} u_j - F^s \delta_i^1 - M \langle \psi_i', \varphi_q \rangle \xi_q \\ \qquad\qquad + \beta M \langle \psi_i', \varphi_q \rangle {\xi_q}^2 + \delta M \langle \psi_i', \varphi_q \rangle {\xi_q}^3, \\ \dot{\xi}_q = \dot{\varepsilon}_q + \dfrac{K}{\nu} \varepsilon_q - \dfrac{M+K}{\nu} \xi_q + \beta \dfrac{M}{\nu} {\xi_q}^2 + \delta \dfrac{M}{\nu} {\xi_q}^3, \end{cases} \tag{5.53}$$

where ε_q is defined in (5.45). The corresponding first-order DAE system (5.46) is quadratic ($\boldsymbol{Q} \neq \boldsymbol{0}$). If $\delta = 0$, the vector of unknowns $\boldsymbol{q}$ is the same as in the linear viscoelastic case (5.51), and the arrays $\boldsymbol{A}$, $\boldsymbol{c}$, $\boldsymbol{L}$, $\boldsymbol{Q}$ are given in the Appendix 5.3. If $\delta \neq 0$, the vector of unknowns is augmented with intermediate variables

$$\boldsymbol{q} = \left(u_1, \ldots, u_{N_e+1}, \dot{u}_1, \ldots, \dot{u}_{N_e+1}, \xi_1, \ldots, \xi_{N_e}, {\xi_1}^2, \ldots, {\xi_{N_e}}^2\right)^\top, \tag{5.54}$$

reaching the size $N_{\boldsymbol{q}} = 4N_e + 2$. Similarly to the case $\delta = 0$, the system (5.53) is rewritten as a first-order quadratic system (5.46).

The settings of the numerical method are the same for all the results presented hereinafter. The equations of motion are discretized using $N_e = 30$ elements, and harmonic balance with $H = 3$ harmonics is used. The continuation of the solution with respect to the angular frequency $\omega = 2\pi f$ is started at the frequency $f = 3.495$ kHz, where the variables are initialized according to the linear viscoelastic case. New variables such as ${\xi_1}^2, \ldots, {\xi_{N_e}}^2$ are initially set to zero. Then, the frequency is decreased stepwise. The ANM threshold is 10^{-8}, while the correction threshold is 10^{-6}. Since the numerical continuation algorithm is adaptive, simulations do not take always the same amount of computational time. With a recent desktop computer (Intel Core i5-4690, 3.5 GHz, 16 Go, 2015), such simulations can last from ten seconds to two minutes.

Figure 5.9 displays the modulus and the phase of the frequency-response function as defined in (5.52), in the vicinity of the first resonance peak. The parameters β, δ in the simulations are given in Table 5.3. The amplitude V of the forcing $F^s(t) = V \sin(2\pi f t)$ in Table 5.3 is varied from its half (curve denoted by $\frac{1}{2}V$) to its double (curve denoted by $2V$). At low forcing amplitudes, the frequency response is superimposed to the one obtained in the linear case. At larger forcing amplitudes, a frequency shift of the resonance peak with increasing amplitudes is observed. At large forcing amplitudes, the curves are multi-valued functions of the frequency. This is similar to the frequency response of the Duffing oscillator, which shows hysteresis depending on the frequency sweep direction.

In Figure 5.10, the influence of the nonlinearity parameters $\beta \neq 0$ and $\delta \neq 0$ with respect to the three first harmonic amplitudes of $\dot{u}|_{x=L}$ is shown. One can

Table 5.3. Reference parameters for the nonlinear resonance simulations.

V (N m^{-2})	β	δ	γ (J m^{-3})	α (J m^{-3} s)
244.75	5×10^3	2×10^{10}	7×10^{-2}	6×10^{-6}

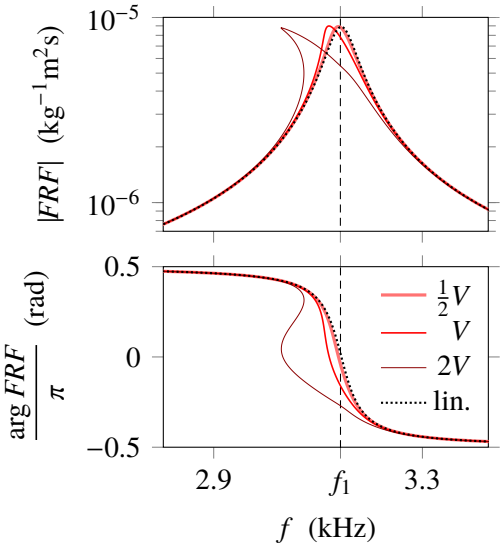

Figure 5.9. Nonlinear viscoelasticity. Frequency response function (5.52) for several forcing amplitudes V, modulus (top) and phase (bottom).

observe that higher-order harmonics are not negligible. The first row of the figure illustrates that β controls the amplitude of the second harmonic. In the second row, one can observe that the parameter δ accounting for cubic nonlinearity controls mainly the amplitude of the third harmonic, and the frequency shift of the resonance peak.

3.2.c. *Linear viscoelasticity with softening*

We consider a linear Zener material with softening ($\beta = \delta = 0$). The influence of the parameters γ, α related to the softening is examined. The semidiscrete weak formulation of the equations of motion (5.44) reads

$$\begin{cases} \rho_0 \langle \psi_i, \psi_j \rangle \ddot{u}_j = -\dfrac{K_{\mathrm{sp}}}{S_{\mathrm{sp}}} \delta_i^{N_e+1} \delta_j^{N_e+1} u_j - F^s \delta_i^1 - M \langle \psi_i', \varphi_q \rangle \xi_q \\ \qquad\qquad + M \langle \psi_i', \varphi_q \rangle (g\xi)_q, \\ \dot{\xi}_q = \dot{\varepsilon}_q + \dfrac{K}{\nu} \varepsilon_q - \dfrac{M+K}{\nu} \xi_q, \\ \dot{g}_q = \dfrac{M}{2\alpha} {\xi_q}^2 + \dfrac{K}{2\alpha} (\varepsilon_q - \xi_q)^2 - \dfrac{\gamma}{\alpha} g_q, \end{cases} \tag{5.55}$$

where $(g\xi)_q = g_q \xi_q$ for all q in $1, \ldots, N_e$, and ε_q is defined in (5.45). The corresponding first-order DAE system (5.46) is quadratic ($\boldsymbol{Q} \neq \boldsymbol{0}$). The vector

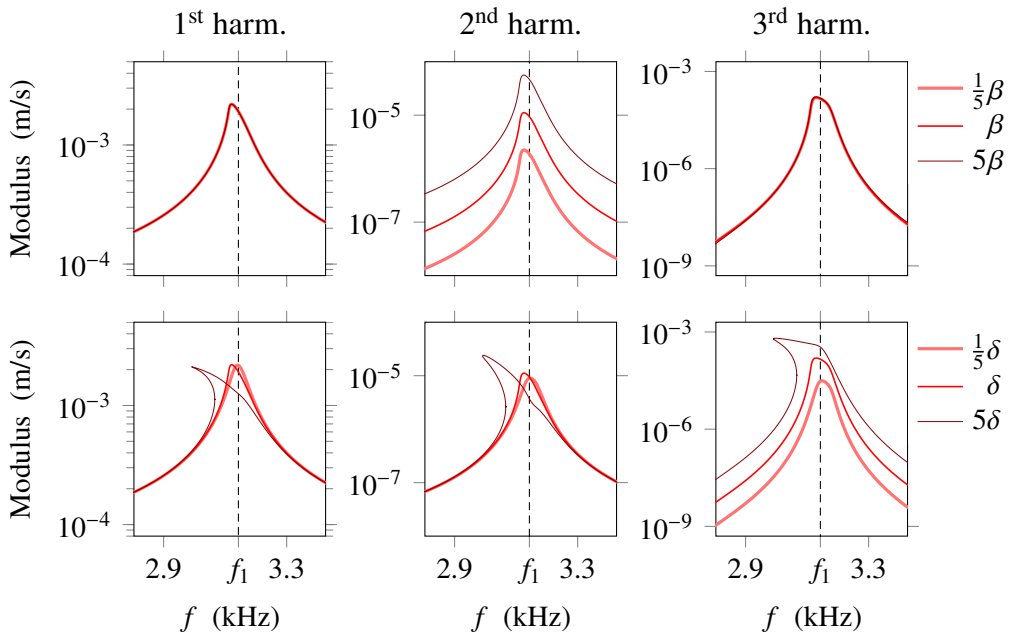

Figure 5.10. Nonlinear viscoelasticity. Frequency-evolution of the first three harmonics of the particle velocity $\dot{u}|_{x=L}$ for several values of β (top) and δ (bottom).

of unknowns $\boldsymbol{q}$ is augmented with intermediate variables

$$\boldsymbol{q} = \begin{array}{l}(u_1, \ldots, u_{N_e+1}, \dot{u}_1, \ldots, \dot{u}_{N_e+1}, \xi_1, \ldots, \xi_{N_e}, \\ g_1, \ldots, g_{N_e}, \varepsilon_1, \ldots, \varepsilon_{N_e})^\top,\end{array} \tag{5.56}$$

reaching the size $N_{\boldsymbol{q}} = 5N_e + 2$.

Figure 5.11 is analogous to Fig. 5.9. The parameters γ, α in the simulations are given in Table 5.3. The amplitude V of the forcing $F^s(t) = V \sin(2\pi f t)$ in Table 5.3 is varied from its half (curve denoted by $\frac{1}{2}V$) to its double (curve denoted by $2V$). A frequency shift of the resonance peak with increasing forcing amplitudes is observed, as well as multi-valued functions at large amplitudes. However, one can observe that the height of the resonance peak is decreasing with increasing forcing amplitudes. This feature is in agreement with experimental observations reported in the literature [43, 55, 107, 135], and was not observed in the nonlinear viscoelastic case (Fig. 5.9).

Figure 5.12 is analogous to Fig. 5.10. With the present model, no second-harmonic generation occurs. The first row details the influence of the material parameter γ accounting for the softening. The figure illustrates that γ controls the frequency shift of the resonance peak. This observation is in agreement with the calculus in [1], where the softening is shown to be inversely proportional to γ. In the second row, one can observe that α controls mainly the height of the peaks. The energy transfer from the first to the third harmonic decreases when α increases.

Similarly to [105, 134], we introduce the strain amplitude ϵ deduced from the displacement at the free edge $x = L$. Up to a factor π which is missing in

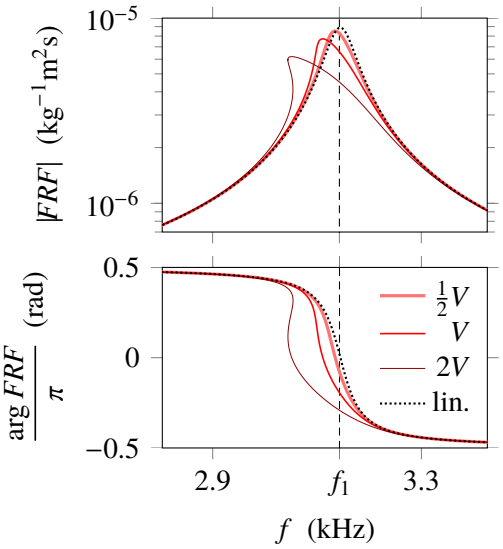

Figure 5.11. Linear viscoelasticity with softening. Frequency response function (5.52) for several forcing amplitudes V, modulus (top) and phase (bottom).

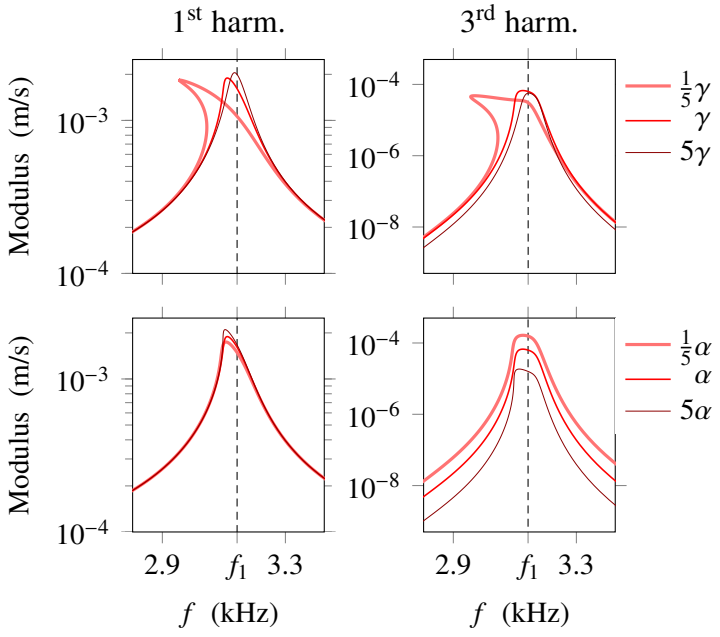

Figure 5.12. Linear viscoelasticity with softening. Frequency-evolution of the first three harmonics of the particle velocity $\dot{u}|_{x=L}$ for several values of γ (top) and α (bottom). Here, no second harmonic is generated.

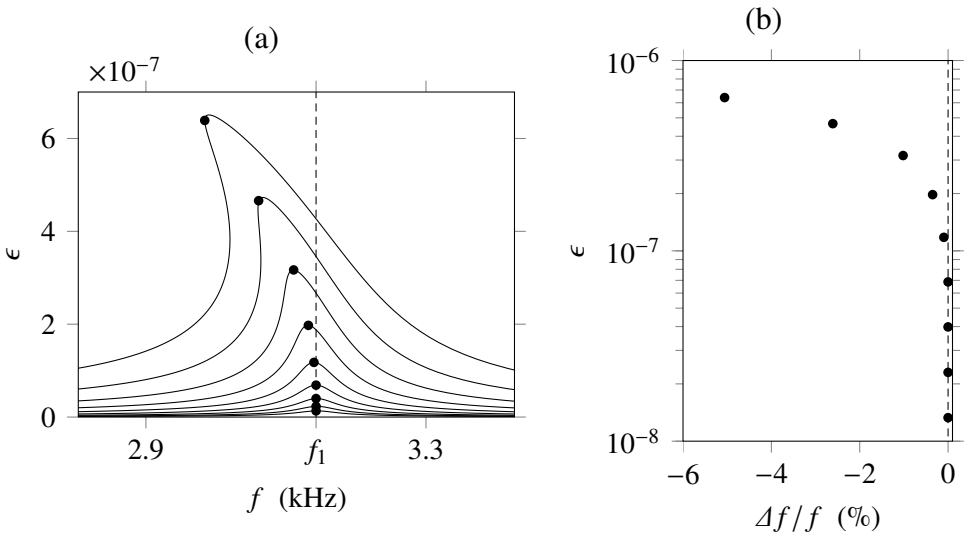

Figure 5.13. Linear viscoelasticity with softening. (a) Strain amplitude resonance curve, where ϵ is defined in (5.57). (b) Evolution of the resonance peak's frequency shift with respect to the strain amplitude.

[105, 134], we define

$$\epsilon \simeq \frac{2\,|c_1(u|_{x=L})|}{L} = \frac{2\,|c_1(\ddot{u}|_{x=L})|}{(2\pi f)^2 L}\,. \tag{5.57}$$

A set of resonance curves is generated for the forcing amplitudes $V^{(n+3)/10}$ where $n = 1, \ldots, 9$, which are equally spaced on a logarithmic scale. For each amplitude, the frequency-evolution of ϵ is displayed in Fig. 5.13a. The relative frequency shift $\Delta f/f$ of the resonance peak with respect to $f_1 = 3.143$ kHz is then reported in Fig. 5.13b. The curves so-obtained are similar to those reported in the literature.

4. Conclusion

In this chapter, the coupling of nonlinear stress-strain relationships with viscoelastic behavior and with slow dynamics has been achieved using internal variables of state. The stiff system of equations so-obtained requires particular care when using numerical methods. Numerical simulations with finite-volume schemes show qualitative agreement with experimental observations from dynamic acousto-elasticity (DAET) and resonance (NRUS) experiments. Using a frequency-domain continuation method, the influence of several model parameters has been examined. A high sensitivity of the harmonic generation with respect to several parameters has been shown. Therefore, the experimental measurement of higher-order harmonics is crucial for fine tuning of the model.

Let us compare both numerical methods. For each forcing amplitude, the computation lasts around 35 min with the finite-volume method, for a small number of points on the curve (Intel Core i5-4690, 3.5 GHz, 16 Go, 2015). Using the harmonic-based continuation method, the computation lasts around 20 s, and a continuous resonance curve is obtained. With the prospects of experimental validations, the drastic reduction of computational time provided by the frequency-

domain method is interesting. However, the transient information is lost with this method. Since the stress is not a conserved variable, it is difficult to impose an arbitrary stress at a boundary of the domain when using finite-volume methods. The finite-element method is much more flexible regarding boundary conditions. Both imposed stress or imposed displacement are possible. A direct comparison between both methods in the same configuration is under consideration.

Modifications and extensions of the present frequency-domain method are currently examined. Firstly, it would be interesting to follow the resonance frequency by performing numerical continuation with respect to the forcing amplitude (backbone curves). Secondly, instead of using finite-element basis functions, the solution could be decomposed on the basis of normal modes of the linear undamped system [18, 56, 136]. Lastly, the equations of motion could be rescaled using the characteristic times of the system.

5. Appendix

5.1. Parameters of the viscoelastic model

Let us consider the case of linear Zener material, which dispersion relation is given by (5.36). If the phase velocity $\omega/\mathrm{Re}\,k$ is equal to $c_{\mathrm{ref}} = \sqrt{M_0/\rho_0}$ at a given angular frequency ω_{ref}, then the relaxed elastic modulus

$$M_{\mathrm{rel}} = M_0\,\mathrm{Re}\left(\left(\frac{1}{N}\sum_{\ell=1}^{N}\frac{1+\mathrm{i}\omega_{\mathrm{ref}}\tau_{\varepsilon\ell}}{1+\mathrm{i}\omega_{\mathrm{ref}}\tau_{\sigma\ell}}\right)^{-1/2}\right)^2 \tag{5.58}$$

is deduced from the expression of the wavenumber k at the angular frequency ω_{ref}. The reciprocal of the quality factor $Q = -\mathrm{Re}(k^2)/\mathrm{Im}(k^2)$ is given by [20, 38]

$$Q^{-1} = \omega\left(\sum_{\ell=1}^{N}\frac{\tau_{\varepsilon\ell}-\tau_{\sigma\ell}}{1+\omega^2{\tau_{\sigma\ell}}^2}\right)\Bigg/\left(\sum_{\ell=1}^{N}\frac{1+\omega^2\tau_{\varepsilon\ell}\tau_{\sigma\ell}}{1+\omega^2{\tau_{\sigma\ell}}^2}\right). \tag{5.59}$$

The method to obtain the coefficients $\tau_{\sigma\ell}$, $\tau_{\varepsilon\ell}$ is described hereinafter.

One can note that the quality factor of the Zener model (5.59) depends only on the angular frequency ω, the number of relaxation mechanisms N_v, and the relaxation times $\tau_{\sigma\ell}$, $\tau_{\varepsilon\ell}$. If a reference frequency-dependent quality factor is known and a number N_v of relaxation mechanisms is chosen, then the distance between the quality factor in (5.59) and the reference quality factor can be minimized with respect to the parameters $\tau_{\sigma\ell}$, $\tau_{\varepsilon\ell}$. In practice, the distance is minimized over a set of $4N_v$ frequencies, which are logarithmically distributed over a frequency range of interest $[f_{\min}, f_{\max}]$. Optimization constraints are imposed to ensure that $\tau_{\varepsilon\ell} > \tau_{\sigma\ell} > 0$, which is necessary for positive spring and dashpot constants

$$M_\ell = \frac{\tau_{\varepsilon\ell}}{\tau_{\sigma\ell}}\frac{M_{\mathrm{rel}}}{N_v}, \qquad K_\ell = \frac{\tau_{\varepsilon\ell}}{\tau_{\varepsilon\ell}-\tau_{\sigma\ell}}\frac{M_{\mathrm{rel}}}{N_v}, \qquad \nu_\ell = \frac{{\tau_{\varepsilon\ell}}^2}{\tau_{\varepsilon\ell}-\tau_{\sigma\ell}}\frac{M_{\mathrm{rel}}}{N_v} \tag{5.60}$$

in the rheological model (Figure 5.1). If the relaxation times $\tau_{\sigma\ell}$ are sorted in descending order, then the constraint $1/\tau_{\sigma N_v} < f_{\max}$ is added to the optimization procedure. The reader is referred to [16] for details about such an optimization.

The frequency evolution of the quality factor's inverse Q^{-1} so-obtained is represented in Figure 5.14b, where a constant reference quality factor $Q = 20$ is chosen, and $N_v = 5$ Zener mechanisms are considered. The corresponding optimized coefficients are given in Table 5.4. In the Figure 5.14b, the reference quality factor is reached by the optimized Zener model over the frequency range [1, 100] kHz of the optimization procedure. The frequency evolution of the phase velocity $\omega/\mathrm{Re}\,k$ deduced from the dispersion relation (5.36) is represented in Figure 5.14a as well as the attenuation $-\mathrm{Im}\,k$. It can be verified that the phase velocity is equal to c_{ref} at the angular frequency ω_{ref}.

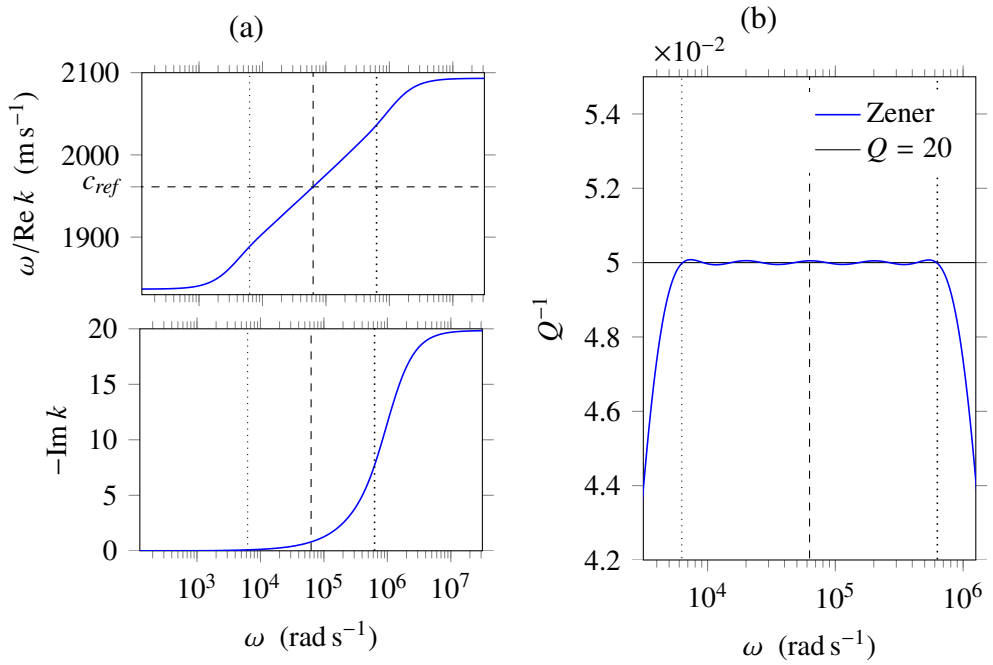

Figure 5.14. (a) Phase velocity (top) and attenuation (bottom) of the generalized Zener model, as a function of the angular frequency. (b) Quality factor of the generalized Zener model (5.59) compared to the reference $Q = 20$. The vertical dashed line marks $\omega_{\mathrm{ref}} = 2\pi \times 10^4$ rad s^{-1}, whereas the vertical dotted lines mark the bounds $2\pi f_{\mathrm{min}} = 0.1\,\omega_{\mathrm{ref}}$ and $2\pi f_{\mathrm{max}} = 10\,\omega_{\mathrm{ref}}$ of the frequency range of optimization.

Table 5.4. Optimized coefficients of the Zener model.

ℓ	$\tau_{\sigma\ell}$ (ms)	$\tau_{\varepsilon\ell}$ (ms)
1	$2.39556647121688 \times 10^{-1}$	$3.26820245620307 \times 10^{-1}$
2	$5.22532018808709 \times 10^{-2}$	$6.37792234728574 \times 10^{-2}$
3	$1.53966793063646 \times 10^{-2}$	$1.87515784083158 \times 10^{-2}$
4	$4.54569618004597 \times 10^{-3}$	$5.62759706637171 \times 10^{-3}$
5	$9.68524210724988 \times 10^{-4}$	$1.40683422528016 \times 10^{-4}$

5.2. Spectrum of the Roe's matrix

The eigenvalues of the matrix $\boldsymbol{A}_{i+1/2}$ are $\{-s^n_{i+1/2}, 0, \ldots, 0, +c^n_{i+1/2}\}$, where $s^n_{i+1/2}$ is given in (5.31). In order to show that $s^n_{i+1/2}$ is real, one must show that the sum of the coefficients $(a_\ell)_{1\leqslant\ell\leqslant N_v}$ is positive. The proof is based on the fact that the variables $\xi_1, \ldots, \xi_{N_v}$ and g satisfy the hyperbolicity condition, i.e. the strain energy $\xi_\ell \mapsto W_\ell(\xi_\ell)$ is restricted to a domain where it is convex, and g is bounded by 1 (cf. section 1.2).

If $(\xi_{\ell^\star})^n_i = (\xi_{\ell^\star})^n_{i+1}$ for some $\ell^\star$ between 1 and N, then the convexity of $W_{\ell^\star}$ and the bound $g < 1$ imply that $a_{\ell^\star}$ is positive (5.30). Otherwise, the coefficient a_ℓ in (5.29) is rewritten as

$$\begin{aligned} a_\ell = {} & \frac{W'_\ell\big((\xi_\ell)^n_{i+1}\big) - W'_\ell\big((\xi_\ell)^n_i\big)}{\rho_0\,\big((\xi_\ell)^n_{i+1} - (\xi_\ell)^n_i\big)} \\ & - g^n_i \frac{W_\ell\big((\xi_\ell)^n_{i+1}\big) - W_\ell\big((\xi_\ell)^n_i\big) - W'_\ell\big((\xi_\ell)^n_i\big)\big((\xi_\ell)^n_{i+1} - (\xi_\ell)^n_i\big)}{\rho_0\,\big((\xi_\ell)^n_{i+1} - (\xi_\ell)^n_i\big)^2} \\ & - g^n_{i+1} \frac{W_\ell\big((\xi_\ell)^n_i\big) - W_\ell\big((\xi_\ell)^n_{i+1}\big) - W'_\ell\big((\xi_\ell)^n_{i+1}\big)\big((\xi_\ell)^n_i - (\xi_\ell)^n_{i+1}\big)}{\rho_0\,\big((\xi_\ell)^n_{i+1} - (\xi_\ell)^n_i\big)^2}\,. \end{aligned} \tag{5.61}$$

Due to the convexity of W_ℓ, the first right-hand side term is positive, as well as the ratios multiplied by $-g^n_i$ and $-g^n_{i+1}$. The bound $g < 1$ implies

$$\begin{aligned} a_\ell \geqslant {} & \frac{W'_\ell\big((\xi_\ell)^n_{i+1}\big) - W'_\ell\big((\xi_\ell)^n_i\big)}{\rho_0\,\big((\xi_\ell)^n_{i+1} - (\xi_\ell)^n_i\big)} \\ & - \frac{W_\ell\big((\xi_\ell)^n_{i+1}\big) - W_\ell\big((\xi_\ell)^n_i\big) - W'_\ell\big((\xi_\ell)^n_i\big)\big((\xi_\ell)^n_{i+1} - (\xi_\ell)^n_i\big)}{\rho_0\,\big((\xi_\ell)^n_{i+1} - (\xi_\ell)^n_i\big)^2} \\ & - \frac{W_\ell\big((\xi_\ell)^n_i\big) - W_\ell\big((\xi_\ell)^n_{i+1}\big) - W'_\ell\big((\xi_\ell)^n_{i+1}\big)\big((\xi_\ell)^n_i - (\xi_\ell)^n_{i+1}\big)}{\rho_0\,\big((\xi_\ell)^n_{i+1} - (\xi_\ell)^n_i\big)^2}\,, \end{aligned} \tag{5.62}$$

and hence, $a_\ell \geqslant 0$. This ends the proof: $\boldsymbol{A}_{i+1/2}$ is a Roe matrix. Eq. (5.61) is also useful to obtain (5.30) by taking the limit as $(\xi_\ell)^n_{i+1} \to (\xi_\ell)^n_i$.

5.3. First-order quadratic recast

We describe the first-order quadratic recast (5.46) in the viscoelastic case (5.53) where $\delta = 0$. The vector of unknowns $\boldsymbol{q}$ given in (5.51) is of size $N_{\boldsymbol{q}} = 3N_e + 2$. According to (5.50), the column vector $\boldsymbol{c}$ reads blockwise

$$\boldsymbol{c} = \begin{pmatrix} (0) \\ -F^s\,(\delta^1_i) \\ (0) \end{pmatrix}, \tag{5.63}$$

and the matrices $\boldsymbol{A}$, $\boldsymbol{L}$ read blockwise

$$\boldsymbol{A} = \begin{pmatrix} (\delta_i^j) & (0) & \dots \\ (0) & \rho_0\,(\langle\psi_i,\psi_j\rangle) & (0) \\ \dots & (0) & (\delta_p^q) \end{pmatrix}, \tag{5.64}$$

$$\boldsymbol{L} = \begin{pmatrix} (0) & (\delta_i^j) & (0) \\ -\frac{K_{\rm sp}}{S_{\rm sp}}\,(\delta_i^{N_e+1}\delta_j^{N_e+1}) & (0) & -M\,(\langle\varphi_p,\psi_j'\rangle)^\top \\ \frac{K}{\nu}\,(T_{pj}) & (T_{pj}) & -\frac{M+K}{\nu}\,(\delta_p^q) \end{pmatrix}. \tag{5.65}$$

The three-dimensional array $\boldsymbol{Q}$ is given blockwise by $(Q_{a\bullet\bullet}) = (0)$ if $a = 1,\dots,N_e+1$,

$$\begin{aligned} (Q_{a\bullet\bullet}) &= \begin{pmatrix} (0) & (0) & (0) \\ (0) & \beta M\,(\delta_p^q\langle\varphi_q,\psi_j'\rangle)^\top & (0) \\ (0) & (0) & (0) \end{pmatrix} \quad \text{if} \quad \begin{array}{l} a = N_e+1+j, \\ j = 1,\dots,N_e+1, \end{array} \\ (Q_{a\bullet\bullet}) &= \begin{pmatrix} (0) & (0) & (0) \\ (0) & \beta\frac{M}{\nu}\,(\delta_p^r\delta_q^r) & (0) \\ (0) & (0) & (0) \end{pmatrix} \quad \text{if} \quad \begin{array}{l} a = 2N_e+2+r, \\ r = 1,\dots,N_e. \end{array} \end{aligned} \tag{5.66}$$

Given the definition of the basis functions (5.42)-(5.43) and of the strains (5.45), one has

$$\begin{aligned} (\langle\psi_i,\psi_j\rangle) &= \frac{L_e}{6}\begin{pmatrix} 2 & 1 & 0 & \dots & \\ 1 & 4 & 1 & 0 & \dots \\ \ddots & \ddots & \ddots & \ddots & \ddots \\ \dots & 0 & 1 & 4 & 1 \\ & \dots & 0 & 1 & 2 \end{pmatrix}, \quad (\langle\varphi_p,\varphi_q\rangle) = L_e\,(\delta_p^q), \\ (\langle\varphi_p,\psi_j'\rangle) &= \begin{pmatrix} -1 & 1 & 0 & \dots & \\ 0 & -1 & 1 & 0 & \dots \\ & \ddots & \ddots & \ddots & \ddots \\ & \dots & 0 & -1 & 1 & 0 \\ & & \dots & 0 & -1 & 1 \end{pmatrix}, \quad (T_{pj}) = \frac{1}{L_e}\,(\langle\varphi_p,\psi_j'\rangle). \end{aligned} \tag{5.67}$$

The same procedure is applied to the other cases (5.54)-(5.56) of the study, where the vector $\boldsymbol{q}$ has additional unknowns.

CHAPTER 6

Conclusion

Nonlinear viscoelasticity is not sufficient to reproduce the dynamic behavior of geomaterials observed in laboratory experiments, in particular the non-instantaneous evolution of the elastic modulus (slow dynamics). Progress in the modeling of such phenomena is crucial to be able to perform predictive numerical simulations related to nondestructive evaluation (NDE). The present thesis introduces a model accounting for slow dynamics, and numerical methods to solve the equations of motion. Elastodynamics with polynomial constitutive laws, widely used in nonlinear acoustics, is studied too. Dynamics of nonlinear solids is addressed from numerous perspectives — continuum mechanics, applied mathematics, scientific computing — with a focus on wave propagation aspects.

1. Outcome

A first part of the dissertation is dedicated to nonlinear elastodynamics with polynomial stress-strain relationships (1D), which is the simplest model of nonlinear solid. The contribution on this topic is twofold. Firstly, the solution to the Riemann problem has been detailed (Chapter 3). In particular, the admissibility of each wave solution — shock wave, rarefaction wave, compound wave — has been examined. The classification of solutions so-obtained is represented in the state space, allowing a graphical prediction of the solution. Secondly, numerical methods have been benchmarked using analytical solutions of initial-value problems, such as the Riemann problem (Chapter 2). Classical finite-volume methods and higher-order methods have been implemented. Their performances have been compared, leading to a rationale behind the choice of a well-suited numerical method. As long as the solution stays smooth, one can use an ADER scheme, which is efficient and highly accurate. However, if the solution is discontinuous, one should rather consider using a finite-volume scheme with flux limiter. Despite its flexibility with respect to the smoothness of the solution, the WENO scheme requires much more computational time than the previous methods to reach a given accuracy.

A second part of the manuscript concerns the modeling of particular dissipative behaviors. The modeling of slow dynamics is carried out within the finite-strain theory (Chapter 4). The softening of a hyperelastic material is accounted for by an internal variable of state g, which evolution is chosen as simple as possible, but in agreement with the principles of thermodynamics. The model is designed to reproduce the softening of the material when an acoustic loading is applied, and the recovery to its initial stiffness after the loading is stopped. From a numerical point of view, accounting for the slow dynamics amounts to add a relaxation term in the time-stepping formula of the flux-limiter finite-volume scheme. This has been implemented in longitudinal configurations (1D), where the hyperelastic stress is a cubic polynomial of the strain. Using dimensional splitting, a similar method has been developed in plane-strain configurations (2D), where the hyperelastic stress is issued from the Murnaghan model.

Viscoelastic behavior is an important mechanical property of real materials. The same theoretical framework is used to model the softening of a nonlinear viscoelastic material of generalized Zener type (Chapter 5). The rheology is described by N_v additional variables of state, where N_v is the number of elementary Zener mechanisms. From a numerical point of view, the coupled equations of slow dynamics and viscoelasticity require particular care, since the right-hand side of this system of balance laws is stiff. Using Strang splitting, a high-order finite-volume method has been developed. The main features of dynamic acoustoelastic testing and nonlinear resonance experiments are reproduced numerically with a qualitative agreement. A frequency-domain numerical method has been used to compute time-periodic solutions. The method combines a finite-element semi-discretization, harmonic balance of the nodal values, and the ANM continuation technique. Due to its efficiency, the software tool is useful to investigate the influence of the model parameters on resonance curves, which is promising for prospective experimental validations.

On the continuum mechanics side, a phenomenological model of nonlinear solids has been proposed. In doing so, the concepts of finite strain and of thermodynamics with internal variables have been transferred from rational mechanics to nonlinear acoustics. The simplicity, the thermodynamical consistency and the three-dimensional writing of the model is a step forward with respect to existing models, in our opinion. Also, the flexibility of the modeling approach is valuable for potential future developments. Indeed, more complex constitutive laws may be inserted in the model if they provide a better fit in direct comparisons with laboratory experiments. For instance, one could account for heat conduction, plasticity, irreversible damage, and even material failure.

On the applied mathematics side, the propagation of nonlinear waves has been investigated both analytically and numerically. An analytical solution has been detailed in the hyperelastic case (1D). The developed software tool (available online) could be useful for the validation of numerical methods, e.g. methods used in seismology or in NDE applications. Concerning finite-volume schemes, a variety of methods has been tested and their performances have been evaluated. Analytical methods have been also used to analyze qualitative properties of the developed internal-variable model. Nevertheless, computational methods

can handle more realistic configurations, such as three-dimensional problems issued from laboratory experiments. In a near future, the finite-volume methods presented in this dissertation will be implemented in the PROSPERO code http://prospero-software.science/. One can note that these methods are generic. Indeed, they can be used for other nonlinear systems of balance laws, for instance other nonlinear solid models. The frequency-domain method for the computation of periodic solutions has the same advantage of being generic.

2. Perspectives

The present work introduces several nonlinear hyperbolic systems of balance laws. Such systems of first-order partial differential equations raise mathematical questions. For most of them, the existence, uniqueness, and regularity of solutions are still open questions. Theoretical investigations could also address problems with boundary conditions, and non-homogeneous problems. Answers to these questions serve as a guide for people who develop models. In facts, arbitrary modeling choices can have important implications on the mathematical properties of a system of equations. In addition, the theoretical analysis of solutions has practical consequences in numerical analysis.

Analytical methods of linear acoustics fail in the context of nonlinear solid dynamics, but also several numerical methods do not generalize straightforwardly to nonlinear problems. To name a few, the Explicit Simplified Interface Method (ESIM) is a high-order method to account for arbitrary interfaces in linear acoustics. However, it is unclear if such a method can be adapted efficiently to the nonlinear case. In the same line, Perfectly Matched Layers (PMLs) which provide optimal absorbing boundaries are frequently used in linear acoustics — e.g., in seismology — to simulate unbounded domain. By construction, it seems difficult to transpose the method to the nonlinear case without a loss of performance. The development of similar methods adapted to nonlinear waves is required, so as to make accurate predictions in complex configurations.

Models are useful if they lead to predictions or to explanations of a given phenomenon. To test the predictive abilities of the model, quantitative comparisons with experiments need to be conducted. Experimental validations may motivate further modeling developments, such as modifications and refinements. Over twenty years, numerous experimental datasets have been obtained with the same samples at Los Alamos National Laboratory. However, the experimental conditions have varied from one measurement to another, so that the results of one experiment may have changed over time. Fine tuning of the model is only possible if a large number of measurements is performed under controlled experimental conditions. The diversity of dynamic experiments (resonance, dynamic acousto-elasticity, pulse propagation) allows to examine a sample of rock under different perspectives, which is useful when performing experimental validations. In particular, the experiment which shows a logarithmic time-evolution of the resonance frequency [133] is not yet reproduced with this type of model.

One weakness of the phenomenological modeling approach is its poverty in terms of explanations. Indeed, the developed model introduces a variable of

state g which is not related to any physical peculiarity of the material. To this day, the phenomenon of slow dynamics is observed experimentally, described by phenomenological models, but still not well-understood. An approach following homogenization theory may lead to a physics-based model, provided that relevant assumptions are made at the microscopic scale. Recent experimental observations are potential steps forward in the understanding of slow dynamics. On the one hand, it seems that resonance experiments induce a temperature increase of $\sim 0.1°C$, which cannot be detected without a dedicated apparatus[1]. Preliminary tests suggest that classical thermoelastic coupling is not sufficient to account for this temperature elevation. This feature could be caused by internal friction at interfaces with material heterogeneities (grains, cracks). This scenario would be in agreement with ultrasonic thermography, which consists in measuring the heat flux generated by a vibrating defect. On the other hand, it seems that moisture plays an important role in the non-classical effects [142]. Indeed, dry samples do not exhibit slow dynamics. Moreover, microscope images show that the water embedded in the material flows into micro-pores when the sample is vibrated[2]. Therefore, capillarity may be a cause of the phenomenon. It is worth noting that a formal analogy between the internal-variable model and a model of wet sticking fibers has been outlined. These remarks imply that the porosity of the material should be taken into account in future models. A next step could be the development of a water-unsaturated porous material model in the framework of the finite-strain theory.

[1] Personal communication with C.M. Donahue (Los Alamos National Laboratory).

[2] Personal communication with J.A. Bittner (University of Illinois, Urbana-Champaign).

APPENDIX A

Résumé substantiel

Le contenu du présent manuscrit de thèse est détaillé ci-après. Le sujet de l'étude porte sur le comportement mécanique des géomatériaux tels que le grès et le béton lorsqu'ils sont soumis à un chargement dynamique. Les travaux de thèse recouvrent la modélisation de milieux continus solides déformables, et le développement de méthodes numériques associées.

1. Introduction

En s'appuyant sur la littérature expérimentale, on constate que les roches et le béton sont des solides non linéaires dissipatifs, dont les particularités sont visibles aux petites déformations. Les résultats d'expériences quasi-statiques mettent en évidence l'hystérésis de la relation contrainte-déformation. Des expériences sous chargement dynamique montrent une génération d'harmoniques. De plus, un amollissement est observé, suivi d'un retour aux propriétés élastiques initiales du matériau après l'arrêt de la sollicitation. Ce phénomène met en jeu de longs temps de relaxation (dynamique lente).

Du point de vue de la modélisation, les modèles de viscoélasticité non linéaire permettent de reproduire plusieurs observations expérimentales, hormis la dynamique lente. En dépit d'un accord expérimental et de liens aux propriétés microscopiques du matériau, les modèles d'hystérésis soulèvent des questions pratiques. Effectivement, peu de travaux les emploient dans le cadre de simulations numériques [22, 70, 88]. Une autre classe de modèles en lien avec la modélisation mécanique de l'endommagement a conduit à plusieurs études numériques. En tant que telle, cette démarche constitue une façon cohérente de représenter l'amollissement/raidissement. Cependant, une telle approche ne permet pas d'analyser l'influence de la microstructure du matériau à ce jour.

Les travaux présentés font suite à [38], et s'inscrivent dans le cadre de l'approche phénoménologique issue de la mécanique de l'endommagement. Étant donnée la présence de non-linéarités dans les relations contrainte-déformation, il est nécessaire de traiter l'élasticité non linéaire. Le 2e chapitre est consacré à ce sujet (p. 15). En particulier, le cas de déformations uniaxiales et de lois de comportement polynomiales est étudié, et des schémas volumes finis sont étudiés.

Le 3e chapitre (p. 45) est consacré au calcul de la solution analytique d'un problème de Cauchy particulier où les données initiales sont discontinues (probème de Riemann). On considère des lois de comportement susceptibles de comporter un point d'inflexion, comme c'est le cas de la loi poynomiale cubique. Cette loi de comportement est utilisée comme exemple tout au long du chapitre, et le calcul de la solution est détaillé. Cette solution est utilisée au 2e chapitre pour évaluer les performances de méthodes volumes finis.

Le 4e chapitre (p. 69) présente un modèle de milieu continu à variable interne, analogue à une variable d'endommagement. Ce dernier est construit dans le cadre de la théorie des déformations finies, et satisfait les principes de la thermodynamique. Visant à reproduire la dynamique lente observée expérimentalement, le modèle le plus simple est recherché. Le développement de méthodes numériques de type volumes finis est abordé, et l'amollissement du matériau est reproduit numériquement.

La nécessité d'incorporer de la dissipation viscoélastique est établie expérimentalement. Un tel comportement est ajouté au modèle d'amollissement dans le 5e chapitre (p. 105), dans le cas de déformations uniaxiales (1D). On présente des méthodes volumes finis adaptées, ainsi qu'une méthode de continuation numérique en fréquence pour le calcul de vibrations périodiques. Les résultats montrent un accord qualitatif avec les observations expérimentales. Les conclusions et perspectives sont détaillées dans le 6e chapitre (p. 137).

2. Ondes longitudinales dans les matériaux hyperélastiques

Ce chapitre concerne la propagation d'ondes longitudinales dans un matériau hyperélastique, c.-à-d. un matériau dont la loi de comportement exprime la contrainte en fonction de la déformation. Ici, on s'intéresse à des lois de comportement polynomiales. Une première partie présente les équations de l'hyperélasticité dans un cadre tridimensionnel, duquel on déduit le cas uniaxial. On compare le modèle de Murnaghan à une loi de comportement polynomiale cubique, tous deux étant fréquemment utilisés en acoustique non linéaire. Les équations du mouvement sont récrites sous la forme d'un système hyperbolique de lois de conservation, permettant ainsi d'implémenter des schémas volumes finis conservatifs.

Dans la partie suivante, on compare les performances et le coût de calcul de plusieurs méthodes volumes finis. Les exemples numériques montrent que les solutions discontinues requièrent une attention particulière. En effet, certains schémas introduisent des oscillations dans la solution numérique au voisinage des discontinuités. Les tests conduisent à favoriser les schémas ADER pour le

calcul de solutions régulières, et les schémas à limiteur de flux pour le calcul de solutions discontinues. Un tel schéma numérique a été utilisé dans la publication [4]. Lorsque la régularité de la solution est inconnue, on peut se tourner vers un schéma WENO, construit à partir d'interpolation d'ordre élevé.

Ce chapitre constitue une étude préliminaire de la propagation d'ondes non linéaire dans les géomatériaux. En effet, il est important d'être conscient de ses particularités lors du développement de méthodes numériques en lien avec des observations expérimentales. Le chapitre suivant détaille le calcul d'une solution analytique particulière dans le cas de l'élastodynamique non linéaire. Les chapitres qui suivent sont dédiés à la modélisation de la dynamique lente et de la viscoélasticité dans les solides. Ces modèles s'insèrent dans le même cadre théorique que celui décrit dans le chapitre 2. Les méthodes numériques présentées dans ce chapitre sont transposables au cas de solides à dynamique lente, et aussi au cas multi-dimensionnel (2D).

3. Le problème de Riemann de l'élastodynamique longitudinale

De nombreuses solutions analytiques sont connues dans le cas de l'élasticité linéaire, où la contrainte est proportionnelle à la déformation. En effet, la méthode des caractéristiques permet de résoudre le problème de Cauchy. De plus, la fonction de Green permet de résoudre le système non homogène (2.23) pour la plupart des termes source.

Dans le cas de l'élasticité non linéaire, aucune solution générale n'est connue. Ce chapitre traite de la résolution analytique d'un problème de Cauchy particulier : le problème de Riemann (où les données initiales sont constantes par morceaux). On restreint l'étude au système de lois de conservation (2.23) sans terme source. Aussi, on s'intéresse à des lois de comportement qui possèdent au plus un point d'inflexion dans le domaine d'hyperbolicité. Cette étude a donné lieu à la publication [2].

La solution du problème de Riemann se compose de deux ondes : une onde qui se propage selon les abscisses croissantes, et une onde qui se propage selon les abscisses décroissantes. Lorsque la contrainte est une fonction strictement convexe ou strictement concave de la déformation, l'étude est similaire à celle du "p-system" de la dynamique des gaz. La solution entropique se compose d'ondes de choc ou d'ondes de détente. En revanche, lorsque la relation contrainte-déformation possède un point d'inflexion, la solution peut comporter des ondes composites, qui combinent un choc et une détente.

Les aspects mathématiques de ce problème sont bien établis dans la littérature. La principale contribution de ce travail est de détailler complètement la résolution du problème de Riemann dans le cas de lois de comportement polynomiales cubiques. Dans cette optique, des outils informatiques ont été développés et mis à disposition à l'adresse https://gchiavassa.perso.centrale-marseille.fr/RiemannElasto/. Ces outils ont été utilisés au chapitre précédent pour valider des méthodes numériques. Le problème de Riemann est un cas test exigeant à cause de la discontinuité et de la non-unicité des solutions faibles, comme on peut le voir notamment en présence d'ondes composites.

4. Matériaux hyperélastiques à dynamique lente

Dans ce chapitre, on aborde la modélisation de la dynamique lente par une approche phénoménologique. Le phénomène observé consiste en un amollissement non permanent du matériau sous chargement dynamique. Ce comportement n'est pas reproduit par les modèles d'hyperélasticité, où la vitesse du son est une fonction de la déformation.

Plusieurs modèles de la littérature prennent en compte cet aspect, notamment le modèle phénoménologique de Vakhnenko et coll. [137, 138]. Ce modèle a les caractéristiques suivants :

- une variable g traduit l'amollissement du matériau ;
- une équation décrivant l'évolution de g met en jeu un temps de relaxation ;
- la prise en compte des effets non classiques requiert peu de paramètres.

Des simulations numériques montrent qu'un tel modèle est en accord qualitatif avec les expériences d'acoustoélasticité dynamique [38]. Cependant, ce modèle a été construit dans un cadre unidimensionnel, et aucune version tridimensionnelle n'est connue. De plus, on montre que ce modèle n'est pas thermodynamiquement admissible (annexe du chapitre).

La première partie est consacrée à la construction d'un modèle phénoménologique 3D, dans le cadre des déformations finies. Les notations sont les mêmes que dans le chapitre 2, où on a présenté les équations de l'hyperélasticité. Par rapport au cas hyperélastique, on ajoute ici une variable d'état interne g, qui décrit l'amollissement du matériau. Une loi de comportement mécanique est déduite de l'inégalité de Clausius–Duhem. De plus, on propose une famille d'équations d'évolution pour la variable interne. Contrairement au modèle de Vakhnenko, ce modèle est thermodynamiquement bien posé et tridimensionnel. Ces travaux ont été publiés dans [1].

La partie suivante illustre la propagation d'ondes longitudinales dans des solides non linéaires à dynamique lente. On montre ici comment adapter les méthodes numériques du chapitre 2 afin de prendre en compte la dynamique lente. Des simulations numériques en domaine non borné donnent un accord qualitatif avec les observations expérimentales. Cette étude fait partie de la publication [4].

La troisième partie est consacrée au cas des déformations planes (2D), où une méthode numérique similaire est appliquée. Par *splitting* dimensionnel, le schéma numérique est construit à partir du schéma volumes finis à limiteur de flux 1D. D'abord, on applique la méthode dans le cas de l'hyperélasticité de Murnaghan. Un exemple illustre le couplage entre les ondes de cisaillement et les ondes de compression, phénomène absent en élasticité linéaire. Ensuite la dynamique lente est incorporée au modèle, et on présente un exemple numérique de propagation d'ondes dans un domaine non borné. Ces travaux ont conduit à une soumission d'article [7].

On notera que l'approche est purement phénoménologique, étant donné que la signification physique de g à l'échelle de la microstructure n'est pas connue.

Pour aller plus loin, l'annexe du chapitre propose des analogies avec d'autres modèles issus de la littérature. En effet, des travaux portant sur la modélisation du comportement mécanique des élastomères chargés présentent une certaine similarité. Dans ce contexte, on parle de l'effet Payne [108] et de l'effet Mullins [33, 81] pour décrire la réponse mécanique du matériau.

On mentionne une limitation du présent travail. Dans la limite des petites déformations, le modèle présenté dégénère vers l'élasticité linéaire. Cette propriété n'est pas en accord avec les résultats d'expériences de résonance. Afin de traiter des problèmes plus réalistes, on se doit d'incorporer a minima de la dissipation viscoélastique dans le modèle. Cet aspect est l'objet du chapitre suivant.

5. Dynamique lente d'une barre viscoélastique

Le comportement viscoélastique est un aspect clé de la modélisation de matériaux réels, notamment en vue de reproduire les courbes de résonance [55, 135]. Dans le cadre de l'élasticité linéaire, la littérature comporte de nombreux modèles rhéologiques constitués d'un ensemble de ressorts et d'amortisseurs. Le modèle de solide linéaire standard, aussi appelé modèle de Maxwell ou de Zener généralisé, est utilisé fréquemment pour décrire la propagation d'ondes sismiques [20, 89]. Il est composé d'un ensemble d'éléments de Zener, dont les paramètres sont obtenus par optimisation du facteur de qualité sur une bande de fréquence [16].

Le couplage entre un comportement viscoélastique non linéaire et la dynamique lente est réalisé par l'utilisation de variables internes adéquates. Ce-faisant, un système raide est obtenu, ce qui nécessite une attention particulière lors du recours aux méthodes numériques. Ici, une stratégie de *splitting* est adoptée, combinant un schéma volumes finis ADER avec une méthode d'intégration adaptative d'ordre élevé. Les résultats numériques sont en accord qualitatif avec les observations expérimentales de résonance non linéaire et d'acousto-élasticité dynamique (travaux publiés dans [3]). Parallèlement, une méthode fréquentielle est développée, en combinant une discrétisation éléments finis mixte, la méthode de l'équilibrage harmonique, et la méthode asymptotique numérique. Les résultats montrent une forte sensibilité de la génération d'harmoniques aux paramètres du modèle. Dès lors, la mesure expérimentale des harmoniques générés est cruciale pour une calibration fine des paramètres.

Pour chaque amplitude de forçage, le calcul d'une courbe de résonance dure environ 35 minutes avec la méthode des volumes finis, pour un faible nombre de points sur la courbe. À titre de comparaison, le calcul dure environ 20 secondes avec la méthode fréquentielle, pour obtenir une courbe de résonance continue. Dans l'optique de calibrer le modèle expérimentalement, cette réduction drastique du temps de calcul est un avantage. Cependant, le régime transitoire n'est pas calculé avec la méthode fréquentielle. Ces résultats préliminaires ont été communiqués dans [5]. Étant donné que la contrainte n'est pas une variable conservée, imposer une condition limite en contrainte est difficile avec les volumes finis. La méthode des éléments finis est plus flexible en termes de conditions limites. En effet, il est possible d'imposer des conditions limites en

déplacement ou en contrainte. Une comparaison directe entre les deux méthodes sur le même cas est à l'étude.

Des modifications de la méthode fréquentielle sont envisagées. Tout d'abord, il serait intéressant de suivre la fréquence de résonance continument par rapport à l'amplitude de forçage (*backbone curves*). Ensuite, on pourrait envisager l'utilisation de la base modale du système linéaire non amorti, au lieu des fonctions de base des éléments finis [18, 56, 136]. Enfin, les équations du mouvement pourraient être adimensionnées par rapport aux constantes caractéristiques du système.

6. Conclusion

Ce manuscrit traite de la dynamique de solides non linéaires particuliers. Sur le sujet de l'élastodynamique non linéaire, les principales contributions sont la résolution du problème de Riemann (chapitre 3) et le développement de méthodes volumes finis (chapitre 2). La suite du document traite de la modélisation de comportements viscoélastiques et de la dynamique lente. La dynamique lente est modélisée à l'aide d'une variable d'état interne, dans le cadre de la théorie des déformations finies (chapitre 4). Des méthodes volumes finis ont été développées (1D et 2D). Le même cadre théorique est employé pour décrire le comportement viscoélastique de type Zener généralisé (chapitre 5). Du point de vue numérique, la raideur des équations obtenues nécessite un traitement particulier. Une méthode volumes finis a été développée, et les résultats sont en accord avec la littérature expérimentale. Aussi, une méthode de continuation des solutions périodiques a été utilisée. Son efficacité en fait un outil privilégié pour des validations futures.

Sur le plan de la mécanique des milieux continus, le principal apport concerne la construction de modèles. Les concepts de déformations finies et de variable d'état interne ont été transférés de la mécanique rationnelle à l'acoustique. La simplicité, les bonnes propriétés thermodynamiques et l'écriture tri-dimensionnelle du modèle constituent une avancée par rapport aux modèles existants. De plus, l'approche permet d'envisager des améliorations du modèle (conduction de la chaleur, plasticité, endommagement, etc.).

Sur le plan des mathématiques appliquées, la propagation d'ondes non linéaire a été étudiée. Une solution analytique est détaillée dans le cas de l'élastodynamique 1D, où les solutions analytiques sont rares. Cette solution a notamment permis de tester un ensemble de méthodes volumes finis. Des méthodes analytiques ont aussi été utilisées pour décrire les propriétés qualitatives du modèle à variables internes proposé. Néanmoins, les méthodes numériques permettent de traiter des configurations plus réalistes, telles que des problèmes issus d'expériences de laboratoire. Dans un futur proche, les méthodes volumes finis de ce manuscrit seront implémentées dans le code PROSPERO `http://prospero-software.science/`. On peut noter que ces méthodes peuvent être utilisées pour d'autres systèmes similaires. La méthode fréquentielle mise en œuvre pour le calcul de solutions périodiques a le même avantage d'être générique.

Dans cette thèse, plusieurs systèmes hyperboliques de lois de conservation ont été présentés. De tels systèmes soulèvent des questions mathématiques théoriques (existence, unicité, régularité des solutions). Répondre à ces questions serait une aide à la construction de modèles et au développement de méthodes numériques. De nombreuses méthodes numériques classiques en acoustique linéaire n'ont pas leur équivalent dans le cas non linéaire. C'est le cas notamment de l'ESIM (*Explicit Simplified Interface Method*) et des PMLs (*Perfectly Matched Layers*). Le développement de telles méthodes pour les ondes non linéaires est important dans l'optique d'avoir des outils prédictifs capables de traiter des situations complexes.

L'utilité d'un modèle se mesure à sa capacité à donner des prédictions correctes, ou bien à sa capacité à expliquer un phénomène. Afin de tester les performances de prédiction du modèle, on doit mener des comparaisons quantitatives avec des expériences. La diversité des expériences dynamiques (résonance, acousto-élasticité dynamique, propagation d'onde) permet d'examiner un échantillon sous différents angles. En particulier, les expériences montrant une évolution temporelle logarithmique de la fréquence de résonance [133] n'ont pas encore été reproduites avec ce type de modélisation.

Une faiblesse de l'approche phénoménologique est le manque d'explications physiques. Une approche multi-échelles pourrait conduire à un modèle justifié par la physique, à condition que des hypothèses pertinentes soient faites à l'échelle microscopique. De récents résultats expérimentaux indiquent deux pistes. Un premier scénario, en accord avec la thermographie ultrasonore, stipule que la friction aux interfaces avec des hétérogénéités (grains, fissures) génère un échauffement local, responsable de la dynamique lente. Un second scénario stipule que l'eau présente dans le matériau est aspirée par capillarité lors de la mise en vibration, indiquant l'importance de prendre en compte la porosité du matériau. Une prochaine étape pourrait être le développement d'un modèle de matériau poreux partiellement imprégné d'eau, dans le cadre de la théorie des déformations finies.

Bibliography

As an author

[1] H. Berjamin, N. Favrie, B. Lombard, G. Chiavassa: "Nonlinear waves in solids with slow dynamics: an internal-variable model", *Proc. R. Soc. A* **473**(2201) (2017), 20170024. DOI: 10.1098/rspa.2017.0024

[2] H. Berjamin, B. Lombard, G. Chiavassa, N. Favrie: "Analytical solution to 1D nonlinear elastodynamics with general constitutive laws", *Wave Motion* **74** (2017), 35–55. DOI: 10.1016/j.wavemoti.2017.06.006

[3] H. Berjamin, B. Lombard, G. Chiavassa, N. Favrie: "Modeling longitudinal wave propagation in nonlinear viscoelastic solids with softening", *Int. J. Solids Struct.* **141–142** (2018), 35–44. DOI: 10.1016/j.ijsolstr.2018.02.009

[4] H. Berjamin, B. Lombard, G. Chiavassa, N. Favrie: "A finite-volume approach to 1D nonlinear elastic waves: Application to slow dynamics", *Acta Acust. united Ac.* **104**(4) (2018), 561–570. DOI: 10.3813/AAA.919197

[5] H. Berjamin, G. Chiavassa, N. Favrie, B. Lombard, E. Sarrouy: "Internal-variable modeling of solids with slow dynamics: Wave propagation and resonance simulations", *Proc. Mtgs. Acoust.* **34**(1) (2018), 022001. DOI: 10.1121/2.0000844

[6] H. Berjamin, G. Chiavassa, N. Favrie, B. Lombard, C. Payan: "A unified treatment of nonlinear viscoelasticity and non-equilibrium dynamics". In: *Nonlinear Ultrasonic and Vibro-Acoustical Techniques for Nondestructive Evaluation*. Ed. by T. Kundu. Springer, 2019. Chap. 11, pp. 471–486. DOI: 10.1007/978-3-319-94476-0_11

[7] H. Berjamin, B. Lombard, G. Chiavassa, N. Favrie: "Plane-strain waves in nonlinear elastic solids with softening", submitted (2018).

Other references

[8] J.D. Achenbach: *Wave Propagation in Elastic Solids*. Elsevier, 1973. DOI: 10.1016/C2009-0-08707-8

[9] F.D. Adams, E.G. Cocker: *An Investigation Into the Elastic Constants of Rocks: More Especially with Reference to Cubic Compressibility*. Carnegie Institution of Washington, 1906.

[10] F.D. Adams: "An experimental investigation into the action of differential pressure on certain minerals and rocks, employing the process suggested by Professor Kick", *J. Geol.* **18**(6) (1910), 489–525.

[11] K. Ahnert, M. Mulansky: "Odeint – Solving Ordinary Differential Equations in C++", *AIP Conf. Proc.* **1389** (2011), 1586–1589. DOI: 10.1063/1.3637934

[12] V. Aleshin, K. Van Den Abeele: "Friction in unconforming grain contacts as a mechanism for tensorial stress-strain hysteresis", *J. Mech. Phys. Solids* **55**(4) (2007), 765–787. DOI: 10.1016/j.jmps.2006.10.001

[13] V. Aleshin, K. Van Den Abeele: "Microcontact-based theory for acoustics in microdamaged materials", *J. Mech. Phys. Solids* **55**(2) (2007), 366–390. DOI: 10.1016/j.jmps.2006.07.002

[14] E. Bécache, A. Ezziani, P. Joly: "A mixed finite element approach for viscoelastic wave propagation", *Comput. Geosci.* **8**(3) (2005), 255–299. DOI: 10.1007/s10596-005-3772-8

[15] F. Birch: "The velocity of compressional waves in rocks to 10 kilobars: 1", *J. Geophys. Res.* **65**(4) (1960), 1083–1102. DOI: 10.1029/JZ065i004p01083

[16] É. Blanc, D. Komatitsch, E. Chaljub, B. Lombard, Z. Xie: "Highly accurate stability-preserving optimization of the Zener viscoelastic model, with application to wave propagation in the presence of strong attenuation", *Geophys. J. Int.* **205**(1) (2016), 427–439. DOI: 10.1093/gji/ggw024

[17] O. Bou Matar, P.-Y. Guerder, Y. Li, B. Vandewoestyne, K. Van Den Abeele: "A nodal discontinuous Galerkin finite element method for nonlinear elastic wave propagation", *J. Acoust. Soc. Am.* **131**(5) (2012), 3650–3663. DOI: 10.1121/1.3693654

[18] I.D. Breslavsky, M. Amabili, M. Legrand: "Nonlinear vibrations of thin hyperelastic plates", *J. Sound Vib.* **333**(19) (2014), 4668–4681. DOI: 10.1016/j.jsv.2014.04.028

[19] X. Cai, J. Qiu, J. Qiu: "Finite volume HWENO schemes for nonconvex conservation laws", *J. Sci. Comput.* **75**(1) (2018), 65–82. DOI: 10.1007/s10915-017-0525-5

[20] J.M. Carcione: *Wave Fields in Real Media: Wave Propagation in Anisotropic, Anelastic, Porous and Electromagnetic Media*. 3rd ed. Elsevier, 2015. DOI: 10.1016/C2013-0-18893-9

[21] M. Cervera, M. Chiumenti, R. Codina: "Mixed stabilized finite element methods in nonlinear solid mechanics. Part I: Formulation", *Comput. Methods Appl. Mech. Eng.* **199**(37–40) (2010), 2559–2570. DOI: 10.1016/j.cma.2010.04.006

[22] S. Chabot, N. Glinsky, E.D. Mercerat, L.F. Bonilla Hidalgo: "A high-order discontinuous Galerkin method for 1D wave propagation in a nonlinear heterogeneous medium", *J. Comput. Phys.* **355** (2018), 191–213. DOI: 10.1016/j.jcp.2017.11.013

[23] L. Chazeau, J.D. Brown, L.C. Yanyo, S.S. Sternstein: "Modulus recovery kinetics and other insights into the Payne effect for filled elastomers", *Polym. Compos.* **21**(2) (2000), 202–222. DOI: 10.1002/pc.10178

[24] G. Chiavassa, R. Donat: "Point value multiscale algorithms for 2D compressible flows", *SIAM J. Sci. Comput.* **23**(3) (2001), 805–823. DOI: 10.1137/S1064827599363988

[25] V.K. Chillara, C.J. Lissenden: "Review of nonlinear ultrasonic guided wave nondestructive evaluation: theory, numerics, and experiments", *Opt. Eng.* **55**(1) (2015), 011002. DOI: 10.1117/1.OE.55.1.011002

[26] K.E. Claytor, J.R. Koby, J.A. TenCate: "Limitations of Preisach Theory: Elastic aftereffect, congruence, and end point memory", *Geophys. Res. Lett.* **36**(6) (2009), L06304. DOI: 10.1029/2008GL036978

[27] B. Cochelin, C. Vergez: "A high order purely frequency-based harmonic balance formulation for continuation of periodic solutions", *J. Sound Vib.* **324**(1–2) (2009), 243–262. DOI: 10.1016/j.jsv.2009.01.054

[28] N.G.W. Cook, K. Hodgson: "Some detailed stress-strain curves for rock", *J. Geophys. Res.* **70**(12) (1965), 2883–2888. DOI: 10.1029/JZ070i012p02883

[29] J.M. Cormack, M.F. Hamilton: "Plane nonlinear shear waves in relaxing media", *J. Acoust. Soc. Am.* **143**(2) (2018), 1035–1048. DOI: 10.1121/1.5023394

[30] C.M. Dafermos: *Hyberbolic Conservation Laws in Continuum Physics*. 2nd ed. Springer, 2005. DOI: 10.1007/978-3-642-04048-1

[31] R. Dargazany, M. Itskov: "Constitutive modeling of the Mullins effect and cyclic stress softening in filled elastomers", *Phys. Rev. E* **88**(1) (2013), 012602. DOI: 10.1103/PhysRevE.88.012602

[32] R. De Pascalis, I.D. Abrahams, W.J. Parnell: "On nonlinear viscoelastic deformations: a reappraisal of Fung's quasi-linear viscoelastic model", *Proc. R. Soc. A* **470**(2166) (2014), 20140058. DOI: 10.1098/rspa.2014.0058

[33] J. Diani, B. Fayolle, P. Gilormini: "A review on the Mullins effect", *Eur. Polym. J.* **45**(3) (2009), 601–612. DOI: 10.1016/j.eurpolymj.2008.11.017

[34] A. Dorfmann, R.W. Ogden: "A pseudo-elastic model for loading, partial unloading and reloading of particle-reinforced rubber", *Int. J. Solids Struct.* **40**(11) (2003), 2699–2714. DOI: 10.1016/S0020-7683(03)00089-1

[35] D.S. Drumheller: *Introduction to Wave Propagation in Nonlinear Fluids and Solids*. Cambridge University Press, 1998.

[36] M. Dumbser, T. Schwartzkopff, C.-D. Munz: "Arbitrary high order finite volume schemes for linear wave propagation". In: *Computational Science and High Performance Computing II*. Ed. by E. Krause, Y. Shokin, M. Resch, N. Shokina. Springer, 2006, pp. 129–144. DOI: 10.1007/3-540-31768-6_11

[37] N. Favrie, S. Gavrilyuk, S. Ndanou: "A thermodynamically compatible splitting procedure in hyperelasticity", *J. Comput. Phys.* **270** (2014), 300–324. DOI: 10.1016/j.jcp.2014.03.051

[38] N. Favrie, B. Lombard, C. Payan: "Fast and slow dynamics in a nonlinear elastic bar excited by longitudinal vibrations", *Wave Motion* **56** (2015), 221–238. DOI: 10.1016/j.wavemoti.2015.02.014

[39] R.P. Fedkiw, B. Merriman, R. Donat, S. Osher: "The penultimate scheme for systems of conservation laws: Finite difference ENO with Marquina's flux splitting", *UCLA CAM Report* (1996).

[40] E. Godlewski, P.-A. Raviart: *Numerical Approximation of Hyperbolic Systems of Conservation Laws*. Springer, 1996. DOI: 10.1007/978-1-4612-0713-9

[41] R.A. Guyer, K.R. McCall, G.N. Boitnott, L.B. Hilbert Jr., T.J. Plona: "Quantitative implementation of Preisach–Mayergoyz space to find static and dynamic elastic moduli in rock", *J. Geophys. Res.-Solid Earth* **102**(B3) (1997), 5281–5293. DOI: 10.1029/96JB03740

[42] R.A. Guyer, K.R. McCall, K. Van Den Abeele: "Slow elastic dynamics in a resonant bar of rock", *Geophys. Res. Lett.* **25**(10) (1998), 1585–1588. DOI: 10.1029/98GL51231

[43] R.A. Guyer, P.A. Johnson: "Nonlinear mesoscopic elasticity: Evidence for a new class of materials", *Phys. Today* **52**(4) (1999), 30–36. DOI: 10.1063/1.882648

[44] R.A. Guyer, P.A. Johnson: *Nonlinear Mesoscopic Elasticity: The Complex Behaviour of Granular Media including Rocks and Soil*. Wiley-VCH, 2009. DOI: 10.1002/9783527628261

[45] Y. Hamiel, Y. Liu, V. Lyakhovsky, Y. Ben-Zion, D. Lockner: "A viscoelastic damage model with applications to stable and unstable fracturing", *Geophys. J. Int.* **159**(3) (2004), 1155–1165. DOI: 10.1111/j.1365-246X.2004.02452.x

[46] Y. Hamiel, V. Lyakhovsky, A. Agnon: "Coupled evolution of damage and porosity in poroelastic media: theory and applications to deformation of porous rocks", *Geophys. J. Int.* **156**(3) (2004), 701–713. DOI: 10.1111/j.1365-246X.2004.02172.x

[47] S. Hassani: "Validation et formulation variationnelle d'une loi de comportement viscoélastique non linéaire en grandes déformations". PhD thesis (in French). École Nationale des Ponts et Chaussées, 1997. TEL: 00529389

[48] D.J. Holcomb: "Memory, relaxation, and microfracturing in dilatant rock", *J. Geophys. Res.-Solid Earth* **86**(B7) (1981), 6235–6248. DOI: 10.1029/JB086iB07p06235

[49] G.A. Holzapfel: "On large strain viscoelasticity: continuum formulation and finite element applications to elastomeric structures", *Int. J. Numer. Methods Eng.* **39**(22) (1996), 3903–3926. DOI: 10.1002/(SICI)1097-0207(19961130)39:22<3903::AID-NME34>3.0.CO;2-C

[50] G.A. Holzapfel: *Nonlinear Solid Mechanics: A Continuum Approach for Engineering*. John Wiley & Sons Ltd., 2000.

[51] D.S. Hughes, J.L. Kelly: "Second-order elastic deformation of solids", *Phys. Rev.* **92**(5) (1953), 1145. DOI: 10.1103/PhysRev.92.1145

[52] M. Ismail, F. Ikhouane, J. Rodellar: "The hysteresis Bouc–Wen Model, a survey", *Arch. Comput. Methods. Eng.* **16** (2009), 161–188. DOI: 10.1007/s11831-009-9031-8

[53] G.-S. Jiang, C.-W. Shu: "Efficient implementation of weighted ENO schemes", *J. Comput. Phys.* **126** (1996), 202–228. DOI: 10.1006/jcph.1996.0130

[54] P.A. Johnson, P.N.J. Rasolofosaon: "Nonlinear elasticity and stress-induced anisotropy in rock", *J. Geophys. Res.-Solid Earth* **101**(B2) (1996), 3113–3124. DOI: 10.1029/95JB02880

[55] P.A. Johnson, B. Zinszner, P.N.J. Rasolofosaon: "Resonance and elastic nonlinear phenomena in rock", *J. Geophys. Res.-Solid Earth* **101**(B5) (1996), 11553–11564. DOI: 10.1029/96JB00647

[56] N. Kacem, S. Baguet, S. Hentz, R. Dufour: "Computational and quasi-analytical models for non-linear vibrations of resonant MEMS and NEMS sensors", *Int. J. Non Linear Mech.* **46**(3) (2011), 532–542. DOI: 10.1016/j.ijnonlinmec.2010.12.012

[57] L. Kachanov: *Introduction to Continuum Damage Mechanics*. Springer, 1986. DOI: 10.1007/978-94-017-1957-5

[58] D. Kondo, H. Welemane, F. Cormery: "Basic concepts and models in continuum damage mechanics", *Revue Européenne de Génie Civil* **11**(7–8) (2007), 927–943. DOI: 10.1080/17747120.2007.9692970

[59] I. Kovacic, M.J. Brennan: *The Duffing Equation: Nonlinear Oscillators and their Behaviour*. John Wiley & Sons, 2011. DOI: 10.1002/9780470977859

[60] A. Kurganov, G. Petrova, B. Popov: "Adaptive semidiscrete central-upwind schemes for nonconvex hyperbolic conservation laws", *SIAM J. Sci. Comput.* **29**(6) (2007), 2381–2401. DOI: 10.1137/040614189

[61] S. Kusakabe: "Kinetic measurements of the modulus of elasticity for 158 specimens of rocks: and a note on the relation between the static and the kinetic values of the same", *The journal of the College of Science, Imperial University of Tokyo, Japan* **20** (1905), 1–29.

[62] P.D. Lax: "Development of singularities of solutions of nonlinear hyperbolic partial differential equations", *J. Math. Phys.* **5**(5) (1964), 611–613. DOI: 10.1063/1.1704154

[63] P.D. Lax: *Hyperbolic Systems of Conservation Laws and the Mathematical Theory of Shock Waves*. SIAM, 1973. DOI: 10.1137/1.9781611970562

[64] A.V. Lebedev, L.A. Ostrovsky: "A unified model of hysteresis and long-time relaxation in heterogeneous materials", *Acoust. Phys.* **60**(5) (2014), 555–561. DOI: 10.1134/S1063771014050066

[65] P.G. LeFloch: *Hyperbolic Systems of Conservation Laws: The Theory of Classical and Nonclassical Shock Waves*. Birkhäuser, 2002. DOI: 10.1007/978-3-0348-8150-0

[66] J. Lemaitre, J.-L. Chaboche: *Mechanics of Solid Materials*. Cambridge University Press, 1990. DOI: 10.1017/CBO9781139167970

[67] J. Lemaitre: *A Course on Damage Mechanics*. 2nd ed. Springer, 1996. DOI: 10.1007/978-3-642-18255-6

[68] R.J. LeVeque: *Numerical Methods for Conservation Laws*. Birkhäuser, 1992. DOI: 10.1007/978-3-0348-8629-1

[69] R.J. LeVeque: *Finite Volume Methods for Hyperbolic Problems*. Cambridge University Press, 2002. DOI: 10.1017/CBO9780511791253

[70] Y. Li, O. Bou Matar, B. Li, X. Chen: "Pseudo-spectral simulation of 1D nonlinear propagation in heterogeneous elastic media", *Wave Motion* **52** (2015), 54–65. DOI: 10.1016/j.wavemoti.2014.08.008

[71] I. Lillamand, J.-F. Chaix, M.-A. Ploix, V. Garnier: "Acoustoelastic effect in concrete material under uni-axial compressive loading", *NDT&E Int.* **43**(8) (2010), 655–660. DOI: 10.1016/j.ndteint.2010.07.001

[72] T.P. Liu: "The Riemann problem for general 2×2 conservation laws", *Trans. Amer. Math. Soc.* **199** (1974), 89–112. DOI: 10.1090/S0002-9947-1974-0367472-1

[73] M. Lott, M.C. Remillieux, P.-Y. Le Bas, T.J. Ulrich, V. Garnier, C. Payan: "From local to global measurements of nonclassical nonlinear elastic effects in geomaterials", *J. Acoust. Soc. Am.* **140** (2016), EL231. DOI: 10.1121/1.4962373

[74] V. Lyakhovsky, Y. Podladchikov, P. Alexei: "A rheological model of a fractured solid", *Tectonophysics* **226**(1–4) (1993), 187–198. DOI: 10.1016/0040-1951(93)90117-3

[75] V. Lyakhovsky, Y. Ben-Zion, A. Agnon: "Distributed damage, faulting, and friction", *J. Geophys. Res.-Solid Earth* **102**(B12) (1997), 27635–27649. DOI: 10.1029/97JB01896

[76] V. Lyakhovsky, Y. Hamiel, J.-P. Ampuero, Y. Ben-Zion: "Non-linear damage rheology and wave resonance in rocks", *Geophys. J. Int.* **178**(2) (2009), 910–920. DOI: 10.1111/j.1365-246X.2009.04205.x

[77] V. Lyakhovsky, Y. Hamiel, Y. Ben-Zion: "A non-local visco-elastic damage model and dynamic fracturing", *J. Mech. Phys. Solids* **59**(9) (2011), 1752–1776. DOI: 10.1016/j.jmps.2011.05.016

[78] V. Lyakhovsky, Y. Ben-Zion: "A Continuum Damage–Breakage Faulting Model and Solid-Granular Transitions", *Pure Appl. Geophys.* **171**(11) (2014), 3099–3123. DOI: 10.1007/s00024-014-0845-4

[79] V. Lyakhovsky, Y. Ben-Zion: "Damage–breakage rheology model and solid-granular transition near brittle instability", *J. Mech. Phys. Solids* **64** (2014), 184–197. DOI: 10.1016/j.jmps.2013.11.007

[80] V. Lyakhovsky, Y. Ben-Zion, A. Ilchev, A. Mendecki: "Dynamic rupture in a damage-breakage rheology model", *Geophys. J. Int.* **206**(2) (2016), 1126–1143. DOI: 10.1093/gji/ggw183

[81] G. Machado, G. Chagnon, D. Favier: "Analysis of the isotropic models of the Mullins effect based on filled silicone rubber experimental results", *Mech. Mater.* **42**(9) (2010), 841–851. DOI: 10.1016/j.mechmat.2010.07.001

[82] G.A. Maugin, W. Muschik: "Thermodynamics with internal variables. Part I. General concepts", *J. Non-Equilib. Thermodyn.* **19**(3) (1994), 217–249. DOI: 10.1515/jnet.1994.19.3.217

[83] G.A. Maugin: *The Thermomechanics of Nonlinear Irreversible Behaviors*. World Scientific Publishing, 1999. DOI: 10.1142/3700

[84] G.A. Maugin: "The saga of internal variables of state in continuum thermo-mechanics (1893–2013)", *Mech. Res. Commun.* **69** (2015), 79–86. DOI: 10.1016/j.mechrescom.2015.06.009

[85] K.R. McCall: "Theoretical study of nonlinear elastic wave propagation", *J. Geophys. Res.-Solid Earth* **99**(B2) (1994), 2591–2600. DOI: 10.1029/93JB02974

[86] B. McKavanagh, F.D. Stacey: "Mechanical hysteresis in rocks at low strain amplitudes and seismic frequencies", *Phys. Earth. Planet. In.* **8**(3) (1974), 246–250. DOI: 10.1016/0031-9201(74)90091-0

[87] G.D. Meegan Jr., P.A. Johnson, R.A. Guyer, K.R. McCall: "Observations of nonlinear elastic wave behavior in sandstone", *J. Acoust. Soc. Am.* **94**(6) (1993), 3387–3391. DOI: 10.1121/1.407191

[88] T. Meurer, J. Qu, L.J. Jacobs: "Wave propagation in nonlinear and hysteretic media — a numerical study", *Int. J. Solids Struct.* **39**(21) (2002), 5585–5614. DOI: 10.1016/S0020-7683(02)00366-9

[89] P. Moczo, J. Kristek: "On the rheological models used for time-domain methods of seismic wave propagation", *Geophys. Res. Lett.* **32**(1) (2005), L01306 1–5. DOI: 10.1029/2004GL021598

[90] S. Müller, A. Voss: "The Riemann problem for the Euler equations with nonconvex and nonsmooth equation of state: Construction of wave curves", *SIAM J. Sci. Comput.* **28**(2) (2006), 651–681. DOI: 10.1137/040619909

[91] F.D. Murnaghan: "Finite deformations of an elastic solid", *Am. J. Math.* **59**(2) (1937), 235–260. DOI: 10.2307/2371405

[92] H. Nagaoka: "IV. Elastic constants of rocks and the velocity of seismic waves", *The London, Edinburgh, and Dublin Philosophical Magazine and Journal of Science* **50**(302) (1900), 53–68. DOI: 10.1080/14786440009463891

[93] V.A. Nazarov, L.A. Ostrovsky, I.A. Soustova, A.M. Sutin: "Nonlinear acoustics of micro-inhomogeneous media", *Phys. Earth Planet. In.* **50**(1) (1988), 65–73. DOI: 10.1016/0031-9201(88)90094-5

[94] V.A. Nazarov, A.B. Kolpakov: "Experimental investigations of nonlinear acoustic phenomena in polycrystalline zinc", *J. Acoust. Soc. Am.* **107**(4) (2000), 1915–1921. DOI: 10.1121/1.428473

[95] V.A. Nazarov, A.V. Radostin, L.A. Ostrovsky, I.A. Soustova: "Wave processes in media with hysteretic nonlinearity. Part I", *Acoust. Phys.* **49**(3) (2003), 344–353. DOI: 10.1134/1.1574363

[96] S. Ndanou, N. Favrie, S. Gavrilyuk: "Criterion of hyperbolicity in hyperelasticity in the case of the stored energy in separable form", *J. Elast.* **115**(1) (2014), 1–25. DOI: 10.1007/s10659-013-9440-7

[97] A.N. Norris: "Finite-amplitude waves in solids". In: *Nonlinear Acoustics*. Ed. by M.F. Hamilton, D.T. Blackstock. Academic press, 1998. Chap. 9, pp. 263–277.

[98] R.W. Ogden: *Non-linear Elastic Deformations*. Ellis Harwood Ltd., 1984.

[99] R.W. Ogden, D.G. Roxburgh: "A pseudo-elastic model for the Mullins effect in filled rubber", *Proc. R. Soc. Lond. A* **455**(1988) (1999), 2861–2877. DOI: 10.1098/rspa.1999.0431

[100] L. Ostrovsky, A. Lebedev: "Modeling of processes in structurally nonlinear media with relaxation", *AIP Conf. Proc.* **1474** (2012), 199–202. DOI: 10.1063/1.4749330

[101] L.A. Ostrovsky, P.A. Johnson: "Dynamic nonlinear elasticity in geomaterials", *Riv. Nuovo Cimento* **24**(7) (2001), 1–46.

[102] L.A. Ostrovsky: "Wave interaction in acoustic resonators with and without hysteresis", *J. Acoust. Soc. Am.* **116**(6) (2004), 3348–3353. DOI: 10.1121/1.1823332

[103] Y. Pan, Z. Zhong: "A viscoelastic constitutive modeling of rubber-like materials with the Payne effect", *Appl. Math. Model.* **50** (2017), 621–632. DOI: 10.1016/j.apm.2017.06.018

[104] Y. Pan, Z. Zhong: "Modeling the Mullins effect of rubber-like materials", *Int. J. Damage Mech.* **26**(6) (2017), 933–948. DOI: 10.1177/1056789516635728

[105] D. Pasqualini, K. Heitmann, J.A. TenCate, S. Habib, D. Higdon, P.A. Johnson: "Nonequilibrium and nonlinear dynamics in Berea and Fontainebleau sandstones: Low-strain regime", *J. Geophys. Res.-Solid Earth* **112**(B1) (2007), B01204. DOI: 10.1029/2006JB004264

[106] C. Payan, V. Garnier, J. Moysan, P.A. Johnson: "Determination of third order elastic constants in a complex solid applying coda wave interferometry", *Appl. Phys. Lett.* **94** (2009), 011904. DOI: 10.1063/1.3064129

[107] C. Payan, T.J. Ulrich, P.Y. Le Bas, T. Saleh, M. Guimaraes: "Quantitative linear and nonlinear resonance inspection techniques and analysis for material characterization: Application to concrete thermal damage", *J. Acoust. Soc. Am.* **136**(2) (2014), 537–546. DOI: 10.1121/1.4887451

[108] A.R. Payne: "The dynamic properties of carbon black-loaded natural rubber vulcanizates. Part I", *J. Appl. Polym. Sci.* **6**(19) (1962), 57–63. DOI: 10.1002/app.1962.070061906

[109] C. Pecorari: "Adhesion and nonlinear scattering by rough surfaces in contact: Beyond the phenomenology of the Preisach–Mayergoyz framework", *J. Acoust. Soc. Am.* **116**(4) (2004), 1938–1947. DOI: 10.1121/1.1785616

[110] C. Pecorari: "A constitutive relationship for mechanical hysteresis of sandstone materials", *Proc. R. Soc. A* **471** (2015), 20150369. DOI: 10.1098/rspa.2015.0369

[111] C. Pecorari: "Modeling the elasto-acoustic hysteretic nonlinearity of dry Berea sandstone", *Wave Motion* **52** (2015), 66–80. DOI: 10.1016/j.wavemoti.2014.09.001

[112] C. Py, R. Bastien, J. Bico, B. Roman, A. Boudaoud: "3D aggregation of wet fibers", *Europhys. Lett.* **77**(4) (2007), 44005. DOI: 10.1209/0295-5075/77/44005

[113] J.-M. Qiu, C.-W. Shu: "Convergence of high order finite volume weighted essentially nonoscillatory scheme and discontinuous Galerkin method for nonconvex conservation laws", *SIAM J. Sci. Comput.* **31**(1) (2008), 584–607. DOI: 10.1137/070687487

[114] J. Régnier, L.-F. Bonilla, P.-Y. Bard, E. Bertrand, F. Hollender, H. Kawase, D. Sicilia, et al.: "International benchmark on numerical simulations for 1D, nonlinear site response (PRENOLIN): Verification phase based on canonical cases", *Bull. Seism. Soc. Am.* **106**(5) (2016), 2112–2135. DOI: 10.1785/0120150284

[115] M.C. Remillieux, R.A. Guyer, C. Payan, T.J. Ulrich: "Decoupling nonclassical nonlinear behavior of elastic wave types", *Phys. Rev. Lett.* **116**(11) (2016), 115501 1–5. DOI: 10.1103/PhysRevLett.116.115501

[116] M.C. Remillieux, T.J. Ulrich, H.E. Goodman, J.A Ten Cate: "Propagation of a finite-amplitude elastic pulse in a bar of Berea sandstone: A detailed look at the mechanisms of classical nonlinearity, hysteresis, and nonequilibrium dynamics", *J. Geophys. Res.-Solid Earth* **122**(11) (2017), 8892–8909. DOI: 10.1002/2017JB014258

[117] G. Renaud, P.-Y. Le Bas, P.A. Johnson: "Revealing highly complex elastic nonlinear (anelastic) behavior of Earth materials applying a new probe: Dynamic acoustoelastic testing", *J. Geophys. Res.-Solid Earth* **117**(B6) (2012), B06202. DOI: 10.1029/2011JB009127

[118] J. Rivière, G. Renaud, R.A. Guyer, P.A. Johnson: "Pump and probe waves in dynamic acousto-elasticity: comprehensive description and comparison with nonlinear elastic theories", *J. Appl. Phys.* **114**(5) (2013), 054905. DOI: 10.1063/1.4816395

[119] R.S. Rivlin: "Large elastic deformations of isotropic materials. IV. Further developments of the general theory", *Philos. T. R. Soc. A* **241**(835) (1948), 379–397. DOI: 10.1098/rsta.1948.0024

[120] E.C. Robertson: "Experimental study of the strength of rocks", *Geol. Soc. Am. Bull.* **66**(10) (1955), 1275–1314. DOI: 10.1130/0016-7606(1955)66[1275:ESOTSO]2.0.CO;2

[121] E. Sarrouy, J.-J. Sinou: "Non-Linear Periodic and Quasi-Periodic Vibrations in Mechanical Systems - On the use of the Harmonic Balance Methods". In: *Advances in Vibration Analysis Research*. Ed. by F. Ebrahimi. InTech, 2011. Chap. 21, pp. 419–434. DOI: 10.5772/15638

[122] M. Scalerandi, P.P. Delsanto, P.A. Johnson: "Stress induced conditioning and thermal relaxation in the simulation of quasi-static compression experiments", *J. Phys. D: Appl. Phys.* **36** (2003), 288–293. DOI: 10.1088/0022-3727/36/3/311

[123] F. Schubert: "Numerical time-domain modeling of linear and nonlinear ultrasonic wave propagation using finite integration techniques — theory and applications", *Ultrasonics* **42**(1–9) (2004), 221–229. DOI: 10.1016/j.ultras.2004.01.013

[124] T. Schwartzkopff, M. Dumbser, C.-D. Munz: "Fast high order ADER schemes for linear hyperbolic equations", *J. Comput. Phys.* **197**(2) (2004), 532–539. DOI: 10.1016/j.jcp.2003.12.007

[125] M. Shearer, Y. Yang: "The Riemann problem for a system of conservation laws of mixed type with a cubic nonlinearity", *Proc. Roy. Soc. Edinb. A* **125**(4) (1995), 675–699. DOI: 10.1017/S0308210500030298

[126] C.-W. Shu, S. Osher: "Efficient implementation of essentially non-oscillatory shock-capturing schemes", *J. Comput. Phys.* **77** (1988), 439–471. DOI: 10.1016/0021-9991(88)90177-5

[127] C.-W. Shu, S. Osher: "Efficient implementation of essentially non-oscillatory shock-capturing schemes, II", *J. Comput. Phys.* **83** (1989), 32–78. DOI: 10.1016/0021-9991(89)90222-2

[128] C.-W. Shu: "High order weighted essentially nonoscillatory schemes for convection dominated problems", *SIAM Rev.* **51**(1) (2009), 82–126. DOI: 10.1137/070679065

[129] J. Smoller: *Shock Waves and Reaction-Diffusion Equations*. 2nd ed. Springer, 1994. DOI: 10.1007/978-1-4612-0873-0

[130] G. Strang: "Accurate partial difference methods I: Linear Cauchy problems", *Arch. Ration. Mech. An.* **12**(1) (1963), 392–402. DOI: 10.1007/BF00281235

[131] J.A. TenCate, K.E.A. Van Den Abeele, T.J. Shankland, P.A. Johnson: "Laboratory study of linear and nonlinear elastic pulse propagation in sandstone", *J. Acoust. Soc. Am.* **100**(3) (1996), 1383–1391. DOI: 10.1121/1.415985

[132] J.A. TenCate: "Slow dynamics in the nonlinear elastic response of Berea sandstone", *Geophys. Res. Lett.* **23**(21) (1996), 3019–3022. DOI: 10.1029/96GL02884

[133] J.A. TenCate, E. Smith, R.A. Guyer: "Universal slow dynamics in granular solids", *Phys. Rev. Lett.* **85**(5) (2000), 1020–1023. DOI: 10.1103/PhysRevLett.85.1020

[134] J.A. TenCate, D. Pasqualini, S. Habib, K. Heitmann, D. Higdon, P.A. Johnson: "Nonlinear and nonequilibrium dynamics in geomaterials", *Phys. Rev. Lett.* **93**(6) (2004), 065501. DOI: 10.1103/PhysRevLett.93.065501

[135] J.A. TenCate: "Slow dynamics of earth materials: An experimental overview", *Pure Appl. Geophys.* **168**(12) (2011), 2211–2219. DOI: 10.1007/s00024-011-0268-4

[136] C. Touzé, O. Thomas, A. Chaigne: "Hardening/softening behaviour in non-linear oscillations of structural systems using non-linear normal modes", *J. Sound Vib.* **273**(1–2) (2004), 77–101. DOI: 10.1016/j.jsv.2003.04.005

[137] O.O. Vakhnenko, V.O. Vakhnenko, T.J. Shankland, J.A. Ten Cate: "Strain-induced kinetics of intergrain defects as the mechanism of slow dynamics in the nonlinear resonant response of humid sandstone bars", *Phys. Rev. E* **70**(1) (2004), 015602. DOI: 10.1103/PhysRevE.70.015602

[138] O.O. Vakhnenko, V.O. Vakhnenko, T.J. Shankland: "Soft-ratchet modeling of end-point memory in the nonlinear resonant response of sedimentary rocks", *Phys. Rev. B* **71**(17) (2005), 174103. DOI: 10.1103/PhysRevB.71.174103

[139] K.E.-A. Van Den Abeele, P.A. Johnson: "Elastic pulsed wave propagation in media with second-or higher-order nonlinearity. Part II. Simulation of experimental measurements on Berea sandstone", *J. Acoust. Soc. Am.* **99**(6) (1996), 3346–3352. DOI: 10.1121/1.414891

[140] K.E.-A. Van Den Abeele, P.A. Johnson, R.A. Guyer, K.R. McCall: "On the quasi-analytic treatment of hysteretic nonlinear response in elastic wave propagation", *J. Acoust. Soc. Am.* **101**(4) (1997), 1885–1898. DOI: 10.1121/1.418198

[141] K.E.-A. Van Den Abeele, P.A. Johnson, A. Sutin: "Nonlinear elastic wave spectroscopy (NEWS) techniques to discern material damage, part I: Nonlinear wave modulation spectroscopy (NWMS)", *Res. Nondestr. Eval.* **12**(1) (2000), 17–30. DOI: 10.1080/09349840009409646

[142] K.E.-A. Van Den Abeele, J. Carmeliet, P.A. Johnson, B. Zinszner: "Influence of water saturation on the nonlinear elastic mesoscopic response in Earth materials and the implications to the mechanism of nonlinearity", *J. Geophys. Res.-Solid Earth* **107**(B6) (2002), 2121. DOI: 10.1029/2001JB000368

[143] E. Verron: "Modélisation du comportement des structures et des matériaux élastomères". Habilitation thesis (in French). Université de Nantes, 2003. TEL: 00833719

[144] A. Visintin: "Mathematical models of hysteresis". In: *The Science of Hysteresis Volume 1*. Ed. by I. Mayergoyz, G. Bertotti. Elsevier, 2005. Chap. 1, pp. 1–123.

[145] A. Voss: "Exact Riemann solution for the Euler equations with nonconvex and nonsmooth equation of state". PhD thesis. RWTH Aachen, 2005.

[146] B. Wendroff: “The Riemann problem for materials with nonconvex equations of state I: Isentropic flow”, *J. Math. Anal. Appl.* **38**(2) (1972), 454–466. DOI: 10.1016/0022-247X(72)90103-5

Modeling wave propagation in nonlinear solids with slow dynamics

■ *Abstract.* Geomaterials such as rocks and concrete are known to soften under a dynamic loading, i.e., the speed of sound diminishes with forcing amplitudes. To reproduce this behavior, an internal-variable model of continuum is proposed. It is composed of a constitutive law for the stress and an evolution equation for the internal variable. Nonlinear viscoelasticity of Zener type is accounted for by using additional internal variables. The equations of motion write as a nonlinear and nonhomogeneous system of conservation laws. This system of partial differential equations is solved numerically using finite-volume methods. An analytical solution to the Riemann problem of nonlinear elastodynamics is provided, which is used to benchmark the performances of the numerical methods. Numerical results are in qualitative agreement with experimental results from resonance experiments (NRUS) and dynamic acousto-elastic testing (DAET). Similar methods are developed in 2D to perform wave propagation simulations. In the framework of harmonic-based continuation methods, a numerical method is developed for the computation of periodic solutions. Based on a finite element discretization of the equations of motion, this frequency-domain method provides fast resonance simulations, which is useful to carry out experimental validations.

Keywords : Nonlinear acoustics, Solid mechanics, Numerical methods.

Modélisation de la propagation d'ondes dans des solides non linéaires à dynamique lente

■ *Résumé.* Les géomatériaux tels les roches et le béton ont la particularité de s'amollir sous chargement dynamique, c.-à-d. que la vitesse du son diminue avec l'amplitude de forçage. Afin de reproduire ce comportement, un modèle de milieu continu à variables internes est proposé. Il est composé d'une loi de comportement donnant l'expression de la contrainte, et d'une équation d'évolution pour la variable interne. La viscoélasticité non linéaire de type Zener est prise en compte par l'ajout de variables internes supplémentaires. Les équations du mouvement forment un système de lois de conservation non linéaire et non homogène. Le système d'équations aux dérivées partielles est résolu numériquement à l'aide de la méthode des volumes finis. Une solution analytique du problème de Riemann de l'élastodynamique non linéaire est explicitée. Elle est utilisée pour évaluer les performances des méthodes numériques. Les résultats numériques sont en accord qualitatif avec les résultats expérimentaux d'expériences de résonance (NRUS) et d'acousto-élasticité dynamique (DAET). Des méthodes similaires sont développées en 2D pour réaliser des simulations de propagation d'ondes. Dans le cadre des méthodes de continuation reposant sur la décomposition en harmoniques, une méthode numérique est développée pour le calcul de solutions périodiques. Sur la base d'une discrétisation éléments finis des équations du mouvement, cette méthode fréquentielle donne des simulations de résonance rapides, ce qui est utile pour mener des validations expérimentales.

Mots-clés : Acoustique non linéaire, Mécanique du solide, Méthodes numériques.